



ARL-CR-0766 • MAR 2015



US Army Research Laboratory Materials Center of Excellence

Dynamic Behavior and Optimization of Advanced Armor Ceramics: January–December 2011 Annual Report

edited by RA Haber
Recipient Program Manager
Director, Center for Ceramic Research
Rutgers, The State University of New Jersey
607 Taylor Road, Piscataway, NJ 08854-8065

and

JW McCauley (Emeritus)
Cooperative Agreement Manager
US Army Research Laboratory
Weapons and Materials Research Directorate, ARL
Aberdeen Proving Ground, MD 21005-5066

under contract W911NF-06-2-0007

Approved for public release; distribution is unlimited.

NOTICES

Disclaimers

The findings in this report are not to be construed as an official Department of the Army position unless so designated by other authorized documents.

Citation of manufacturer's or trade names does not constitute an official endorsement or approval of the use thereof.

Destroy this report when it is no longer needed. Do not return it to the originator.



US Army Research Laboratory Materials Center of Excellence

Dynamic Behavior and Optimization of Advanced Armor Ceramics: January–December 2011 Annual Report

edited by RA Haber
Recipient Program Manager
Director, Center for Ceramic Research
Rutgers, The State University of New Jersey
607 Taylor Road, Piscataway, NJ 08854-8065

and

JW McCauley (Emeritus)
Cooperative Agreement Manager
US Army Research Laboratory
Weapons and Materials Research Directorate, ARL
Aberdeen Proving Ground, MD 21005-5066

under contract W911NF-06-2-0007

Approved for public release; distribution is unlimited.

REPORT DOCUMENTATION PAGE				Form Approved OMB No. 0704-0188	
<p>Public reporting burden for this collection of information is estimated to average 1 hour per response, including the time for reviewing instructions, searching existing data sources, gathering and maintaining the data needed, and completing and reviewing the collection information. Send comments regarding this burden estimate or any other aspect of this collection of information, including suggestions for reducing the burden, to Department of Defense, Washington Headquarters Services, Directorate for Information Operations and Reports (0704-0188), 1215 Jefferson Davis Highway, Suite 1204, Arlington, VA 22202-4302. Respondents should be aware that notwithstanding any other provision of law, no person shall be subject to any penalty for failing to comply with a collection of information if it does not display a currently valid OMB control number.</p> <p>PLEASE DO NOT RETURN YOUR FORM TO THE ABOVE ADDRESS.</p>					
1. REPORT DATE (DD-MM-YYYY) March 2015		2. REPORT TYPE Annual Report		3. DATES COVERED (From - To) 1 January–31 December 2011	
4. TITLE AND SUBTITLE US Army Research Laboratory Materials Center of Excellence Dynamic Behavior and Optimization of Advanced Armor Ceramics: January–December 2011 Annual Report				5a. CONTRACT NUMBER W911NF-06-2-0007	
				5b. GRANT NUMBER	
				5c. PROGRAM ELEMENT NUMBER	
6. EDITOR(S) RA Haber and JW McCauley				5d. PROJECT NUMBER	
				5e. TASK NUMBER	
				5f. WORK UNIT NUMBER	
7. PERFORMING ORGANIZATION NAME(S) AND ADDRESS(ES) Director, Center for Ceramic Research US Army Research Rutgers, The State University of New Laboratory Jersey RDRL-WM 607 Taylor Road Aberdeen Proving Ground, Piscataway, NJ 08854-8065 MD 21005-5069				8. PERFORMING ORGANIZATION REPORT NUMBER	
9. SPONSORING/MONITORING AGENCY NAME(S) AND ADDRESS(ES) US Army Research Laboratory ATTN: RDRL-WM Aberdeen Proving Ground, MD 21005-5069				10. SPONSOR/MONITOR'S ACRONYM(S) ARL	
				11. SPONSOR/MONITOR'S REPORT NUMBER(S) ARL-CR-0766	
12. DISTRIBUTION/AVAILABILITY STATEMENT Approved for public release; distribution is unlimited.					
13. SUPPLEMENTARY NOTES					
14. ABSTRACT This Materials Center of Excellence program has been conducted as a seamless, synergistic collaboration among the following institutions: Rutgers Malcolm G McLaren Center for Ceramic Research, Penn State Particulate Research Center, The Johns Hopkins Center for Advanced Metal and Ceramic Systems, and the US Army Research Laboratory's Weapons and Materials Research Directorate. The following tasks are reviewed: Nanostructured Armor Ceramics: Boron Carbide Powder Synthesis; the Role of Microstructure in the Ballistic Performance for Silicon Carbide; High-Strain-Rate Behavior and Dynamic Failure of Armor Ceramics; Identification of Fundamental Deformation and Failure Mechanisms in Armor Ceramics; Multiscale Computational Investigations of Interfaces Relevant to Structural Ceramics; Microstructural Tailoring: Particle Coating for Silicon Carbide; Study of US Silicon Carbide Powder Variations; Defining Microstructural Tolerance Limits of Defects for Silicon Carbide; and Nondestructive Characterization.					
15. SUBJECT TERMS armor ceramics, boron carbide, silicon carbide, powders, modeling, high strain-rate testing, NDC					
16. SECURITY CLASSIFICATION OF:			17. LIMITATION OF ABSTRACT UU	18. NUMBER OF PAGES 236	19a. NAME OF RESPONSIBLE PERSON James W McCauley
a. REPORT Unclassified	b. ABSTRACT Unclassified	c. THIS PAGE Unclassified			19b. TELEPHONE NUMBER (include area code) 410-306-0711

Contents

List of Figures	viii
List of Tables	xvii
1. Introduction	1
1.1 Core Programs	1
1.2 Supplementally Funded Program Modifications	1
1.3 Supplemental Funded Programs through Rutgers' Ceramic, Composite, and Optical Materials Center (CCOMC)	2
2. Task 1: Nanostructured Armor Ceramics, Maneuver Center of Excellence (MCOE) Core Program and Task 6: B₄C Powder Synthesis (supplementally funded program)	3
2.1 Long-Range Objectives	3
2.2 Background	3
2.3 Current Status of the Rapid Carbothermic Reduction Furnace	4
2.4 B ₄ C Precursor Preparation	7
2.5 Production of B ₄ C in the Rapid Carbothermic Reduction Furnace	8
2.5.1 BC-ST1	10
2.5.2 BC-DR1	10
2.5.3 BC-DR7	11
2.5.4 BC-SF1	11
2.5.5 X-ray Diffraction	12
2.6 Spark-Plasma-Sintered B ₄ C	16
2.7 Conclusions and Future Work	16
2.8 References	18
3. Task 2: The Role of Microstructure in the Ballistic Performance of Silicon Carbide (SiC), Core Program and Task 8: Microstructural Tailoring: Particle Coating for SiC, US Army Research Laboratory (ARL) Supplemental	19
3.1 Long-Range Objectives	19

3.2	Objectives for Calendar Year 2011	19
3.3	Background	20
3.4	Summary of Previous Results	23
3.5	Experimental Procedure	23
3.6	Results	24
3.7	Conclusion and Future Work	31
3.8	References	32
4.	Task 3: High-Strain-Rate Behavior and Dynamic Failure of Armor Ceramics, Core Program	34
4.1	Long-Range Objectives	34
4.2	Accomplishments	34
4.3	Collaborative Interactions	37
4.4	Publications and Presentations	37
5.	Task 4: Identification of Fundamental Deformation and Failure Mechanisms in Armor Ceramics	38
5.1	Long-Range Objectives	38
5.2	Planned Objectives for 2011 Calendar Year	38
5.3	Introduction	39
5.4	Experimental Procedure	39
5.4.1	Materials	39
5.5	Equipment	41
5.6	Results and Discussion	42
5.6.1	Surface Indentation Damage	42
5.6.2	Subsurface Indentation Damage	46
5.6.3	Indentation Stress-Strain	50
5.6.4	Work of Indentation	53
5.7	Conclusions	60
5.8	References	62
6.	Task 5: Education and Outreach Activities, Core Program	65
6.1	Long-Range Objectives	65

6.2	Objectives for the Period	65
6.3	Progress on Objectives	65
6.3.1	Ceramic Armor Industrial Group Workshops	65
6.3.2	Review/Planning Meetings	66
7.	Task 6: Boron Carbide (B₄C) Powder Synthesis, Supplemental Program Attached to Task 1	67
7.1	Long-Range Objectives	67
8.	Task 7: Multiscale Computational Investigations of Interfaces Relevant to Structural Ceramics	68
8.1	Long-Range Goals	68
8.2	Background: Armor Ceramic Materials	68
8.3	Multiscale Computational Approach	69
8.4	Project Overview	71
8.5	SiC/B ₄ C Interfaces: Introduction	71
8.6	Computational Methods	73
8.6.1	DFT Calculations	73
8.6.2	DFT-MD Simulations	75
8.7	Results and Discussion	76
8.7.1	Geometry Optimization of B ₄ C Isomers	77
8.7.2	Geometry Optimization of SiC Unit Cells	79
8.7.3	Nanoscale SiC/B ₄ C Interfaces	80
8.7.4	Four B ₄ C/IGF Interfaces: Introduction	82
8.8	Computational Methods	85
8.8.1	DFT Calculations	85
8.8.2	DFT-MD Simulations	85
8.9	Results and Discussion	86
8.10	Expected Implications	89
8.11	Future Work	90
8.12	References	92
	Task 9: Study of US Silicon Carbide Powder Variations	98
9.1	Long-Range Goals	98

9.2	Background	98
9.3	Experimental Approach	99
9.4	Results and Discussion	103
9.5	Future Work	116
9.6	References	117
Task 10: Defining Microstructural Tolerance Limits of Defects for Silicon Carbide Armor		118
10.1	Long-Range Goal	118
10.2	Introduction	118
10.3	Initiation of Study/NDE/Tile Selection	119
10.4	Bend Bar Machining	125
10.5	MOR/Weibull Analysis	126
10.6	Primary Fracture Location/NDE Map Overlay Diagrams	139
10.7	Fractography	144
10.8	NDE Analysis	154
10.9	Future Work	160
10.10	References	161
Task 11: Nondestructive Characterization of Armor Ceramic		163
11.1	Long-Range Objectives	163
11.2	Objectives for Performance Period	163
11.3	Accomplishments	164
11.4	Background	164
11.5	Current Work	165
11.5.1	Full-Wave Acoustic Signal Analysis Software, by Andrew Portune, Steve Bottiglieri, and Vincent DeLucca	165
11.5.2	Technique Optimization: An Understanding of Scattering in Ceramics, by Steve Bottiglieri	171
11.5.3	Ultrasonic NDE for Homogeneity of SiC-N, by Vincent DeLucca	173
11.5.4	Ultrasonic NDC for Grain Size Determination in Spinel, by Vincent DeLucca	176

11.5.5	Ultrasonic NDC for Grain Size Determination in Zirconium Dioxide Absorption, by Steve Bottiglieri	179
11.5.6	Ultrasonic NDE Analysis and Microstructural Comparison of Al_2O_3 Densification Variation Samples, by Vincent DeLucca	183
11.6	Evaluation of Microstructural Evolution Al_2O_3 Sample Series: Grain Size, Ultrasonic Attenuation Coefficient, and Hardness Relationships, by Steve Bottiglieri	189
11.7	Development of a Relationship Between Ultrasonic Attenuation Coefficient and Grain Size Variation in Al_2O_3	193
11.8	Investigation of Acoustic Absorption and Secondary Phase Size Distributions in Custom-Engineered Al_2O_3 , by Steve Bottiglieri	203
11.9	Future Work	211
11.9.1	Spinel Standard Sample Set for the Determination of Grain Size	211
11.9.2	Custom-Engineered Alumina Sample Set: Varying TiC Concentration	211
11.9.3	Custom-Engineered SiC Sample Set: Varying Grain Size and Additive Concentration	211
11.9.4	Ultrasound NDC to Determine Microstructural Homogeneity in SiC Mirrors	212
11.10	References	213
	List of Symbols, Abbreviations, and Acronyms	214
	Distribution List	216

List of Figures

Fig. 2.1	Rapid carbothermic reduction furnace design	5
Fig. 2.2	Cu cold finger design	6
Fig. 2.3	Rapid carbothermic reduction furnace with Cu cold finger and screw feed.....	7
Fig. 2.4	Basic B ₄ C precursor preparation method.....	7
Fig. 2.5	SEM micrograph of static (batch) processed B ₄ C; average particle size = 6.7 μ m	10
Fig. 2.6	SEM micrographs of B ₄ C from a 2-g drop test using lampblack as a C source; average particle size = 1.2 μ m.....	11
Fig. 2.7	SEM micrographs of B ₄ C from a 2-g drop test using corn starch as a C source; D(0.9) = 1.27 μ m	11
Fig. 2.8	SEM micrograph of B ₄ C from a screw feed sample using lampblack as a C source; average particle size = 1.15 μ m	12
Fig. 2.9	XRD spectra for a static run (BC-ST1), a drop test run (BC-DR1), and a commercial powder	13
Fig. 2.10	B-to-C ratios of Rutgers and commercial B ₄ C powders shown in B ₄ C phase field	15
Fig. 2.11	SEM micrographs of (left) spark-plasma-sintered B ₄ C from screw feed sample BC-SF1 using lampblack as a C source and (right) Knoop hardness indent at 1 kg.....	16
Fig. 2.12	Experiment matrix showing processing parameters	17
Fig. 3.1	SEM micrographs of a) ball-milled and b) precipitated 40% AlN and 60% Y ₂ O ₃ mol of additives, c) ball-milled and d) precipitated 60% AlN and 40% Y ₂ O ₃ mol of additives, and e) ball-milled and f) precipitated 80% AlN and 20% Y ₂ O ₃ mol of additives	26
Fig. 3.2	Knoop hardness graphs of a) ball milled and b) precipitated samples	27
Fig. 3.3	TEM images of the prepared a) ball-milled and b) co-precipitated samples.....	27
Fig. 3.4	Ball-milled TEM micrographs of a) elemental mapping consisting of Y, Al, and O; b) dark field image; c) mapping of Y; d) mapping of Al; and e) mapping of O	29
Fig. 3.5	Co-precipitated TEM micrographs of a) elemental mapping of Y, Al, and O; b) dark field image; c) mapping of Y; d) mapping of Al; and e) mapping of O	30
Fig. 4.1	Failure mechanism map in the confining stress and strain-rate space	35

Fig. 4.2	Bright-field TEM imaging of an AlN fragment, capturing a transgranular crack being arrested interior of the crystal, with profuse dislocations either along the crack path or at the crack tip. Insets are zoom-in views of the crack tip stopping interior of the crystal and selected area electron diffraction of the AlN crystal, respectively.	36
Fig. 4.3	Specimen assembly a) and b) profuse dislocations observed after deformation (shock stress ~10 GPa)	36
Fig. 5.1	DIC images showing the typically observed cracking modes in the fine-grained spinel after the application of (a) 50-N, (b) 100-N, and (c) 200-N maximum compressive forces, using a 261- μ m-radius diamond indenter	43
Fig. 5.2	DIC images showing the typically observed cracking modes in the coarse-grained spinel after the application of (a) 50-N, (b) 100-N, and (c) 200-N maximum compressive forces, using a 261- μ m-radius diamond indenter	43
Fig. 5.3	DIC images showing the typically observed cracking modes in AlON after the application of (a) 50-N, (b) 100-N, and (c) 200-N maximum compressive forces, using a 261- μ m-radius diamond indenter	43
Fig. 5.4	DIC images showing the typically observed cracking modes in AlN after the application of (a) 50-N, (b) 100-N, and (c) 200-N maximum compressive forces, using a 261- μ m-radius diamond indenter. A ring (yellow) and radial (white) crack are arrowed.	43
Fig. 5.5	Optical micrograph showing an example of deformation cleavage (dark bands) inside an 80-N indentation in AlON produced with 261- μ m-radius diamond indenter.....	45
Fig. 5.6	Profilometer line scans showing the typical surface profiles at maximum loads of 50 N, 100 N, and 200 N of a) fine-grained spinel, b) coarse-grained spinel, c) AlON, and d) AlN as a function of the applied force. All indentations were made using a 261- μ m-radius diamond indenter.	46
Fig. 5.7	SEM micrographs showing the fractured surface of a 4-point bend bar, in which an indentation of 300 N was placed in the fine-grained spinel prior to bend failure. The arrow points to a remnant indenter surface impression and intergranular fracture region below the indentation site. Away from the contact region, the fracture surface is transgranular and believed to be a result of only the bend stresses.	47
Fig. 5.8	SEM micrographs showing the fractured surface of a 4-point bend bar, in which an indentation of 200 N was placed in AlON prior to bend failure. The arrow points to a remnant indenter surface impression and microcracked fracture region below the indentation site. Away from the contact region, the fracture surface is transgranular and results from the bend stresses.	48

Fig. 5.9	SEM micrographs showing the fractured surface of a 4-point bend bar, in which an indentation of 200 N was placed in AlN prior to bend failure. The arrow points to a remnant indenter surface impression and median-crack below the indentation site. Away from the contact region, the fracture surface is also intergranular as is the region directly below the contact.	48
Fig. 5.10	SEM micrographs showing the 2 corresponding fractured surface of a 4-point bend bar and the transgranular cleavage steps and microcracks observed on the surfaces of cone crack.....	49
Fig. 5.11	Representative corrected force-displacement curves at maximum loads of 50 N, 100 N, and 200 N, showing the full loading and unloading sequence for a) fine-grained spinel, b) coarse-grained spinel, c) AlON, and d) AlN using a 261- μ m-radius diamond indenter	51
Fig. 5.12	Comparison of indentation stress-strain curves for the fine-grained spinel, coarse-grained spinel, AlON, and AlN using a 261- μ m radius diamond indenter. Error bars correspond to the standard deviation within each given test condition. The solid trend line shows the linear elastic behavior.	52
Fig. 5.13	Comparison of indentation load and the indentation strain for the fine-grained spinel, coarse-grained spinel, AlON, and AlN using a 261- μ m-radius diamond indenter. Trend lines show the power law fits to the data.	53
Fig. 5.14	Schematic showing a) total work of indentation, W_T , b) the elastic work of indentation, W_E , and c) the plastic work of indentation, W_P , components extracted from a typical load-displacement curve	55
Fig. 5.15	Comparison of the total work of indentation, W_T , as a function of the indentation strain for the fine-grained spinel, coarse-grained spinel, AlON, and AlN using a 261- μ m-radius diamond indenter. Trend lines show the power law fits to the data.....	56
Fig. 5.16	Comparison of the plastic work of indentation, W_P , as a function of the indentation strain for the fine-grained spinel, coarse-grained spinel, AlON, and AlN using a 261- μ m-radius diamond indenter. Trend lines show the power law fits to the data.....	57
Fig. 5.17	Comparison of the ratio of plastic to total work of indentation, W_P/W_T , and the indentation strain for the fine-grained spinel, coarse-grained spinel, AlON, and AlN using a 261- μ m-radius diamond indenter. Trend lines show the power law fits to the data.....	57
Fig. 5.18	Elastic (green) and elastic-plastic (red) contributions to the indentation strain energy density	59
Fig. 5.19	Linear correlation between the total work of indentation, W_T , and the indentation strain energy density	60
Fig. 8.1	Computational materials science provides tools that cross scales over both length and time.....	70

Fig. 8.2	The 4H polytype (left) and 6H polytype (right) of SiC. The Si atoms are turquoise and the C atoms are black.	72
Fig. 8.3	B ₄ C structure: polar atoms within the icosahedron are black, the equatorial are light gray, and those in the sidechain are dark gray	72
Fig. 8.4	Relative stabilities of several proposed B ₄ C structures	73
Fig. 8.5	Optimized a) B ₁₂ CCC, b) B ₁₂ CBC, c) B ₁₁ C _e CBC, and d) B ₁₁ C _p CBC structures. Blue atoms are B and black are C.	77
Fig. 8.6	4H polytype (left) and 6H polytype (right) of SiC with hydrogen (H) atoms added for structural integrity. Si atoms are turquoise, C atoms black, and H atoms light gray.	79
Fig. 8.7	Single unit cell of 6H-SiC (left) is scaled up to a 3 × 3 × 1 supercell of 6H-SiC(ABCACB) (right); color scheme the same as in Fig. 8.6.....	81
Fig. 8.8	B ₁₂ CCC polytype of B ₄ C hexagonal unit cell of 45 atoms a) and b) 3 × 3 × 3 supercell of 1,215 atoms.....	87
Fig. 8.9	B ₁₂ CBC polytype of B ₄ C hexagonal unit cell of 45 atoms a) and b) 3 × 3 × 3 supercell of 1,215 atoms.....	87
Fig. 8.10	B ₁₁ C _e CBC polytype of B ₄ C hexagonal unit cell of 45 atoms a) and b) 3 × 3 × 3 supercell of 1,215 atoms.....	88
Fig. 8.11	B ₁₁ C _p CBC polytype of B ₄ C hexagonal unit cell of 45 atoms a) and b) 3 × 3 × 3 supercell of 1,215 atoms.....	88
Fig. 9.1	SiC piece retrieved from a carbothermic reactor. The samples for analysis were collected from different zones as indicated by consecutive numbers in the direction of increasing distance from the electron edge toward the metallurgical-grade SiC edge.	103
Fig. 9.2	LZ representation of phonon dispersion spectra in various SiC polytypes. The position of the special points on the reduced momentum axis and the Raman active modes for each polytype are related to the number of atoms in the unit cell of a respective polytype. Also shown are equivalent Raman modes at q = 0 in the BZ.	101
Fig. 9.3	Typical Raman spectrum of SiC showing bands specific to a particular SiC polytype (red) and overlapping bands of several SiC polytypes (blue). Only 2 bands at 766 and 977 cm ⁻¹ should be observed in 3C SiC.....	102
Fig 9.4	Raman spectra of carbothermically reacted SiC collected from the areas near graphitic electrode: as-received samples (top) and sintered ceramics (bottom). The trace of B ₄ C is originated from the sintering aids.	106
Fig. 9.5	Raman spectra of carbothermically reacted SiC collected from the areas between graphitic electrode and metallurgical-grade edge: as-received samples (top) and sintered ceramics (bottom). The traces of C and B ₄ C are originated from the sintering aids.	106

Fig. 9.6	Raman spectra of carbothermically reacted SiC collected from the areas far from graphitic electrode, near metallurgical-grade edge: as-received samples (top) and sintered ceramics (bottom). The traces of C and B ₄ C are originated from the sintering aids.	107
Fig. 9.7	Distribution of selected SiC polytypes and graphitic C content in carbothermically reacted SiC: a) as-received samples, b) powders after jet milling, and c) sintered samples (with sintering aids). Analysis was done based on the number of observation of Raman bands pertaining to a particular SiC polytype/graphitic C.	108
Fig. 9.8	Particle size analysis results for powders 1–11; powders in green have been milled over 15 times. The average particle size is near 1 μ m for powders subjected to repeated jet milling.....	110
Fig. 9.9	Optical images of Knoop indents in selected sintered samples: a) 1, b) 3, c) 5, d) 6, e) 8, and f) 9. Absence of visible cracking and the regular shape of most indents suggest that selected localized areas in the sintered samples are fully densified.	111
Fig. 9.10	Density (bottom) and 1-kgf Knoop hardness (top) data on samples produced with the use of the sintering aids as a function of the distance from the electrode. Only reliable hardness data has been included in this illustration. The hardness data marked by white arrows is obtained on samples with density near 97% ρ_{th}	112
Fig. 9.11	Correlation between hardness (top) and compositions (bottom) for selected SiC samples densified using SPS method without the use of sintering aids. All samples have been sintered to density of approximately 97% ρ_{th}	114
Fig. 9.12	Distribution of metal impurities (top) and unreacted (bottom) C and Si inclusions in carbothermically reduced SiC, as a function of the distance from the graphite electrode	115
Fig. 10.1	Acoustic spectrum of Olympus ultrasound transducer	120
Fig. 10.2	Representative ultrasound trace	120
Fig. 10.3	Group 1, tile 8; high mean attenuation coefficient	122
Fig. 10.4	Group 2, tile 11; high mean longitudinal velocity	122
Fig. 10.5	Group 3, tile 4; high mean shear modulus	123
Fig. 10.6	Group 4, tile 31; low mean attenuation coefficient.....	123
Fig. 10.7	Group 5, tile 2; high zone variations.....	124
Fig. 10.8	Group 6, tile 19; low zone variations.....	124
Fig. 10.9	Bend bar machining diagram; tile 11, 17 rows of bars	125
Fig. 10.10	Weibull analysis; Group 1, tile 8	127
Fig. 10.11	Weibull analysis; Group 2, tile 11	128
Fig. 10.12	Weibull Analysis; Group 3, tile 4	129

Fig. 10.13 Weibull plot; Group 4, tile 31	130
Fig. 10.14 Weibull plot; Group 5, tile 2	131
Fig. 10.15 Weibull plot; Group 6, tile 19	132
Fig. 10.16 Errant machining scratch; tensile surface of low-strength bend bar (A)	133
Fig. 10.17 Fracture surface; left and right faces, low-strength bend bar (A)	134
Fig. 10.18 Errant machining scratch; tensile surface of low-strength bend bar (B)	135
Fig. 10.19 Fracture surface; left and right faces, low-strength bend bar (B)	136
Fig. 10.20 Fracture surface; left and right faces, low-strength bend bar (C)	138
Fig. 10.21 Fracture location overlay, attenuation coefficient; Group 1, all layers	140
Fig. 10.22 Fracture location overlay, longitudinal velocity; Group 2, all layers	141
Fig. 10.23 Fracture location overlay, shear modulus; Group 3, all layers	141
Fig. 10.24 Fracture location overlay, attenuation coefficient; Group 4, all layers	142
Fig. 10.25 Fracture location overlay, attenuation coefficient; Group 5, all layers	142
Fig. 10.26 Fracture location overlay, attenuation coefficient; Group 6, all layers	143
Fig. 10.27 Bar 1, fracture surface end faces, composite (200× magnification) ..	145
Fig. 10.28 Bar 2, fracture surface end faces, composite (200× magnification) ..	146
Fig. 10.29 Bar 3, fracture surface end faces, composite (200× magnification) ..	147
Fig. 10.30 Bar 1, fracture path (200× magnification)	148
Fig. 10.31 Bar 2, fracture path (200× magnification)	149
Fig. 10.32 Bar 1, B ₄ C inclusion (3,750× magnification)	150
Fig. 10.33 Bar 2, B ₄ C inclusion (2,230× magnification)	151
Fig. 10.34 Bar 2, B ₄ C inclusion (7,150× magnification)	152
Fig. 10.35 Bar 3, amorphous C region (757× magnification)	153
Fig. 10.36 Bar 3, amorphous C region (4,160× magnification)	154
Fig. 10.37 Screenshot, Hermes NDE data analysis program	156
Fig. 10.38 Bend bar MOR vs. attenuation coefficient; Group 1, tile 8	157
Fig. 10.39 Bend bar MOR vs. attenuation coefficient; Group 2, tile 11	157
Fig. 10.40 Bend bar MOR vs. attenuation coefficient; Group 3, tile 4	158
Fig. 10.41 Bend bar MOR vs. attenuation coefficient; Group 4, tile 31	158
Fig. 10.42 Bend bar MOR vs. attenuation coefficient; Group 5, tile 2	159

Fig. 10.43	Bend bar MOR vs. attenuation coefficient; Group 6, tile 19	159
Fig. 11.1	Data recorded by TomoView after a full C-scan. The sample examined was a defect-engineered SiC tile characterized using the TRS 64 element phased-array probe.	166
Fig. 11.2	Export data window from TomoView, allowing for control of x and y bounds as well as the time duration of the A-scan signals	166
Fig. 11.3	Zeus GUI. Top window shows an A-scan corresponding to the point at the crosshairs in the C-scan. The B-scan corresponds to the horizontal line on the C-scan, while the D-scan corresponds to the vertical line. The panels on the right allow for control of sample properties, designation of measurements, gate assignments, and statistics related to the current point.	167
Fig. 11.4	Digital gate assignment options present in the Zeus software	168
Fig. 11.5	Zeus GUI after measurements have been run	169
Fig. 11.6	Zeus optional display modes showing a) the power spectral density of a peak of interest as determined by the STFT and b) the frequency-dependent attenuation coefficient spectrum. The B- and D-scan displays have been changed to show these property variations across horizontal and vertical sample lines.....	170
Fig. 11.7	Idealized attenuation coefficient spectra showing dominant scattering regimes. Abscissa is normalized frequency and ordinate is normalized attenuation coefficient. For single particles, the degree of attenuation actually increases from Rayleigh to diffuse scattering.	172
Fig. 11.8	Convolution of 3 scattering types	172
Fig. 11.9	Overall attenuation coefficient C-scan maps for SiC-N hexagons	174
Fig. 11.10	A-scan data from spinel sample 24-0275-3 showing direct reflections in the bulk	176
Fig. 11.11	Frequency-dependent attenuation coefficient from spinel sample 24-0275-3	177
Fig. 11.12	Curve fit for spinel sample 24-0275-3 attenuation spectrum, 10–18 MHz	178
Fig. 11.13	Attenuation coefficient spectrum of ZrO ₂ sample	180
Fig. 11.14	FESEM image of ZrO ₂ microstructure.....	181
Fig. 11.15	Normalized particle size histogram of ZrO ₂ sample.....	182
Fig. 11.16	Overall attenuation coefficient C-scan maps for Al ₂ O ₃ lots DIP6 and DIP6H	184
Fig. 11.17	Micrographs of “horseshoe” pattern in sample DIP6-4.....	187
Fig. 11.18	Micrographs of red “spot” in sample DIP6-4	187
Fig. 11.19	Micrographs of high attenuation region at the bottom of sample DIP6-4.....	188

Fig. 11.20	Micrographs of dark red “spot” in sample DIP6-1	189
Fig. 11.21	Acoustic attenuation coefficient spectra of 9 arbitrarily chosen Al_2O_3 samples from the Microstructural Evolution Alumina set.....	190
Fig. 11.22	Acoustic attenuation coefficient spectra of samples from the Microstructural Evolution Alumina set: a) T0 held constant, b) T0+50 held constant, and c) T0+100 held constant.....	191
Fig. 11.23	Acoustic attenuation coefficient spectra of samples from the Microstructural Evolution Alumina set: (a) D0 held constant, (b) D0+5 held constant, and (c) D0+15 held constant.....	191
Fig. 11.24	Attenuation coefficient spectrum of second round of arbitrarily selected samples from the Microstructural Evolution Alumina sample series	192
Fig. 11.25	Micrograph images from each Al_2O_3 sample from the grain size variant set. Note the differences in magnification for each image. Arrows indicate order of grain size increase between samples.	193
Fig. 11.26	Statistical data from measured grain size distributions; (x,y) represents (+temperature [Celsius] increase from standard, +dwell time (hours) from standard). The 2 operable scattering regimes are shown based on size scale.	194
Fig. 11.27	Stereographic effects on FESEM micrograph images	195
Fig. 11.28	Statistical data from measured grain size distributions. Corrected for stereographic effects: (x,y) represents (+Temperature [Celsius] increase from standard; +Dwell time [hours] from standard). The 2 operable scattering regimes shown are based on size scale.	195
Fig. 11.29	A-curve fit parameter as a function measured average grain diameter cubed for each sample. Graph shows that a linear relationship does not exist.	196
Fig. 11.30	Rayleigh C_R scattering prefactors. Note the large standard deviation.....	197
Fig. 11.31	Rayleigh C_S scattering prefactors. Note the smaller standard deviation.....	197
Fig. 11.32	Comparison of measured mean grain size (corrected for stereography) and predicted grain sizes using Rayleigh and stochastic scattering...	198
Fig. 11.33	Comparison of measured mean grain size (corrected for stereography) and predicted grain sizes using a) Rayleigh and b) stochastic scattering. Linear fits reveal how well the predicted data matches with measured data.....	199
Fig. 11.34	Overall attenuation coefficient C-scan images (20 MHz) of 3 randomly chosen Al_2O_3 samples	200
Fig. 11.35	Point attenuation coefficient spectra: a) Alumina A, b) Alumina B, and c) Alumina C	200

Fig. 11.36 Overall attenuation coefficient C-scan images (75 MHz) of 3 randomly chosen Al_2O_3 samples. Map inconsistency in the maps is due to sample nonuniformity. Red sections indicate where smaller area scans occurred.....	201
Fig. 11.37 Ultrasound-predicted mean grain size maps of Alumina A. Numbers above maps show average values for entire map. Small map in center is the 75-MHz overall attenuation coefficient C-scan image used to create the grain size maps. Notice the similarity in behavior between C-scan image and predicted mean grain size map.	201
Fig. 11.38 Ultrasound-predicted mean grain size maps of Alumina B. Numbers above maps show average values for entire map. Small map in center is the 75-MHz overall attenuation coefficient C-scan image used to create the grain size maps. Notice the similarity in behavior between C-scan image and predicted mean grain size map.	202
Fig. 11.39 Ultrasound-predicted mean grain size maps of Alumina C. Numbers above maps show average values for entire map. Small map in center is the 75-MHz overall attenuation coefficient C-scan image used to create the grain size maps. Notice the similarity in behavior between C-scan image and predicted mean grain size map.	202
Fig. 11.40 a) Measured particle size distribution of 100% Al_2O_3 sample and b) ultrasound beam volume normalized particle size distribution of 100% Al_2O_3 sample	205
Fig. 11.41 PSD of 20-MHz central frequency transducer (joules).....	206
Fig. 11.42 Force output of 20-MHz central frequency transducer (newtons).....	206
Fig. 11.43 Attenuation coefficient spectra of tailor-made samples: a) 10–62 MHz and b) 10–30 MHz	208
Fig. 11.44 XRD spectra of sample set containing between 1- and 5-wt% SiO_2 . Arrows mark major 2:1 mullite peaks.	209
Fig. 11.45 Ultrasonic particle size distribution of SiO_2 sample set.....	210
Fig. 11.46 Reconstructed ultrasonic particle size distributions.....	210

List of Tables

Table 2.1	Summary of Rutgers B ₄ C produced by rapid carbothermic reduction.	9
Table 2.2	Lattice parameters and calculated C content from various commercial B ₄ C powders and 3 initial Rutgers B ₄ C produced by rapid carbothermic reduction.....	14
Table 2.3	B-to-C ratios of Rutgers and various commercial B ₄ C powders.....	15
Table 3.1	Compositions of 3 powders	24
Table 3.2	Results of SPS of SiC with 10% additives	25
Table 5.1	Properties of the spinels, AlON, and AlN	40
Table 5.2	Observed indentation load ranges for the onset of ring and radial cracking in the spinels, AlON, and AlN, using a 261- μ m-radius diamond indenter.....	44
Table 8.1	B–B, B–C, and C–C bond lengths (\AA) from our B3LYP/6-31G(d) calculations as well as previous works.....	77
Table 8.2	Si–C, Si–H, and C–H bond lengths (\AA) for the 4H and 6H polytypes of SiC from our B3LYP/6-31G(d) calculations as well as those from Ching et al. have been used to terminate SiC clusters.	80
Table 9.1	Summary of the results of Raman analysis of unprocessed SiC	103
Table 9.2	Summary of the results of Raman analysis of crushed SiC powders	104
Table 9.3	Summary of the results of Raman analysis of milled SiC powders.	104
Table 9.4	Summary of the results of Raman analysis of sintered SiC ceramics (with sintering aids).....	105
Table 9.5	Summary of the results of Raman analysis of sintered SiC ceramics (no sintering aids).....	105
Table 9.6	Density and Knoop hardness of sintered samples (with sintering aids)	109
Table 9.7	Density and Knoop hardness of sintered samples (no sintering aids)	113
Table 9.8	Summary of the results of chemical analysis of unprocessed carbothermally reduced SiC	116
Table 10.1	Group breakdown/NDE map type and values.....	125
Table 10.2	Tile 8 MOR/Weibull moduli.....	127
Table 10.3	Tile 11, MOR/Weibull moduli.....	128
Table 10.4	Tile 4, MOR/Weibull moduli.....	129
Table 10.5	Tile 31, MOR/Weibull moduli.....	130
Table 10.6	Tile 2, MOR/Weibull moduli.....	131

Table 10.7	Tile 19, MOR/Weibull moduli.....	132
Table 10.8	Breakdown of bend bars.....	137
Table 10.9	Ultrasound data, standard deviation as a percentage of average value.....	154
Table 10.10	MOR data, standard deviation as a percentage of average value.....	155
Table 11.1	Scattering regime, size-to-wavelength relationship, and attenuation coefficient dependence	171
Table 11.2	Measured elastic properties for SiC-N hexagons.....	175
Table 11.3	Thermal properties of MgAl ₂ O ₄ spinel and LiF.....	179
Table 11.4	Frequencies where peaks occur in attenuation and their relation to sizes according to intraparticle and interparticle absorption	181
Table 11.5	Measured sizes and their correspondence to calculated intraparticle and interparticle frequencies	182
Table 11.6	Curve fit parameters for each sample spectra	196
Table 11.7	Density and ultrasound measurements of the tailor-engineered alumina sample sets.....	207

1. Introduction

This Materials Cooperative Research Program will be conducted as a seamless, synergistic collaboration among the following institutions: Rutgers Malcolm G McLaren Center for Ceramic Research (CCR), Penn State Particulate Research Center, the Johns Hopkins Center for Advanced Metal and Ceramic Systems (CAMCS), and the US Army Research Laboratory's (ARL) Weapons and Materials Research Directorate (WMRD). This will enable the program to utilize the capabilities of each organization to focus the program on substantial and continuous improvement of the scientific and technical understanding of advanced armor ceramics.

As part of year 6 of this program, 5 armor programs within the Ceramic Armor Subgroup of the CCR have been jointly funded within the Cooperative Research Program and 3 additional programs will receive supplemental funding from ARL, including the following:

1.1 Core Programs

- Task 1: Nanostructured Armor Ceramics: Boron carbide (B_4C) Powder Synthesis
- Task 2: The Role of Microstructure in the Ballistic Performance for Silicon Carbide (SiC)
- Task 3: High-Strain-Rate Behavior and Dynamic Failure of Armor Ceramics
- Task 4: Identification of Fundamental Deformation and Failure Mechanisms in Armor Ceramics
- Task 5: Education and Outreach

1.2 Supplementally Funded Program Modifications

- Task 6: B_4C Powder Synthesis (part of Task 1)
- Task 7: Multiscale Computational Investigations of Interfaces Relevant to Structural Ceramics
- Task 8: Microstructural Tailoring: Particle Coating for SiC (attached to Task 2)

- Task 9: Study of US SiC Powder Variations

1.3 Supplemental Funded Programs through Rutgers' Ceramic, Composite, and Optical Materials Center (CCOMC)

- Task 10: Defining Microstructural Tolerance Limits of Defects for SiC Armor
- Task 11: Nondestructive Characterization (NDC) of Armor Ceramic

2. Task 1: Nanostructured Armor Ceramics, Maneuver Center of Excellence (MCOE) Core Program and Task 6: B₄C Powder Synthesis (supplementally funded program)

Core Faculty: R Haber, D Niesz

ARL Leader: J McCauley, J LaSalvia, T Jessen, R Dowding

Research Faculty: W Rafaniello

Research Associate: S Miller

Graduate Student: F Toksoy

2.1 Long-Range Objectives

- Synthesize “clean” single-phase submicron-equiaxed stoichiometric B₄C powder with a narrow size distribution.
- Develop superior dense bodies.
- Determine residual graphite effect on amorphization.
- Clarify the source of carbon (C) from strain.
- Provide a means of doping B₄C C-C-C chain with Si or aluminum (Al) to alter amorphization and properties.
- SiC-B₄C binary would provide a density benefit to SiC.
- Potential clarification of B₄C phase diagram.

2.2 Background

B₄C is one the hardest known materials and as such is particularly useful as an armor ceramic material. For this application, it is desirable to use highly pure, single-phase, equiaxed, monodispersed B₄C powders with an average grain size of less than 1 μm. Such powders, when subject to densification through hot-pressing or spark plasma sintering, should yield a higher quality ceramic part.

Most commercial B₄C powder is manufactured by carbothermically reducing boron oxide (B₂O₃) in an electric arc furnace in the presence of a C source. Most commercial methods use coal or petroleum coke as a C source, which leads to a final product containing the impurities found in the raw material. The use of an electric arc furnace results in very high localized heating and slow conductive heating of the remaining batch. The entire heating and cooling process takes place

over a period of days. This results in nonuniform process conditions and nonuniform chemical composition in the final product; that is, unreacted raw materials and variations in final product stoichiometry may be realized. Further, the kinetics and thermodynamics of the slow heating process causes the B_2O_3 to pass through the liquid phase, resulting in a nucleation limited step and the formation of large grains.¹

Ultrafine B_4C powders have been synthesized by vapor phase reactions of B- and C-containing compounds using laser pyrolysis. These powders were shown to be equiaxed and have a narrow size distribution. They were fully densified into superior parts with a fine microstructure and hardness values higher than those reported for high-quality B_4C powders produced by more traditional methods such as in an electric arc furnace.² However, this method is not suited for high-quantity production and would not be cost effective.

Approximately 20 years ago, work done at Dow Chemical Company by William (Bill) Rafaniello and others demonstrated that the rapid heating of a highly reactive mixture containing B_2O_3 and a C source for a sufficient length of time resulted in the formation of a uniform submicron B_4C powder.³ For this work, a specific furnace design was implemented that allowed for raw materials to be maintained at nonreactive temperatures until just prior to exposure to sufficiently high temperatures for a vapor-phase reaction similar to spray pyrolysis. This furnace was capable of producing quantities above laboratory scales. In addition to demonstrating the ability to make a monodisperse submicron powder, these powders were also shown to be of high purity and could be consolidated into a ceramic part with superior properties.

Since the rapid heating process avoids many of the negative attributes of traditional B_4C synthesis, such as the presence of unreacted C and variations in B_4C stoichiometry, it is believed that a furnace of this type can be used to investigate of the impact of C on the amorphization of B_4C in high strain-rate applications, provide a means of doping the B_4C structure with appropriate elements leading to potential property improvements and potentially lead to a SiC- B_4C binary system. Additionally, the ability to produce a superior B_4C part with a pure, monodispersed, submicron powder can be reconfirmed.

2.3 Current Status of the Rapid Carbothermic Reduction Furnace

The work on this project began in May 2010. Several meetings were held with Bill Rafaniello to discuss the important aspects of the furnace, the most important aspect being the ability of the furnace to keep the precursor temperature below 450 °C

prior to entering the furnace hot zone where the temperature will be maintained at 1,700 °C or higher. From these discussions the general furnace design shown in Fig. 2.1 was developed. An existing 3.5- × 6-inch (hot zone size) graphite furnace (Thermal Technologies) was completely rebuilt and the hot zone size expanded to 4.5 × 6 inches to accommodate the graphite components that are necessary to maintain the appropriate temperature and manage movement of reaction gases out of the furnace. The previously mentioned graphite components were designed by the Rutgers team and machined by Weaver Industries. All assembly of the furnace body and internal components have been completed and tested.

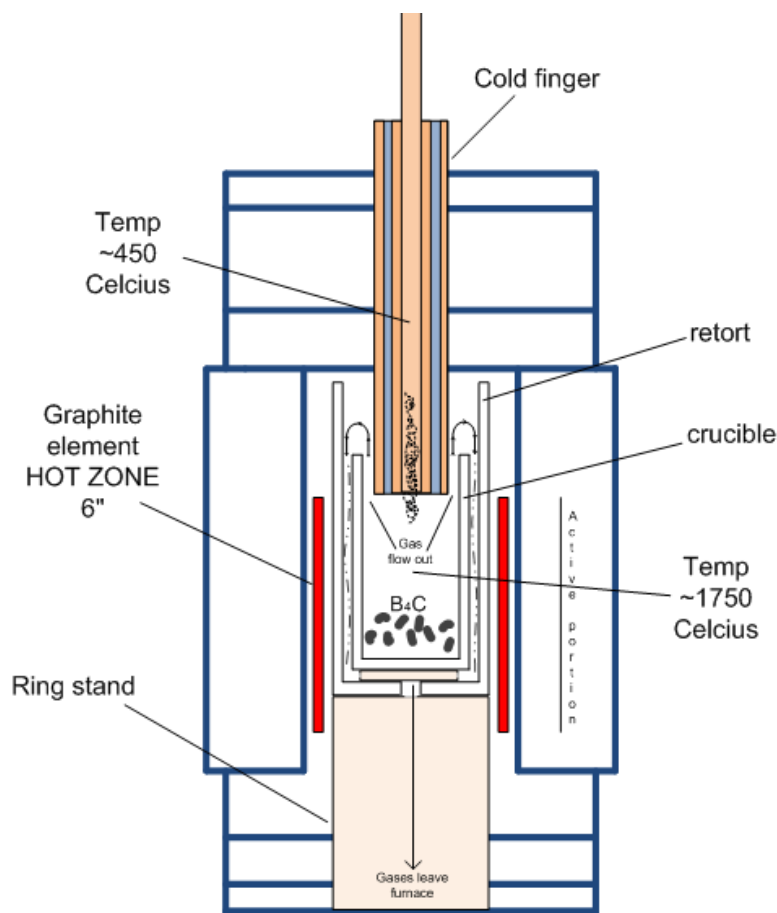


Fig. 2.1 Rapid carbothermic reduction furnace design

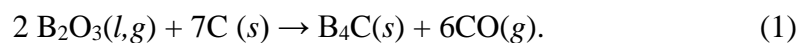
To maintain the precursor temperature below 450 °C before entering the furnace hot zone, a cold finger design was used. This is a jacketed copper (Cu) tube through which chilled water will be pumped. Copper is being used because of its high thermal conductivity. To minimize the number of solder joints, it is being constructed of 3 interlocking components bored from solid Cu. The final design of the Cu cold finger is shown in Fig. 2.2 and was built by the Rutgers Physics Department machine shop. It has been helium leak tested and installed in the furnace.



Fig. 2.3 Rapid carbothermic reduction furnace with Cu cold finger and screw feed

2.4 B₄C Precursor Preparation

The chemical reaction equation for the B₄C by carbothermic reduction is the following:



From Eq. 1 it is clear that the preparation of an intimate mixture of B₂O₃ and C is a necessary and important part of the rapid carbothermic reduction process. Figure 2.4 shows a basic flowchart of the B₄C precursor preparation process.

Fig. 2.4 Basic B₄C precursor preparation method

Simply, boric acid is dissolved in warm water and mixed with a C-H₂O slurry and thoroughly stirred. The mixture is dried of unbound water and pulverized. The mixture is then calcined at a temperature sufficient to dehydrate the boric acid, converting it to B₂O₃, and liquify the B₂O₃ (T_m ≈ 450 °C). After cooling, the precursor material is milled to the desired particle size.

There are several aspects to this process that can affect the efficacy of the precursor material. The choice of the C source is particularly important. Various C blacks and toner inks are a source of very pure, high-surface-area, and highly reactive C. However, these C sources can be difficult to make into stable slurries, as the C tends to flocculate. So far we have produced precursors using lampblack (lower surface area) and Vulcan XC-72 (higher surface area), a commercially produced C source (Cabot, Inc.). The aid of a dispersant such as Triton X-100 was necessary to produce a slurry using the Vulcan product. In both cases, constant mixing during the drying process is necessary to prevent separation of the C and B₂O₃ as the water is removed. The use of each of these in the production of B₄C was successful, but no conclusion as to the benefit of each has been drawn.

The use of corn starch as an organic C source is also being investigated. Cornstarch is easily dispersed in water and during the calcining process may form B complexes that help maintain the intimate mixture necessary for an effective precursor. Initial results with cornstarch have been promising.

The thermodynamics of the carbothermic reduction process favor a reaction above 1,542 °C, where it becomes exothermic. However, the sublimation temperature of B₂O₃ is approximately 1,500 °C. Therefore, even when this reaction occurs rapidly, maintaining a completely stoichiometric reaction is difficult. Since unreacted C is difficult to remove from B₄C and excess B₂O₃ is easily removed to through mild acid washing, completely reacting all the C is necessary. This can be achieved by preparing precursor materials with an amount of B₂O₃ in excess of that which is necessary for a stoichiometric reaction. We have prepared precursors with excess B₂O₃ in the amounts of 20%, 30%, and 50% in excess of stoichiometry. Initial results suggest 30% excess B₂O₃ may be sufficient to completely react all the C while easily removing any excess B₂O₃.

2.5 Production of B₄C in the Rapid Carbothermic Reduction Furnace

Using the rapid carbothermic reduction furnace described, B₄C production experiments may be carried out in the following 3 ways:

- A static (batch) process where the precursor is placed in a graphite crucible inside the hot zone of the furnace. It is then heated at a predetermined rate to the reaction temperature, held at that temperature, and allowed to cool.
- A drop test where a small amount of precursor is allowed to drop through the Cu cold finger into a crucible in the hot zone of the furnace already at the reaction temperature. The drop test serves 2 functions: it simulates what might be dropped during a single pulse of a screw feed and it allows for rapid experimentation where many parameters may be subject to variation (i.e., temperature, cold finger position).
- A screw feed process where large amounts of precursor (currently up to approximately 200 g) are placed in a hopper and a screw feed mechanism allows the precursor to fall through the Cu cold finger at a fixed rate into the preheated crucible in the hot zone of the furnace. In its current configuration, the screw feed allows for feed rates of 0.75–2.50 g/min.

As of the writing of this report, 14 B₄C synthesis runs have been made. Table 2.1 provides a summary of those runs.

Table 2.1 Summary of Rutgers B₄C produced by rapid carbothermic reduction

Sample Name	Test Type	Precursor Name	Carbon Source	% Excess B ₂ O ₃	Temp (°C)	Precursor Weight (g)	Charge Size (μm)	Carbon per Lattice Para (%)	Free Carbon (%)
BC-ST1	Static	P1LB20EX	Lampblack	20%	1750	25.0	150-425	20.0	40.0
BC-DR1	Drop	P1LB20EX	Lampblack	20%	1750	2.0	150-425	20.2	31.0
BC-DR2	Drop	P2LB50EX	Lampblack	50%	1750	2.0	150-425	19.6	13.9
BC-DR3	Drop	P3LB30EX	Lampblack	30%	1750	2.0	150-425	19.8	4.4
BC-DR4	Drop	P3LB30EX	Lampblack	30%	1800	2.0	150-425	19.6	9.4
BC-DR5	Drop	P3LB30EX	Lampblack	30%	1850	2.0	150-425	19.8	3.4
BC-DR6	Drop	P5VC30EX	Vulcan XC-70	30%	1850	2.0	150-425	19.9	1.3
BC-DR7	Drop	P6CS30EX	Cornstarch	30%	1850	2.0	150-425	20.2	---
	Drop	P1LB20EX	Lampblack	20%	1750	0.5	150-425		
	Drop	P2LB50EX	Lampblack	50%	1750	0.5	150-425		
	Drop	P3LB30EX	Lampblack	30%	1750	0.5	150-425		
	Drop	P3LB30EX	Lampblack	30%	1800	0.5	150-425		
	Drop	P3LB30EX	Lampblack	30%	1850	0.5	150-425		
BC-SF1	Screw Feed	P7LB30EX	Lampblack	30%	1800	46.0	150-425	19.9	7.7

Whenever possible, samples are subject to the following characterization techniques: scanning electron microscopy (SEM), X-ray diffraction (XRD), particle size analysis, and C and B determination (through chemical analysis). Small initial sample sizes preclude these analyses for many of the initial runs. The following are results for 4 relevant samples: BC-ST1, BC-DR1, BC-DR7, and BC-SF1.

2.5.1 BC-ST1

This was a static run where 25 g of precursor was reacted at 1,750 °C for 30 min. The precursor used lampblack as a C source and had 20% excess B₂O₃. The average particle size, as determined using SEM micrographs similar to that in Fig. 2.5, was 6.7 μm. Using XRD, lattice C was determined to be 20%, or B_{4.00}C, and free C was determined to be 40%. The SEM images show narrowly distributed equiaxed crystallites with areas of nanosized free C distributed among the crystallites.

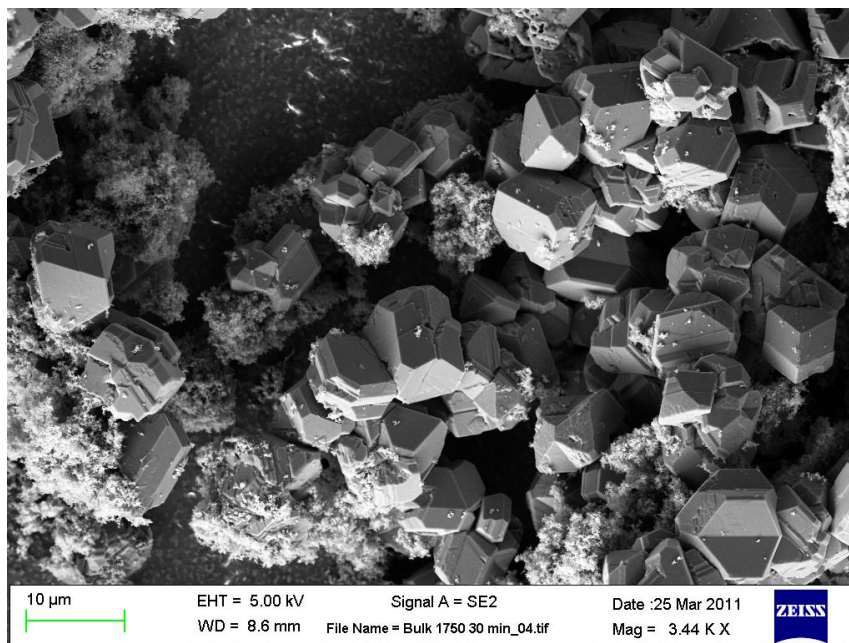


Fig. 2.5 SEM micrograph of static (batch) processed B₄C; average particle size = 6.7 μm

2.5.2 BC-DR1

This was a drop test where 2 g of precursor material was dropped into the preheated furnace at 1,750 °C and allowed to dwell for 2 min. The precursor used lampblack as a C source and had 20% excess B₂O₃. The average particle size, as determined using SEM micrographs similar to that in Fig. 2.6, was 1.2 μm. Using XRD, lattice c was determined to be 20.2%, or B_{3.95}C, and no free C was detected. The SEM images show narrowly distributed equiaxed crystallites with areas of nanosized free C distributed among the crystallites.

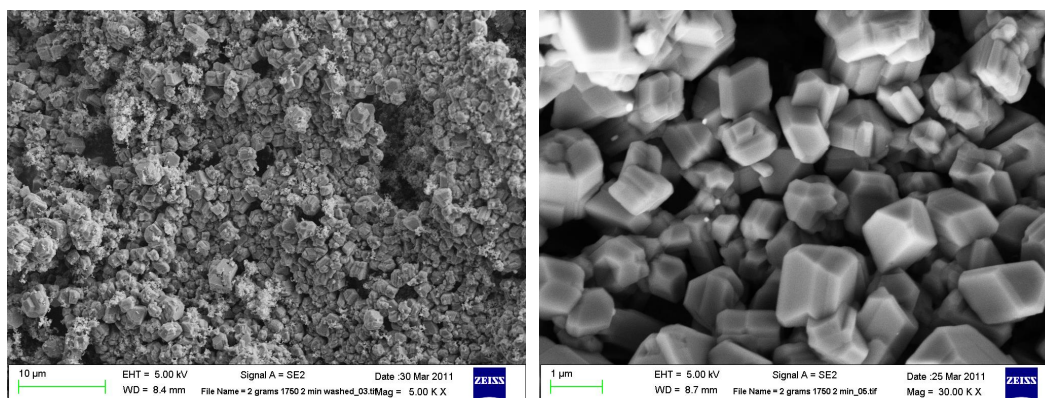


Fig. 2.6 SEM micrographs of B₄C from a 2-g drop test using lampblack as a C source; average particle size = 1.2 μm

2.5.3 BC-DR7

This was a drop test where 2 g of precursor material was dropped into the preheated furnace at 1,850 °C and allowed to dwell for 2 min. The precursor used corn starch as a C source and had 30% excess B₂O₃. The d(0.9) using light scattering was 1.27 μm. Using XRD, lattice C was determined to be 20.1%, or B_{3.98}C, and free C was determined to be 31%. The SEM images, shown in Fig. 2.7, show a more widely distributed equiaxed crystallites with no free C. Nanometer-sized crystallites can be seen with necking between them.

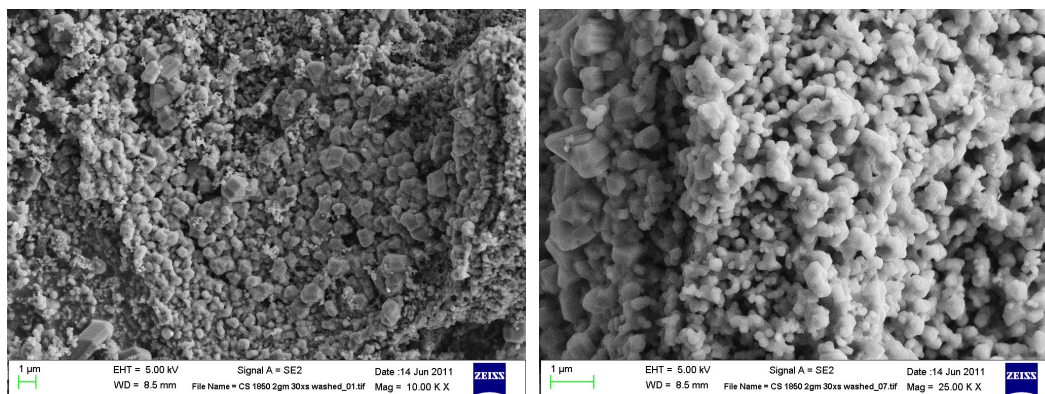


Fig. 2.7 SEM micrographs of B₄C from a 2-g drop test using corn starch as a C source; D(0.9) = 1.27 μm

2.5.4 BC-SF1

This was a screw feed run where approximately 46 g of precursor material was fed into the preheated furnace at 1,800 °C at a rate of 1 g/min. The precursor used lampblack as a C source and had 30% excess B₂O₃. The d(0.9) using light scattering was 1.15 μm. Using XRD, lattice C was determined to be 19.9%, or B_{4.10}C, and free C was determined to be 7.7%. The SEM images, shown in Fig. 2.8, show narrowly distributed equiaxed crystallites with some free C.

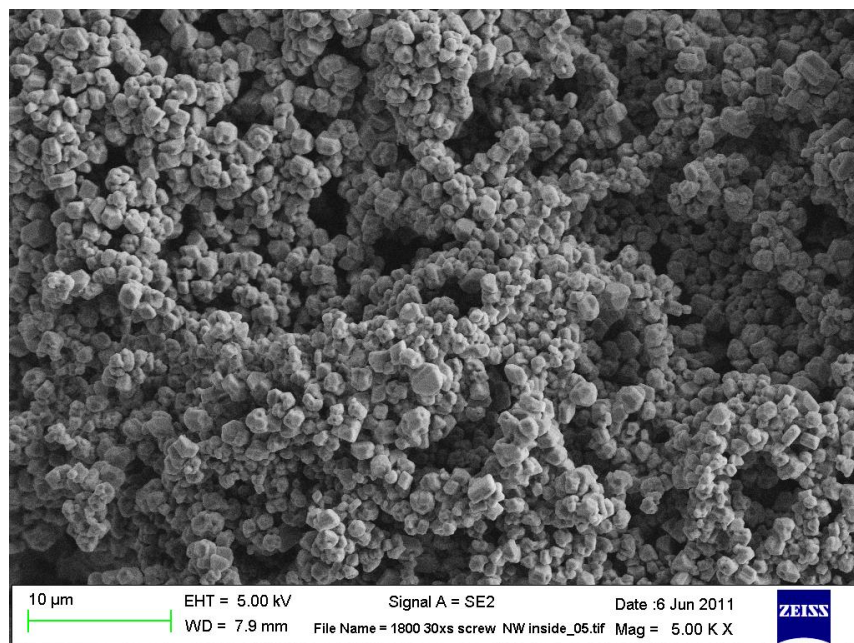


Fig. 2.8 SEM micrograph of B₄C from a screw feed sample using lampblack as a C source; average particle size = 1.15 µm

2.5.5 X-ray Diffraction

XRD analysis is used to verify the B₄C structure and estimate free C and stoichiometry. Figure 2.9 shows the XRD spectra for samples BC-ST1, BC-DR1, and a commercial B₄C. The peak positions confirm the icosahedra-based rhombohedral lattice structure of B₄C. The C peak confirms that free C is present. However, the lower relative peak intensity and broader lines suggest less free C than the commercial B₄C and that the C is smaller, consistent with that seen in the SEM images in Fig. 2.8. Additionally, the broader B₄C peaks suggest finer crystallite size than the commercial product.

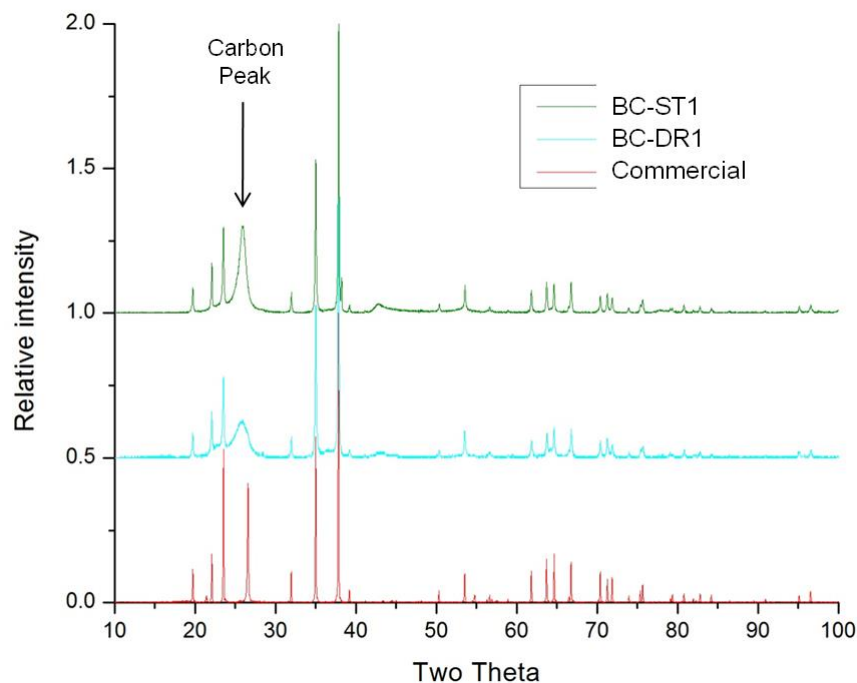


Fig. 2.9 XRD spectra for a static run (BC-ST1), a drop test run (BC-DR1), and a commercial powder

XRD may also be used to determine the stoichiometry of B_4C . Based on the work by Aselage and Tissor,⁴ there appears to be a linear relationship between the lattice parameters of B_4C and the C concentration in atomic percent. Using this information and data provided by Rutgers' Dr William Mayo (Personal communication, 2011, unreferenced), the lattice parameters and calculated C content for samples BC-ST1, BC-ST1, and BC-SF1 are presented in Table 2.2. Also included are the lattice parameters and calculated C content for several commercial B_4Cs . This table clearly demonstrates that the Rutgers B_4C produced by rapid carbothermic reduction is closer to stoichiometric B_4C .

Table 2.2 Lattice parameters and calculated C content from various commercial B₄C powders and 3 initial Rutgers B₄C produced by rapid carbothermic reduction

Sample ID	Lattice Parameters (Å)		Calculated Carbon Content (at %)		
	a	c	Based on a	Based on c	Average
Starck GradeMS	5.6096	12.097	17.0	18.1	17.5
ESK Tetrabor 3000F	5.6259	12.124	12.7	16.2	14.5
UK Abrasive 0.5 µm	5.6174	12.111	15.0	17.1	16.0
UK Abrasive 1.3 µm	5.6141	12.103	15.8	17.6	16.7
Electro Abrasives 2.5 µm	5.6071	12.089	17.7	18.6	18.2
Electro Abrasives 1200	5.6029	12.079	18.8	19.3	19.1
SSI GradeB	5.6114	12.100	16.6	17.9	17.2
Superior Graphite GradeM	5.6154	12.107	15.5	17.4	16.4
Rutgers BC-DR1	5.5975	12.0687	20.2	20.0	20.1
Rutgers BC-ST1	5.5983	12.0694	20.0	20.0	20.0
Rutgers BC-SF1	5.5987	12.0785	19.9	19.3	19.6

To more clearly show how the Rutgers B₄C compares with the commercial powders, the B-to-C ratio was calculated and stack ranked against the commercial powders, as shown in Table 2.3, and their relative positions within the B₄C phase field, as shown in Fig. 2.10. While the Rutgers powders appear to be stoichiometric B₄C, all of the commercial powders appear to be substantially in the B-rich region of the B₄C phase field.

Table 2.3 B-to-C ratios of Rutgers and various commercial B₄C powders

Sample ID	Approximate Composition
ESK Tetrabor 3000F	B _{5.90} C
UK Abrasive 0.5μm	B _{5.25} C
Superior Graphite Grade M	B _{5.10} C
UK Abrasive 1.3 μm	B _{4.99} C
SSI Grade B	B _{4.81} C
Starck Grade MS	B _{4.71} C
Electro Abrasives 2.5 μm	B _{4.49} C
Electro Abrasives 1200	B _{4.24} C
Rutgers BC-SF1	B _{4.10} C
Rutgers BC-ST1	B _{4.00} C
Rutgers BC-DR1	B _{3.98} C

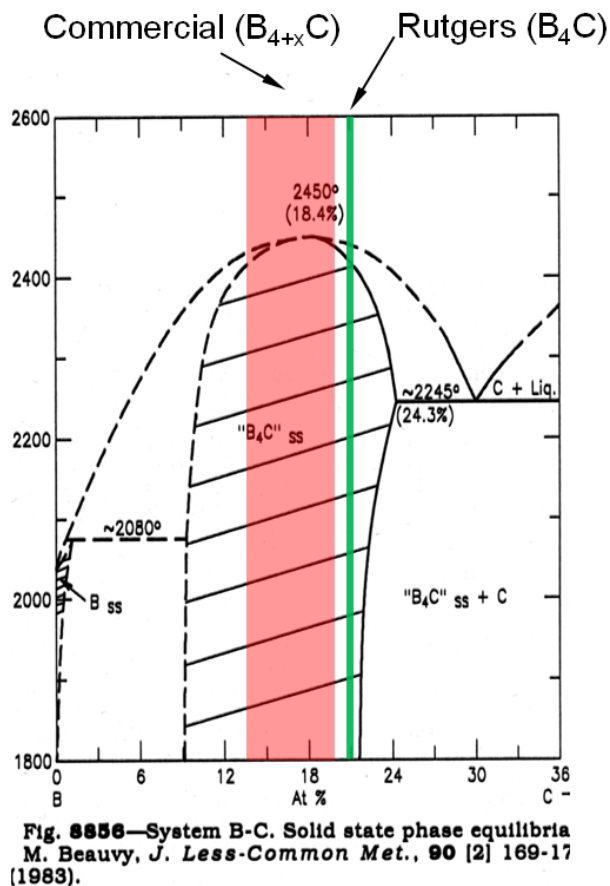


Fig. 2.10 B-to-C ratios of Rutgers and commercial B₄C powders shown in B₄C phase field (adapted from reference cited below figure)

2.6 Spark-Plasma-Sintered B₄C

To demonstrate the ability to densify the B₄C produced from rapid carbothermic reduction, 4 g of unrefined B₄C material from BC-SF1 (screw feed sample) was spark plasma sintered at 1,850 °C for 20 min at a pressure of 50 MPa. The density of the material was determined using the Archimedes method to be 2.485 g/cm³. Since the unrefined B₄C powder had 7.7% free C, hardness measurements were only considered from indents where no C inclusions were present. Based on these, average Knoop hardness was determined to be 2,237. A SEM micrograph of the polished sample and a Knoop indent are shown in Fig. 2.11.

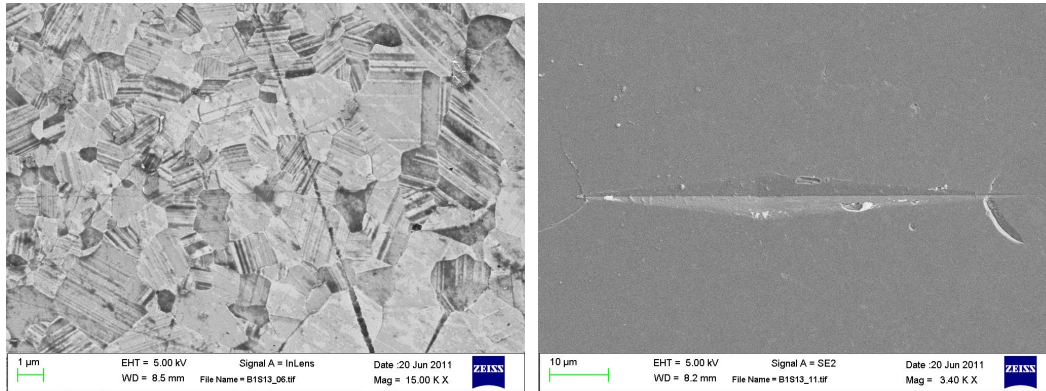


Fig. 2.11 SEM micrographs of (left) spark-plasma-sintered B₄C from screw feed sample BC-SF1 using lampblack as a C source and (right) Knoop hardness indent at 1 kg

2.7 Conclusions and Future Work

The results described herein represent the initial attempts in synthesizing B₄C using rapid carbothermic reduction. The ability to produce submicron equiaxed B₄C has been demonstrated. Additionally, every sample has resulted in stoichiometric (B₄C, a 4:1 B-to-C ratio) B₄C based on XRD analysis. However, further refinement of the processing parameters (precursor component ratio, temperature, feed rate, etc.) must be completed such that grain size may be controlled while resulting in no free C. Figure 2.12 shows a multidimensional matrix that will be used to determine the optimal processing conditions.

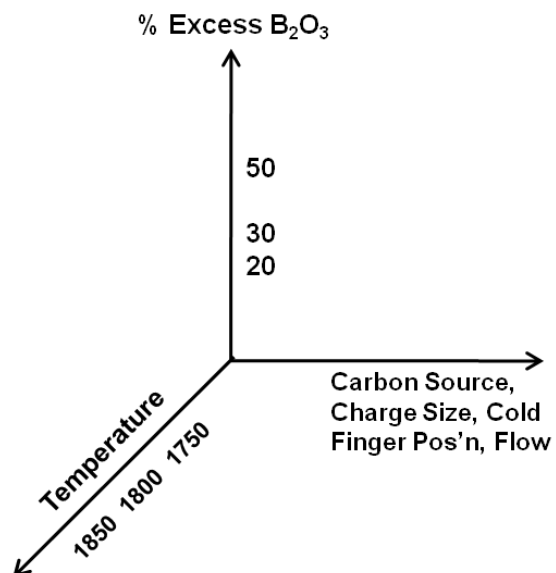


Fig. 2.12 Experiment matrix showing processing parameters

Methods for adequate B and C determination to corroborate XRD analysis are currently being established and tested. As the processing conditions are optimized, increasing work on densification will be undertaken. Compounds for use as potential dopants are currently being investigated.

2.8 References

1. Weimer A, Moore W, Roach R, Hitt J, Dixit R, Pratsinis S. Kinetics of carbothermal reduction synthesis of boron carbide. *J Am Ceram Soc.* 1992;75(9):2509.
2. Knudsen A. Laser-driven synthesis and densification of ultrafine boron carbide powders. *Advances in Ceramics: Ceramic Powder Science.* 1987;21:237.
3. Rafaniello W, Moore W, inventors; The Dow Chemical Company, assignee. Heating reactive mixture of boric oxide and carbon yields submicron size particles. United States patent US 4,804,525 A. 1989 Feb 14.
4. Aselage TL, Tissot RG. Lattice constants of boron carbide. *J Am Ceram Soc.* 1992;75(8):2207–2212.

3. Task 2: The Role of Microstructure in the Ballistic Performance of Silicon Carbide (SiC), Core Program and Task 8: Microstructural Tailoring: Particle Coating for SiC, US Army Research Laboratory (ARL) Supplemental

Core Faculty: R Haber, D Niesz

ARL Leaders: T Jessen, J McCauley

ARL Collaborators: J Campbell, J LaSalvia, H Miller

Post-Doc: S Miller

Graduate Students: B Bianchini, S Mercurio

3.1 Long-Range Objectives

- Develop a better understanding of the relationship of microstructural characteristics and ballistic performance for SiC.
- Quantify the effect of grain boundary characteristics on the ballistic performance of fine-grain-size spark-plasma-sintered (SPSed) SiC.

3.2 Objectives for Calendar Year 2011

First Quarter

- Further evaluation of mechanical properties of fine-grained, coprecipitated SPS SiC.
- Characterize the microstructure and properties of nitrogen (N)–containing compositions.
- Obtain transmission electron microscopy (TEM) samples for energy-dispersive X-ray spectroscopy (EDS) analysis using focused-ion-beam methods for sample prep.
- Provide dense samples to ARL for dielectric characterization.

Second Quarter

- Extend coating work to investigate reduced percentage of additive.
- Continue microstructure characterization of N-processed SiC.

- Initiate high-resolution TEM (HRTEM) characterization of grain-boundary-modified samples.

Third Quarter

- Analyze phases present in SiC–aluminum nitride (AlN)–yttrium oxide (Y_2O_3) systems.
- Continue HRTEM characterization of grain-boundary-modified samples.
- Investigate methods for modifying starting powder characteristics (oxygen, impurities, surface area, etc).
- Evaluate possibilities with additives other than rare earth based systems.

Fourth Quarter

- Analyze the effect of phases on nanoidentation of AlN-rich samples.
- Examine finer grain-size powders and grain-size dependence on properties.
- Examine effects of heat treatments on microstructure and properties.

3.3 Background

Research into the relationship between microstructure and the ballistic performance of SiC-based armor ceramics began in June 2006. An initial survey of relevant literature indicated that while many researchers have suggested relationships between ballistic performance and microstructural features, no definite correlations or figures of merit have been established. Work by Bakas et al.¹ demonstrated the importance of eliminating anomalous defects such as poor mixing of sintering aids, agglomerated particles, and porosity, which lead to undesirable inhomogeneities in the final microstructure. Other research by Raczka² indicated that extraneous C additions or poor mixing of C can greatly reduce the grain growth of nearby SiC grains, leaving a large C inclusion inside a fine SiC matrix. This type of inclusion can serve as a crack initiation site and adversely affect the mechanical behavior.

On the other hand, controlled and purposeful microstructural changes can modify and enhance the resultant mechanical properties. Krell's³ work on Al_2O_3 indicated a Hall-Petch type of relationship where decreasing the grain size yielded an increase in hardness, Ray et al.⁴ studied 6 different compositions of SiC under varied processing conditions and found clear variation in microstructures, mechanical properties, and ballistic performance. No clear and strong correlation could be found between any specific mechanical property and an improvement in ballistic performance.

These results still indicate many possibilities for improving armor performance, but greater understanding and innovative approaches are required. Wilkins,⁵ in the 1960s, did extensive ballistic testing on a number of different materials and systems and determined that many properties inherent to most ceramics, such as hardness and compressive strength, were important for good ballistic performance, yet alone were not indicative of one material outperforming another. Wilkins⁶ instead argued that some tradeoff with these properties would be necessary to encourage some others, like fracture toughness and plasticity, which he believed was the most influential property required. The work of Chen et al.⁷ later suggested the importance of effective plasticity in the ballistic behavior of alumina (aluminum oxide or Al_2O_3). Achieving plasticity in ceramic materials is difficult, however, under conventional methods of processing. To develop plasticity in ceramic like SiC, new fracture mechanisms and interesting behaviors need to be developed and exploited. A promising methodology to achieve this is through improved processing to eliminate the defects and grain boundary engineering to unlock the new behaviors.

More recent work on understanding grain boundary phases and behavior in SiC suggest engineering the grain boundaries can influence the fracture behavior in very specific ways. Work by Choi et al.⁸ indicated that SiC sintered with AlN and oxide additives form a melt that stays behind as a residual intergranular film. This film varies in thickness with the compositions of the additives and can have a marked effect on the properties of the resulting SiC. Other work by Zhou et al.⁹ shows the strong influence of rare earth additions and intergranular properties on the mechanical properties of SiC. A better understanding of the sintering process and development of intergranular phases could lead to the ability to engineering armor materials that display desired behaviors.

As previously described, the initial research in this project aimed to further improve the mixing of sintering additives by moving away from bulk powders and simple resins and toward using engineered surfactants as sources of C and boron (B). The surfactants are specifically formulated to adhere to the surface of SiC and provide controlled amounts of C, B, and N upon burnout. This is a considerable improvement upon methods that leave excess C behind, creating defects. Thermodynamic calculations of the amount of C required to remove the silicon oxide (SiO_2) layer helped improve the estimates of the amount of C needed, but the bulk mixing of C black or resins still resulted in poor mixing.¹⁰ The engineered surfactant helps improve both the mixedness of sintering aids and reduce the amount of C needed, resulting in improved microstructures with reduced flaws.^{11,12}

The surfactant was shown to provide improved densification and develop microstructures similar to solid-state-sintered SiC, but the mixing of the HX3 (Huntsman Chemical, Austin, TX) surfactant and SiC was not as homogenous as desired. The surfactant offered a slight improvement in the temperature required for densification, but temperatures greater than 2,000 °C were still required with the surfactant alone. Further attempts to modify the processing proved difficult, and it was ineffective to couple any other interesting additives directly to the HX3 surfactant. Dry mixing of AlN and the surfactant was used to develop compositions with a range of grain sizes and some improved hardness results as described in previous research and reports,¹² but the poor mixing and inconsistent temperatures required for densification indicated further improvement was possible.

It was believed that introducing nanoscale additives into the process would solve these issues and further improve the coating and sinterability of the SiC. For this reason, research shifted toward processing methods allowing for better mixing and more varied sintering additives. In conjunction with the improvements offered by co-precipitation processing, it was desired to further lower the sintering temperatures, enabling more control over grain sizes and microstructure. By adding new sintering aids such as rare earth oxides, it was hoped that the ability to engineer the grain boundaries of SiC, when coupled with the better processing, would yield SiC with enhanced properties and new fracture mechanisms. These improvements, in turn, could offer the potential for improved ballistic performance.

Co-precipitation has been used as an effective method of adding fine nanoscale additives into many systems. As a colloidal processing method, it has the added benefit of reducing defects through improved mixing and elimination of processing defects. Research on Si₃N₄ has revealed improved homogeneity and mechanical properties with coprecipitation of sintering additives.^{13,14} Albano and Garrido¹⁵ found improvements in green density and sintered density of Si₃N₄ through coprecipitation as a means of coating. Although much research has been done on coprecipitation for Si₃N₄, little has been done on using it as a method for introducing sintering aids for SiC. Limited work on coprecipitation in SiC has shown improved sintering kinetics, greatly decreased grain size, and improved mechanical properties.^{16,17}

It is believed the fine and homogenous distribution of sintering aids obtained from coprecipitation and colloidal processing will reduce the number of defects in SiC armor ceramics and lead to improved performance.

3.4 Summary of Previous Results

This report represents a transition in direction and student relative to the previous reports. A larger summary of much of the research covered on this project since 2006 can be found in the thesis of the previous student, S. Mercurio, which was defended in December 2010. In brief, the co-precipitation process was shown to be a versatile and effective method of introducing Al_2O_3 - Y_2O_3 and rare earth-based sintering aids into SiC. Steps were taken to ensure a uniform particle-size distribution and controlled slurry conditions. These process improvements allowed for the coprecipitation process to yield a fine reactive coating of nanoscale sintering aids. Zeta potential analysis, TEM, and fluorescence measurements were employed as characterization methods to show the success of coating the sintering aids onto SiC templates. Additionally, it was observed that the improved mixedness introduced from co-precipitation did not just develop materials with less defects, but through XRD analysis it was shown that minor amounts of different phases were indeed formed. This implied the importance of mixing as more than just reducing defects; it is also as a methodology of creating additional and controlled phases. Although both co-precipitated and ball-milled systems showed microstructures with intergranular glassy phases, the regions where crystallization occurred during sintering showed Al_2O_3 and yttrium silicate phases in the ball-milled systems; coprecipitated systems indicated the formation of 2:1 mullite phases. Standard characterization of microstructure and hardness revealed small, subtle differences. Analysis of high-load hardness indents and observed cracking behaviors from these indents indicated considerable differences in mechanical behavior between the varied materials.

After the results showed benefits of improved processing for liquid-phase-sintered SiC systems, it was desired to further expand the study to include exploration of additional processing variables not covered in the previous work. It is also desired to initiate the study of systems other than Al_2O_3 - Y_2O_3 because of interesting differences in mechanical properties in systems where AlN is used as a sintering aid. This report initiates the study into the alternative AlN- Y_2O_3 system, with research led by R Bianchini.

3.5 Experimental Procedure

Commercially available α -SiC (UF-25, H.C. Stark, Karlsruhe, Germany), AlN (Dow Chemical Co., Midland, MI), and $\text{Y}(\text{NO}_3)_3 \cdot 6\text{H}_2\text{O}$ (Alfa Aesar, Ward Hill, MA) were used as starting powders. Three batches of powders were created using 90% SiC and 10% AlN and Y_2O_3 additives; the compositions are listed in Table 3.1. SiC and AlN powders were placed in a Nalgene flask and milled in SiC media (3/16

inch) for 2 h as a thick slurry mix in isopropanol. Then the slurry was filtered through a 1.18-mm mesh. Once this mixture was dried in a drying oven, yttrium nitrate was mixed using the precipitation process at room temperature under a controlled pH of 9.5 and stirred using a Cole-Parmer laboratory overhead stirrer. The precipitate separated from isopropanol over 24 h and again dried in the drying oven. Later, hydroxides were extracted from this mixture in a tube furnace with argon gas flow. The same powder compositions were prepared by low-energy ball-milling of SiC, AlN, and Y₂O₃ in an isopropanol slurry.

Table 3.1 Compositions of 3 powders

Sample Designation	wt% SiC	wt% AlN	wt% Y₂O₃
N1	90	1.08	8.92
N2	90	2.14	7.86
N3	90	4.21	5.79

A Thermal Technologies Model SPS 10-4 SPS unit was used to densify the powders. Four grams were placed in a 20-mm inner-diameter Isocarb 85 graphite die and loaded into the SPS chamber. The cycle started at a 200 °C/min rate up to 1,400 °C. Once the uniaxial pressure reached 50 MPa, the furnace temperature ramped up to 1,900 °C at the same rate. These conditions dwelled for 10 min in the argon atmosphere before the cycle ended and returned to starting conditions.

The newly sintered ceramics were sand-blasted to dispose the remains of graphite foil. The densities were found using the Archimedes method. These highly dense samples were cut using a low-speed Buehler saw, compressed into a mounding compound, and placed on the Buehler EPOMET-F unit to polish the surfaces. Then the polished faces were indented using a Knoop hardness indenter. Once the specimens were removed from the mounding compound, the samples were dry-plasma-etched using SPI Supplies Plasma Prep II Plasma Etcher in a CF₄ atmosphere containing 8% oxygen for 2 h. These finished ceramics were placed in the SEM to analyze the microstructure, Knoop indents, and cracking behavior.

Highly dense, ball-milled, and co-precipitated SiC-Al₂O₃-Y₂O₃ samples were prepped for TEM analysis by Sandia. EDS mapping and line-scan technique discovered interesting results. TEM micrographs of the elemental analysis along with dark field images were recorded.

3.6 Results

The SPS of SiC with 10% additives led to highly dense ceramics with submicron grain sizes, as shown in Table 3.2. Calculated density values decrease with smaller Y₂O₃ weight percent, as expected. JF Li and R Watanabe showed the elastic

modulus decreased slightly with an increase in AlN content due to the mixing of low-stiffness material,¹⁸ but these values were consistently similar regardless of composition. Many authors^{19–21} have observed a decrease in SiC grain size with an increase in AlN content. This is not the case with these samples. The lower temperature and time to achieve full density for samples with less Y₂O₃ content would result in grain growth at these sintering conditions.

Table 3.2 Results of SPS of SiC with 10% additives

Sample Designation	Calculated Density	Elastic Modulus	Average Grain Size
	(g/cm ³)	(GPa)	(μm)
N1-P ^a	3.29	355	0.477
N1-BM ^b	3.29	349	0.583
N2-P	3.27	353	0.448
N2-BM	3.29	354	0.635
N3-P	3.26	348	0.613
N3-BM	3.25	362	0.997

^aPrecipitated

^bBall-milled

Figure 3.1 shows 3 molar ratios of ball-milled and precipitated SEM images. The addition of an oxide additive in SiC ceramics has been shown to cause a glassy phase around the grains by liquid phase sintering, so the grain boundaries diminish with decreasing Y₂O₃ composition.^{19,20,22} AlN does increase the liquid phase during sintering from surface oxides by creation of Al₂O₃,¹⁹ but this may not compensate for the decrease amount of Y₂O₃ initially added.

The starting SiC powder is submicron and was measured on the average of 500 nm, which is about the same as the grains themselves due to the inhibition of grain growth by the AlN. The liquid phase during sintering is expected to facilitate grain growth by the solution-reprecipitation method, but the addition of N in the liquid increases the viscosity. This may be explained by the additional bond N has compared with the O-containing liquid phase.^{19,23} In addition, the diffusion of AlN in the SiC grains may reduce the mass transfer. If this additive remains in the grain boundary, it may act as a pinning effect to inhibit grain growth. With increasing AlN content, Hotta¹⁹ and Suzuki²⁰ have proved that 4-H SiC peak intensity decreases and may disappear according to the amount of AlN is present, while the 2-H SiC phase peak increases. AlN and 2-H SiC phase may form a solid solution because both have wurzite.

The core-shell structure of the grains has been analyzed and a variation of AlN in the SiC grains was found.^{24,25} In the grains, 2–5 mol% AlN was located in the cores but larger amounts were found in the shells, i.e., 15–22 mol%. The AlN gradient in the grains, shown in Fig. 1a–f, vary according to the amount present. The systems

with higher AlN content show distinct and larger cores in the core-shell structure. This phenomenon has yet to be explained, but it is suggested that the AlN enters the grains at different stages during sintering.

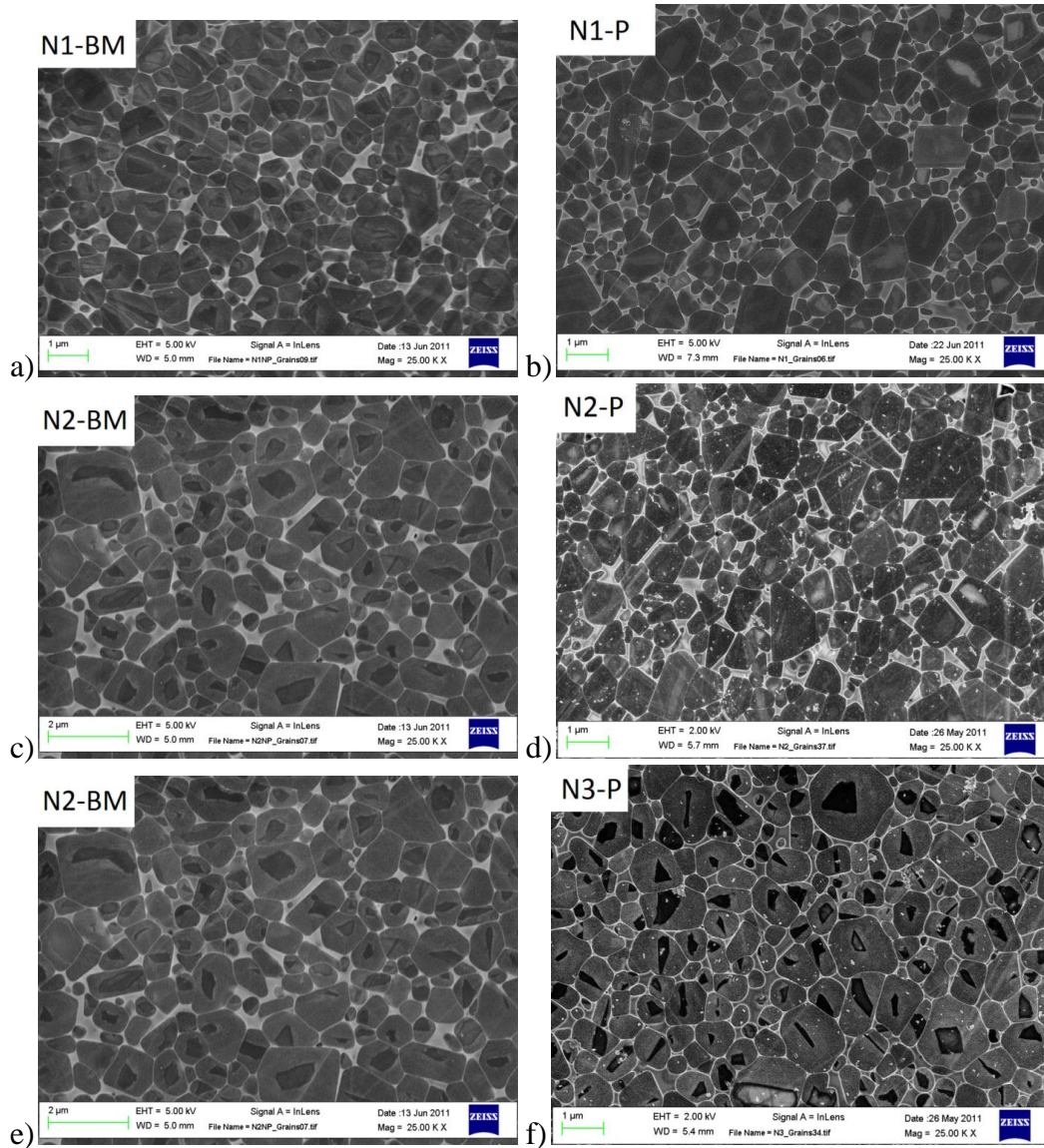


Fig. 3.1 SEM micrographs of a) ball-milled and b) precipitated 40% AlN and 60% Y₂O₃ mol of additives, c) ball-milled and d) precipitated 60% AlN and 40% Y₂O₃ mol of additives, and e) ball-milled and f) precipitated 80% AlN and 20% Y₂O₃ mol of additives

Knoop hardness values are shown in Fig. 3.2. That the precipitated samples have overall higher hardness compared with the ball-milled samples may be due to the smaller grains in the microstructures. According to JF Li,¹⁸ the hardness of SiC-AlN alloys has been shown have similar values with those presented.

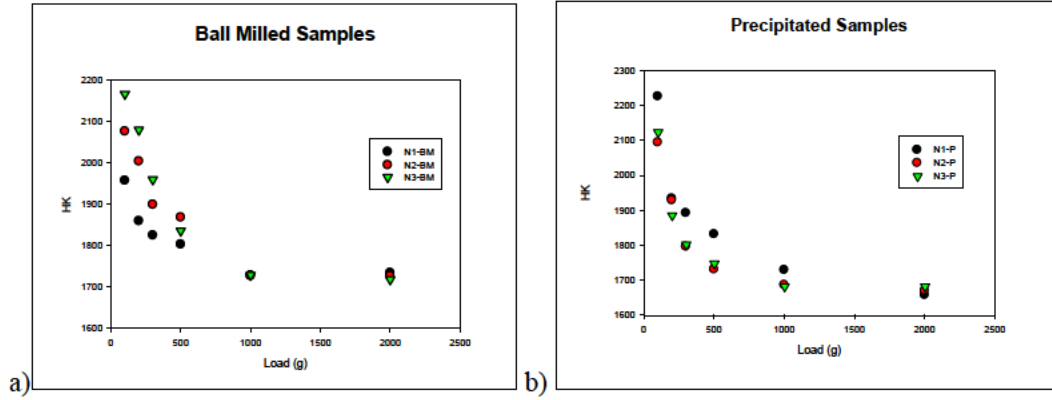


Fig. 3.2 Knoop hardness graphs of a) ball milled and b) precipitated samples

TEM micrographs were recorded on 2 samples of the same composition: 95 wt% SiC, 3.22 wt% Al_2O_3 , and 1.78 wt% Y_2O_3 . Figure 3.3 displays the samples prepared by Sandia National Laboratory. These samples differ in mixing processes: 3a was ball-milled and 3b was co-precipitated. The prepared powders were densified in the SPS under the same sintering conditions of 1,800 °C for 5 min and 1,900 °C for 5 min at 50 MPa in argon gas. The key and obvious difference between the 2 samples is the level of mixedness developed by the different processing routes.

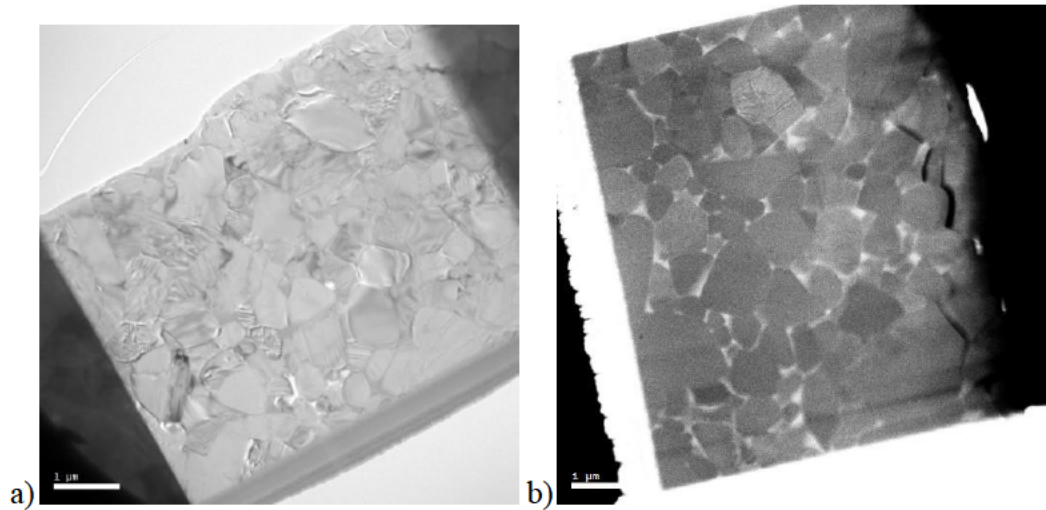


Fig. 3.3 TEM images of the prepared a) ball-milled and b) co-precipitated samples

Figure 3.4 shows the elemental map of the ball-milled sample of clear regions strongly rich in Al_2O_3 and absent of Y_2O_3 . This indicates a poor mixing condition where the coarse starting Al_2O_3 powder and the Y_2O_3 do not associate when mixing. This can result in compositional variations between local regions (poor mixing) and is confirmed by the XRD on similar prepared samples in previous work. The XRD was able to detect discrete Al_2O_3 in the microstructure in ball-milled samples.

The map of the co-precipitated sample (Fig. 3.5) indicates a much more favorable processing condition. The distribution of the phases in this sample is much more uniform; there do not appear to be regions of Al_2O_3 alone. The well-mixed uniform colors in the image indicates improved mixing as expected from coprecipitation processing. Accompanying XRD again supports this result, as there were no peaks indicating a discrete Al_2O_3 phase in co-precipitated samples.

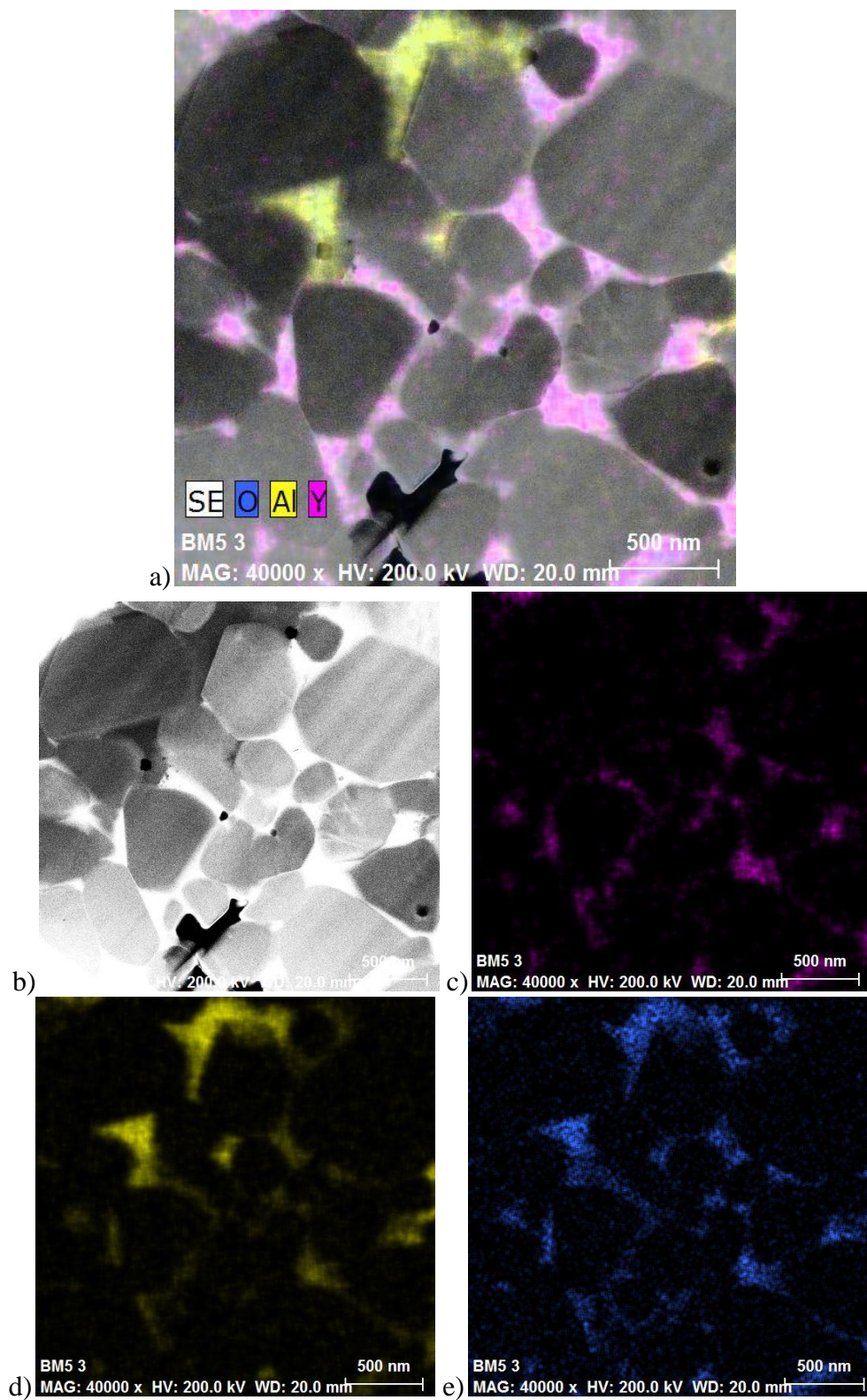


Fig. 3.4 Ball-milled TEM micrographs of a) elemental mapping consisting of Y, Al, and O; b) dark field image; c) mapping of Y; d) mapping of Al; and e) mapping of O

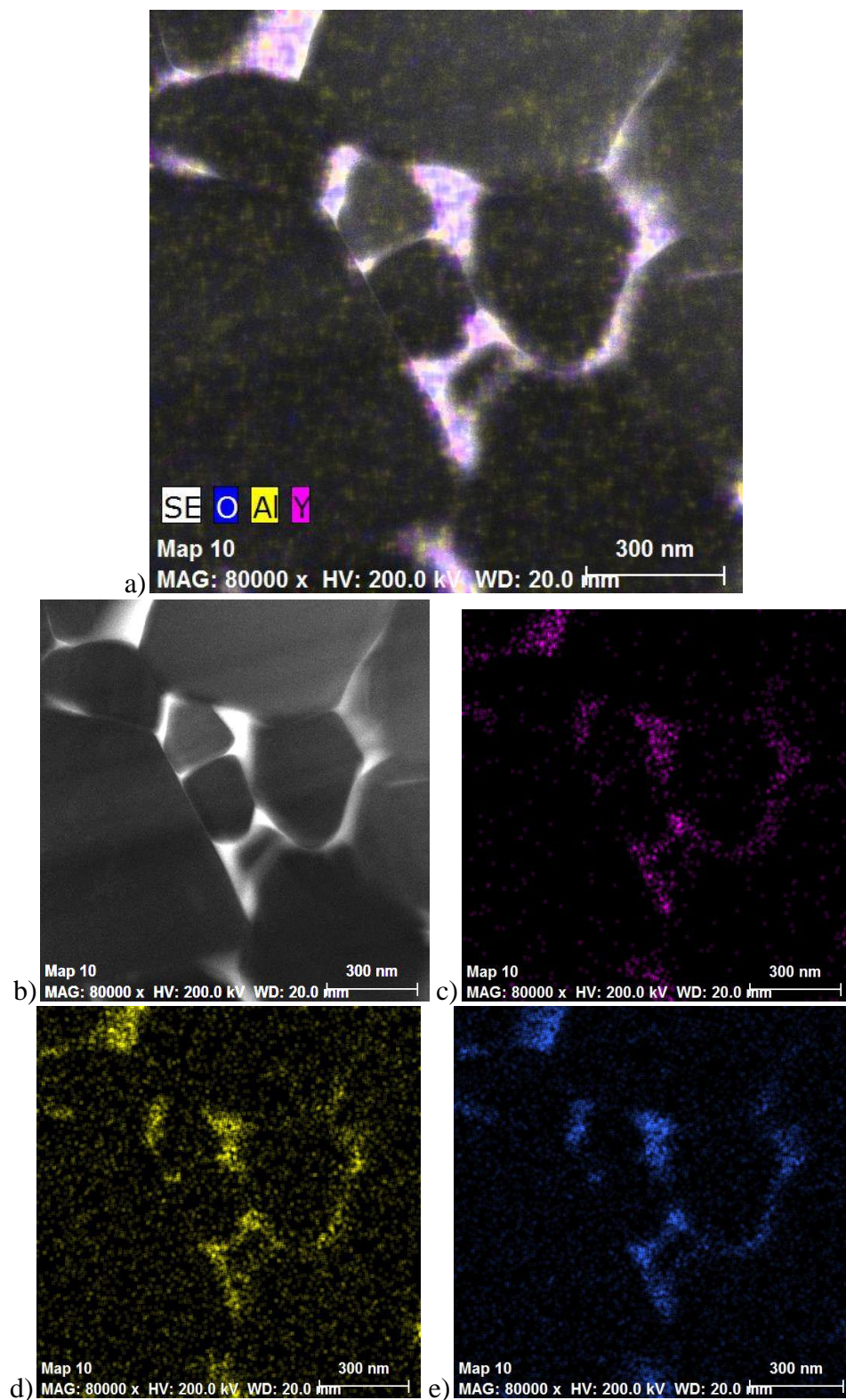


Fig. 3.5 Co-precipitated TEM micrographs of a) elemental mapping of Y, Al, and O; b) dark field image; c) mapping of Y; d) mapping of Al; and e) mapping of O

3.7 Conclusion and Future Work

Further analysis of the SiC with AlN and Y₂O₃ additives is required for full comparison and conclusion of presented results. The samples have shown high relative densities. According to the previously mentioned literature, grain growth is expected to decrease with increasing AlN content, although the SEM micrographs showed larger grains in the microstructures with higher AlN. This could be due to a long dwelling time and/or high holding temperature during sintering. Core-shell behavior becomes more apparent with increasing AlN in the system. Precipitated samples have displayed higher Knoop hardness values than ball-milled samples. The precipitation process is expected to improve mechanical and physical properties compared over milling techniques. In the future, the phases present in the SiC-AlN-Y₂O₃ samples will be investigated. Nanoindentation will also be performed to compare the hardness of the core-shell structure.

3.8 References

1. Bakas M, Greenhut VA, Niesz DE, Adams J, McCauley J. Relationship between defects and dynamic failure in silicon carbide. *Ceramic Engineering and Science Proceedings*. 2003;24(3):351–358.
2. Raczka M, Gorny G, Stobierski L, Rozniatowski K. Effect of carbon content on the microstructure and properties of silicon carbide-based sinters. *Materials Characterization*. 2001;46:245–249.
3. Krell A. Processing of high-density submicrometer Al_2O_3 for new applications. *J Am Ceram Soc*. 2003;86(4):546–553.
4. Ray D, Flinders M, Anderson A, Cutler R, Campbell J, Adams J. Effect of microstructure and mechanical properties on the ballistic performance of SiC-based ceramics. *Advances in Ceramic Armor II, Ceramic Engineering and Science Proceedings*. 2006;27(7).
5. Wilkins ML. Third progress report of light armor program. Livermore (CA): Lawrence Livermore Laboratory; 1968. Report No.: UCRL-50460.
6. Wilkins ML. Fifth progress report of light armor program. Livermore (CA): Lawrence Livermore Laboratory; 1971. Report No.: UCRL-50980.
7. Chen MW, McCauley JW, Dandekar DP, Bourne NK. Dynamic plasticity and failure of high-purity alumina under shock loading. *Nature Mater*. 2006;5:614–618.
8. Choi HJ, Kim YW, Mitomo M, Nishimura T, Lee JH, Kim DY. Intergranular glassy phase free SiC ceramics retain strength at 1,500 °C. *Scripta Materialia*. 2004;50(9):1203–1207.
9. Zhou Y, Hirao K, Toriyama M, Yamuchi Y, S Kanzaki. Effects of intergranular phase chemistry on the microstructure and mechanical properties of silicon carbide ceramics densified with rare-earth oxide and alumina additions. *J Am Ceram Soc*. 2001;84(7):1642–1644.
10. Kaza A. Effect of gas phase composition in pores during initial stage of sintering. [dissertation] [New Brunswick (NJ)]: Rutgers University; 2006.

11. Ziccardi C, Demirbas V, Haber R, Niesz D, McCauley J. Means of using advance processing to eliminate anomalous defects on SiC armor. *Ceramic Engineering and Science Proceedings*, 2005;26(4).
12. Mercurio SR, Haber RA Silicon carbide microstructure improvements for armor applications. Presented at 31st International Cocoa Beach Conference & Exposition on Advanced Ceramics & Composites; 2007 Jan 21–26; Daytona Beach, FL.
13. Yang J, Oliveira FJ, Silva RF, Ferreira JMF. *Journal of the European Ceramic Society*. 1999;19:433–439.
14. Shaw TM, Pethica BA. Preparation and sintering of homogeneous silicon nitride green compacts. *J Am Ceram Soc*. 1986;69(21):88–93.
15. Albano MP, Garrido LB. *Ceramics International*. 2003;29:829–836.
16. Sciti D, Balbo A, Bellosi A. Comparison of ZrB₂-ZrC-SiC Composites fabricated by spark plasma sintering and hot-pressing. *Advanced Engineering Materials* 2005;7(3):159–163.
17. Balbo A, Sciti D, Costa A, Bellosi A. Effects of powder processing on colloidal and microstructural characteristics of β – SiC powders. *Materials Chemistry and Physics*. 2007;103:70–77.
18. Li JF, Watanabe R. *Journal of Materials Science*. 1991;26:4813.
19. Hotta M, Hojo J. *J Euro Ceram Soc*. 2010;30:2117–2122.
20. Suzuki K, Sasaki M. *Ceramics International*. 2005;31:749–755.
21. Pan Y, Tan S. *Journal of Materials Science*. 1998;33:1233–1237.
22. Balestra RM, Ribeiro S, Taguchi SP, Motta FV, Bormio-Nunes C. *J Euro Ceram Soc*. 2006;26:3881–3886.
23. Hojo J, Matsuura H, Hotta M. *Key Engineering Materials*. 2009;403:177–178.
24. Hu J, Gu H, Chen Z, Tan S, Jiang D, M Ruhle. *Acta Materialia*. 2007;55:5666–5673.
25. Sigl L, Kleebe H. *J Am Ceram Soc*. 1993;76:773–776.

4. Task 3: High-Strain-Rate Behavior and Dynamic Failure of Armor Ceramics, Core Program

Core Faculty: KT Ramesh, L Graham-Brady

US Army Research Laboratory (ARL) Leader: J McCauley

ARL Collaborators: J LaSalvia, T Jessen, ESC Chin, T Weerasooriya, P Patel, S Schoenfeld, J Campbell, T Sano, TW Wright

Graduate Student: Guangli Hu

4.1 Long-Range Objectives

- Provide direct links between dynamic mechanical properties, processing routes, and preexisting defect structures in armor ceramics.
- Develop qualitative understanding of dynamic deformation and failure mechanisms in armor ceramics.
- Develop models for high-rate deformation of intact and failed ceramics under multiaxial loading.

4.2 Accomplishments

Failure and deformation mechanism transition: We have conducted quasi-static, uniaxial dynamic, and confined dynamic experiments on AlN. After experiments, the following deformed fragments were recovered for extensive SEM and TEM study.

- A fracture mechanism map has been constructed in the confining stress and strain rate space, as shown in Fig. 4.1. At low strain rate and low confining stress, intergranular fracture is dominant. With increase of the strain rate, transgranular fracture becomes dominant. At high strain rate with confining stress, interphase failure becomes viable, along with both intergranular and transgranular fracture.
- Dynamic fracture mechanics are used to analyze the intergranular fracture to transgranular fracture transition under different loading rates based on the crack deflection criteria, while wing crack micromechanics are recalled to interpret the interphase failure with increasing confining stress.

- Deformation mechanisms of AlN change with pressure. Below the transition pressure (approximately 2 GPa), material response is controlled by internal defects, while beyond the transition pressure, material response is increasingly controlled by dislocation mechanisms. The transition is substantiated both by macroscopic strength data and microscopic observations. Around the transition pressure regime, both fracture and dislocation activities exist. A mechanistic bilinear failure envelope is obtained for sintered AlN, which can be extended to other brittle material systems, such as Al_2O_3 and SiC.
- TEM study on specimens tested at different loading conditions not only confirmed the existence of dislocation activities under confined dynamic loading, substantiating the proposed mechanism-based failure envelope, but also revealed the microcrack-dislocation interaction at small length scales, implying the plasticity affecting the material behavior to a significant extent, as shown in Fig. 4.2.

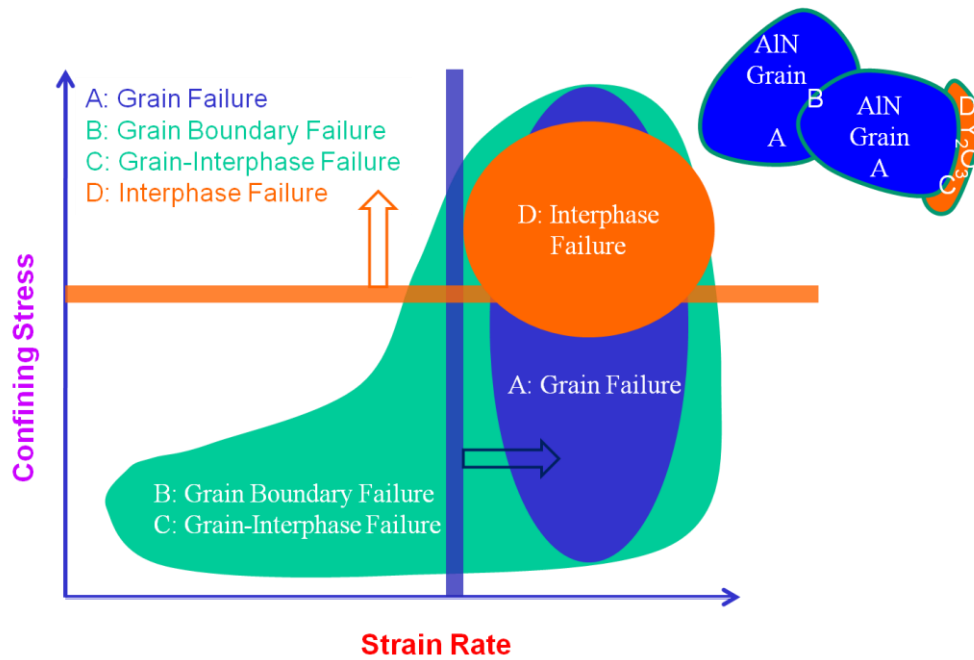


Fig. 4.1 Failure mechanism map in the confining stress and strain-rate space

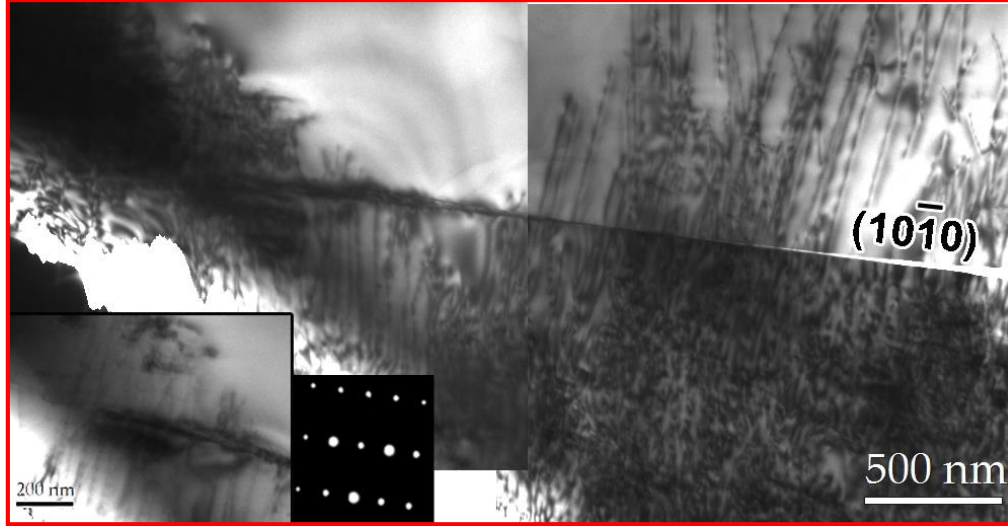


Fig. 4.2 Bright-field TEM imaging of an AlN fragment, capturing a transgranular crack being arrested interior of the crystal, with profuse dislocations either along the crack path or at the crack tip. Insets are zoom-in views of the crack tip stopping interior of the crystal and selected area electron diffraction of the AlN crystal, respectively.

To validate the proposed dislocation controlled region, shock recovery experiments on AlN were designed and conducted, as shown in Fig. 4.3a. We used the tungsten carbide flyer plate, launched at approximately 500 m/s, generating the longitudinal shock stress of approximately 10 GPa in the AlN specimen. The corresponding pressure can be estimated as 5.4 GPa, which resides in the dislocation controlled region. Fragments were recovered after the experiment for the TEM characterization and profuse dislocation arrays were observed, as shown in Fig. 4.3b.

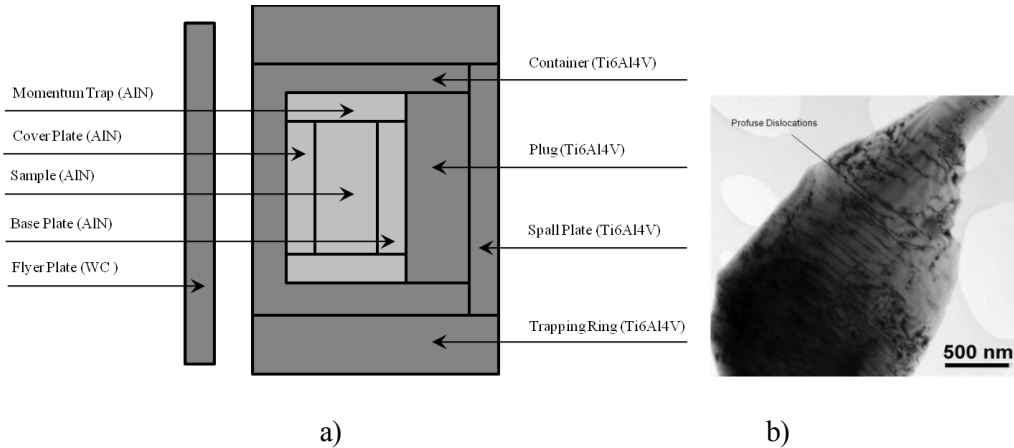


Fig. 4.3 Specimen assembly a) and b) profuse dislocations observed after deformation (shock stress ~10 GPa)

4.3 Collaborative Interactions

We collaborated with Cyril Williams from ARL on the shock recovery experiments. Helpful discussion with Dr Dandekar from ARL, Dr Grady from the South West Division of Applied Research Associates, and Dr Gray from Los Alamos National Laboratory was greatly appreciated.

4.4 Publications and Presentations

1. Hu G, Ramesh KT, Cao B, McCauley JW. The compressive failure of aluminum nitride considered as a model advanced ceramic. *Journal of the Mechanics and Physics of Solids*. 2011;59(5):1076–1093.
2. Hu GL, Chen CQ, Ramesh KT, McCauley JW. Mechanisms of dynamic deformation and dynamic failure in aluminum nitride. *Acta Materialia*. 2012;60:3480–3490.
3. Hu G, Ramesh KT, McCauley JW. Loading rate and size effects on mechanical response of aluminum nitride. Presented at the 35th International Conference and Exposition on Advanced Ceramics and Composites; 2011 Jan; Daytona Beach, FL.
4. Hu G, Williams C, Chen CQ, Ramesh KT, McCauley JW. Dynamic response of aluminum nitride under very high strain rate and pressure. Presented at SEM Annual Conference & Exposition on Experimental and Applied Mechanics; 2011 Jun; Uncasville, CT.
5. Hu G, Chen CQ, Williams C, Ramesh KT, McCauley JW. Deformation mechanism of aluminum nitride under shock loading. Presented at the 17th APS SCCM Conference; 2011 Jun; Chicago, IL.

5. Task 4: Identification of Fundamental Deformation and Failure Mechanisms in Armor Ceramics

Core Faculty: DJ Green

Associated Faculty: D Niesz, R Haber, KT Ramesh

US Army Research Laboratory (ARL) Collaborators: J LaSalvia, J Swab, T Jessen

Graduate Student: A Muller

Oak Ridge National Laboratory Adviser: A Wereszczak

5.1 Long-Range Objectives

- Demonstrate that information obtained from Hertzian indentation can be used to assess the quality and variability of armor ceramics. Identify role of cone cracking in the indentation process and compare the indentation stress–strain behavior in candidate armor materials.
- Evaluate the influence of grain boundary engineering on contact damage.
- Identify microstructure or atomic structure features and defects that relate to variability in the strength and deformation behavior of armor ceramics.

5.2 Planned Objectives for 2011 Calendar Year

- First Quarter (Phase IV)
 - Daytona Beach presentation (indentation stress-indentation-strain data for 2 spinels with different grain sizes).
 - Measure indentation stress–indentation strain data for silicon carbide (SiC) and boron carbide (B₄C) material (smaller indenter).
 - Determine yield stresses and strain hardening behavior.
 - Measure surface topography of indentation impressions.
 - Determine degree of densification.
 - Measure plastic work associated with deformation process.
 - Scanning electron microscopy (SEM) observations.
- Second Quarter (Phase IV)

- Aluminum nitride (AlN) and aluminum oxynitride (AlON) material using same approach as in first quarter.
- Third Quarter (Phase IV)
 - Progress Report.
 - Complete thesis.
 - Thesis defense (July 29).
- Fourth Quarter
 - Submit Paper 3 to the *Journal of The American Ceramic Society*.

5.3 Introduction

The purpose of this study was to investigate variations in the damage of 4 candidate ceramic armor materials, i.e., surface cracking, yielding behavior, and the mutual interaction of these effects using spherical indentation. A particular goal of the study was to compare the penetration resistance for spinel (MgAl_2O_4) with 2 different grain sizes, a transparent large-grained AlON and a small-grained sintered AlN. To probe the behavior of these materials, an instrumented indentation system was used that was built in a previous study¹ and capable of continuous force-displacement measurement, which allows the contact area to be determined during the indentation cycle. The approach used in converting the experimental data for these 4 materials into the indentation stress-strain behavior so as to determine indentation yield stress and the post-yielding behavior of the material below the contact area has been described.² To quantify penetration resistance of these materials, a work of indentation approach was taken. This method, which involves the extraction of total work of indentation, or its elastic and plastic components from the force-displacement, was first proposed by Stilwell and Tabor in 1961 as way to estimate materials hardness. It has been used more recently by others,³⁻⁷ to relate the hardness and predict erosion behavior of various material. A figure of merit based on the total work of indentation and indentation strain energy density was also developed to compare the materials evaluated in this study.

5.4 Experimental Procedure

5.4.1 Materials

Four candidate armor materials were evaluated in this investigation: 2 transparent fine-grained spinels with substantially different grain sizes, referred to as fine-grained and coarse-grained AlON and AlN. Both fine-grained and coarse-grained spinels were produced at the Fraunhofer-Institut für Keramische Technologien und

Systeme (IKTS, Dresden, Germany) under a contract to the US Army Research Laboratory, using techniques developed by Krell et al.^{8,9} The AlON ($\text{Al}_{23}\text{O}_{27}\text{N}_5$) material investigated was procured from Surmet Corporation (Burlington, MA) and the AlN material was procured from Dow Chemical Company (Midland, MI). This sintered AlN material is not currently commercially available in the form tested but is similar to that reported by Tajika et. al.^{10–13} MgAl_2O_4 and AlON have a cubic crystal structure and exhibit excellent transmission from the ultraviolet to the mid-infrared region in their polycrystalline forms, making them ideal candidates for both visible and infrared window applications.¹⁴ In contrast, AlN has a hexagonal crystal structure and is opaque, making this material better suited for vehicular, equipment, and personal armor applications.¹⁵

Young's modulus, E , and the Poisson's ratio, ν , of these materials were determined using ultrasonic velocity according to the procedures outlined in ASTM E494-05.¹⁶ The values obtained for the 2 spinels, previously measured,² are shown in Table 5.1 along with the values measured for AlON and AlN in this study. The average bulk density found using the Archimedes method and the Knoop hardness determined using a maximum indentation load of 2 kg on a microhardness tester (V100-C1; Leco, St. Joseph, MI) are also given in Table 5.1. Average grain sizes of the materials tested were determined by the linear intercept method described in ASTM E112.¹⁷ Values for the 2 spinels, reported previously,² were determined from several SEMs of optically polished (0.25- μm finish) and chemically etched (boiling phosphoric acid) specimens. For AlON and AlN, the average grain size was determined from several optical micrographs (Olympus BX60M; Center Valley, PA) after relief polishing with colloidal silica.

Table 5.1 Properties of the spinels, AlON, and AlN

Property	Fine-Grained Spinel ²	Coarse-Grained Spinel ²	AlON	AlN
Density (g/cm^3)	3.57	3.57	3.67	3.29
E_s (GPa)	260.5	260.5	319.0	321.5
Poisson's ratio	0.26	0.26	0.24	0.21
Knoop hardness, HK_2 (GPa)	12.3 ± 0.4	12.3 ± 0.3	14.9 ± 0.4	9.62 ± 0.17
Average grain size (μm)	0.40	1.4	210	5.0

The average grain size of AlON materials is relatively large compared with the other materials, and it follows that the indentation contact sizes, encountered in this study for AlON, are less than the grain size. Thus, the indentation event is occurring mainly within a single crystal. To average this behavior, 30 indents were performed for each specimen when determining the Knoop hardness.

Optical profilometry (Wyko NT1100; Veeco, Tuscon, AZ) showed the nominal peak-to-valley surface roughness of the as-received optically polished spinel and AlON specimens to be 25–40 and 25–30 nm, respectively.¹ The AlN specimen, which was mechanically polished to a 0.05- μm final polish using aluminum oxide (Al_2O_3) powder, had a resulting peak-to-valley surface roughness of 110–130 nm. Optical observation showed this roughness was a result of a minor degree of grain pull-out.

5.5 Equipment

A custom-built instrumented indenter,¹ which was mounted to a load cell on the crosshead of a universal testing machine (Model 5866; Instron Corp., Norwood, MA) was used for all subsequent indentation experiments. This instrumented indentation system was used to continuously monitor-force-displacement behavior during the loading and unloading cycles. The fine- and coarse-grained spinel materials tested had nominal thicknesses of 5.95 and 5.97 mm, respectively, while the AlON and AlN materials tested had a nominal thicknesses of 10.00 and 16.10 mm, respectively.

A small-radius custom spherical diamond ($E = 1,141 \text{ GPa}$, $\nu = 0.07$) indenter (Gilmore Diamond, Attleboro, MA), radius 261 μm , was selected to assess the elastic–plastic and fracture behavior of the 4 candidate armor materials. This indenter size was chosen to ensure yielding occurred prior to fracture. The indenter radius was measured by fitting the equation of a circle to a multitude of 2-dimensional line scans of the indenter tip and measured to be 4.4% greater than the manufacturer’s quoted nominal value (see Table 5.1). For all indentation experiments, specimens were loaded using a force-controlled, triangular waveform at a constant rate of 1 N/s to several selected maximum compressive forces. Specimens were then unloaded at a constant rate of 1 N/s. To ensure that the stress fields and ensuing cracks did not interact, indents were spaced approximately 4 mm from center to center. Maximum indentation forces of 50, 60, 80, 100, 130, 160, 200, 250, and 300 N were chosen for the spinel materials. For the AlON and AlN materials, maximum indentation forces of 30, 40, 50, 60, 80, 100, 125, 150, and 200 N were chosen. A minimum of 5 indentations were made at each selected load to produce a comprehensive data set. Prior to indentation, all surfaces were cleaned with isopropyl alcohol to remove any debris and organic contamination remaining on the surfaces due to handling. All tests were performed under ambient conditions.

After indentation, surface impressions were examined using differential interference contrast (DIC) imaging techniques in an optical microscope. The optical

profilometer was also used to examine the surface topography and to measure the radius and depth of the residual indentations because it could be used to quantify the pile-up of the indented surface. For this study, all measurements of the impression radii were made to include pile-up of the indented surface. Indentation stress-strain curves were determined from these experimental data using the analysis discussed elsewhere.² This process involves measuring the post-loading impression radius and depth, calibrating the displacement data and calculating the contact radius during loading from the displacement data.¹ Work of indentation was determined from the force-displacement data collected during the indentation cycle. The analysis approach for calculating these data will be discussed later in this report.

Subsurface indentation damage was examined in the SEM on the fractured halves of spherically indented bar specimens, prepared in accordance to ASTM C 1161.¹⁸ Particular attention was paid to the region directly below the contact area revealed by the bending fracture. To prepare these specimens, a single indent is placed in the center of each bar using the indentation procedure described earlier. The maximum compressive force applied using the instrumented indentation system was 300 N for both of the spinels and 200 N for both of the AlON and AlN materials. Indented bars were then aligned in a 4-point bend fixture to ensure that fracture occurred through the indentation site and loaded to failure using a loading rate of 1 N/s.

5.6 Results and Discussion

5.6.1 Surface Indentation Damage

Indentation damage patterns are shown at 3 selected maximum indentation forces for the spinels, AlON, and AlN in Figs. 5.1–5.4. These series of optical micrographs taken following indentation confirm that all materials behaved in an elastic-plastic fashion, yielding prior to cracking, slightly below 50 N for the spinels and below 30 N for the AlN. Although cracking is evident in AlON at the lowest indentation load shown in Fig. 5.3, it also exhibited an initial elastic-plastic response similar to the other materials, yielding prior to fracture, slightly below 40 N. Yielding was seen to initiate at increasing loads in AlN followed by AlON, then coarse-grained spinel and, lastly, fine-grained spinel. Additionally, when comparing the residual impression radii for all 4 materials, it is obvious that they are the largest for AlN at the same indentation loads, indicating that the mechanisms responsible for inelastic deformation are activated earlier in this particular material.

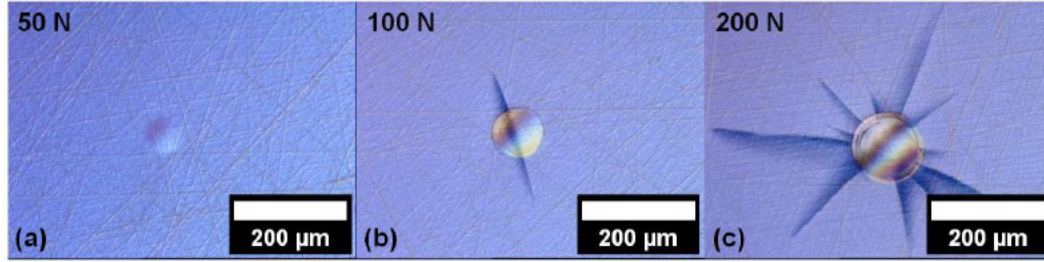


Fig. 5.1 DIC images showing the typically observed cracking modes in the fine-grained spinel after the application of (a) 50-N, (b) 100-N, and (c) 200-N maximum compressive forces, using a 261-μm-radius diamond indenter

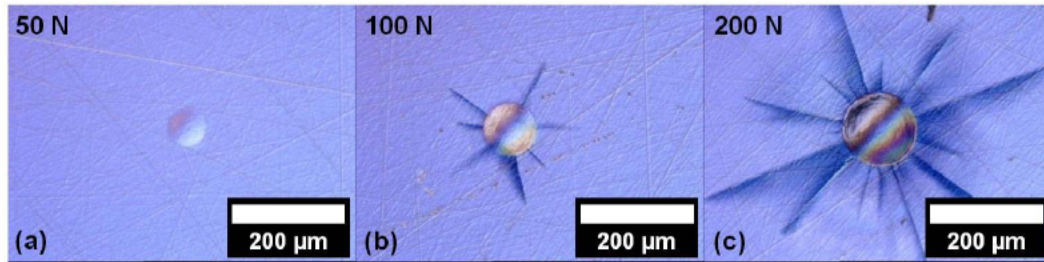


Fig. 5.2 DIC images showing the typically observed cracking modes in the coarse-grained spinel after the application of (a) 50-N, (b) 100-N, and (c) 200-N maximum compressive forces, using a 261-μm-radius diamond indenter

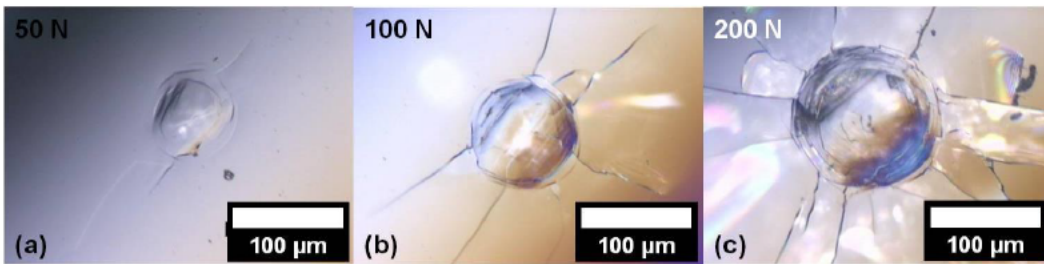


Fig. 5.3 DIC images showing the typically observed cracking modes in AlON after the application of (a) 50-N, (b) 100-N, and (c) 200-N maximum compressive forces, using a 261-μm-radius diamond indenter

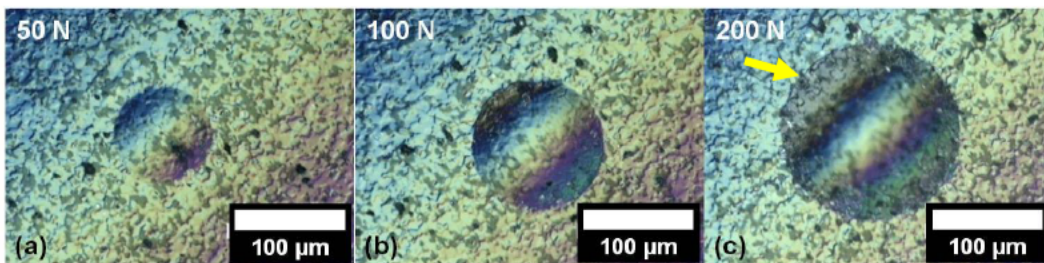


Fig. 5.4 DIC images showing the typically observed cracking modes in AlN after the application of (a) 50-N, (b) 100-N, and (c) 200-N maximum compressive forces, using a 261-μm-radius diamond indenter. A ring (yellow) and radial (white) crack are arrowed.

In Table 5.2, the loads detected for the onset for ring and radial cracking are shown for the spinels, AlON, and AlN based on postindentation observations of the indentation sites. The presence of inelastic deformation can alter the fracture behavior when compared with a strictly elastic case because it significantly modifies the stress field in the region of the contact area.^{19–21} Ring cracking and radial cracks were observed in AlON at slightly lower loads compared with the fine- and coarse-grained spinels and much lower loads compared with AlN. The number and length of the radial cracks appearing on the surface of the materials increased as peak load increased for all 4 materials.

Table 5.2 Observed indentation load ranges for the onset of ring and radial cracking in the spinels, AlON, and AlN, using a 261- μ m-radius diamond indenter

	Fine-Grained Spinel ²	Coarse- Grained Spinel ²	AlON	AlN
Onset of ring cracking (N)	60–80	50–60	40–50	80–100
Onset of radial cracking (N)	80–100	60–80	50–60	100–125

At higher indentation loads, ring and radial cracking were the primary cracking modes observed on the surfaces of all 4 materials. While the presence of ring and radial cracks are more evident for the fine-grained spinel, coarse-grained spinels, and the AlON, they were less apparent in the AlN even at higher indentation loads. Concentric ring cracks and numerous radial cracks were also present at the higher indentation loads in the fine-grained spinel, coarse-grained spinel, and AlON. However, only radial cracks could be detected on the surface of the AlN for the indentation loads studied here.

Anisotropic cracking behavior seen in the AlON is a result of the fact that many of the indentations are located primarily within a single grain. Surface steps, as shown in Fig. 5.5, also appear within the indentation for AlON, suggesting cleavage cracks are forming on specific crystal planes. These cleavage steps resulted from the high applied stresses underneath the indenter and were often present at low indentation loads. Overall, cracking was seen to initiate at lower loads and was more severe in the AlON, followed by the coarse-grained spinel, then fine-grained spinel, and finally the AlN.

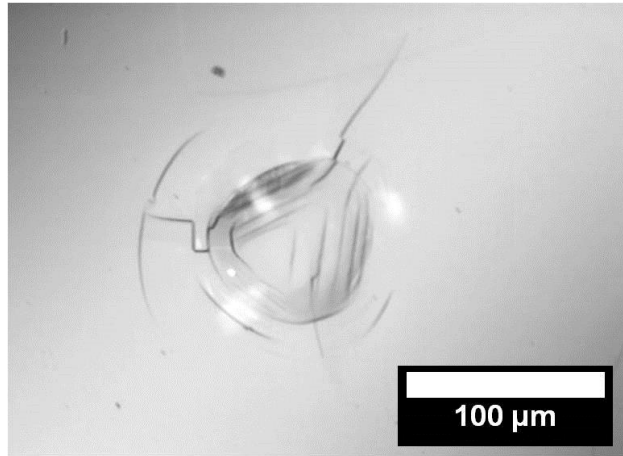


Fig. 5.5 Optical micrograph showing an example of deformation cleavage (dark bands) inside an 80-N indentation in AlON produced with 261-μm-radius diamond indenter

Figure 5.6 shows the corresponding surface profiles for the fine-grained spinel, coarse-grained spinel, AlON, and AlN micrographs shown earlier. Line scans through the center of the indentations were extracted from profilometer scans of the surface, and 4 separate measurements per indentation were averaged to determine the radius and depth of the residual impressions. It is obvious from these line scans that the residual impression radii and depth of the residual impression for AlN is the greatest when comparing similar maximum indentation loads. This behavior is a product of its low indentation hardness, measured early, and is also echoed in the optical micrographs. Discontinuities corresponding to the surface steps can be readily observed in the line scans of AlON especially at the 2 higher indentation loads shown. The surface profile scans also suggest that the hardness of the fine-grained spinel is highest because the residual impression depths were smallest for this material. Further details regarding the indentation hardness and elastic recovery of the 2 spinels have been discussed previously.²

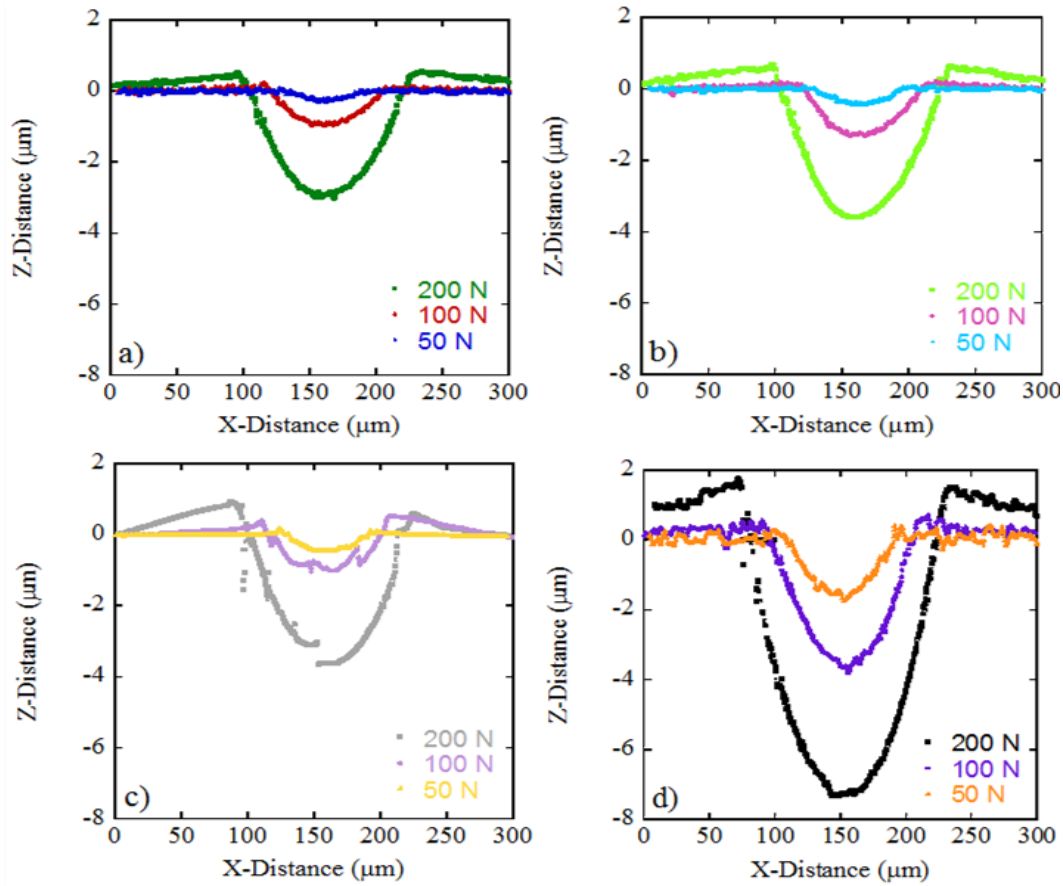


Fig. 5.6 Profilometer line scans showing the typical surface profiles at maximum loads of 50 N, 100 N, and 200 N of a) fine-grained spinel, b) coarse-grained spinel, c) AlON, and d) AlN as a function of the applied force. All indentations were made using a 261- μm -radius diamond indenter.

5.6.2 Subsurface Indentation Damage

To explore the underlying mechanisms of deformation and fracture in the 4 materials, the fractured surface of the indented bend bars, Figs. 5.7–5.9, were examined in the SEM. Figure 5.7 is representative of both the fine- and coarse-grained spinel. The top surface of each bend bar shows the residual impression created during indentation. For each of the 4 materials, an inspection of the fracture path revealed that the impression was intersected by the bending-induced fracture along radial and ring cracks created during the indentation event, though this is less apparent in the AlN. Directly underneath the indentation site, in the region subjected to the high contact stresses, a region of intergranular fracture was observed in the fine-grained spinel, coarse-grained spinel, and AlN. The intergranular region in the fine- and coarse-grained spinels is evidence that the inelastic zone below the indenter involves the creation of grain boundary microcracks as fracture away from this region was transgranular. This same

region revealed transgranular cleavage microcracks in the AlON. Microcracks have also been observed to occur readily in the deformed regions underneath a Berkovich indenter during nanoindentation on this same material.²² Similar features were also revealed in the fragmented piece of AlON tested under dynamic compression.²³ Figure 5.10 shows transgranular cleavage steps observed on the surfaces of a cone crack in AlON in more detail.

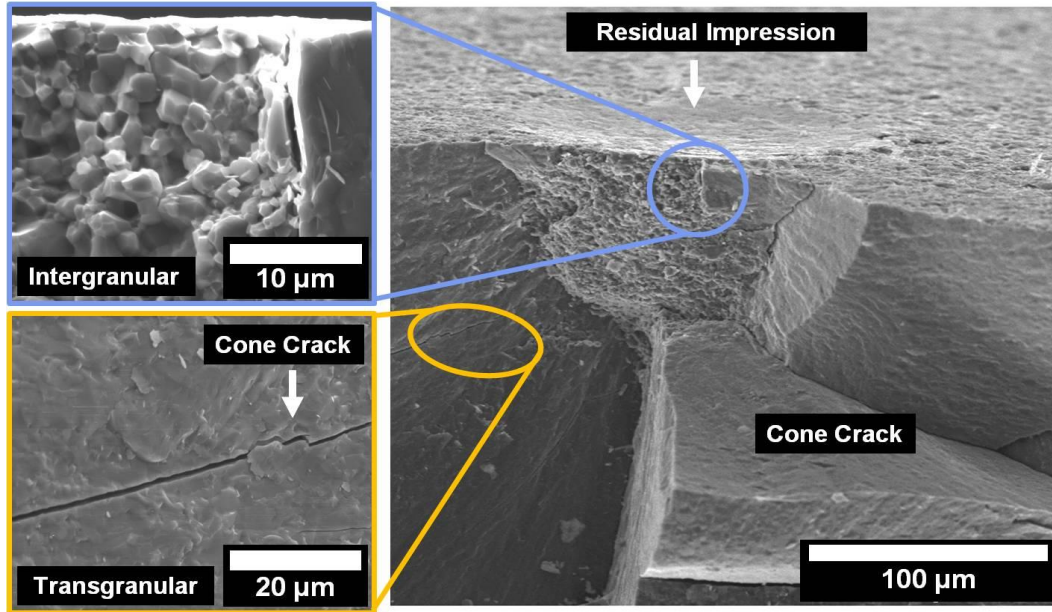


Fig. 5.7 SEM micrographs showing the fractured surface of a 4-point bend bar, in which an indentation of 300 N was placed in the fine-grained spinel prior to bend failure. The arrow points to a remnant indenter surface impression and intergranular fracture region below the indentation site. Away from the contact region, the fracture surface is transgranular and believed to be a result of only the bend stresses.

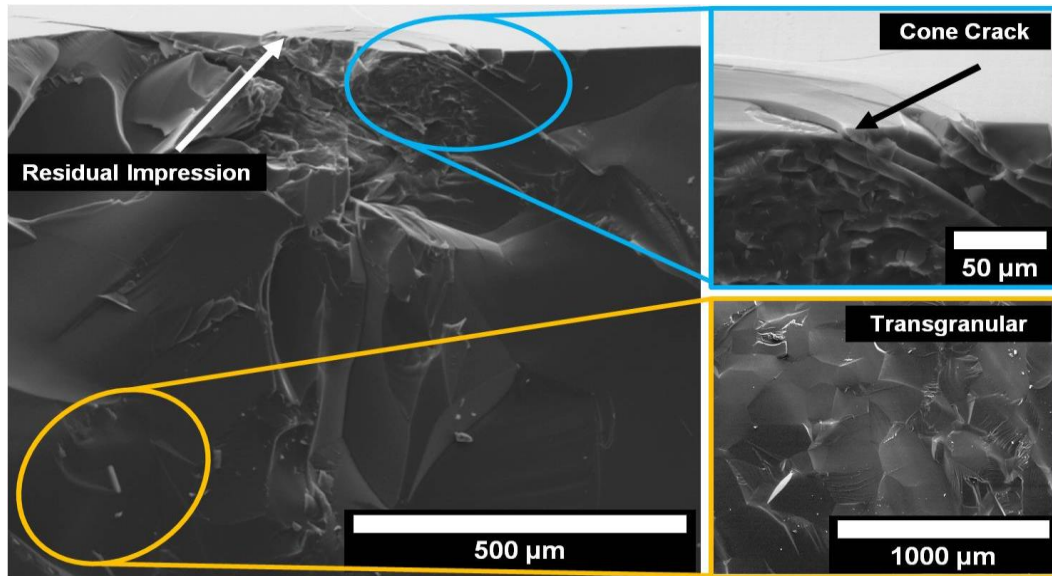


Fig. 5.8 SEM micrographs showing the fractured surface of a 4-point bend bar, in which an indentation of 200 N was placed in AlON prior to bend failure. The arrow points to a remnant indenter surface impression and microcracked fracture region below the indentation site. Away from the contact region, the fracture surface is transgranular and results from the bend stresses.

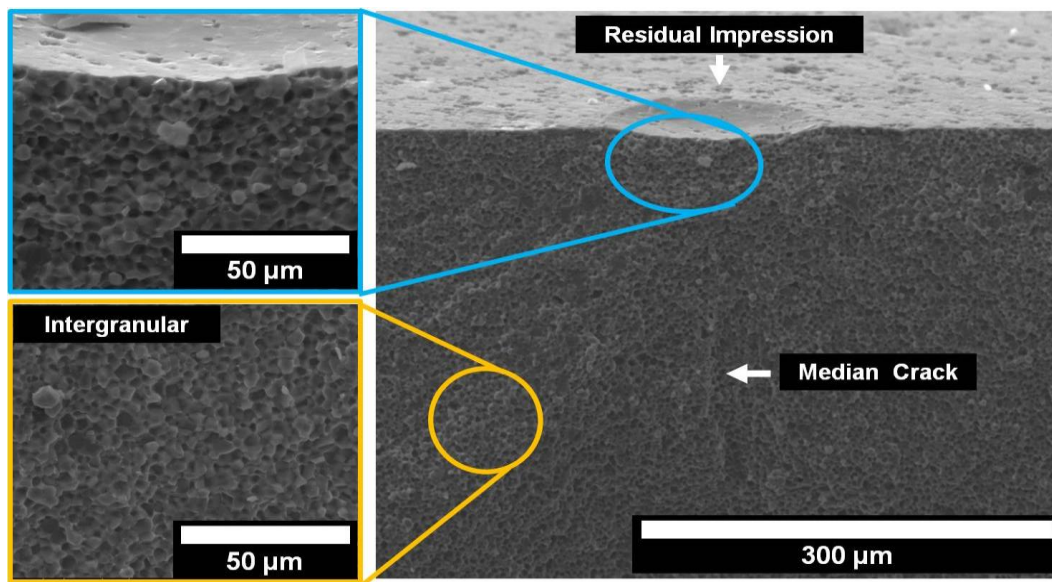


Fig. 5.9 SEM micrographs showing the fractured surface of a 4-point bend bar, in which an indentation of 200 N was placed in AlN prior to bend failure. The arrow points to a remnant indenter surface impression and median-crack below the indentation site. Away from the contact region, the fracture surface is also intergranular as is the region directly below the contact.

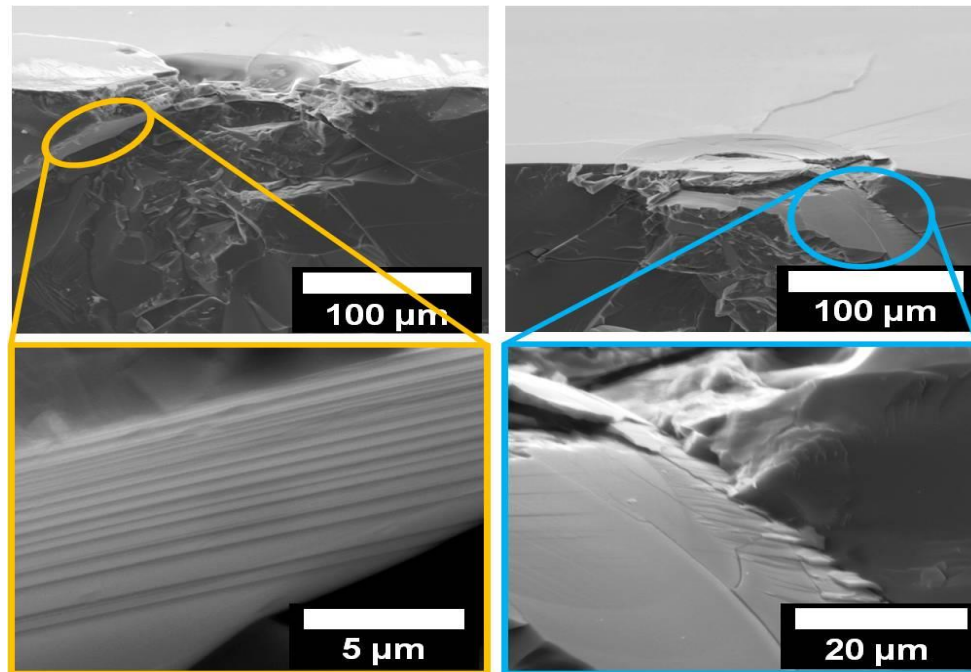


Fig. 5.10 SEM micrographs showing the 2 corresponding fractured surface of a 4-point bend bar and the transgranular cleavage steps and microcracks observed on the surfaces of cone crack

Ring and cone crack are also evident in the micrographs of the fine-grained, coarse-grained spinels, as well as the AlON. Although the ring and cone-cracked regions are clearly visible in the spinels at these indentation loads, this was not the case for AlN even at much higher indentation loads. The defining features, which evolved in AlN with increasing indentation load, were median, ring, and radial cracking. A transgranular fracture region formed as a result of the ensuing bend fracture is observed in both the fine- and coarse-grained spinels and AlON, while an intergranular region is observed in AlN. Intergranular fracture is observed in the region directly below the contact area as well as the region produced as a result of the bend fracture for AlN, whereas the fine- and coarse-grained spinels and AlON displayed both transgranular and intergranular fracture regions.

While the approach in this work involved inspection of the fractured surface of bend bars to observe the subsurface damage zone, a similar method of observing the subsurface damage below an indentation site has been used previously to show damages zones of indented bonded specimens subjected to blunt contact.²⁴ Subsurface damage zones observed for various materials using this method were analogues to those seen in this study.

5.6.3 Indentation Stress-Strain

Load-displacement curves corresponding to the optical micrographs and surface profilometry scans shown earlier for the spinels, AlON, and AlN are shown in Fig. 5.11. These force-displacement curves are indicative of elastic-plastic material behavior as it can be seen that the contact depth includes both elastic and plastic contributions to the total displacement. There is also a permanent displacement associated with the surface impression after unloading and hysteresis between the loading and unloading curves. The measured displacements have been corrected for machine compliance using the Modified Bushby Method described previously.² This method, similar to that outlined by Bushby,²⁵ uses the elastic properties of the indenter and specimen to determine a machine compliance that gives the correct combined modulus, E^* . The measured permanent displacement and residual impression radius found by means of the optical profilometer are used to determine the E^* value in this procedure because they can account for pile-up of the material surface. This procedure was used to determine the machine compliance and correct the displacement data for each of the 4 materials using the independently measured elastic properties (see Table 5.1).

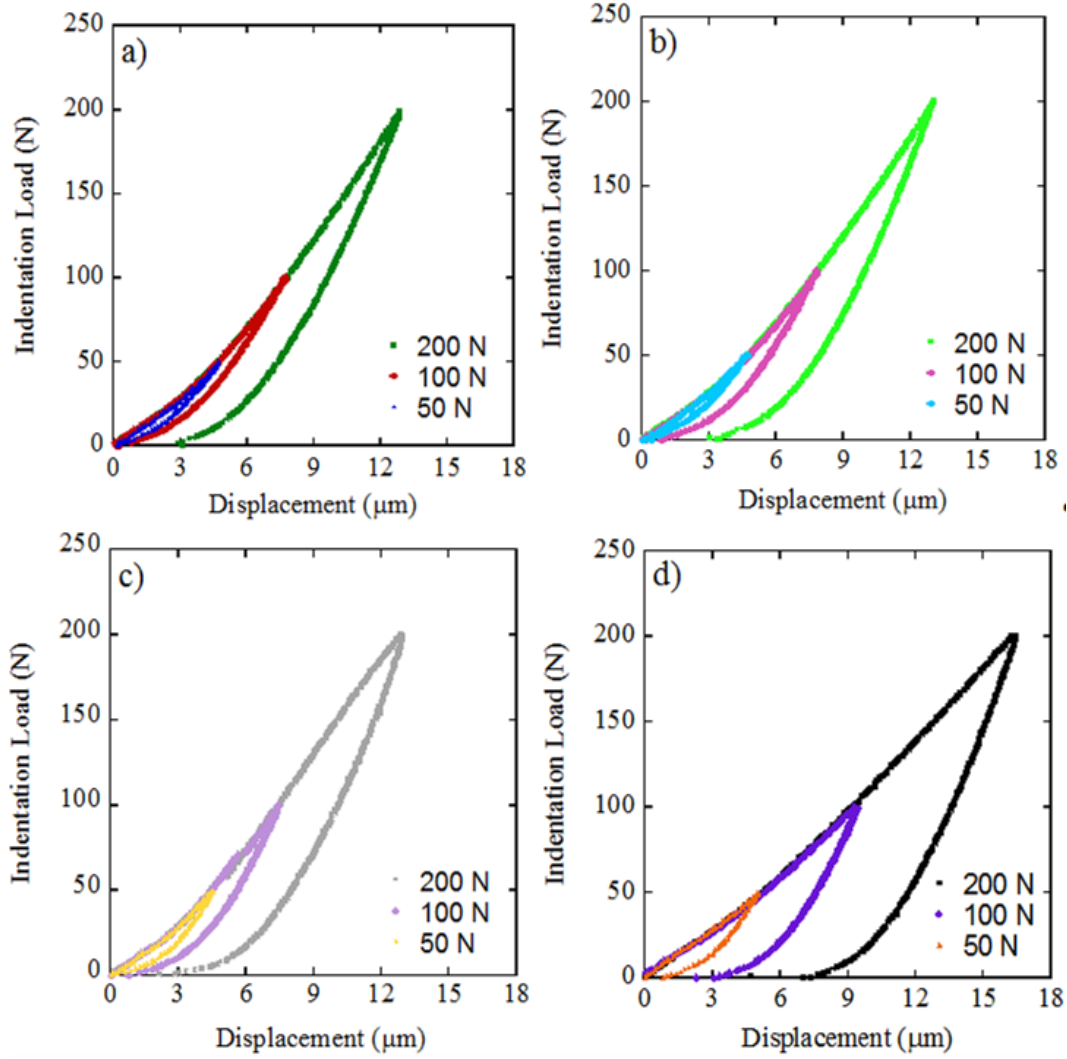


Fig. 5.11 Representative corrected force-displacement curves at maximum loads of 50 N, 100 N, and 200 N, showing the full loading and unloading sequence for a) fine-grained spinel, b) coarse-grained spinel, c) AlON, and d) AlN using a 261- μm -radius diamond indenter

Extraction of the stress-strain response from the force-displacement curves allows the yielding stress to be identified and the post-yielding behavior to be described, providing a useful way to compare the 4 materials.^{24,26,27} Figure 5.12 compares the indentation stress-strain behavior for fine-grained spinel, coarse-grained spinel, AlON, and AlN determined from the force-displacement curves that were corrected using the Modified Bushby Method of resolving the machine compliance described earlier.² It can be seen that the fine-grained spinel, coarse-grained spinel, and AlON exhibits similar stress values for all given strains, differing by only 1%–15% depending on the given strain. Conversely, AlN exhibits a much lower stress values for all given strains when compared with the other 3 materials, a 25%–35% difference.

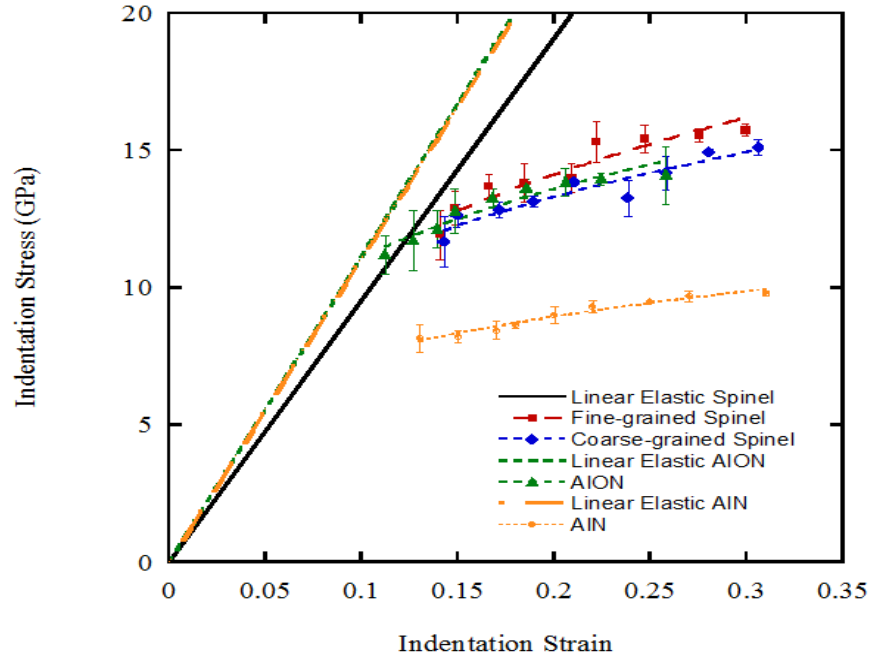


Fig. 5.12 Comparison of indentation stress-strain curves for the fine-grained spinel, coarse-grained spinel, AlON, and AlN using a 261- μm radius diamond indenter. Error bars correspond to the standard deviation within each given test condition. The solid trend line shows the linear elastic behavior.²⁸

Based on the slope of the indentation stress-strain curves for these materials, the indentation strain-hardening rates are also quite similar, differing only slightly between these 4 materials, with the fine-grained spinel having a slightly higher strain-hardening coefficient than the AlON, coarse-grained spinel, and AlN. A power law fit revealed indentation strain-hardening exponents of 0.34, 0.28, 0.29, and 0.25 for the fine-grained spinel, coarse-grained spinel, AlON, and AlN, respectively. Extrapolation of these power law fits to the linear elastic stress-strain solution,²⁸ also plotted in Fig. 5.12, revealed similar yield stresses of approximately 12.1, 11.5, and 11.1 GPa for the fine-grained spinel, coarse-grained spinel, and AlON, respectively, while AlN was significantly lower at 6.65 GPa.

Although there was a grain size difference of more than a factor of 3 between the fine- and coarse-grained spinels, and an even greater difference between the fine-grained spinel, coarse-grained spinel, and AlON, this factor does not seem to be very prominent. While grain size differences did not appear to be very potent in distinguishing the differences between the 4 materials, the deformation mechanisms observed in the inelastic zone of these materials may be influential. Intergranular failure was predominant in the region directly below the impression area for the spinels and AlN. Cleavage microcracking was seen in AlON, and this

process apparently initiated in the impression. Various authors^{29–31} have discussed, in their constitutive based models, the importance of microcracking in the comminuted zone when predicting the compressive behavior of hard ceramics.

To distinguish the indentation behavior of the fine-grained spinel, coarse-grained spinel, AlON, and AlN, the indentation strain was plotted as a function of maximum indentation load (Fig. 5.13) by compiling all of the indentation data for each of the 4 materials. While it is clear from this plot that the load required to produce an equivalent strain in AlN was significantly lower than that required for the other materials, this method of comparison, however, offered no additional insight into the penetration resistance of the 4 materials that was not also apparent in the indentation stress-strain curves. It was postulated that energetic approach of comparing the penetration resistance of these materials, such as work of indentation, could give more insight.

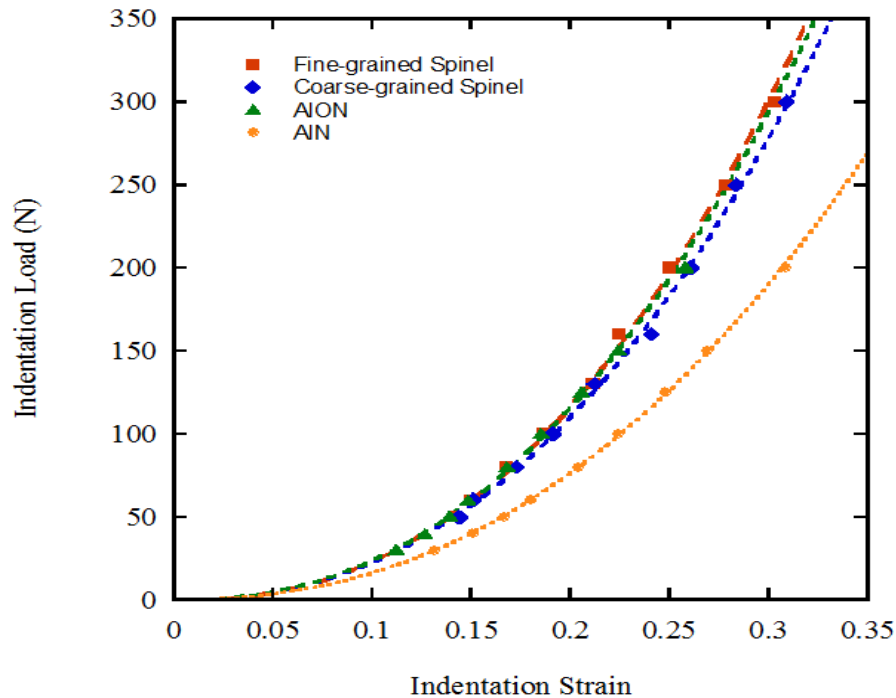


Fig. 5.13 Comparison of indentation load and the indentation strain for the fine-grained spinel, coarse-grained spinel, AlON, and AlN using a 261- μm -radius diamond indenter. Trend lines show the power law fits to the data.

5.6.4 Work of Indentation

It is believed that the work of the indentation approach could potentially provide some practical insight into both the plastically dominated responses of armor materials and the fractured dominated responses. Recent investigations have shown promising results in predicting both the hardness and erosion behaviors of various

materials from work of indentation.³⁻⁷ Instrumented indentation affords the unique opportunity to calculate the energetic characteristics of the indentation process because it continually monitors the indenter depth of penetration into the specimen as well as the applied load, allowing a work of indentation to be calculated from force-displacement curves like those shown in Fig. 5.11. The area under the loading curve gives the total work of indentation, W_T , done by the instrumented indenter during indentation, while the reversible or elastic contribution to the total work, W_E , can be deduced from the area under the unloading curve. The area enclosed between the loading and unloading curves represents the energy absorbed by the irreversible or plastic work of indentation. Thus the total work of indentation is the summation of both the reversible and irreversible work of indentation components and is given by the following equation:

$$W_{total} = W_{elastic} + W_{plastic}. \quad (1)$$

These individual components, represented by the bounded regions shown in Fig. 5.14 are found by numerically integrating the load with respect to the penetration depth. To determine the total work of indentation, the loading curve is integrated from a displacement of zero until the maximum displacement.

$$W_T = \int_0^{h_{max}} Pdh. \quad (2)$$

Elastic work of indentation is found by integrating the unloading curve from the residual displacement, indicated by the intersection of unloading curve with the x-axis, to the maximum displacement.

$$W_E = \int_{h_r}^{h_{max}} Pdh. \quad (3)$$

The region enclosed by the loading and unloading curve, plastic work of indentation, is found simply subtracting the integral parts W_E from W_T .

$$W_P = \int_0^{h_{max}} Pdh - \int_{h_r}^{h_{max}} Pdh. \quad (4)$$

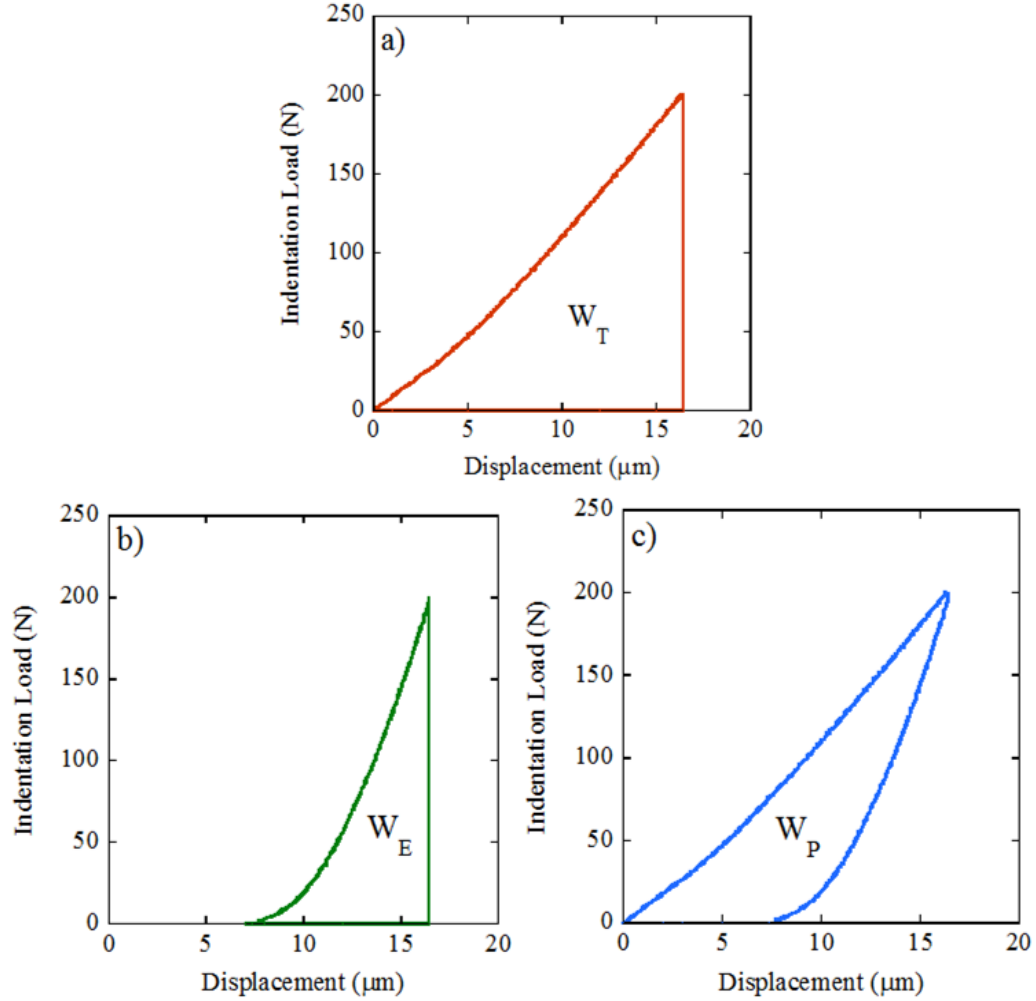


Fig. 5.14 Schematic showing a) total work of indentation, W_T , b) the elastic work of indentation, W_E , and c) the plastic work of indentation, W_P , components extracted from a typical load-displacement curve

The approach taken here to compare the behavior of the fine-grained spinel, coarse-grained spinel, AlON, and AlN is based on analyzing the complete set of experimental load-displacement data. Figure 5.15 shows the total work of indentation as a function of indentation strain, and Fig. 5.16 shows the plastic work of indentation as a function indentation strain. The trends observed in Fig. 5.15, which are well described by power law fits, are identical to those observed in Figs. 5.12 and 5.13 for all 4 materials. While little distinction can be made between the fine-grained spinel, coarse-grained spinel, and AlON, AlN registers significantly lower W_T values for equivalent strains. W_P is, however, similar for most strains, suggesting there is a smaller contribution of W_E in AlN than the other materials. A comparison of the ratio of plastic to total work of indentation for a given set of indentation stains (Fig. 5.17) confirms that W_E has the least contribution in AlN, then AlON, coarse-grained spinel, and lastly fine-grained

spinel. The percent contribution of the W_E ranges 20%–55% in AlN and only 10%–40% in the fine-grained spinel, depending on the strain. Overall, it is suggested that the total work is the key parameter in describing penetration resistance, as both elastic and plastic work is being expended.

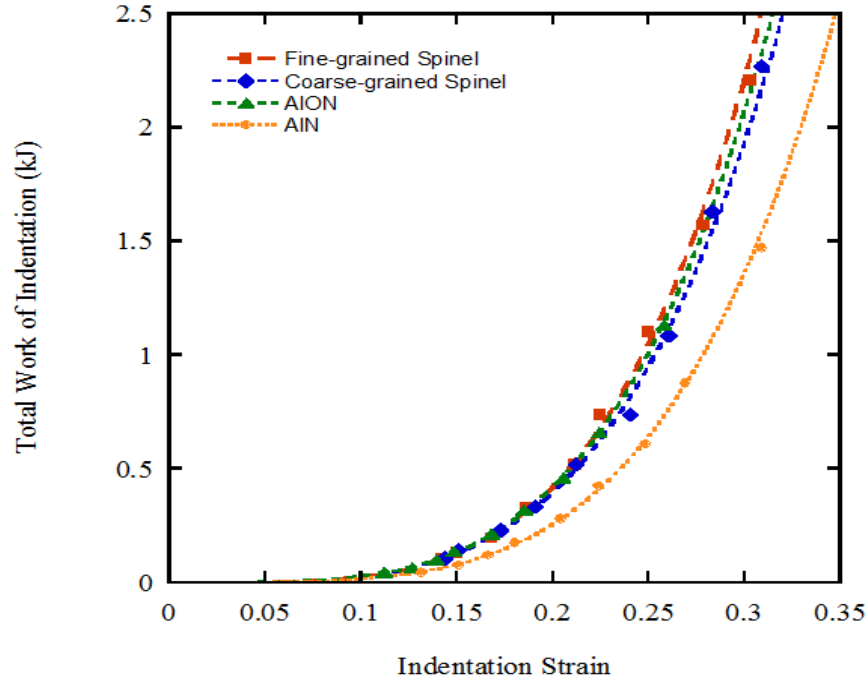


Fig. 5.15 Comparison of the total work of indentation, W_T , as a function of the indentation strain for the fine-grained spinel, coarse-grained spinel, AlON, and AlN using a 261- μm -radius diamond indenter. Trend lines show the power law fits to the data.

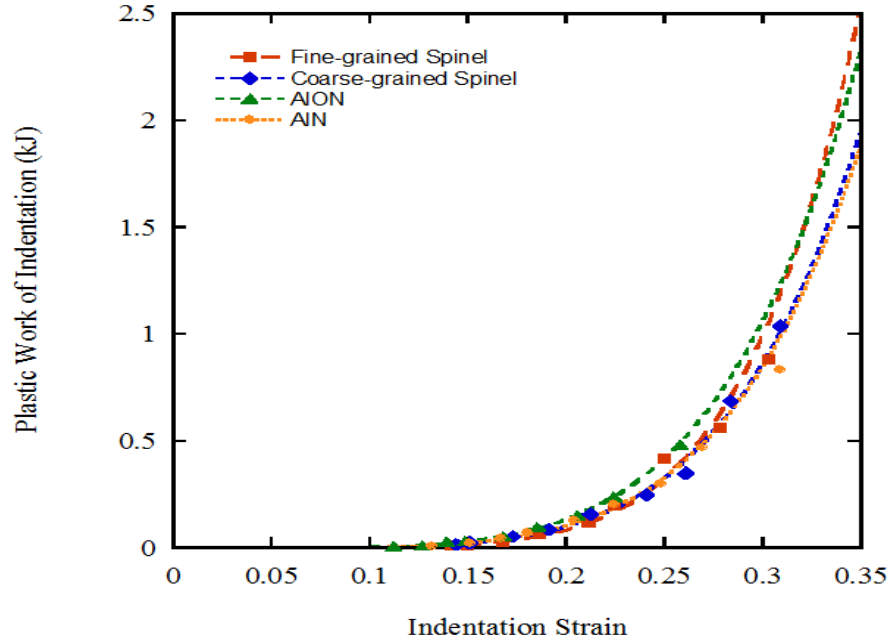


Fig. 5.16 Comparison of the plastic work of indentation, W_P , as a function of the indentation strain for the fine-grained spinel, coarse-grained spinel, AlON, and AlN using a 261- μm -radius diamond indenter. Trend lines show the power law fits to the data.

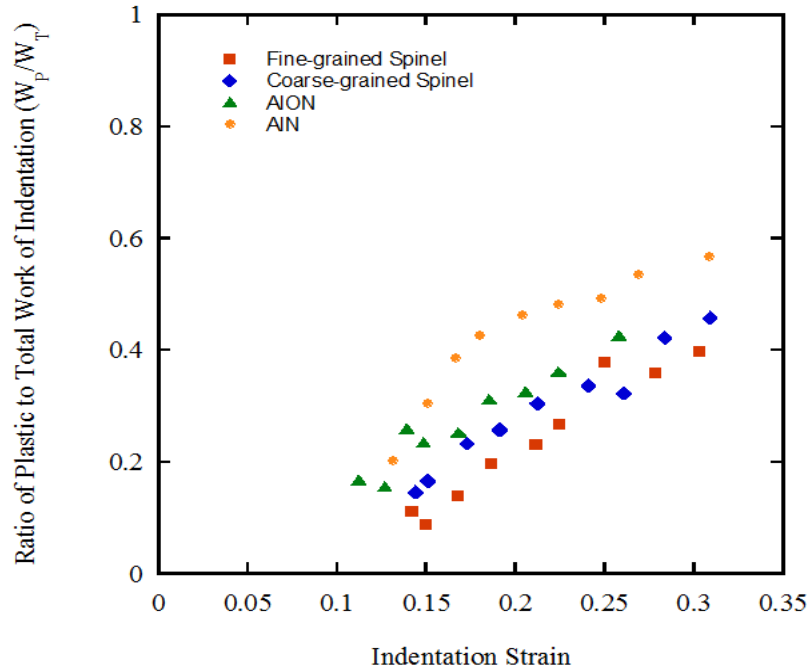


Fig. 5.17 Comparison of the ratio of plastic to total work of indentation, W_P/W_T , and the indentation strain for the fine-grained spinel, coarse-grained spinel, AlON, and AlN using a 261- μm -radius diamond indenter. Trend lines show the power law fits to the data.

To delineate the penetration resistance of the 4 materials a figure of merit based on a parameter termed indentation strain energy density, U_E , is proposed. In uniaxial loading, the area under the stress-strain curve equals the strain energy density. By analogy, we define the indentation strain energy density as the area under the indentation stress-strain curve (Fig. 5.12). If the indentation stress is integrated with respect to the indentation strain, one finds the following:

$$\begin{aligned}
 U_E &= \int_0^{\varepsilon_y} \frac{4E^* \varepsilon}{3\pi} d\varepsilon + \int_{\varepsilon_y}^{\varepsilon_{\max}} K \varepsilon^n d\varepsilon \\
 &= \frac{2E^* \varepsilon_y^2}{3\pi} + \frac{K \varepsilon_{\max}^{n+1}}{n+1} - \frac{K \varepsilon_y^{n+1}}{n+1}, \\
 &= \frac{2E^* \varepsilon_y^2(n+1) + 3\pi K(\varepsilon_{\max}^{n+1} - \varepsilon_y^{n+1})}{3\pi(n+1)}
 \end{aligned} \tag{5}$$

so that the strain energy density to a maximum strain, ε_{\max} , can be calculated. This integral is broken into both the elastic and elastic-plastic contributions to the strain energy density shown schematically in Fig. 5.18. To determine elastic contribution the equation representing the linear elastic behavior of the material²⁸ is integrated from zero until the yield strain, ε_y . The elastic-plastic contribution is found by integrating the indentation stress-strain behavior occurring after yielding, typically described using an empirical equation,²⁸ from ε_y until the selected ε_{\max} . For the sake of comparison, a maximum indentation strain of 0.25 was selected to compare the 4 materials studied here because it was within the tested maximum strains for all materials. The total work of indentation occurring at this selected strain was found by interpolating the data in Fig. 5.15.

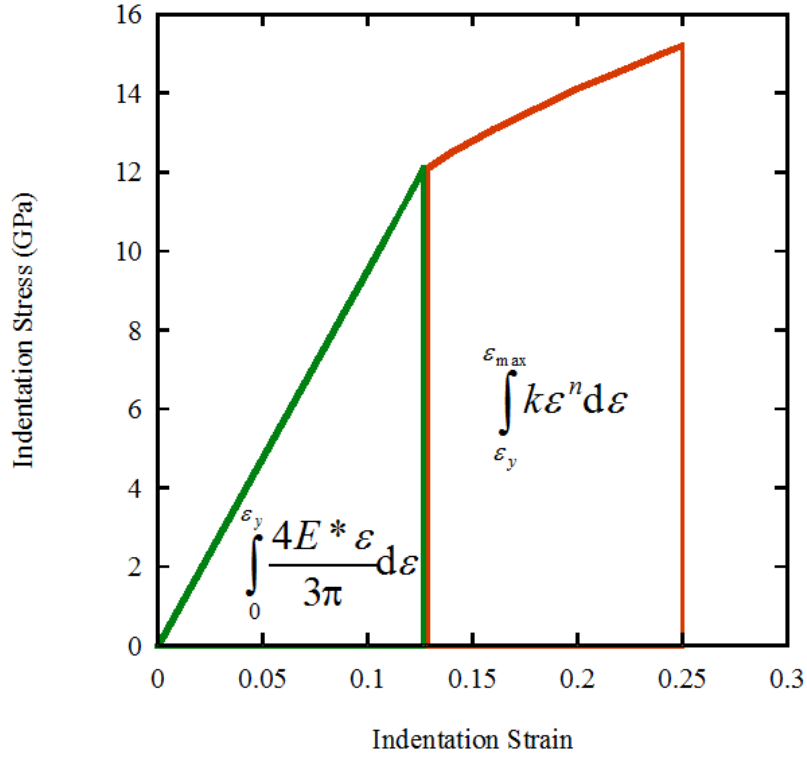


Fig. 5.18 Elastic (green) and elastic-plastic (red) contributions to the indentation strain energy density

A linear correlation is observed in the resulting plot of the total work of indentation and indentation strain energy density (Fig. 5.19). It can be seen that this approach of comparing the total work of indentation and the indentation strain energy density can clearly distinguish the penetration behavior of the 4 materials. According to this plot, the fine-grained spinel shows the greatest resistance to penetration followed closely by the AlON, coarse-grained spinel, and finally the AlN. Because this approach contains inputs from both the elastic and plastic components, it is suggested that this approach could potentially be a useful way to compare the actual penetration behavior of a variety of materials at given maximum strains.

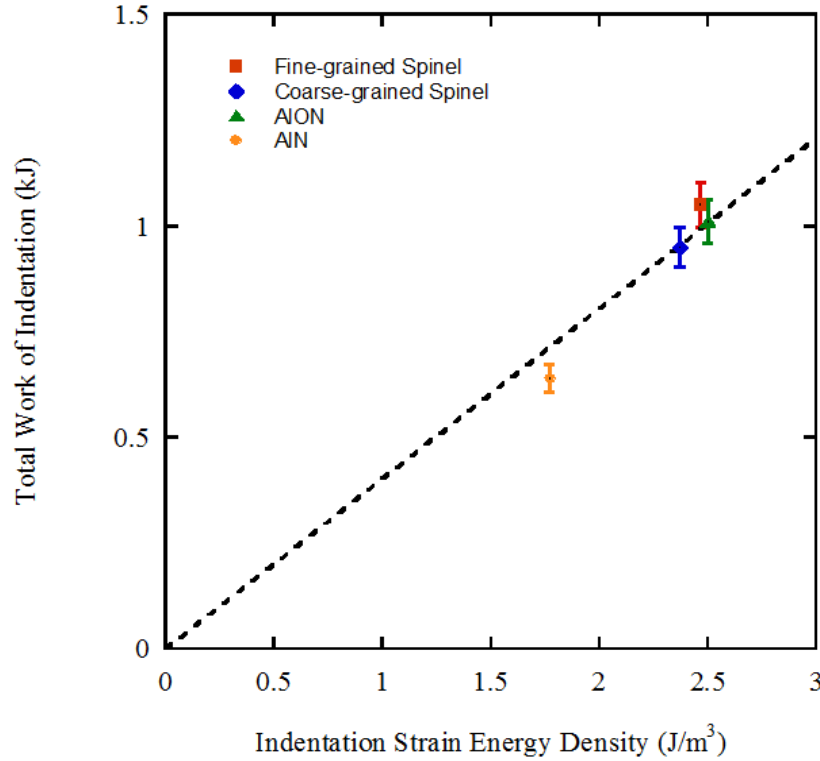


Fig. 5.19 Linear correlation between the total work of indentation, W_T , and the indentation strain energy density

5.7 Conclusions

The indentation stress-strain and work of indentation behavior of a fine-grained spinel, coarse-grained spinel, AlON, and AlN were evaluated. Postindentation observations of the surface damages revealed the presence of surface ring and radial cracks in all 4 materials. Examination of the subsurface indentation damage found evidence of grain boundary microcracking in the inelastic zone directly below the contact site in the fine- and coarse-grained spinel and cleavage microcracking in AlON. Cleavage cracks were visible within the inelastic zone directly below the contact area in AlON, and these cleavage planes were revealed on fracture surfaces. Inspection of the fractured surfaces of indented bend bars revealed transitions from intergranular to transgranular fracture in the fine- and coarse-grained spinel, AlON showed a transition from multiple cleavage microcracks to transgranular fracture. AlN, however, showed only intergranular fracture. Indentation stress-strain data showed little difference in the yielding behaviors of fine- and coarse-grained spinel and AlON. In contrast, AlN showed a much lower yield value. Given the grain size difference between the fine- and coarse-grained spinel and AlON, it is found that the onset of yield does not depend strongly on grain size, yet there is a slight difference in the post-yielding behavior of these materials. Comparisons of both the

indentation stress-strain and work of indentation behavior of the 4 materials revealed that these methods of comparison may be useful in describing a materials penetration resistance. An assessment of the work of indentation and the strain energy density revealed promising results, illustrating the subtle difference of the materials tested. In conclusion, this work suggests that a comparison of the work of indentation and indentation strain energy density approaches, which are correlated, appears to be a good basis for evaluating the penetration resistance of various materials.

5.8 References

1. Muller AM, Green DJ. Elastic indentation response of float glass surfaces. *J Am Ceram Soc.* 2009;93(1):209–216.
2. Muller A, Green DJ. Comparison of the elastic-plastic indentation response of MgAl_2O_4 , AlON, and AlN. *J Am Ceram Soc.* 2013;96(4):1263–1270.
3. Stillwell NA, Tabor D. Elastic recovery of conical indentation. *Proc Phys Soc London.* 1961;78:169-179.
4. Tuck JR, Korsunsky AM, Bull SJ, Davidson RI. On the application of the work-of-indentation approach to depth-sensing indentation experiments in coated systems. *Surf Coat Technol.* 2001;137:217–24.
5. Cheng Y, Cheng C. Relationship between hardness, elastic modulus, and the work of indentation. *Appl Phys Lett.* 1998;75(5):614–16.
6. Sakai M. Energy principle of the indentation-induced inelastic surface deformation and hardness of brittle materials. *Acta Metall Mater.* 1993;41(6):1751–59.
7. Bull SI. Using work of indentation to predict erosion behavior in bulk materials and coatings. *J Phys D Appl Phys.* 2006;39:1626–34.
8. Krell A, Hutzler T, Klimke J, Potthoff A. Fine-grained transparent spinel windows by the processing of different nanopowders. *J Am Ceram Soc.* 2010;93(9):2656–2666.
9. Krell A, Klimke J, Hutzler T. Advanced spinel and sub- μm Al_2O_3 for transparent armour applications. *J Eur Ceram Soc.* 2009;29(2):275–81.
10. Tajika M, Matsubara H, Rafaniello W. Effect of grain contiguity on the thermal diffusivity of aluminum nitride. *J Am Ceram Soc.* 1999;82(6):1573–1575.
11. Tajika M, Rafaniello W, Niihara K. Sintering behavior of direct nitrided AlN powder. *Materials Letters.* 2000;46(2/3):98–104.
12. Hu G, Ramesh KT, Cao B, McCauley JW. *J Mech Phys Sol.* 2011;59(5): 1076–93.
13. Rafaniello W. Development of aluminum nitride: a new low-cost armor: final report. US Army Research Office internal report; 1992 Dec.

14. Harris DC. Optical properties of window materials. In: O'Shea DC, editor. Infrared window and dome materials. Bellingham (WA): SPIE; 1992. p 40.
15. Holmquist TJ, Rajendran AM, Templeton DW, Bishnoi KD. A ceramic armor materials database. Warren MI: US Army Tank Automotive Research, Development and Engineering Center; 1999. Technical Report No.: 13754.
16. ASTM E494-05. Standard practice for measuring ultrasonic velocity in material. West Conshohocken (PA): ASTM International; 2005.
17. ASTM E112-96. Standard test methods for determining average grain size. West Conshohocken (PA): ASTM International; 1996.
18. ASTM C1161-02c. Flexural strength of advanced ceramics at ambient temperature. West Conshohocken (PA): ASTM International; 2008.
19. Evans AG, Wilshaw TR. Quasi-static solid particle damage in brittle solids I. observations analysis and implications. *Acta Met.* 1976;24(10):939–56.
20. Swain MV, Hagan JT. Indentation plasticity and the ensuing fracture of glass. *Journal of Physics D: Applied Physics.* 1976;9(15):2201.
21. Cook RF, Pharr GM. Direct observation and analysis of indentation cracking in glasses and ceramics. *J Am Ceram Soc.* 1990;73(4):787–817.
22. Guo JJ, Wang K, Fujita T, McCauley JW, Singh JP, Chen WW. Nanoindentation characterization of deformation and failure of aluminum oxynitride. *Acta Met.* 2011;59:1671–79.
23. Kimberly J, Ramesh KT. Dynamic response of transparent ceramic MgAl_2O_4 spinel. *Scripta Materialia* 2011. Doi: 10.1016/j.scriptamat.2011.07.044.
24. Lawn BR, Wilshaw TR. Indentation of ceramics with spheres: a century after hertz. *J Am Ceram Soc.* 1998;81(8):1977–94.
25. Bushby A. Nano-indentation using spherical indenters. *Non-Destructive Testing Evaluation.* 2001;17(4/5):213–34.
26. Swain MV, Lawn BR. A study of dislocation arrays at spherical indentations in LiF as a function of indentation stress and strain. *Phys Stat Solidi.* 1969;35(2):909–23.
27. Mesarovic SD, Fleck NA. Spherical indentation of elastic-plastic solids. *Proc Roy Soc: Mathematical, Physical and Engineering Sciences.* 1999;455 (1987):2707–2728.
28. Tabor D. The hardness of metals. Oxford (UK): Clarendon Press; 1951.

29. Deshpande VS, Evans AG. Inelastic deformation and energy dissipation in ceramics: a mechanism-based constitutive model. *J Mech Phys Solids*. 2008;6(10):3077–3100.
30. Paliwal B, Ramesh KT. An interacting micro-crack damage model for failure of brittle materials under compression. *J Mech Phys Solids*. 2008;56(3):896–923.
31. Deshpande VS, Gamble EA, Compton BG, McMeeking TM, Zok FW. A constitutive description of the inelastic response of ceramics. *J Am Ceram Soc*. 2011;94(1):s204–s214.

6. Task 5: Education and Outreach Activities, Core Program

Core Faculty: R Haber and D Niesz

US Army Research Laboratory (ARL) Leaders: J McCauley, J LaSalvia

6.1 Long-Range Objectives

- Educational components, as determined
- Outreach component, national and international activities

6.2 Objectives for the Period

- Hold one-day topical workshop of the Ceramic Armor Industrial Subgroup of the Ceramic, Composite and Optical Materials Center (CCOMC) at the Cocoa Beach/Daytona Meeting of the American Ceramic Society.
- Hold one-day topical workshops of the Ceramic Armor Industrial Subgroup of the Ceramic and Composite Materials Center at Rutgers University.
- Hold one-day topical workshop at ARL.

6.3 Progress on Objectives

6.3.1 Ceramic Armor Industrial Group Workshops

This group has been formed as a subgroup within the CCOMC and is serving as a focal point for outreach to the industrial armor producers. It is also being used to identify and focus on key scientific and technical issues for ceramic armor manufacture and to provide real-time feedback to the armor producers for the results of this program. The current members of the group are BAE Systems, Ceradyne/ESK Ceramics, CoorsTek, Corning, M Cubed, Morgan Advanced Materials, Schott North America, Saint Gobain, Kennametal, PPG, Industrie Bitossi, Superior Graphite, Northwest Mettech, UK Abrasives, Greenleaf, Washington Mills, and the US Army (ARL, Tank Automotive Research, Development and Engineering Center [TARDEC], and the Natick Soldier Center). Several other companies are considering membership. A one-day Multiscale Modeling Linked to Processing Workshop for the group was held in conjunction with a meeting of the Engineering Ceramics Division of the American Ceramic Society in January 2011. This meeting had an excellent symposium on ceramic armor with 112 attendees. A second workshop was held on 20 April 2011 at Rutgers University in conjunction with the semiannual review meeting of the Ceramic and

Composite Materials Center. A third workshop was held at Clemson University in conjunction with the semiannual review meeting of the Ceramic and Composite Materials Center on 19 October 2010.

6.3.2 Review/Planning Meetings

A review meeting/workshop was held at The Johns Hopkins University on 3 February 2011. A second workshop was held at ARL on 24 June 2011.

7. Task 6: Boron Carbide (B₄C) Powder Synthesis, Supplemental Program Attached to Task 1

Core Faculty: R Haber, D Niesz

ARL Leader: J McCauley, J LaSalvia, T Jessen, R Dowding

Research Faculty: W Rafaniello

Research Associate: S Miller

7.1 Long-Range Objectives

- Examine the nanostructured silicon carbide (SiC)–B₄C binary.
- Approach: Replicate Dow Spray Pyrolysis methodology for producing B₄C and provide real comparison with conventional B₄C and anecdotally superior B₄C.
- Determine residual graphite effect on amorphization.
- Provide a means of doping B₄C C-C-C chain with Si, titanium (Ti), or aluminum (Al) to alter amorphization.
- SiC-B₄C binary would provide a density benefit to SiC.
- SiC-B₄C has the potential for producing an Acheson-type carbide alloy that would be scalable.
- Directly links with Modeling Project.

8. Task 7: Multiscale Computational Investigations of Interfaces Relevant to Structural Ceramics

Core Faculty: RA Haber, DA Niesz

US Army Research Laboratory (ARL) Collaborators: J McCauley, T Jessen, J LaSalvia, J Synowczynski

Postdoctoral Associate: CP Morrow

Acknowledgments: Dr Christin Morrow gratefully acknowledges support from the National Science Foundation's Industry & University cooperative Research Program Ceramic, Composite, and Optical Materials Center and the ARL Materials Center of Excellence via grant DOD-W911NF-06-2-0007 as well as computational resources provided by the National Center for Supercomputing Applications and the TeraGrid clusters via Startup Allocation DMR100115. In addition, Dr Vlad Domnich, Dr Steven Miller, Dr Steven Mercurio, Dr Sara Reynaud, and Mr Daniel Maiorano of the Department of Materials Science and Engineering at Rutgers University are gratefully acknowledged for stimulating discussions, and Dr Karsten Krogh-Jespersen of Rutgers' Department of Chemistry is gratefully acknowledged for assistance with computational strategies. Dr Alexander Goldberg and Dr Jianjie Liang of Accelrys, Inc., are gratefully acknowledged for assistance with the preparation of the silicon carbide (SiC) and boron carbide (B₄C) supercells, respectively, in Materials Studio.

8.1 Long-Range Goals

- To develop molecular scale understanding of B₄C synthesis.
- To characterize B₄C surface structure at interface with intergranular films (IGFs).
- To provide insight into structures of composite SiC/B₄C materials.
- To employ computational tools that cross spatial and temporal scales.

8.2 Background: Armor Ceramic Materials

Improvement of material properties and ballistic performance of armor materials is an active area of research. Efficient synthesis methods to maximize performance of these materials are paramount to this improvement. During synthesis, adding sintering aids to armor material precursors controls the prevalence of various polytypes and the ensuing structural artifacts. Each of these is intricately related to

the ballistic performance of a material. Despite the existence of several experimental methods for studying armor ceramics, developing an accurate molecular-scale picture of processes occurring in the material is still an elusive challenge. To understand the synthesis of armor materials from a molecular perspective, computational methods must become another tool used to probe the behavior of these systems.

Synthesis of armor materials is a multistep process characterized in part by adding sintering aids, forming polytypes, and the presence of microstructural defects within samples made. Sintering aids added during synthesis to SiC, for example, include B,¹⁻⁴ C,¹⁻⁴ B₄C and C,^{5,6} Al,³⁻⁶ and aluminum nitride (AlN).^{5,6} However, the effect of these phases on ballistic performance is also not currently understood.^{4,5} In addition, the mechanism through which these aids act is not known,^{1,2} but several possibilities exist in this regard. Sintering aids may lower the activation energy required to make these materials⁶ and thus act as a catalyst, stabilize higher energy polytypes and allow them to be more prevalent in a sample,^{3,4} or form intermediates that affect the pathway and therefore polytypes formed. Several polytypes are present within a given sample, and their varying stabilities affect the concentration of each. Each sample has an inherent microstructure, characterized by grain size, grain shape, grain boundaries,¹⁻³ stacking faults, and microcracks. The ballistic performance of a material is heavily dependent upon the synthesis pathway, and therefore understanding each step in the processing is imperative for improving these materials.

8.3 Multiscale Computational Approach

Within the field of armor ceramic materials, many questions remain that concern the mechanisms through which sintering aids act as well as the effects of phases at the grain boundaries, and atomistic computational tools permit investigations into these phenomena and provide molecular scale insight. The strength of atomistic computational methods is the ability to describe a molecular scale picture of an individual phenomenon within a greater physicochemical scheme. Several temporal and spatial scales are possible using computational tools, and these regimes range from tens of atoms on the femtosecond scale to millions of atoms without a timescale.⁷ The challenge, however, is to include enough chemical information so the calculations provide molecular information while simultaneously representing a system size or timescale that provides meaningful insight. Further, this challenge is compounded by the size of the system that can be studied. Smaller systems are required to include chemical information such as electronic structure,⁷ and these calculations are tractable up to about 50 atoms.

Larger systems of 10^2 – 10^6 atoms can also be modeled, but the tradeoff is that the electronic structure is not included,⁷ which permits these calculations to remain feasible.

A number of methods are available that vary in size of system (both length and number of atoms) and timescale that can be simulated. Figure 8.1 shows the size and time regimes for a number of computational methods currently employed.^{8–13} Starting from the smallest to the largest regime, there are density functional theory (DFT), DFT–molecular dynamics (DFT-MD), classical molecular dynamics (MD), mesoscale, and continuum theory approaches. DFT models the electronic structure of each atom in a system, while DFT-MD allows for the inclusion of electronic structure as well as the motion of atoms over time. Classical MD also allows for the movement of atoms via Newtonian physics, but electrostatic interactions are modeled with fitted potentials, enabling larger system sizes than DFT-MD.⁷ In the mesoscale approach, collections of phenomena and molecular regimes are modeled, and continuum models are used to simulate properties of bulk materials.¹⁴

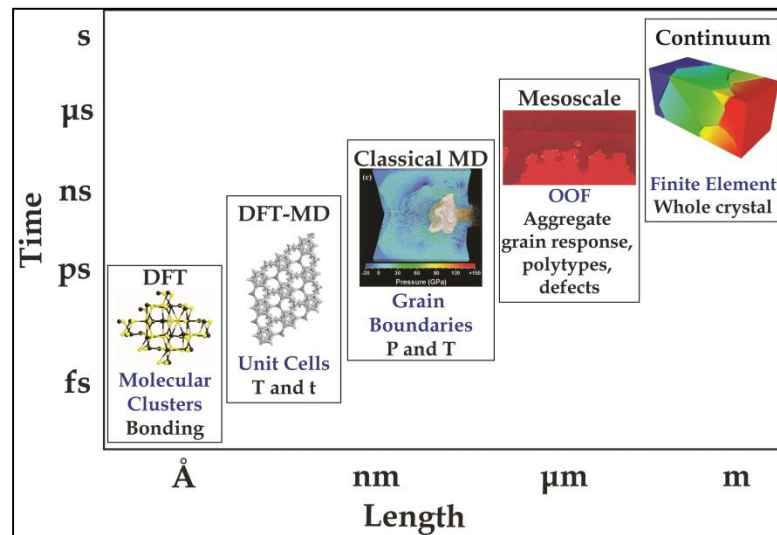


Fig. 8.1 Computational materials science provides tools that cross scales over both length and time.^{8–13}

Computational investigations across both time and length scales are required for in-depth understanding of armor ceramic materials. As an example, one may consider the impact of a projectile on a target and the ensuing degradation of the material. Simulating such an event would require the use of each method in Fig. 1, and important information regarding the ballistic event would be given by each. If one traces aspects of a ballistic event from the largest to the smallest regime, the analysis would be as follows. A continuum theory approach would include the simulation of a target with a series of shockwaves moving through it. Moving to

the next-smallest regime, a mesoscale approach would also model a shockwave in the target, but now the shockwave is made of individual particles as opposed to a bulk continuum. In the classical MD approach, the target is made of particles that have a specific identity (SiC). A DFT-MD approach allows for a description of the electronic structure of each Si and C atom while at the same time permitting movement of the Si and C atoms. Lastly, DFT calculations include a quantum mechanical description of the electronic structure of Si and C atoms, thus one would have the most accurate structure of polytypes. Throughout the series of methods included in Fig. 8.1, one sacrifices system size for chemical information, but each regime enables prediction of aspects of a ballistic event.

8.4 Project Overview

This project is comprised of 2 main goals. The first is to design a multiscale computational investigation of armor ceramic materials, which is accomplished by employing DFT calculations and DFT-MD simulations. The second is to investigate interfaces relevant to these materials, which are accomplished by examining SiC/B₄C and B₄C/IGF interfaces. The former are investigated both by DFT calculations and DFT-MD simulations while the latter are simulated with only the DFT-MD approach.

The DFT calculations optimize molecular clusters representing single surface sites along SiC/B₄C interfaces. These clusters allow for the identification of the bond lengths within each structure and the relative stabilities of the structures chosen. At the same time, DFT-MD simulations of SiC/B₄C interfaces and IGFs along B₄C grains are performed on the picosecond (ps) timescale, and relative stabilities of interfaces resulting from different B₄C structures are identified. Further, these simulations will be performed at 2 different temperatures to identify any temperature effects. Employment of this multiscale computational approach provides insight into synthesis methods and composite materials by enabling a molecular-scale description that incorporates quantities and phenomena observed experimentally. These 2 computational methods will be combined for a multiscale investigation that crosses both spatial and temporal scales and enables the successful attainment of the long-range goals listed at the beginning of this report.

8.5 SiC/B₄C Interfaces: Introduction

For a systematic molecular-scale picture of armor ceramic materials to be developed, one must first describe the structure of each material under investigation. The SiC structure is composed of tetra-coordinated Si atoms bonded to tetra-coordinated C atoms, and a number of polytypes are possible that differ in

packing of the crystal as well as the number of repeating units along the c-axis.¹⁵ Depictions of the 4H and 6H polytypes via GaussView¹⁶ appear in Fig. 8.2, where the 4H polytype has 8 atoms and the 6H polytype 12 atoms.¹⁷ The B₄C structure, on the other hand, is currently under debate, but common agreement lies with the presence of a 12-atom icosahedron bonded to a sidechain composed of 3 atoms.^{18–22} A representation of the B₄C structure appears in Fig. 8.3.¹⁹ Recently, Fanchini et al.²⁰ used DFT calculations to determine the relative stabilities of 20 different B₄C isomers, and the comparison of structures appears in Fig. 8.4.

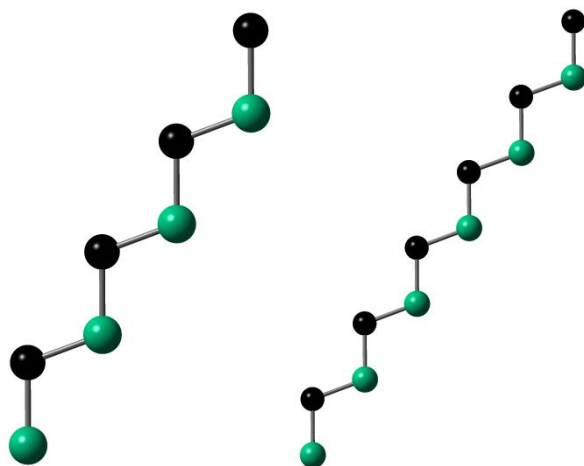


Fig. 8.2 The 4H polytype (left) and 6H polytype (right) of SiC.^{16,17} The Si atoms are turquoise and the C atoms are black.

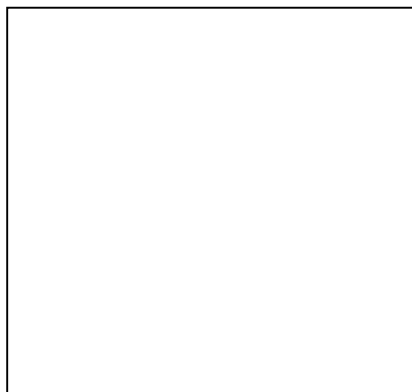


Fig. 8.3 B₄C structure: polar atoms within the icosahedron are black, the equatorial are light gray, and those in the sidechain are dark gray¹⁹

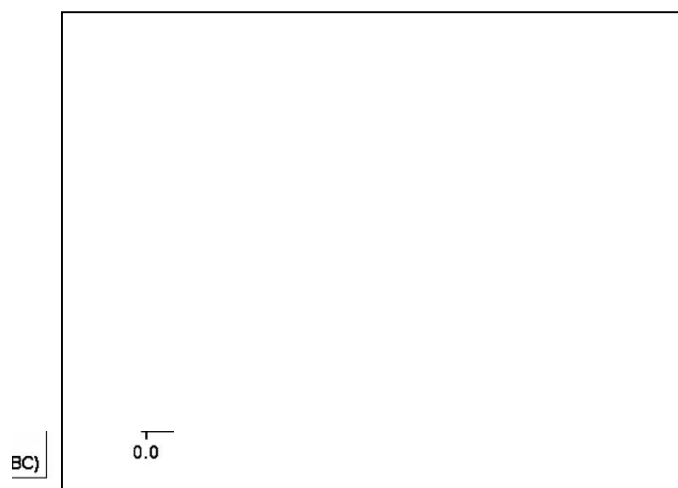


Fig. 8.4 Relative stabilities of several proposed B₄C structures²⁰

Both SiC and B₄C are used as armor ceramics because of their material properties^{4,5,23–25} and performance under high temperature and pressure conditions.^{3–5,23–25} Currently these materials are evaluated separately despite the use of B₄C sintering aids during synthesis of SiC^{1–6} and development of SiC/B₄C composite materials.^{26–32} Therefore, investigating SiC/B₄C interfaces is necessary to improve the synthesis of SiC and understand the nature of SiC/B₄C composites. However, no investigation of the SiC/B₄C interface has been performed to date. Further, a molecular scale study is warranted to probe the atomic interactions at the interface. Employment of a computational approach allows one to focus on a single phenomenon within the overall physicochemical process and to calculate experimentally measured quantities. In particular, the advantage is that a computational approach enables insight into experimental observations.

8.6 Computational Methods

8.6.1 DFT Calculations

8.6.1.1 Functionals

The main thrusts of the DFT calculations are to optimize SiC unit cells and B₄C isomers as well as to determine how stabilities of interface structures are affected by bonding to various Si atoms within the unit cell and by presence of different B₄C isomers. For this reason, 2 functionals are chosen, B3LYP and M06-L, both of which are included in the Gaussian09 software package.³³ The B3LYP functional is the most commonly used DFT functional,³⁴ and along with other functionals in its class, B3LYP includes both exchange and correlation, deconstructs electronic energy into manageable components, and enables feasible computation times.³⁵

Specifically, the B3LYP hybrid density functional is comprised of an exchange-correlation functional,^{36–39} a generalized gradient approximation (GGA) component,^{38,39} and a contribution of Hartree-Fock exchange.³⁴ Recent investigations employ this functional to investigate the structures of several SiC isomers,⁴⁰ SiC nanotubes (NTs),⁴¹ and the decomposition pathway of a new explosive containing Si-C bonds.⁴²

Despite its prevalence in the literature, B3LYP is suited neither for all applications nor all systems.³⁴ For this reason, a more recently developed and more strenuously examined functional is also employed. The M06-L functional is a local functional that performs well for both main group and transition metal chemistry⁴³ and for a number of thermochemical, structural, and electrostatic applications.^{43,44} This local meta-GGA exchange correlation functional⁴³ blends the broad applicability of the M05 functional⁴⁵ with the flexibility of the VSXC (Van Voorhis Scuseria eXchange-Correlation) local functional.⁴⁶ The M06-L functional captures elements of local spin density, spin density gradient, and spin kinetic-energy density within the exchange-correlation energy, and the uniform electron gas limit is also satisfied by this functional.⁴³ Unlike B3LYP, M06-L does not contain Hartree-Fock exchange, which renders the latter functional advantageous in its performance for transition metals and in its added computational efficiency.⁴³ The training set of the M06-L functional includes both B- and Si-containing compounds, bond length and frequency tests, and barrier height calculations.⁴³ Recent investigations employ the M06-L functional to calculate the band gap of SiC⁴⁷ as well as the bond dissociation energy of Si-C bonds in a new explosive.⁴²

8.6.1.2 Basis Set

Although there are not any transition metals in these calculations, there are atoms with expanded octets, namely Si, C, and B. Therefore, the 6-31G(d) and 6-311+G(d,p) basis sets^{48,49} are used in combination with these 2 functionals. Preliminary data are collected with the 6-31G(d) basis set, and the d orbitals included for nonhydrogen elements enable representation of Si, C, and B effectively. The diffuse functions are included in the 6-311+G(d,p) basis set for their applicability to loosely bound electrons,⁵⁰ such as those in atoms with expanded octets, and the p orbitals for H atoms are present because these atoms maintain tetrahedral structural integrity around Si and C atoms in SiC unit cells. Similar basis sets are employed for calculating band gaps in SiC,⁴⁷ the structure of SiC NTs,⁴¹ and the structure of a new explosive that contains Si-C bonds.⁴²

8.6.1.3 Systems Under Study

Molecular clusters are designed to represent the SiC/B₄C interface using single-unit cells of SiC and single icosahedra of B₄C. Initially, the 4 most stable B₄C isomers proposed by previous researchers^{18–22} are energy-minimized to determine the bond lengths within each. Unit cells of the 4H and 6H polytypes of SiC are also energy-minimized because these have been shown to be 2 of the most stable⁵¹ and most commonly observed polytypes.^{4,5} Structures residing at an energy minimum are characterized by the absence of negative frequencies. Once the energy-minimized structures have been isolated, a series of molecular clusters are designed to represent the interfaces that result from the combination of each B₄C isomer and SiC unit cell. These interface clusters are used to determine how the bond lengths within the B₄C and SiC portions of the cluster change as a result of this interface. In addition, the effect of the location of B₄C icosahedra within the SiC unit cell is also investigated. The relative stability of each interface is calculated with respect to the separate constituent B₄C and SiC units.

8.6.2 DFT-MD Simulations

8.6.2.1 Description of Method

The main goal of the DFT-MD simulations is to transition from single unit cells of SiC and icosahedra of B₄C into bigger systems that enable the investigation of several adsorption sites of B₄C simultaneously. Therefore, DFT-MD simulations are employed to model this interface on a nanometer size scale to examine how it changes over time and determine how temperature affects the structure and stability of it. This computational tool allows for both bond-breaking and bulk-scale phenomena to be investigated within one modeling scheme, and such an approach is desirable for the investigation of SiC/B₄C interfaces. DFT-MD simulations present an advantage over classical MD simulations in that potentials or fitting parameters do not lead to nonphysical behaviors in the system studied.⁵²

DFT-MD simulations combine representations of the electronic structure of atoms with time scales over which physicochemical processes occur. Separation of nonreacting core electrons from valence electrons via pseudopotentials enables efficient representation of electronic structure.⁵³ The Vienna Ab-initio Simulation Package (VASP)^{54–57} approximates the band structure via a plane wave representation, which is attained with a projector augmented wave (PAW) approach.⁵⁸ The PAW approach removes iterative calculations of core electrons from the computation scheme and replicates chemical behaviors of all-electron methods.⁵⁹ Kresse and Joubert expand upon Blöchl's original formulation, and

these changes are particularly suited for Si-containing systems because the training set included a siliceous compound.⁵⁴ Several recent analyses of SiC polytypes^{15,17,51,60–62} and B₄C structures^{19,21,63} differ in their representation of the k points in the Brillouin zone; however, recommended values for k are 9 for metals and 4 for semiconductors.⁶⁴ Further, the energy cutoff value for these systems is approximately 500 eV in recent investigations.^{15,21}

VASP is employed here because it was designed for materials science applications, particularly in its inclusion of parameter-free functionals.^{53,59} Evaluation of forces on atoms and stresses on the unit cell are possible in this plane-wave approach.^{53,59} Recent applications of VASP have included modeling the shear strength of polytypes in SiC,¹⁵ relative stabilities of B₄C structures,²¹ and energy minimization of B₄C lattice parameters.¹⁰

8.6.2.2 System Under Study

Four SiC/B₄C interfaces are designed using the 6H polytype of SiC as the substrate, and each interface varies with the B₄C isomer adsorbed to the surface. The 4 B₄C isomers represent the most stable structures^{18–22} from Fig. 8.4.²⁰ The substrate is comprised of 9 unit cells ($3 \times 3 \times 1$), for a total of 108 atoms, and 3 B₄C adsorbates, constituting the rhomahedral unit cell, are bonded to the substrate for a total of 45 atoms. Thus, each interface is comprised of 153 atoms. Simulations are performed over 10 ps, with 5 ps for equilibration and 5 ps for data analysis. Moreover, a recent investigation of crystal and amorphous B₄C structures employs a similar time scale.⁶⁵ These simulations are performed at 300 and 2,400 K to investigate how these systems behave at both ambient and high-temperature experimental conditions.^{1,2,4–6,26,66,67}

8.7 Results and Discussion

The data summarized in this section relate to the determination of how B₄C affects the SiC structure within the unit cell and structural features of B₄C adsorbates bound to SiC substrates. These initial calculations are primarily focused on optimizing the geometries of the constituent structures that will be used for each system. Unit cells of the 6H and 4H polytypes of SiC and 4 B₄C isomers were energy-minimized with DFT calculations, and comparisons to previous data are also given. In addition, preliminary calculations on nanoscale SiC/B₄C interfaces are described, where the goal is to scale up the DFT calculations to model multiple surface sites simultaneously.

8.7.1 Geometry Optimization of B₄C Isomers

DFT calculations were employed to energy-minimize the B₁₂CCC, B₁₂CBC, B₁₁C_eCBC, and B₁₁C_pCBC isomers of B₄C, and these were selected because they have been shown to be the most stable.^{18–22} The optimized isomers appear in Fig. 8.5 and were visualized with GaussView.¹⁶ The B3LYP/6-31G(d) methodology was employed here for its computational feasibility and for ease in comparing with data from previous computational studies. The bond lengths calculated from our calculations are listed in Table 8.1, and previous data from the literature are also included.^{10,63,68,69}

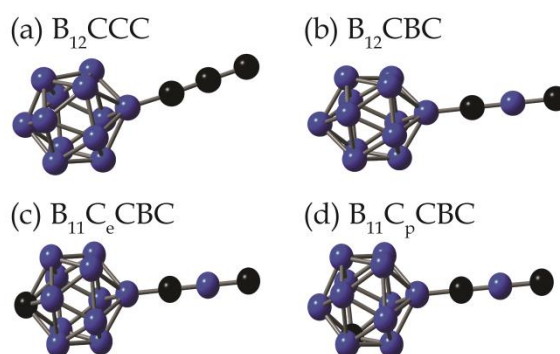


Fig. 8.5 Optimized a) B₁₂CCC, b) B₁₂CBC, c) B₁₁C_eCBC, and d) B₁₁C_pCBC structures. Blue atoms are B and black are C.

Table 8.1 B–B, B–C, and C–C bond lengths (Å) from our B3LYP/6-31G(d) calculations as well as previous works.^{10,63,68,69}

Isomer	Bond Type					Reference
	B*–B*	B–B	B–C _{side}	B–C _{subst}	C–C	
B ₁₂ CCC	1.72 – 1.87	1.62 – 1.86	1.49		1.28 – 1.31	This work
B ₁₂ CBC	1.76–1.79	1.65–1.78	1.35–1.52			This work
B ₁₁ C _e CBC	1.78	1.65 – 1.68	1.35 – 1.52	1.75 – 1.76		This work
B ₁₁ C _p CBC	1.76 – 1.80	1.62 – 1.72	1.35 – 1.52	1.67 – 1.72		This work
			1.30 – 1.81			Lazzari et al. 1999
		1.75 – 1.80				Balakrishnarajan et al. 2007
		1.714 – 1.813				Aydin and Simsek 2009
**		1.836				Konovalikhin and Ponomarev 2010
			1.43, 1.59			Balakrishnarajan et al. 2007
			1.409 – 1.788			Aydin and Simsek 2009
					1.328 – 1.336	Aydin and Simsek 2009

**Bond lengths are from several possible B₄C isomers. See references for details.

The B3LYP/6-31G(d) methodology was employed here because initial calculations with more stringent functional and basis set combinations failed to converge. After consulting with a colleague (K Krogh-Jespersen, unreferenced), the B3LYP/6-31G(d) approach was determined to be an appropriate preliminary method. Regardless of the chosen computational method, however, the icosahedron/sidechain angle continued to minimize to 180° versus the reported value of 99° .¹⁰ The presence of this 180° angle can be seen in Fig. 8.5, and one possibility reason for this discrepancy could be from the use of gas-phase approximations in DFT instead of periodic boundary condition approaches. At the same time, several previous approaches investigated icosahedral boron and B₄C structures with gas-phase approximations without difficulty.^{10,69,70} Perhaps additional investigation is necessary to elucidate the root cause of this issue.

Several challenges have arisen during the energy-minimization of these structures. The B₁₂CBC isomer has a doublet spin state as its ground electronic state, meaning it has one unpaired electron, and such an electronic state is often challenging to optimize from a DFT perspective. Instead, a smaller basis set, 6-31G(d), was employed. However, this structure was determined to be at an energy minimum, characterized by the absence of negative frequencies, and is depicted in Fig. 8.5b.

In addition, effectively modeling the difference between a polar and an equatorial substitution in the absence of additional icosahedra required some chemical intuition. The icosahedron is essentially 2 pentagonal pyramids bonded together,⁷⁰ and each site within it should be chemically equivalent. Defining polar and equatorial sites hinges upon the location of the C substitution with respect to the sidechain. The equatorial substitution was added to the site 180° from the attachment of the sidechain, as shown in Fig. 8.5c, and this site is within the hexagonal chair of the icosahedron.¹⁰ On the other hand, the polar substitution was attained by adding the C atom to the face on the bottom of the icosahedron, as shown in Fig. 8.5d. This approach will be continued for the model interface structures as well.

Lastly, the B₁₁C_pCBC isomer continually rearranged during optimization. The C substitution within the icosahedron prefers an exo-icosahedral site^{10,69} and migrates to a position where it bonds to 4 B atoms within the cage. As such, the B–C bond connecting this C atom in its initial position in the base of a pentagonal pyramid to the B atom at the apex breaks each time this structure is optimized without constraints. Therefore, the B₁₁C_pCBC isomer is optimized with constraints on this particular bond. However, the resulting geometry is characterized as an energy minimum because negative frequencies are absent.

The bond lengths from the B₄C structures optimized in this work fall within the range of those from previous calculations, as listed in Table 8.1. In our calculations, however, we further categorized the B–B bonds as those adjacent to the sidechain (B*–B*) and those remaining throughout the icosahedron (B–B). This is particularly important because those bonds adjacent to the sidechain are more elongated. Shorter B–B bonds are present on those B atoms directly opposite the equatorial B atom to which the sidechain is bonded, likely an effect of excess electron density donated by the sidechain, while those B atoms farther away maintain shorter bond lengths. Moreover, the structure of the icosahedra are distorted such that the positions of the B atom to which the sidechain is attached as well as the atom diametrically opposed from it, either B or C, are not entirely symmetrical.

8.7.2 Geometry Optimization of SiC Unit Cells

As with energy-minimization of B₄C isomers, DFT calculations were employed to energy-minimize unit cells of 4H-SiC and 6H-SiC, and these polytypes were chosen for their prevalence in experimental samples^{4,5} as well as their known stability with respect to other SiC polytypes.⁵¹ The optimized structures appear in Fig. 8.6 and were visualized with GaussView.¹⁶ The B3LYP/6-31G(d) methodology was employed here for its computational feasibility. The bond lengths calculated from our calculations are listed in Table 8.2, and previous data from the literature are included.⁷¹

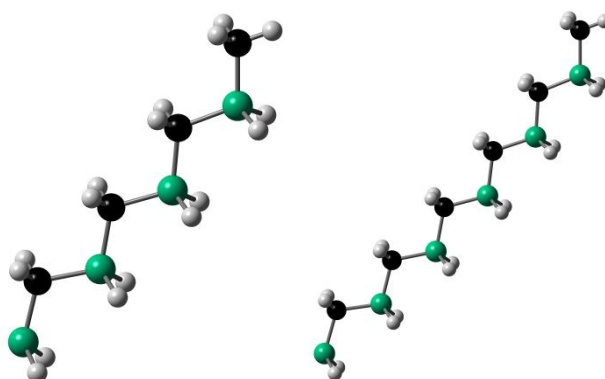


Fig. 8.6 4H polytype (left) and 6H polytype (right) of SiC with hydrogen (H) atoms added for structural integrity.¹⁸ Si atoms are turquoise, C atoms black, and H atoms light gray.

Table 8.2 Si–C, Si–H, and C–H bond lengths (Å) for the 4H and 6H polytypes of SiC from our B3LYP/6-31G(d) calculations as well as those from Ching et al.⁷² have been used to terminate SiC clusters.⁶²

Polytype	Bond Type			Reference
	Si–C	Si–H	C–H	
4H	1.89 – 1.90	1.49	1.09 – 1.10	This work
6H	1.89	1.49	1.10	This work
4H	1.890,1.887	Ching et al. 2006
6H	1.890,1.887	Ching et al. 2006

The initial model clusters representing the 4H and 6H unit cells (Fig. 8.1) were composed solely of the 4 Si and 4 C atoms (4H) or 6 Si and 6 C atoms (6H) that constitute the respective unit cells. However, these clusters minimize to structures devoid of tetrahedral structural integrity. To overcome this issue, H atoms were added to each Si and C to complete the octet (Fig. 8.6). Two H atoms were added to the terminal Si atom in each unit cell to leave a vacant site for bonding to B₄C.

Although the tetrahedral geometry is maintained, one must consider whether H atoms have a chemical effect. This is particularly important because our goal is to understand the relative energetic stability of each interface modeled. The bond lengths listed in Table 8.2 are identical to those from the literature, and thus the presence of these H atoms is not altering the structure. This shows that the H atoms contribute minimally to the energy of each system, which is expected, as H atoms have previously.

Addition of an odd number of H atoms throughout these unit cells changed the electronic state from singlet to doublet. This led to similar challenges to those seen with the B₁₂CBC structure described previously. Each atom has a completed octet within these clusters with the exception of the terminal Si atom, where a bond vacancy was left for the Si-B bond that models the SiC/B₄C interface. This, therefore, creates a doublet state within the SiC unit cells. However, these model clusters of the SiC unit cells with H atoms in them were successfully energy-minimized with the B3LYP/6-31G(d) methodology and subsequently with the B3LYP/6-311+G(d,p) methodology. These SiC unit cells will be bonded to the optimized B₄C isomers to form model clusters of SiC/B₄C interfaces.

8.7.3 Nanoscale SiC/B₄C Interfaces

Our investigation of SiC/B₄C interfaces continues with employment of DFT-MD simulations. DFT calculations are scaled up in size, allowing for identification of long-range effects, and inclusion of time, temperature,^{1,2,4–6,26,66,67} and pressure,

facilitating incorporation of more experimental conditions. Additional experimental parameters such as use of the 6H-SiC polytype^{4,5} and energetically stable B₄C isomers^{18–22} are also included. In addition to experimental parameters such as time, temperature, and pressure, use of several different B₄C isomers to form these interfaces permits a comparison of how they behave with respect to one another, and such a comparison can be quantified via changes to the energy of the system, bond lengths at the interface, and structural orientation of either component at the interface.

In particular, energy-minimization of a $3 \times 3 \times 1$ supercell of the 6H-SiC(ABCACB) substrate is currently underway. Experimental coordinates⁷² were used to create the substrate, which is visualized in Fig. 8.7 via Materials Studio.⁷³ This polytype was chosen because the 6H-SiC polytype is prevalent in experimental samples^{4,5} and it is the most stable 6H polytype.⁵¹ A $3 \times 3 \times 1$ sample constitutes a desirable size because there are multiple sites to which B₄C structures can adsorb and because a substrate of approximately 100 atoms maintains computational feasibility.

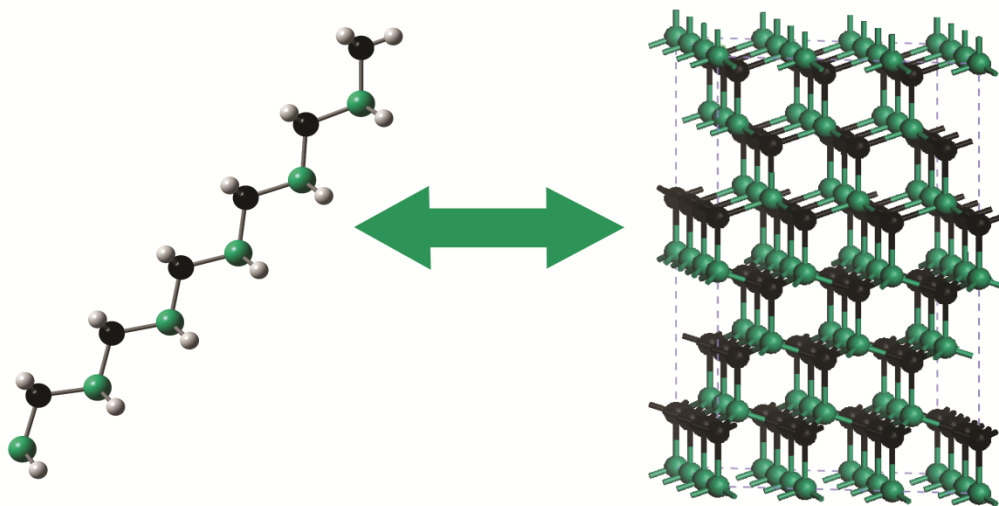


Fig. 8.7 Single unit cell of 6H-SiC (left) is scaled up to a $3 \times 3 \times 1$ supercell of 6H-SiC(ABCACB) (right); color scheme the same as in Fig. 8.6.

Once the 6H-SiC(ABCACB) substrate is energy-minimized, the various B₄C isomers will be optimized using VASP.^{54–57} These isomers in combination with the 6H-SiC(ABCACB) polytype will be used to investigate the bonding and orientation characteristics of B₄C on SiC. Four bonding configurations are possible with Si atoms from the substrate and B atoms within the B₁₂CCC structure: a polar site, an equatorial site, both a polar and an equatorial site (i.e., multisite), and a sidechain

site. Each of these possibilities will be evaluated in turn, and the lowest energy configuration will be employed to model the SiC/B₄C interfaces over 10 ps at both 300 and 2,400 K.

8.7.4 Four B₄C/IGF Interfaces: Introduction

Recent attention to atomistic descriptions of B₄C via computational approaches is extensive, where particular focus resides on the structures, relative stabilities, and characterization of polytypes of this material. While the B₄C structure is currently under debate, common agreement lies with the presence of a 12-atom icosahedron bonded to a sidechain composed of 3 atoms,^{18–22} and a representation of the B₄C structure appears in Fig. 8.3.¹⁹ In addition, the material properties of B₄C are linked to the polytypes within a given sample,^{18,63,65,68,74} and the relative stabilities affect the concentration of each polytype. Structural characterization of B₄C samples facilitates a description of which polytypes are present. Moreover, employment of atomistic computational methods enables molecular-scale insight into each of these aspects of B₄C, and development of a multiscale computational infrastructure allows for the identification of which parameters contribute to overall observations.

The presence of an icosahedron within the B₄C structure stems from the ability of elemental B to form caged structures with a variety of sizes,^{75,76} and the icosahedron is essentially 2 pentagonal pyramids bonded together.⁷⁰ As such, 2 types of chemically distinct sites are possible within the icosahedron, polar sites, and equatorial sites. The polar sites correspond to those atoms that link icosahedra together, and 2 planes opposite one another composed of 3 atoms each constitute the polar atoms within the cage. The equatorial sites, on the other hand, are those to which the sidechains are bonded, and these sites form a hexagonal chair within the icosahedron.¹⁰ Sidechains within this material are thought to be composed of B and/or C atoms, and possible combinations include CCC,^{18–20,22,68,76–78} CBC,^{10,18–22,68,74,76–80} CCB,^{19,20,22} CBB,^{19–22,76,79} BCB,²⁰ and BBB,^{21,63} where the presence of each depends upon the stoichiometry of the sample.^{10,21,63,69,79}

With the identification of many possible polytypes, efforts to investigate their relative stabilities are ongoing.^{18–22,63,68} Fanchini et al.²⁰ determined the free energy per site of more than 20 possible B₄C polytypes; their findings are shown in Fig. 8.4. They and others^{18–20,22,63,68} describe the most stable polytype of B₄C to be the B₁₁C_pCBC structure, where one C atom substitutes into a polar position in the icosahedron and a B atom resides in the central position of the sidechain. However, agreement of previous studies ends there. The next-most-stable polytype is predicted to be B₁₂CCC,²⁰ B₁₁C_eCBC,^{18,19,22,63,68} or B₁₂CBC,²¹ for example.

Reasons for this discrepancy are unclear, but the most likely explanation is the approximation of electronic structure within the computational methodology.^{10,19,21,34,63}

In addition to descriptions of structures and their relative stabilities, characterization of this material has included calculation of band gaps,^{10,22,76} material properties,^{18,63,65,68,74} and effects of pressure.^{20,76–78,80} Investigations into conductivity of B₄C polytypes showed that the B₁₂CBC polytype is metallic in character while the remaining polytypes are semiconductors, yielding B₄C samples that are semiconductors overall.^{10,22,76} Recent determinations of material properties for B₄C focus on the bulk moduli^{18,63,65,68} and Vickers hardness.^{63,74} In particular, 2 studies calculated a value for the bulk modulus for B₁₁C_pCBC that was identical to experiment,^{18,68} while those calculated in another study varied by up to 10%.⁶³ The challenges in comparing these data are 2-fold. First, variations in computational approaches, and thus the calculation of electronic structure, yield different values between studies. Second, there is also spread among experimental data. Thus comparison is difficult because of inherent methodologies of both computation and experiment.

Lastly, pressure dependence of phase changes,²⁰ band gap,⁷⁶ and the onset of amorphization^{24,77,78,80} shows that structural changes occur as a result of an increase in pressure. Precisely what is occurring at the atomistic level as pressure increases is currently not understood. However, the separation of B and C phases²⁰ and the decrease in band gap⁷⁶ show that atomic rearrangement occurs within B₄C samples in these extreme environments.⁸⁰ In a similar vein, amorphization is thought to occur within B₄C samples under these conditions,^{77,78,80} particularly during unloading.⁸⁰ Here again, atomic rearrangement is very likely the controlling force, as buckling at the sidechain leads to additional bonding between the central sidechain atom and neighboring icosahedra.⁸⁰ Moreover, preliminary findings show structural changes depend upon the polytype,^{77,78} and atomic substitutions to the lattice may prevent amorphization.⁷⁸ Despite these ongoing investigations, understanding of the molecular-scale processes of the response of B₄C to a high-pressure environment is largely unknown.

Until this point, the challenges discussed of investigating B₄C have been strictly limited to the structure itself. However, some additives remain within the ceramic sample once synthesis is completed. These can be present as microscale localized regions, grain-sized inclusions, or IGFs as examples. IGFs are amorphous layers approximately 1–2 nm in width that exist within the grain boundaries.⁸¹ The mechanisms through which IGFs develop remain elusive, but they are thought to essentially form via rapid solidification of liquid remaining from sintering.⁸¹ The presence of IGFs within a ceramic sample has an effect on the sound velocity⁸² as

well as chemical,^{81–86} microstructural,⁸⁷ mechanical,^{81–86,88,89} and fracture properties,^{81–83,86} where fracture moves from transgranular to intergranular patterns and may suggest an increase in fracture toughness.⁸¹ IGFs have been observed in Al_2O_3 ,^{81,84,85} mullite,⁸¹ $\text{Si}_2\text{N}_2\text{O}$,⁸¹ Si_3N_4 ,^{81–84,86,88,89} SiC ,^{81,87} $\text{Si}_3\text{N}_4\text{-SiC}$,⁸¹ and $\text{TiO}_2\text{-SiO}_2$.^{81,90} While the effects of IGFs on ceramic materials have been examined, no conclusions have been drawn as to whether an improvement or a deleterious effect arises with their presence in a sample, particularly since only effects to fracture toughness have systematically been examined.⁸¹

Building upon current understanding of structures, stabilities, and material properties, one question that remains is what effect IGFs have on B_4C . There is some disagreement regarding whether IGFs even exist within B_4C samples.⁹¹ However, investigation of the structure, stability, and material properties of a B_4C sample containing an IGF requires accurate and atomic level understanding of the B_4C polytype(s) present, their surface termination, the composition of the IGF, and the atomic arrangement at the interface of the B_4C and the IGF. Surface termination of B_4C polytypes, particularly in terms of topography and reactivity, will contribute to how the ceramic and glassy phases interact at the interface. The composition of possible IGFs for B_4C is not currently well-defined, and the effects of various additives within the B-O matrix have yet to be investigated. The atomic arrangement at the interface enables descriptions of what effects diffusivity and geometric effects within these systems as well. Atomic descriptions of these systems provide insight into what is happening within the microstructure, which in turn has an effect on the fracture mechanics of these systems.

Although technology exists for a multiscale modeling approach, no systematic computational investigation of B_4C materials exists to date. Success of such an effort hinges in part on the description of these systems as accurately as possible within the regime simulated. For example, the strength of a classical MD simulation is heavily dependent upon electrostatic potentials that model the atomic interactions effectively. However, the challenges for atomistic simulations of B_4C are that there are few potentials for B⁹² and a very limited number of functionals exist within the DFT approach.⁴³ In addition, using multiple tools that overlap in time and size scales allows for identification of which parameters contribute to overall observations. The inclusion of relative stabilities of B_4C polytypes^{18–22,63,68} within a molecular scale description of grain boundaries allows computational observations to be more reliable. Until recently,⁸⁰ computational investigations of B_4C on the nanometer scale have involved static processes.^{10,21,22,65} Computational approaches can have a lasting impression on understanding of B_4C systems, but investigations into dynamic processes such as degassing, diffusion, and aggregation must be performed to facilitate this development.

8.8 Computational Methods

8.8.1 DFT Calculations

At this time, no investigation of B₄C polytypes via DFT calculations is being performed. Our collaborators at ARL are currently investigating this system,^{77,93} so we are choosing to focus on alternative aspects of B₄C systems using this method. Moreover, the research outlined below regarding IGFs on B₄C grains is also in collaboration with our colleagues at ARL, and thus we are completing the “multiscale computational investigation” portion of this project via our interaction with them.

8.8.2 DFT-MD Simulations

8.8.2.1 Description of Method

The main goal is to investigate IGFs that form on B₄C grains and the effects that surface termination due to polytype have on the stabilities of these interfaces. Therefore, DFT-MD simulations are employed to model this interface on a nanometer size scale to examine how it changes over time and to determine how temperature and pressure affect the structure and stability of it. This computational tool allows for both bond-breaking and bulk-scale phenomena to be investigated within one modeling scheme, and such an approach is desirable for the investigation of B₄C/IGF interfaces. DFT-MD simulations present an advantage over classical MD simulations in that potentials or fitting parameters do not lead to nonphysical behaviors in the system studied.⁵²

DFT-MD simulations combine representations of the electronic structure of atoms with timescales over which physicochemical processes occur. Separation of nonreacting core electrons from valence electrons via pseudopotentials enables efficient representation of electronic structure.⁵³ VASP^{54–57} approximates the band structure by means of a plane-wave representation, which is attained with a PAW approach.⁵⁸ The PAW approach removes iterative calculations of core electrons from the computation scheme and replicates chemical behaviors of all-electron methods.⁵⁹ Kresse and Joubert⁵⁴ expand upon Blöchl’s original formulation. Several recent analyses of B₄C structures^{19,21,63} differ in their representation of the k points in the Brillouin zone; however, recommended values for k are 9 for metals and 4 for semiconductors.⁶⁴ Further, the energy cutoff value for these systems is approximately 500 eV in a recent investigation.²¹

VASP is employed here because it was designed for materials science applications, particularly in its inclusion of parameter-free functionals.^{53,59} Evaluation of forces

on atoms and stresses on the unit cell are possible in this plane-wave approach.^{53,59} Recent applications of VASP have included modeling the relative stabilities of B₄C structures²¹ and energy minimization of B₄C lattice parameters.¹⁰

8.8.2.2 System Under Study

Four B₄C/IGF interfaces are designed using the 4 most common polytypes from Fig. 8.4²⁰ and a glassy phase designed by our collaborators at ARL, which may contain a combination of B, Al, Si, or O atoms.⁹⁴ The B₄C substrates are $3 \times 3 \times 3$ supercells with the dimensions of approximately $17 \times 17 \times 36$ Å.³ These dimensions are similar to those in recent investigations of IGFs on structural ceramic materials,^{82–85,88,89} and the length in the c direction is intended to overcome any physical effects that may arise due to adsorption of the glassy phase, despite the fact that physical effects have not been observed in DFT calculations on these systems (personal communication with D Taylor and J McCauley, ARL, 2011, unreferenced). As with the investigation of SiC/B₄C interfaces, simulations are performed over 10 ps, with 5 ps for equilibration and 5 ps for data analysis. The optimized B₄C slabs are used as substrates to which the glassy phase is adsorbed for use in classical MD simulations, which are performed by our ARL collaborators (personal communication with J Synowczynski and JC LaSalvia, ARL, 2011, unreferenced) in a manner similar to that for an IGF of Si-O-N on Si₃N₄.⁸³

8.9 Results and Discussion

The 4 substrates are the B₁₂CCC (Fig. 8.8), the B₁₂CBC (Fig. 8.9), the B₁₁C_eCBC (Fig. 8.10), and the B₁₁C_pCBC (Fig. 8.11) polytypes. Atomic positions and lattice parameters are taken from a recent investigation and reflect 20-mol% C.⁹³ Despite the fact that the B₁₂CBC polytype is actually 13-mol% C, the lattice parameters are nearly the same as for 20-mol% C,⁹³ and, therefore, their use is not anticipated to cause any nonphysical effects. Moreover, the energy-minimization and equilibration of these structures will slightly alter the atomic positions and lattice parameters as a result of locating the lower energy structures.

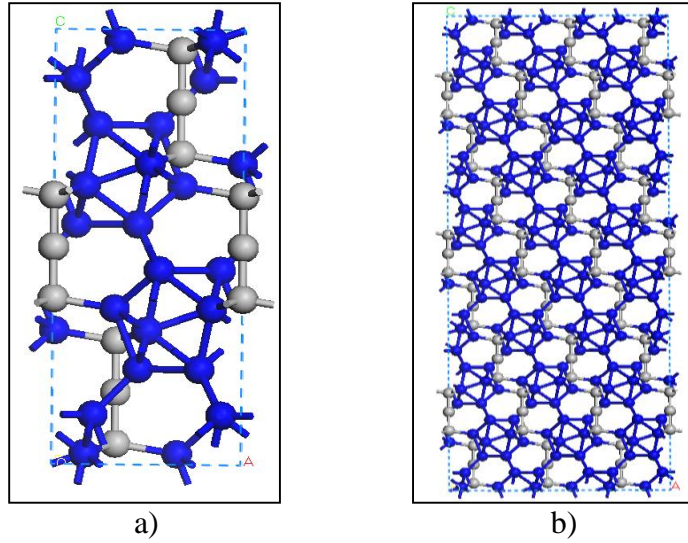


Fig. 8.8 B₁₂CCC polytype of B₄C hexagonal unit cell of 45 atoms a) and b) 3 × 3 × 3 supercell of 1,215 atoms

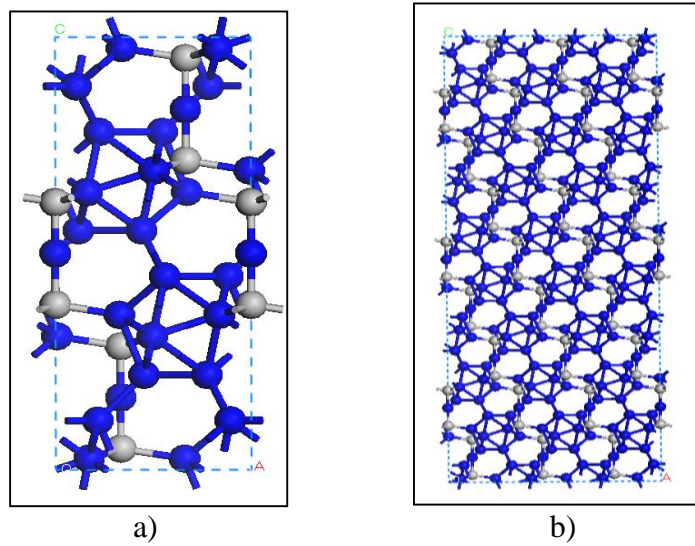


Fig. 8.9 B₁₂CBC polytype of B₄C hexagonal unit cell of 45 atoms a) and b) 3 × 3 × 3 supercell of 1,215 atoms

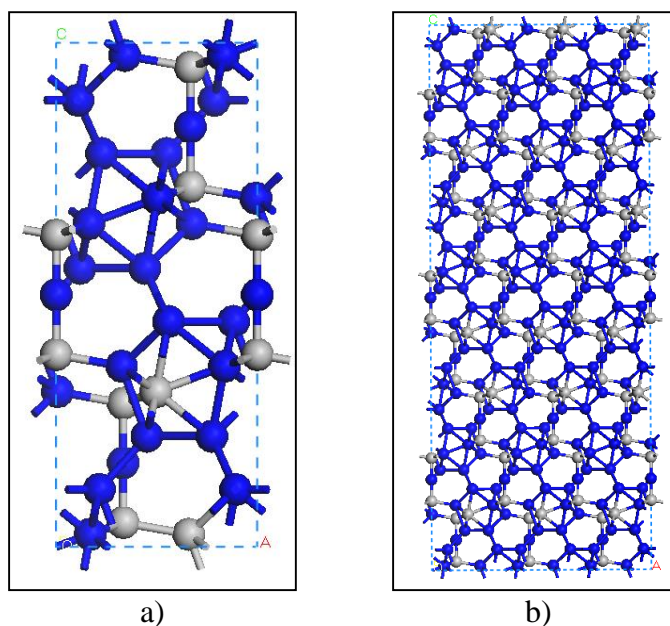


Fig. 8.10 $B_{11}C_{\epsilon}CBC$ polytype of B_4C hexagonal unit cell of 45 atoms a) and b) $3 \times 3 \times 3$ supercell of 1,215 atoms

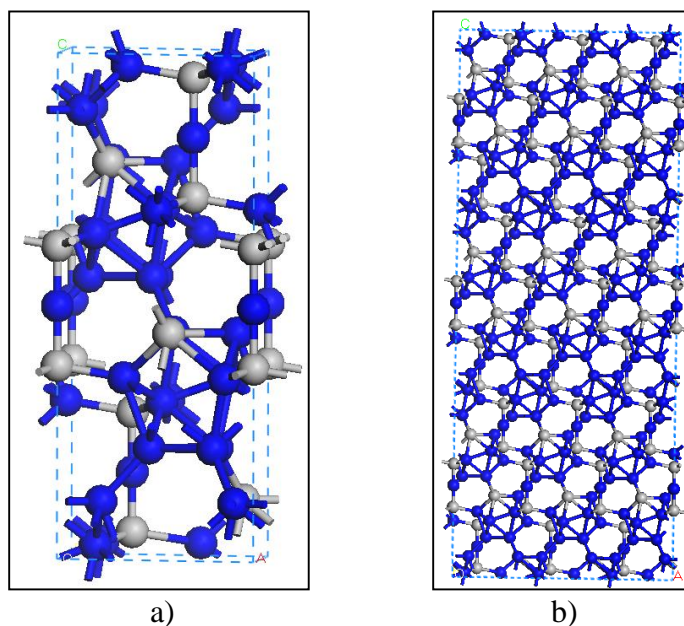


Fig. 8.11 $B_{11}C_pCBC$ polytype of B_4C hexagonal unit cell of 45 atoms a) and b) $3 \times 3 \times 3$ supercell of 1,215 atoms

For both the $B_{11}CCBC$ polytypes, C–C bonds between sidechains and icosahedra were avoided. As far as the literature suggests, these bonds do not exist in the purest or most desirable forms of B_4C . Certainly C inclusions are possible within any B_4C sample, but design of future B_4C samples can consider such inclusions. Moreover, the formation of graphitic sheets^{20,24} and resulting amorphization during

unloading⁸⁰ are separate phenomena that may result from the presence of C–C bonds within these systems. For these reasons, careful avoidance of C–C bonds in the samples described here was employed.

Once these bulk structures are energy-minimized, they will be cut to surface planes that are experimentally relevant (personal communication with J Synowczynski and JC LaSalvia, ARL, 2011, unreferenced) in accordance with methods appropriate for this methodology.⁹⁴ Then simulations will be performed at experimentally relevant temperature and pressure regimes. The goals of characterizing the bulk and slab forms of these polytypes are to determine the surface topography and the polytypes with the lowest surface energies. Then these conclusions can be compared with experiment. Particular attention is to be given to whether B or C atoms preferentially reside at the surface and what effect passivating these surface with H atoms (i.e., avoid dangling bonds) has on these conclusions (personal communication with J Synowczynski and JC LaSalvia, ARL, 2011, unreferenced). Future work will include incorporations of dopants into the structure as well as investigating the effects of chemical composition of the IGF on material properties (personal communication with J Synowczynski and JC LaSalvia, ARL, 2011, unreferenced).

8.10 Expected Implications

The DFT calculations discussed in this report are focused on understanding bonding between B₄C isomers and Si atoms within SiC unit cells. Those structures described in Sections 8.7.1–8.7.2 will be bonded via one Si-B bond, varying the Si atom within the unit cell. Thus the dependence of the interface stability with respect to bonding within the SiC unit cell will be isolated. In SiC samples sintered with B₄C, SiC is the majority component, and therefore the current approach has been adopted in these calculations to probe the significance of attachment of B₄C isomers to various Si atoms within the SiC unit cell. Moreover, Si-B bonds are formed in these calculations because our hypothesis is that they would be more stable than Si-C bonds, as the C atoms are present as electron donors in these substances; further expanding their octets would be energetically unfavorable.

The expected implications of these DFT calculations pertain to providing insight into the structure and stability of possible SiC/B₄C interfaces. Using these molecular clusters allows us to investigate the stability of bonding B₄C isomers to SiC unit cells. In addition, varying the Si atom to which the B₄C is bonded enables the determination of how the location of the B₄C within the unit cell affects

the stability of the interface. From these calculations, we can predict which SiC polytypes and B₄C isomers form the most stable interfaces and thus which of these interfaces are more likely to form overall.

The expected implications of these DFT-MD simulations are primarily to understand what effects system size, time, and temperature have on SiC/B₄C interfaces. Scaling up the DFT calculations to move from one single Si-B bonding site to several throughout an interface permits the determination of whether separate surface sites behave similarly. In addition, the MD component of DFT-MD simulations allows for the investigation of systems with respect to time and temperature, and therefore the effects of each of these parameters in turn may also be ascertained relative to structural or energy changes throughout the simulation.

The expected implications of the DFT-MD simulations of the B₄C/IGF interfaces are 3-fold. First, atomic-level description of surface terminations of these polytypes enables better structural characterization of this material and therefore provides insight into contributions of polytypes to spectral results, and expansion of these simulations to high-pressure and high-temperature regimes enables descriptions of molecular scale processes under these condition. Second, investigation of IGFs on B₄C will show whether such phases at the grain boundaries are possible and which chemical compositions are most likely. Lastly, few previous computational investigations have included dynamics within B₄C systems, but high-pressure examinations include preliminary results to date.^{77,78,80}

8.11 Future Work

The expected implications of this study relate to the development of a molecular-scale description of SiC/B₄C interfaces by employing multiscale computational tools. A molecular-scale understanding will be gained through use of cluster- and unit-cell-sized models of SiC/B₄C interfaces. In particular, the effect of bonding B₄C structures to various Si atoms within the SiC unit cell on both the geometrical configuration of atoms and the relative stability will be identified. From here, a prediction can be made about which interfaces are likely to form. Increasing the system size from molecular clusters to several unit cells with multiple binding sites provides insight into the long-range effects of Si-B bonding at the interface. Moreover, inclusion of time and temperature parameters allows for the incorporation of more experimental effects into these computational studies. Computational methodologies facilitate a molecular-scale understanding by focusing on a specific phenomenon within a physicochemical process and through the simulation of size scales and timescales difficult to attain experimentally.

Future directions include determining the relative stabilities of molecular clusters representing the SiC/B₄C interfaces formed with the 4H and 6H polytypes of SiC and the 4 most stable B₄C isomers identified by Fanchini et al.²⁰ Energy-minimized constituent structures will be used to design the model interfaces, and these interfaces will in turn be energy-minimized. The B3LYP and M06-L functionals will be used for these calculations. Both the relative stabilities of each interface as well as of the bonding sites within the SiC unit cells are anticipated to be completed.

Parallel to these DFT calculations, the nanoscale SiC/B₄C interfaces will be modeled over 10 ps at 300 and 2,400 K over the next 6 months. The initial DFT-MD simulations will be model the bonding configuration of B₄C adsorbates to the 6H-SiC(ABCACB) substrate. Once completed, the interfaces composed of the 6H-SiC(ABCACB) polytype substrate of approximately 100 atoms with 3 B₄C adsorbates will be simulated at 300 and 2,400 K over 10 ps. Again, the goal is to predict which interfaces are likely to form under the conditions modeled. The bonding configuration study is anticipated to require 3 months of computation time, while the simulation of the SiC/B₄C interfaces at 300 and 2,400 K are anticipated to require a minimum of 3 months. Thus, the DFT-MD simulations will be well underway within 6 months.

Upon the successful completion of the work described in this report, additional DFT calculations and DFT-MD simulations are planned. After determining how bonding within the SiC unit cell affects the SiC/B₄C interface, the effect of bonding within the B₄C isomer will also be examined. The goal of these DFT calculations will be to determine the energetic effects of bonding to the B₄C isomer. In addition, future simulations of the SiC/B₄C interface using 6H-SiC(ABCBCB) and 4H-SiC substrates are also planned. These simulations in conjunction with those outlined in the present report represent the most energetically stable constituents possible for SiC/B₄C interfaces, and this systematic approach enables a well-described molecular scale picture of these systems.

The 6-month plan for investigation of B₄C/IGF interfaces is largely fundamental. First, the 4 supercells need to be energy-minimized with VASP. Next, the most experimentally relevant cleavage planes need to be identified and the supercells will be cleaved as such and energy-minimized. Then all of these should be sent or given to Ms Jennifer Synowczynski at ARL for comparison with her energy-minimized structures with classical MD. She then plans to create an IGF of them, with composition and structure of it still to be determined at present. In terms of long-term directions for this project, these are currently rather open-ended and should be discussed with Dr Richard Haber and our collaborators at ARL.

8.12 References

1. Stobierski L, Gubernat A. *Ceramics International*. 2003;29:287.
2. Stobierski, L.; Gubernat, A. *Ceramics International*. 2003;29:355.
3. Zhang X F, Yang Q, De Jonghe LC. *Acta Materialia*. 2003;51:3849.
4. Ray D, Flinders RM, Anderson A, Cutler RA, Rafaniello W. Effect of room-temperature hardness and toughness on the ballistic performance of SiC-based ceramics. *Advances in Ceramic Armor: Ceramic Engineering and Science Proceedings*. 2005;26:131.
5. Ray D, Flinders RM, Anderson A, Cutler RA, Campbell J, Adams JW. effect of microstructure and mechanical properties on the ballistic performance of SiC-based ceramics. *Advances in Ceramic Armor II: Ceramic Engineering and Science Proceedings*. 2007;27:85.
6. Ray DA, Kaur S, Cutler RA, Shetty DK. *Journal of the American Ceramic Society*. 2008;91:1135.
7. Leach AR. *Molecular modeling: principles and applications*; New York: Pearson Prentice Hall; 2001.
8. FlexFEM Software. Albuquerque (NM): Sandia National Laboratories. http://www.cs.sandia.gov/materials_methods/news1.html.
9. Chawla N, Patel BV, Koopman M, Chawla KK, Saha R, Patterson BR, Fuller ER, Langer SA. *Materials Characterization*. 2003;49:395.
10. Balakrishnarajan MM, Pancharatna PD, Hoffmann R. *New Journal of Chemistry*. 2007;31:473.
11. Becker, R. High level view of multiscale modeling. In JOWOG32M, June 18 2007.
12. Eker S, Durandurdu M. *Europhysics Letters*. 2009;87:36001.
13. Branicio PS, Kalia RK, Nakano A, Vashishta P. *Applied Physics Letters*. 2010;97:111903.
14. Buehler MJ, Ackbarow T. *Materials Today*. 2007;10:46.
15. Umeno Y, Kinoshita Y, Kitamura T. *Strength of Materials*. 2008;40:2.

16. Dennington R, II, Keith T, Millam J. GaussView, Version 4.1.2. Shawnee Mission (KS): Semichem, Inc.; 2007.
17. Konstantinova E, Bell MJV, Anjos V. *Intermetallics*. 2008;16:1040.
18. Vast N, Besson JM, Baroni S, Dal Corso A. *Computational Materials Science*. 2000;17:127.
19. Mauri F, Vast N, Pickard CJ. *Physical Review Letters*. 2001;87:085506.
20. Fanchini G, McCauley JW, Chhowalla M. *Physical Review Letters*. 2006;97:35502.
21. Saal JE, Shang S, Liu ZK. *Applied Physics Letters*. 2007;91:231915.
22. Vast N, Sjakste J, Betranhandy E. *Journal of Physics: Conference Series*. 2009;176:012002.
23. Bakas M, Greenhut VA, Niesz DE, Adams J, McCauley J. Relationship between defects and dynamic failure in silicon carbide. In: Kriven WM, Lin H-T, editors. 27th annual Cocoa Beach conference on advanced Ceramics and composites: A: ceramic engineering and science proceedings; 2003; Cocoa Beach, FL. Hoboken (NJ): John Wiley & Sons, Inc.; Vol. 24. DOI: 10.1002/9780470294802.ch52.
24. Chen MW, McCauley JW, Hemker KJ. *Science*. 2003;299:1563.
25. David NV, Gao XL, Zheng JQ. *Applied Mechanics Reviews*. 2009;62:050802.
26. Magnani, G, Beltrami G, Minoccari GL, Pilotti L. *Journal of the European Ceramic Society*. 2001;21:633.
27. Shipilova LA, Petrovskii VY. *Powder Metallurgy and Metal Ceramics*. 2002;41:147.
28. Lee KS, Han IS, Chung YH, Woo SK, Lee SW. *Eco-Materials Processing & Design VI*. 2005;245:486–487.
29. Tkachenko YG, Britun VF, Prilutskii EV, Yurchenko DZ, Bovkun GA. *Powder Metallurgy and Metal Ceramics*. 2005;44:196.
30. Hayun S, Frage N, Dariel MP. *Journal of Solid State Chemistry*. 2006;179:2875.
31. Hayun S, Dariel MP, Frage N, Zaretsky E. *Acta Materialia*. 2010;58:1721.

32. Hayun S, Weizmann A, Dariel MP, Frage N. *Journal of the European Ceramic Society*. 2010;30:1007.
33. Frisch MJ, Trucks GW, Schlegel HB, Scuseria GE, Robb MA, Cheeseman JR, Scalmani G, Barone V, Mennucci B, Petersson GA, Nakatsuji H, Caricato M, Li X, Hratchian HP, Izmaylov AF, Bloino J, Zheng G, Sonnenberg JL, Hada M, Ehara M, Toyota K, Fukuda R, Hasegawa J, Ishida M, Nakajima T, Honda Y, Kitao O, Nakai H, Vreven T, Montgomery JA Jr, Peralta JE, Ogliaro F, Bearpark M, Heyd JJ, Brothers E, Kudin KN, Staroverov VN, Kobayashi R, Normand J, Raghavachari K, Rendell A, Burant JC, Iyengar SS, Tomasi J, Cossi M, Rega N, Millam NJ, Klene M, Knox JE, Cross JB, Bakken V, Adamo C, Jaramillo J, Gomperts R, Stratmann RE, Yazyev O, Austin AJ, Cammi R, Pomelli C, Ochterski JW, Martin RL, Morokuma K, Zakrzewski VG, Voth GA, Salvador P, Dannenberg JJ, Dapprich S, Daniels AD, Farkas Ö, Foresman JB, Ortiz JV, Cioslowski J, Fox DJ. *Gaussian09; Revision A.01*. Wallingford (CT): Gaussian, Inc.; 2009.
34. Sousa SF, Fernandes PA, Ramos MJ. *Journal of Physical Chemistry A*. 2007;111:10439.
35. Foresman JB, Frisch A. *Exploring chemistry with electronic structure methods*; 2nd ed. Pittsburgh (PA): Gaussian, Inc.; 1996.
36. Vosko SH, Wilk L, Nusair M. *Canadian Journal of Physics*. 1980;58:1200.
37. Lee C, Yang W, Parr RG. *Physical Review B*. 1988;37:785.
38. Becke AD. *Journal of Chemical Physics*. 1993;98:1372.
39. Becke AD. *Journal of Chemical Physics*. 1993;98:5648.
40. Duan XF, Wei J, Burggraf L, Weeks D. *Computational Materials Science*. 2010;47:630.
41. Mpourmpakis G, Froudakis GE, Lithoxoos GP, Samios J. *Nano Letters*. 2006;6:1581.
42. Liu WG, Zybin SV, Dasgupta S, Klapotke TM, Goddard WA. *Journal of the American Chemical Society*. 2009;131:7490.
43. Zhao Y, Truhlar DG. *Journal of Chemical Physics*. 2006;125.
44. Zhao Y, Truhlar DG. *Accounts of Chemical Research*. 2008;41:157.
45. Zhao Y, Gonzalez-Garcia N, Truhlar DG. *Journal of Physical Chemistry A*. 2005;109:2012.

46. Van Voorhis T, Scuseria GE. *Journal of Chemical Physics*. 1998;109:400.
47. Zhao Y, Truhlar DG. *Journal of Chemical Physics*. 2009;130.
48. Krishnan R, Binkley JS, Seeger R, Pople JA. *Journal of Chemical Physics*. 1980;72:650.
49. Clark T, Chandrasekhar J, Spitznagel GW, von Rague Schleyer P. *Journal of Computational Chemistry*. 1983;4:294.
50. Jensen, F. *Introduction to computational chemistry*. New York (NY): John Wiley and Sons, Inc.;1998.
51. Kobayashi K, Komatsu S. *Journal of the Physical Society of Japan*. 2008;77:084703.
52. Tunega D, Gerzabek MH, Lischka H. *Journal of Physical Chemistry B*. 2004;108:5930.
53. Hafner J. *Computer Physics Communications*. 2007;177:6.
54. Kresse G, Joubert D. *Physical Review B*. 1999;59:1758.
55. Vienna Ab-initio Simulation Package (VASP) Group Page. <http://cms.mpi.univie.ac.at/vasp/>.
56. Kresse G, Furthmuller J. *Computational Materials Science*. 1996;6:15.
57. Kresse G, Furthmuller J. *Physical Review B*. 1996;54:11169.
58. Blochl PE. *Physical Review B*. 1994;50:17953.
59. Hafner J, Wolverton C, Ceder G. *MRS Bulletin*. 2006;31:659.
60. Lindefelt U, Iwata H, Oberg S, Briddon PR. *Physical Review B*. 2003;67.
61. Kohyama, M. *Physical Review B*, 2002;65.
62. Hara H, Morikawa Y, Sano Y, Yamauchi K. *Physical Review B*. 2009;79:153306.
63. Aydin S, Simsek M. *Physica Status Solidi B-Basic Solid State Physics*. 2009;246:62.
64. Eichler A. Sampling the Brillouin-zone. VASP Workshop; 2003. <http://cms.mpi.univie.ac.at/vasp-workshop/slides/k-points.pdf>.
65. Ivashchenko VI, Shevchenko VI, Turchi PEA. *Physical Review B*. 2009;80.
66. Thévenot F. *Journal of the European Ceramic Society*. 1990;6:205.

67. Raczka M, Gorny G, Stobierski L, Rozniatowski K. *Materials Characterization*. 2001;46:245.
68. Lazzari R, Vast N, Besson JM, Baroni S, Dal Corso A. *Physical Review Letters*. 1999;83:3230.
69. Konovalikhin SV, Ponomarev VI. *Russian Journal of Physical Chemistry A*. 2010;84:1445.
70. Jemmis ED, Balakrishnarajan MM. *Bulletin of Materials Science*. 1999;22:863.
71. Ching WY, Xu YN, Rulis P, Ouyang LZ. *Materials Science and Engineering A-Structural Materials Properties Microstructure and Processing*. 2006;422:147.
72. Shaffer PTB. *Acta Crystallographica*. 1969;B25:477.
73. Materials Studio. San Diego (CA): Accelrys.
74. Guo XJ, He JL, Liu ZY, Tian YJ, Sun J, Wang HT. *Physical Review B*. 2006;73.
75. Hosmane NS, Maguire JA, Yinghuai Z. *Main Group Chemistry*. 2006;5:251.
76. Shirai K. *Journal of Superhard Materials*. 2010;32:205.
77. Taylor D, Wright T, McCauley J. First principles calculation of stress induced amorphization in boron carbide. Presented at International Conference and Exposition on Advanced Ceramics and Composites (ICACC); 2011; Daytona Beach, FL.
78. Ching WY, Aryal S. Modeling amorphization in boron carbide under uniaxial compression; International Conference and Exposition on Advanced Ceramics and Composites (ICACC); 2011; Daytona Beach, FL.
79. Konovalikhin SV, Ponomarev VI. *Russian Journal of Inorganic Chemistry*. 2009;54:197.
80. Yan XQ, Tang Z, Zhang L, Guo JJ, Jin CQ, Zhang Y, Goto T, McCauley JW, Chen MW. *Physical Review Letters*. 2009;102.
81. Subramaniam A, Koch CT, Cannon RM, Ruhle M. *Materials Science and Engineering A-Structural Materials Properties Microstructure and Processing*. 2006;422:3.

82. Ching WY, Rulis P, Ouyang LZ, Aryal S, Misra A. *Physical Review B* 2010;81.
83. Rulis P, Chen J, Ouyang L, Ching WY, Su X, Garofalini SH. *Physical Review B*. 2005;71:235317.
84. Garofalini SH. *Materials Science and Engineering a-Structural Materials Properties Microstructure and Processing*. 2006;422:115.
85. Garofalini SH, Zhang SH. *Journal of Materials Science*. 2006;41:5053.
86. Zhang SG, Garofalini SH. *Journal of the American Ceramic Society*. 2009;92:147.
87. Choi HJ, Kim YW. *Journal of the European Ceramic Society*. 2004;24:3795.
88. Ching WY, Rulis P, Ouyang L, Misra A. *Applied Physics Letters*. 2009;94.
89. Garofalini SH, Zhang SH. *Journal of the American Ceramic Society*. 2010;93:235.
90. Luo J, Chiang YM. *Annual Review of Materials Research*. 2008;38:227.
91. Celik Y, Goller G, Yucel O, Sahin F. *Advances in Science and Technology*. 2010;63:79.
92. Lawson JW, Bauschlicher CW, Daw MS. Ab initio computations of the electronic, mechanical, and thermal properties of ultra high temperature ceramics (UHTC) ZrB₂ and HfB₂. Presented at International Conference and Exposition on Advanced Ceramics and Composites (ICACC); 2011; Daytona Beach, FL.
93. Kwei GH, Morosin B. *Journal of Physical Chemistry*. 1996;100:8031.
94. Morrow CP. Crossing scales with computational tools: applications to divalent silicate dissolution [doctoral dissertation]. [State College (PA)]: Pennsylvania State University; 2010.

Task 9: Study of US Silicon Carbide Powder Variations

Core Faculty: RA Haber, DE Niesz

US Army Research Laboratory (ARL) Collaborator: T Jessen

Research Associate: V Domnich

Undergraduate Student: M Freeman

9.1 Long-Range Goals

- Develop a better understanding of the reaction during carbothermic production of silicon carbide (SiC).
- Quantify the effects of precursor impurities, reaction time, and spatial location on chemistry and crystallinity of SiC for dynamic energy dissipation applications.

9.2 Background

It is difficult, if not impossible, to fabricate high-quality ceramic components without control of the powders comprising them. US-based companies supplying many strategic ceramic components have seen the erosion of domestic suppliers over the past 2 decades. Many critical-material-based systems for high-strain-rate mechanical or thermal-loading applications rely on unique, highly specified powders. Applications ranging from personnel or vehicular armor, to high-intensity mirrors, to missile radomes, to rocket nozzles are fabricated using powders coming more and more from countries such as India, China, and Russia than the United States. The consequence of this eroded domestic supply base has been the inability of component manufacturers to design powders for a specific application, rather sorting or treating highly variable commodity powders to impart the requisite material “uniqueness” for an application.

For commercial-scale operations, SiC powders are produced by the carbothermic reduction of a silicon oxide (SiO₂) in contact with a carbon (C) source. This is known as the Acheson process.¹ The resultant powder is coarse in grain size and must be comminuted to produce micron to submicron-sized particles required for ceramic processing. In many cases, lower cost, lower-specified end-use applications, such as abrasives, have introduced new developing-world powder suppliers. With greater dependence on foreign sources, supplied quality has become variable. Furnace reactors were once large-scale operations, but now small

producers can introduce very small, highly variable product into a distribution stream. As an example, one supplier can produce 500 lb while a second producer can produce 5–10 tons. Precursor raw materials are also in question. Traditional C sourcing used to be high-grade-petroleum-derived coke; however, in China it is not uncommon to see anthracite coal used. The consequence is a highly chemically variable end product. For carbide powders, the impact of trace impurity variations is to provide variable levels of crystallinity into the supply stream. Component suppliers are now faced with how to make a consistent product meeting today's military specifications. The concepts related to improving component performance for the future can no longer include changing the initial powder—it is no longer in our control.

By losing control of powder processing, the United States has reached a point where variability in carbide powders are expected, tolerated, and in many cases ignored. Process treatments are developed to “treat” variable powders to improve their overall uniformity. However, this results in dense components whose microscale variability reflects the intrinsic variability of the parent powder. From a simple business or logistic point of view, manufacturers can no longer assure that the carbide powders used in highly specified components will meet strict testing requirements.

In this research program we will investigate how new phenomenological performance enhancements can be achieved by manipulating the intrinsic properties of powders used in processing. Keeping in mind that the goal of this research will be to manage future strategic defense materials, we will examine how SiC powders can be manipulated during their synthesis, thereby providing a bases for creating or improving the limited domestic supply chain. We will also examine the limitations an uncontrollable imported powder supply has on the prospects for improved materials in the future.

9.3 Experimental Approach

A piece of SiC produced by carbothermic reaction was acquired from Washington Mills (Niagara Falls, NY). To investigate variations in chemical composition and properties of SiC as a function of distance from electrode, samples were retrieved in successive 2-inch steps from the electrode edge to the metallurgical-grade edge, as illustrated in Fig. 9.1. As the first step in powder reduction, a Fritsch Pulverisette jaw crusher was used to reduce the samples to particles of 1–10 mm in size. Final jet milling of powders to submicron sizes was achieved in a Sturtevant Qualification Micronizer. Particle size analysis was performed using a Mastersizer unit by Malvern Instruments. Densification of the samples was done using a

Thermal Technology spark plasma sintering (SPS) unit at the maximum temperature of 1,950 °C. To achieve maximum density of the samples, about 1% of boron carbide (B_4C) and excess C as graphite (B/C mole ratio of 0.72) were mixed with SiC powders prior to sintering. These samples are referred to as samples with sintering aids. Once the jet milling and sintering parameters to produce ceramics with near theoretical density have been established, new batches of powders were sintered without the use of the sintering aids.

#1 #2 #3 #4 #5 #6 #7 #8 #9 #10 #11

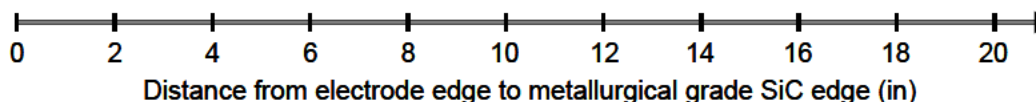


Fig. 9.1 SiC piece retrieved from a carbothermic reactor. The samples for analysis were collected from different zones as indicated by consecutive numbers in the direction of increasing distance from the electron edge toward the metallurgical-grade SiC edge.

The density of the sintered samples was determined using the Archimedes method. Elastic properties (elastic modulus, bulk modulus, and shear modulus) of the sintered samples were determined using a high-frequency ultrasound system, developed at Rutgers University, capable of pulse amplitude and time-of-flight (TOF) C-scan imaging and acoustic spectroscopy via fast Fourier transform (FFT) analysis of sample peak response. Hardness measurements were performed on a Leco hardness tester using a Knoop indenter at 1-kg load. Hardness data were averaged over 30 measurements on each sample.

Raman spectroscopy analysis was performed using a Renishaw InVia unit equipped with a 633-nm wavelength laser and a 1,200/mm diffraction grating. A 20× objective lens was used, which allowed focusing the laser beam to a 4-μm

spot on the sample surface. Spectra were acquired both at maximum and reduced laser power to verify that no artifacts were introduced by overheating of materials within the laser illuminated area. On each sample, spectra were acquired from 10 randomly selected areas to obtain statistically significant results.

Raman analysis of SiC polytypes was based on the methodology developed by Patrick et al.²⁻⁵ Because different SiC polytypes have different numbers of atoms per unit cell, they have different number of phonon branches in the Brillouin zone (BZ). For a periodic crystal, Raman measurements can access only the phonons with vectors $q = 0$ in the BZ scheme. In the large zone (LZ) representation, which unfolds the BZ phonon dispersion curves in the axial direction up to q_{\max} , the phonon dispersion curves become nearly independent of polytype (Fig. 9.2). Points of this common LZ spectrum accessible to Raman measurements have special values of the reduced momentum $X = q/q_{\max}$ that are equivalent to $q = 0$ in the BZ representation. These special points on the phonon dispersion curves in the LZ are characterized by small energy discontinuities for all accessible reduced momentum values except for $X = 0$.

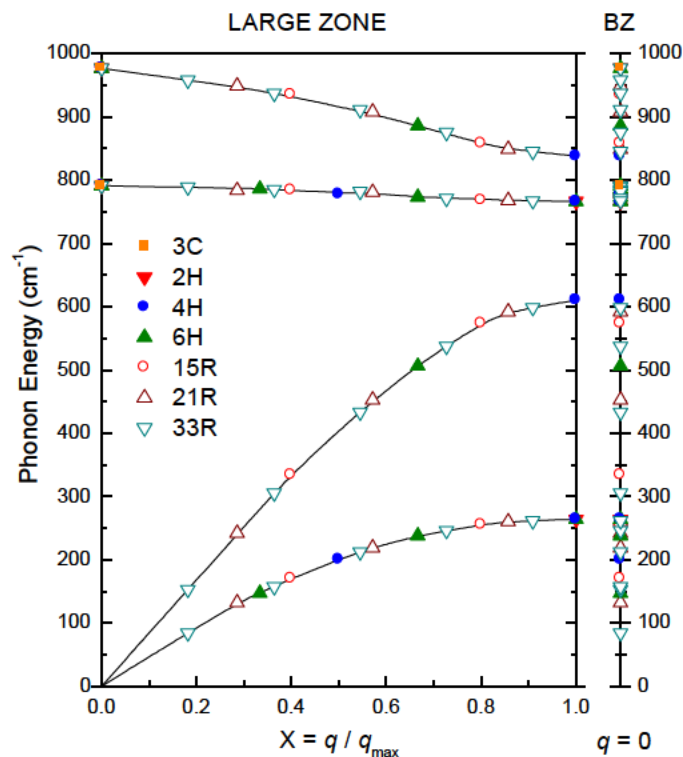


Fig. 9.2 LZ representation of phonon dispersion spectra in various SiC polytypes. The position of the special points on the reduced momentum axis and the Raman active modes for each polytype are related to the number of atoms in the unit cell of a respective polytype. Also shown are equivalent Raman modes at $q = 0$ in the BZ.

The use of the LZ scheme allows identification of different SiC polytypes by Raman spectroscopy measurement. In particular, the bands at 200 cm^{-1} , 610 cm^{-1} , and 837 cm^{-1} are unique to the 4H polytype; the bands at 147 cm^{-1} , 238 cm^{-1} , 506 cm^{-1} , and 886 cm^{-1} are unique to the 6H polytype; the bands at 170 cm^{-1} , 255 cm^{-1} , 334 cm^{-1} , 573 cm^{-1} , and 858 cm^{-1} are unique to the 15R polytype; the bands at 132 cm^{-1} , 219 cm^{-1} , 453 cm^{-1} , 592 cm^{-1} , and 908 cm^{-1} are unique to the 21R polytype; and the bands at 84 cm^{-1} , 305 cm^{-1} , 433 cm^{-1} , 537 cm^{-1} , 598 cm^{-1} , 875 cm^{-1} , and 958 cm^{-1} are unique to the 33R polytype (Fig. 9.3). At the same time, the bands in the range of 238–264 cm^{-1} , 766–791 cm^{-1} , and the bands at 977 cm^{-1} may belong to any of 3C, 2H, 4H, 6H, 15R, 21R, or 33R polytypes and therefore only allow identification of SiC without providing exact information on its polytype structure.

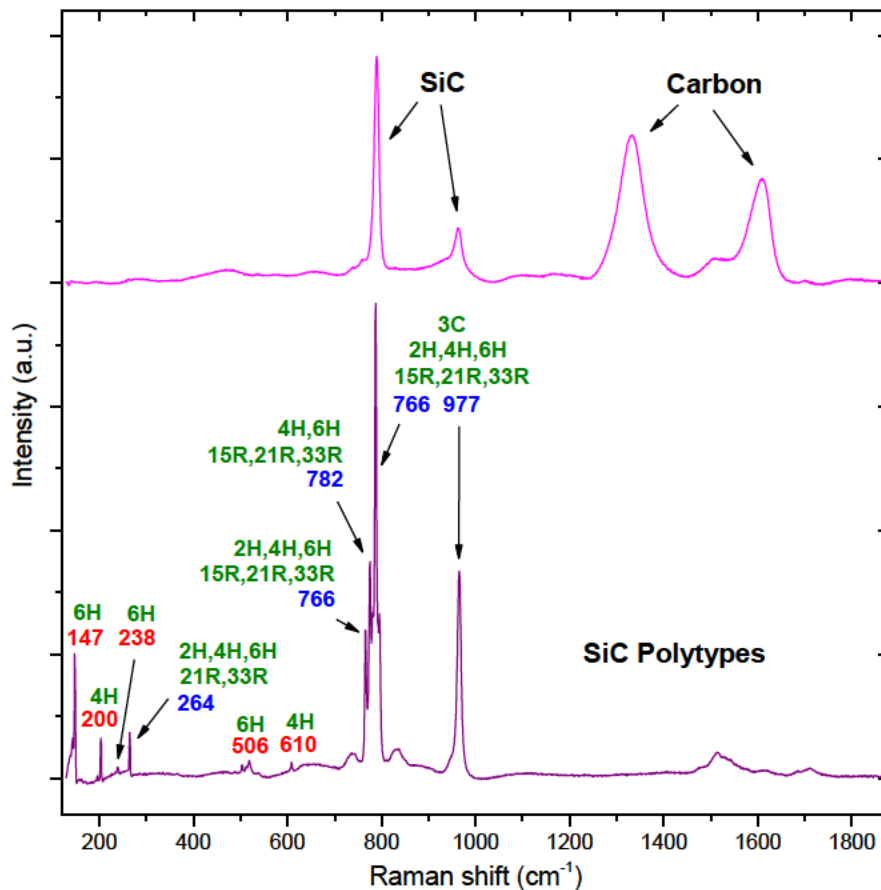


Fig. 9.3 Typical Raman spectrum of SiC showing bands specific to a particular SiC polytype (red) and overlapping bands of several SiC polytypes (blue). Only 2 bands at 766 and 977 cm^{-1} should be observed in 3C SiC.

In addition to various SiC polytypes, free Si (a single narrow band at 520 cm^{-1})⁶ and graphitic C (D and G bands)⁶ were indentified in selected samples by Raman spectroscopy (Fig. 9.3).

9.4 Results and Discussion

The results of our Raman analysis of the samples obtained from various zones in the carbothermally reduced SiC piece corresponding to different steps of powder reduction and sintering are summarized in Tables 9.1–9.5. According to Raman data, 6H polytype is the major component in areas 1–4 (Fig. 9.4). Further, as shown in Fig. 9.5, the 4H SiC polytype often becomes a predominant component in areas 6–9 (midzone between the SiC edge adjacent to graphitic electrode and the furthest from the electrode metallurgical-grade SiC edge). The 15R SiC polytype and free Si are also sometimes observed in areas 6–9. In areas 10 and 11, identification of polytype structure of SiC becomes problematic, although the presence of SiC can be confirmed in most cases. Closer to the metallurgical-grade edge (areas 8–11), free C becomes a predominant component in the sample chemistry (Fig. 9.6). We also note the presence of the 33R SiC polytype as a minor contribution in some analyzed samples. The results of our Raman analysis for 6H SiC, 4H SiC, 15R SiC, and free C are displayed in Fig. 9.7. As evident from Fig. 9.7, powder processing and sintering with the use of sintering aids do not change qualitatively the distribution of the main chemical components; the quantitative change is in the increased amount of 4H and 15R SiC in the midzone as the powders are reduced to micron size.

Table 9.1 Summary of the results of Raman analysis of unprocessed SiC

Sample No.	Distance from Electrode Edge (inches)	SiC Polytypes Identified (% of all observations)						Graphitic C Detected	Free Si Detected
		3C	2H	4H	6H	15R	33R		
1	0	+-	+-	0	100	0	30	0	0
2	2	+-	+-	0	100	0	40	0	0
3	4	+-	+-	0	100	0	30	0	0
4	6	+-	+-	0	100	0	30	0	0
5	8	+-	+-	10	80	0	30	0	0
6	10	+-	+-	70	20	20	20	0	10
7	12	+-	+-	40	30	10	30	0	10
8	14	+-	+-	70	20	10	10	10	0
9	16	+-	+-	30	70	10	20	70	0
10	18	+-	+-	10	10	0	30	70	0
11	20	+-	+-	10	10	0	10	100	0

Table 9.2 Summary of the results of Raman analysis of crushed SiC powders

Sample No.	Distance from Electrode Edge (inches)	SiC Polytypes Identified (% of all observations)						Graphitic C Detected	Free Si Detected
		3C	2H	4H	6H	15R	33R		
1	0	+-	+-	0	100	0	10	0	0
2	2	+-	+-	0	100	0	10	0	0
3	4	+-	+-	0	100	0	10	0	10
4	6	+-	+-	20	80	10	10	0	20
5	8	+-	+-	30	70	10	10	0	10
6	10	+-	+-	40	70	20	30	0	0
7	12	+-	+-	70	30	10	10	0	0
8	14	+-	+-	10	80	20	30	40	0
9	16	+-	+-	30	70	0	50	70	0
10	18	+-	+-	20	40	0	60	60	0
11	20	+-	+-	10	30	0	50	100	20

Table 9.3 Summary of the results of Raman analysis of milled SiC powders

Sample No.	Distance from Electrode Edge (inches)	SiC Polytypes Identified (% of all observations)						Graphitic C Detected	Free Si Detected
		3C	2H	4H	6H	15R	33R		
1	0	+-	+-	10	100	0	0	0	0
2	2	+-	+-	0	100	10	0	0	0
3	4	+-	+-	0	100	0	10	0	0
4	6	+-	+-	40	100	20	0	0	0
5	8	+-	+-	100	100	60	0	0	0
6	10	+-	+-	100	90	50	10	0	0
7	12	+-	+-	100	70	30	0	0	0
8	14	+-	+-	90	100	10	0	30	0
9	16	+-	+-	80	100	30	0	40	0
10	18	+-	+-	10	80	10	0	90	0
11	20	+-	+-	20	60	0	0	100	0

Table 9.4 Summary of the results of Raman analysis of sintered SiC ceramics (with sintering aids)

Sample No.	Distance from Electrode Edge (inches)	SiC Polytypes Identified (% of all observations)						Graphitic C Detected	Free Si Detected
		3C	2H	4H	6H	15R	33R		
1	0	+-	+-	0	100	0	0	0	0
2	2	+-	+-	0	100	0	0	0	0
3	4	+-	+-	0	100	0	0	0	0
4	6	+-	+-	80	100	20	0	0	0
5	8	+-	+-	90	100	30	0	0	0
6	10	+-	+-	90	50	20	0	0	0
7	12	+-	+-	100	30	0	0	0	0
8	14	+-	+-	80	60	20	0	70	0
9	16	+-	+-	100	50	20	0	50	0
10	18	+-	+-	50	90	30	0	100	0
11	20	+-	+-	80	90	30	0	100	0

Table 9.5 Summary of the results of Raman analysis of sintered SiC ceramics (no sintering aids)

Sample No.	Distance from Electrode Edge (inches)	SiC Polytypes Identified (% of all observations)						Graphitic C Detected	Free Si Detected
		3C	2H	4H	6H	15R	33R		
1	0	NA	NA	NA	NA	NA	NA	NA	NA
2	2	+-	+-	0	100	0	0	0	0
3	4	NA	NA	NA	NA	NA	NA	NA	NA
4	6	+-	+-	90	100	0	0	0	0
5	8	NA	NA	NA	NA	NA	NA	NA	NA
6	10	+-	+-	90	60	10	0	0	0
7	12	+-	+-	100	40	0	0	0	0
8	14	NA	NA	NA	NA	NA	NA	NA	NA
9	16	+-	+-	90	70	10	0	0	0
10	18	+-	+-	80	100	10	0	0	0
11	20	NA	NA	NA	NA	NA	NA	NA	NA

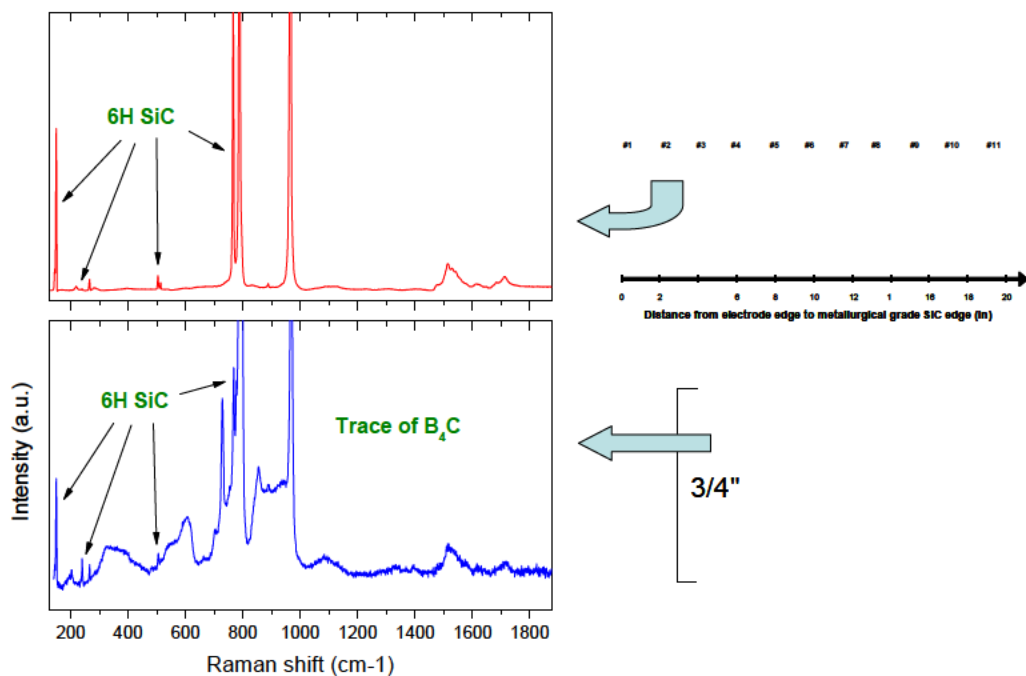


Fig. 9.4 Raman spectra of carbothermally reacted SiC collected from the areas near graphitic electrode: as-received samples (top) and sintered ceramics (bottom). The trace of B₄C is originated from the sintering aids.

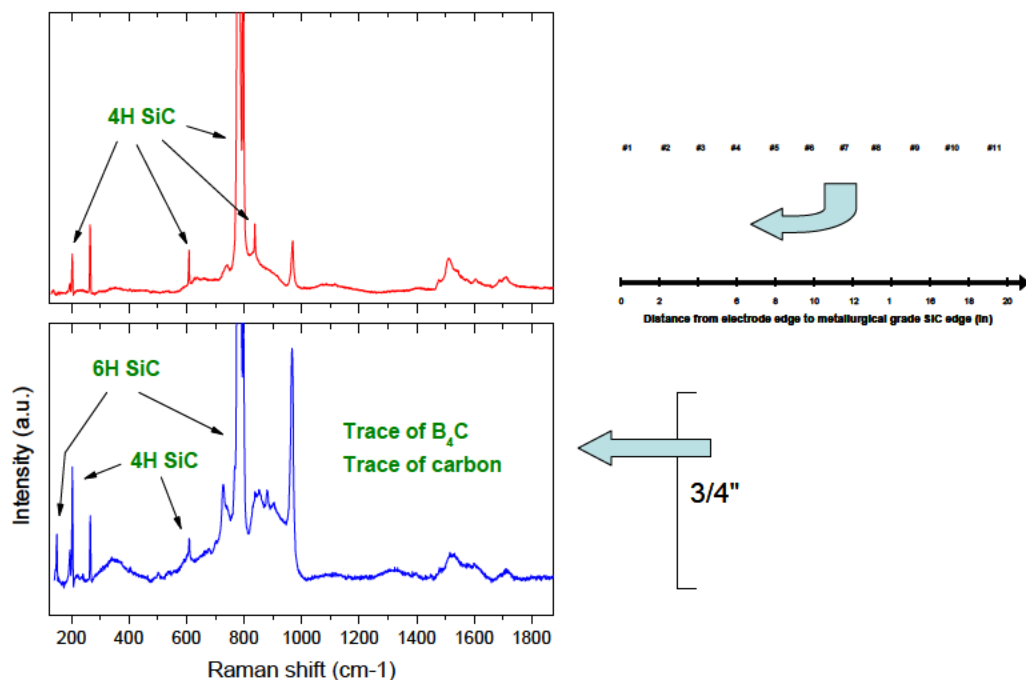


Fig. 9.5 Raman spectra of carbothermally reacted SiC collected from the areas between graphitic electrode and metallurgical-grade edge: as-received samples (top) and sintered ceramics (bottom). The traces of C and B₄C are originated from the sintering aids.

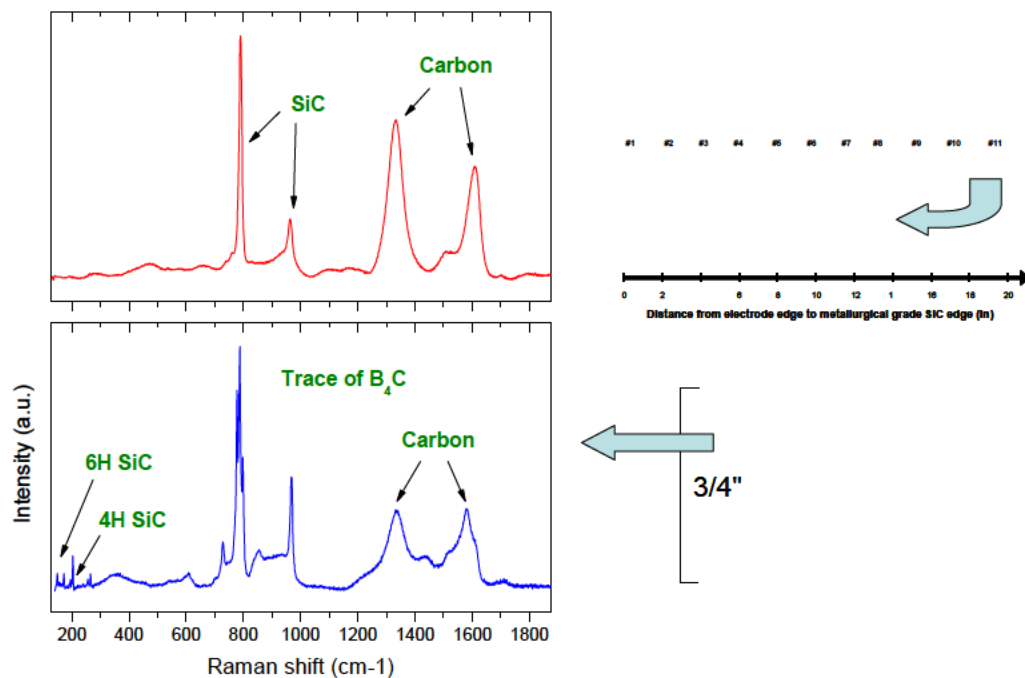


Fig. 9.6 Raman spectra of carbothermally reacted SiC collected from the areas far from graphitic electrode, near metallurgical-grade edge: as-received samples (top) and sintered ceramics (bottom). The traces of C and B₄C are originated from the sintering aids.

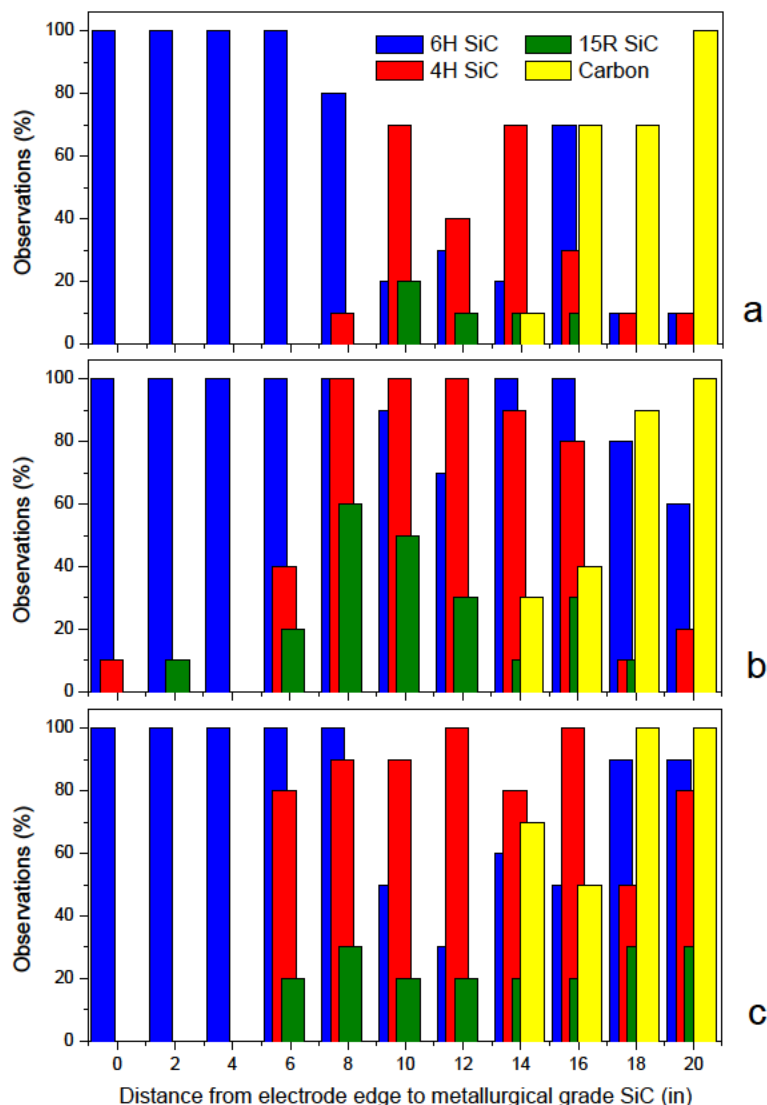


Fig. 9.7 Distribution of selected SiC polytypes and graphitic C content in carbothermally reacted SiC: a) as-received samples, b) powders after jet milling, and c) sintered samples (with sintering aids). Analysis was done based on the number of observation of Raman bands pertaining to a particular SiC polytype/graphitic C.

To evaluate the mechanical properties of the sintered samples, Knoop hardness measurements were carried out. As follows from the data shown in Table 9.6, the density of many sintered samples appeared significantly lower than the theoretical density of SiC (3.21 g/cc). This was found to be a consequence of insufficient milling, as the analyzed powders exhibited multimodal size distribution, with some particles extending into the dimensions of tens of microns (red curves in Fig. 9.8). Repeated (up to 20 times) milling was adopted and density of the powders comminuted using this method to this date is shown in Fig. 9.8 as green curves. The particle distribution of the powders milled repeatedly is centered at around 1–2 μm ,

with a single mode distribution. These powders densified to density of approximately 97% ρ_{th} during sintering. As shown in Fig. 9.9, it was possible in most cases to locate highly densified areas even on the generally porous samples, and Knoop indents were placed within these areas for hardness measurements. Homogeneous appearance of the analyzed sample surface, as well as the regular shape of the indents and the absence of extended cracking, all suggest that these data can give a reliable estimate of the hardness of sintered samples corresponding to different areas within the carbothermic reactor. To this date, reliable hardness measurements were not possible only for samples 3 and 5.

Table 9.6 Density and Knoop hardness of sintered samples (with sintering aids)

Sample No.	Density (g/cc)	Relative Density (%ρ_{th})	Knoop Hardness (kgf/mm²)
1	3.03	94.4	2169 \pm 70
2	3.14	97.8	2152 \pm 64
3	2.63	81.9	NA
4	3.14	97.8	2080 \pm 59
5	2.91	90.7	NA
6	3.13	97.5	2067 \pm 61
7	3.13	97.5	2137 \pm 85
8	2.86	89.9	2193 \pm 57
9	3.14	97.8	2098 \pm 65
10	3.14	97.8	1949 \pm 51
11	2.78	86.6	1934 \pm 50

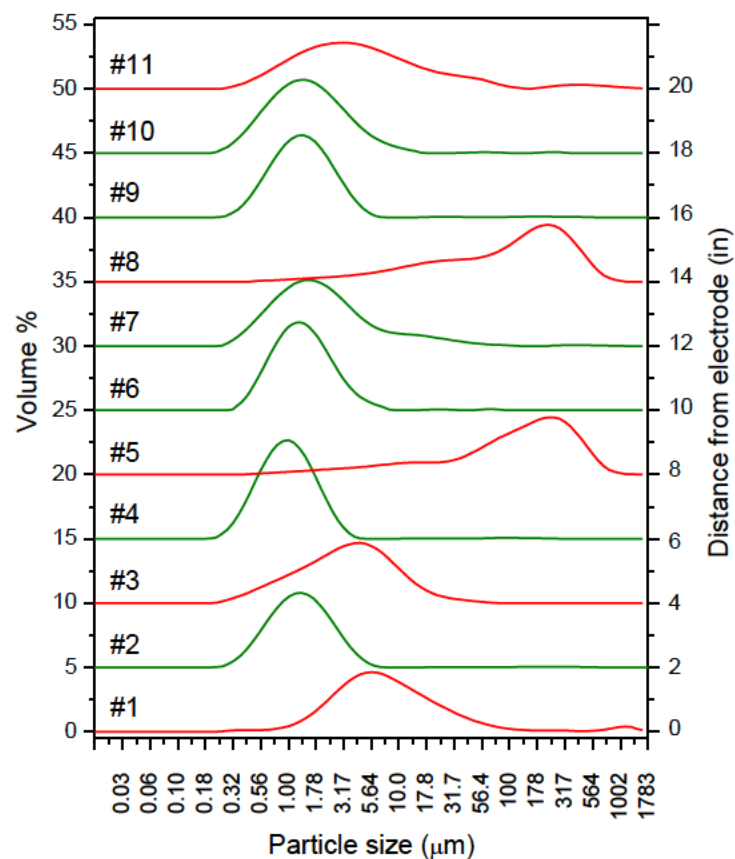


Fig. 9.8 Particle size analysis results for powders 1–11; powders in green have been milled over 15 times. The average particle size is near 1 μm for powders subjected to repeated jet milling.



Fig. 9.9 Optical images of Knoop indents in selected sintered samples: a) 1, b) 3, c) 5, d) 6, e) 8, and f) 9. Absence of visible cracking and the regular shape of most indents suggest that selected localized areas in the sintered samples are fully densified.

Density and 1-kgf Knoop hardness of selected samples sintered with the use of sintering aids are shown in Fig. 9.10 as a function of the distance from the electrode. These data show correlation with the SiC polytype and C distribution in the same samples shown in Fig. 9.7c.

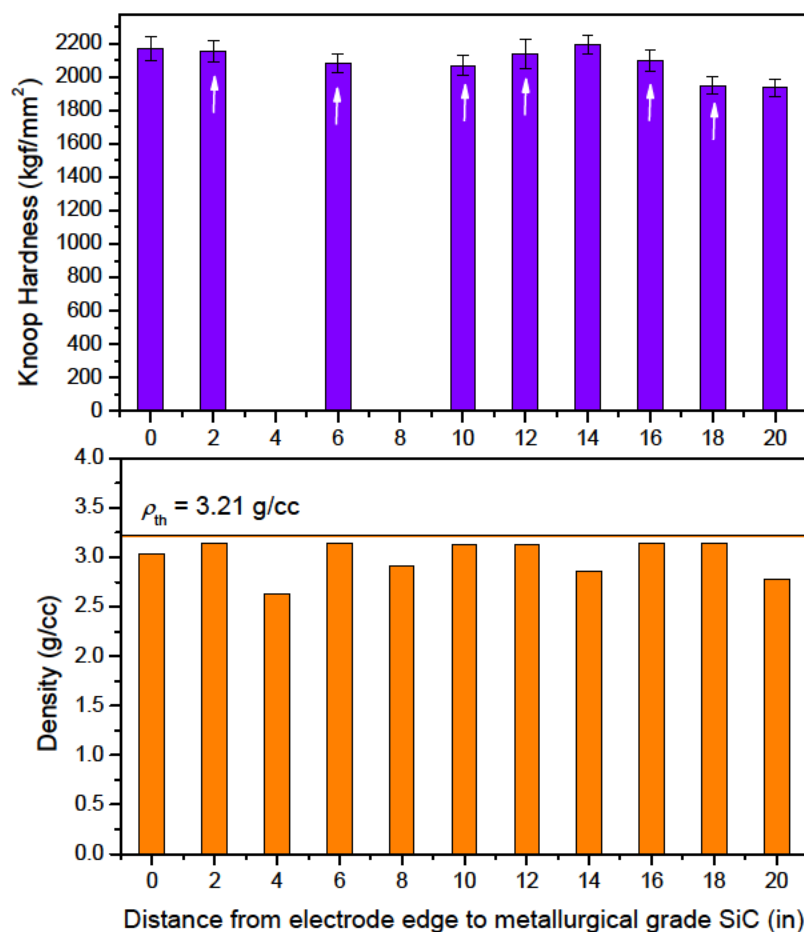


Fig. 9.10 Density (bottom) and 1-kgf Knoop hardness (top) data on samples produced with the use of the sintering aids as a function of the distance from the electrode. Only reliable hardness data has been included in this illustration. The hardness data marked by white arrows is obtained on samples with density near 97% ρ_{th} .

It was established that subjecting powders to repeated jet milling was leading to an improved packing during sintering and resulted in near theoretical density of the sintered material produced without the use of sintering aids. The density and Knoop hardness of the sintered sample nos. 2, 4, 6, 7, 9, and 10 produced without sintering aids are shown in Table 9.7. These data are compared with composition of the same samples in Fig. 9.11. There appears to be a similar correlation between hardness and SiC polytype composition as the one observed for samples sintered with the use of sintering aids shown in Figs. 9.7 and 9.10. The hardness is highest for samples consisting of 6H SiC polytype and lowest near the metallurgical-grade SiC edge. Formation of the 4H SiC polytype lowers hardness to some extent. One notable difference between Figs. 9.7 and 9.11 is the absence of free C near the metallurgical-grade edge in the samples sintered without

the use of sintering aids. This suggests that all free C is reacted in this case. Negligible effect on the hardness of the free C can be explained by the selection of only regularly shaped indents adopted in this work; apparently these indents were not affected by structural imperfections such as C inclusions. Additional work on comparative measurements of macro-mechanical properties of the samples sintered with and without the use of sintering aids will be required to clarify this issue.

Table 9.7 Density and Knoop hardness of sintered samples (no sintering aids)

Sample No.	Density (g/cc)	Relative Density ($\% \rho_{th}$)	Knoop Hardness (kgf/mm²)
1	NA	NA	NA
2	3.13	97.5	1985 \pm 64
3	NA	NA	NA
4	3.14	97.8	1931 \pm 52
5	NA	NA	NA
6	3.11	96.9	1964 \pm 57
7	3.13	97.5	1979 \pm 59
8	NA	NA	NA
9	3.12	97.2	1912 \pm 54
10	3.14	97.8	1825 \pm 53
11	NA	NA	NA

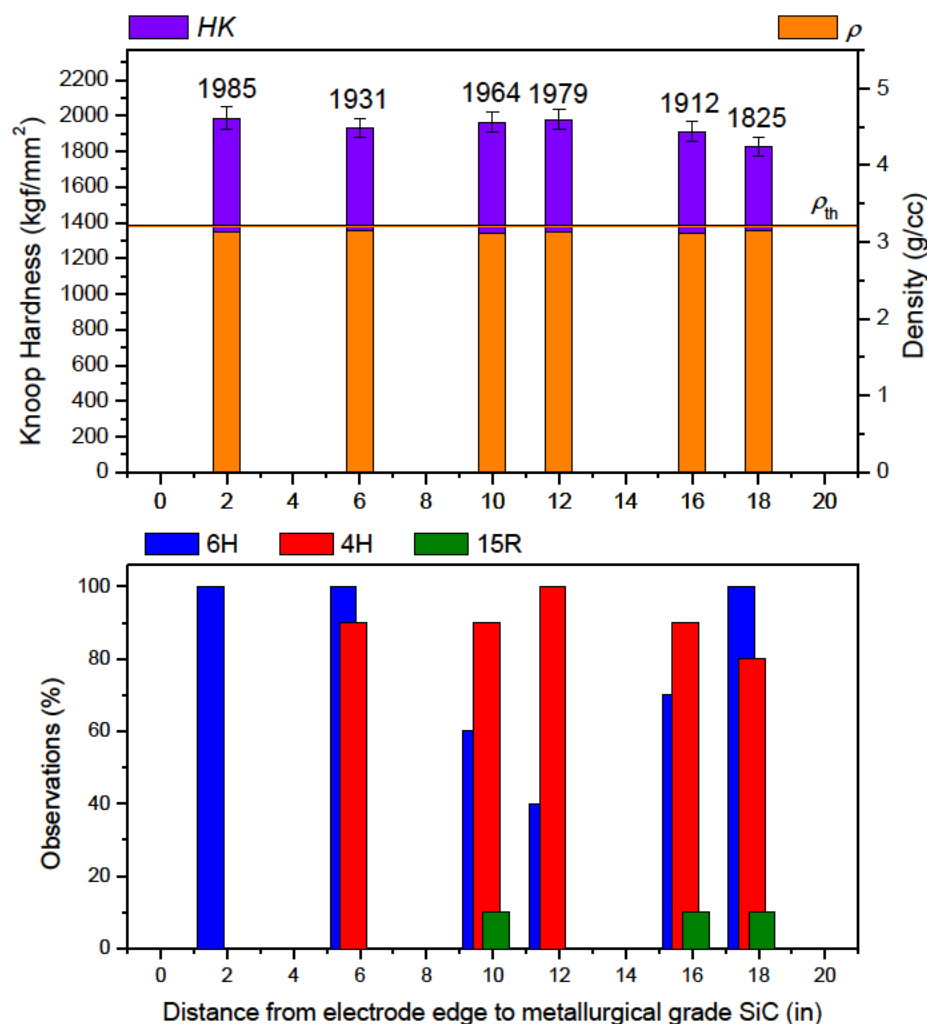


Fig. 9.11 Correlation between hardness (top) and compositions (bottom) for selected SiC samples densified using SPS method without the use of sintering aids. All samples have been sintered to density of approximately 97% ρ_{th} .

The results of chemical analysis of the unprocessed samples are shown in Fig. 9.12 and Table 9.8. The presence of unreacted Si and C, as well as manganese (Mg), aluminum (Al), calcium (Ca), titanium (Ti), vanadium (V), iron (Fe), and zirconium (Zr) impurities have been detected in the samples. Increased concentrations of free C were observed near the metallurgical-grade edge, similar to the X-ray diffraction (XRD) and Raman results. The increased free C content is correlated with the increased concentrations of metal impurities, as shown in Fig. 9.12. Increased concentrations of free Si were observed in the crystalline-grade zone adjacent to the boundary with the metallurgical-grade SiC. However, no direct correlation between the formation of 4H SiC polytype and the presence of metal impurities could be established.

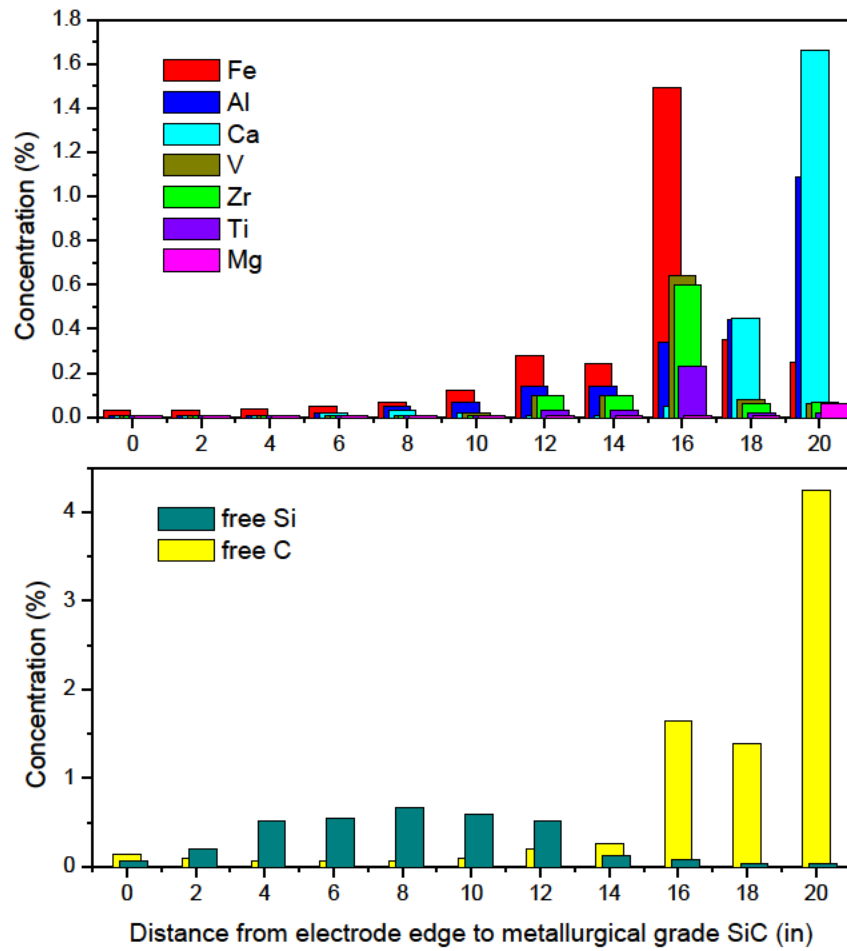


Fig. 9.12 Distribution of metal impurities (top) and unreacted (bottom) C and Si inclusions in carbothermally reduced SiC, as a function of the distance from the graphite electrode

Table 9.8 Summary of the results of chemical analysis of unprocessed carbothermally reduced SiC

Sample No.	Distance from Electrode Edge (inches)	Metallic Impurities (%)							Free C (%)	Free Si (%)
		Mg	Al	Ca	Ti	V	Fe	Zr		
1	0	0.01	<0.01	0.01	<0.01	<0.01	0.03	<0.01	0.06	0.14
2	2	0.01	<0.01	<0.01	<0.01	<0.01	0.03	<0.01	0.20	0.10
3	4	0.01	<0.01	0.01	<0.01	<0.01	0.04	<0.01	0.51	0.07
4	6	0.01	0.02	0.02	<0.01	<0.01	0.05	<0.01	0.55	0.07
5	8	0.01	0.05	0.03	<0.01	<0.01	0.07	<0.01	0.66	0.06
6	10	0.01	0.07	0.02	<0.01	0.02	0.12	<0.01	0.59	0.09
7	12	0.01	0.14	0.01	0.03	0.10	0.28	0.10	0.51	0.21
8	14	0.01	0.14	<0.01	0.03	0.10	0.24	0.10	0.13	0.26
9	16	0.01	0.34	0.05	0.23	0.64	1.49	0.60	0.08	1.65
10	18	0.01	0.44	0.45	0.02	0.08	0.35	0.06	0.03	1.39
11	20	0.06	1.09	1.66	0.02	0.06	0.25	0.07	0.03	4.24

9.5 Future Work

Repeated jet milling will be used for reducing the remaining powders to the size close to 1 μm . Chemical analysis of milled powders will be performed once sufficient quantities of powders have been prepared. Samples representing various zones in the carbothermic reactors will be sintered with and without the use of sintering aids. Additionally, hydrofluoric acid washing will be used for the same powders prior to sintering to remove excess oxygen and metal impurities. Physical and mechanical properties of the sintered samples will be evaluated and correlated with chemistry and polytypism of the starting material.

9.6 References

1. Weimer AW, editor. Carbide, boride, and nitride materials synthesis and processing. London: Chapman & Hall; 1997.
2. Patrick L, Hamilton DR, Choyke WJ. Growth, luminescence, selection rules, and lattice sums of SiC with wurtzite structure. *Phys Rev.* 1966;143:526–536.
3. Patrick L. Infrared Absorption in SiC Polytypes. *Phys Rev.* 1968;167(3):809–813.
4. Feldman DW, Parker JH Jr, Choyke WJ, Patrick L. *Phys Rev.* 1968;170:698–704.
5. Feldman DW, Parker JH Jr, Choyke WJ, Patrick L. Phonon dispersion curves by Raman scattering in SiC, polytypes 3C, 4H, 6H, 15R, and 21R. *Phys Rev.* 1968;173(3):787.
6. Merlin R, Pinczuk A, Weber WH. Overview of phonon Raman scattering in solids. In: Weber WH, Merlin R, editors. *Raman scattering in materials science*. New York: Springer; 2000; p. 1–29.
7. Ferrari AC, Robertson J. Interpretation of Raman spectra of disordered and amorphous C. *Phys Rev B.* 2000;61:14095.

Task 10: Defining Microstructural Tolerance Limits of Defects for Silicon Carbide Armor

Core Faculty: Richard A Haber, Rutgers University

Graduate Student: Douglas M Slusark

10.1 Long-Range Goal

This project aims to define the upper limit of acceptable defects (i.e., porosity and inclusions) in commercial microstructures of silicon carbide (SiC) used in armor applications. The key goal within this program is to develop an understanding of the factors critical to the design, fabrication, and testing of micro-/macro-tailored ceramics with enhanced multihit dynamic performance. This understanding will establish a good/bad acceptance criterion for the selection of armor materials.

10.2 Introduction

A study was undertaken to determine if a correlation exists between nondestructive evaluation (NDE) by ultrasound and mechanical properties and microstructure in commercially available SiC armor plates. The aim of the work is to determine the contribution of porosity, inclusions such as B_4C and C, and grain size to the resulting ultrasound NDE map. This study was performed to build upon the work done at Rutgers by MV Demirbas and RA Brennan. Demirbas used a number of techniques for quantifying a microstructure and the spatial analysis of defects. These techniques included nearest-neighbor distance distributions, tessellation analysis, average pore size, and pore size distributions. It was found that these methods did provide indications as to whether a microstructure was clustered or random.¹⁻³ In collaboration with RA Brennan, a sintered SiC tile was examined by ultrasound scanning to determine if a link existed between C-scan image maps and microstructural quantification methods. A distinction was made between “high” and “low” amplitude regions in the NDE image maps. Serial sectioning of the tile was performed to determine if a difference in microstructure existed between the 2 regions. Statistical analysis showed that the difference in size of the largest defect between the high and low regions was significant, while it was also found that clustering of defects did occur in certain low-amplitude regions.⁴

10.3 Initiation of Study/NDE/Tile Selection

Forty-one pressureless sintered SiC tiles were received from Saint-Gobain in July 2008. All tiles were approximately $101.5 \times 101.5 \times 14$ mm. Archimedes density measurements were carried out on all 41 tiles, resulting in an average value of 3.17 g/cm^3 .

NDE of the tiles was carried out by ultrasound C-scan using an Olympus 20-MHz planar unfocused transducer in pulser/receiver configuration. Scanning parameters included a 0.1-mm lateral step size, resulting in NDE maps containing over one million data points. The transducer used has a frequency range of 16–32 MHz, as shown in Fig. 10.1. The bandwidth of the transducer was determined at the wavelengths where the emission had decreased to one-quarter of the amplitude at the central frequency.⁵ At each scanning position, an oscilloscope trace of amplitude versus time, or A-scan, is recorded. A representative A-scan, shown in Fig. 10.2, contains characteristic peaks that correspond to reflections of ultrasound energy from the top and bottom surfaces of the tile. From the position of the surface reflection peaks, it is possible to determine the longitudinal wave and shear wave times of flight ($\text{TOF}_{\text{Longitudinal}}$ and $\text{TOF}_{\text{Shear}}$), as well as the thickness of the sample (x). Knowing these, the longitudinal (c_L) and shear velocity (c_S) can be calculated, and from these, Poisson's ratio (ν) and the elastic modulus (E).^{6,7}

$$C_{L,S} = \frac{2x}{\text{TOF}_{\text{Longitudinal, Shear}}} . \quad (1,2)$$

$$\nu = \frac{1 - 2(C_S/C_L)^2}{2 - 2(C_S/C_L)^2} . \quad (3)$$

$$E_{C,L}^2 \rho = \frac{(1 - 2\nu)(1 + \nu)}{(1 - \nu)} . \quad (4)$$

$$\alpha = \frac{8.686}{2x} \ln(A_2/A_1)^2 . \quad (5)$$

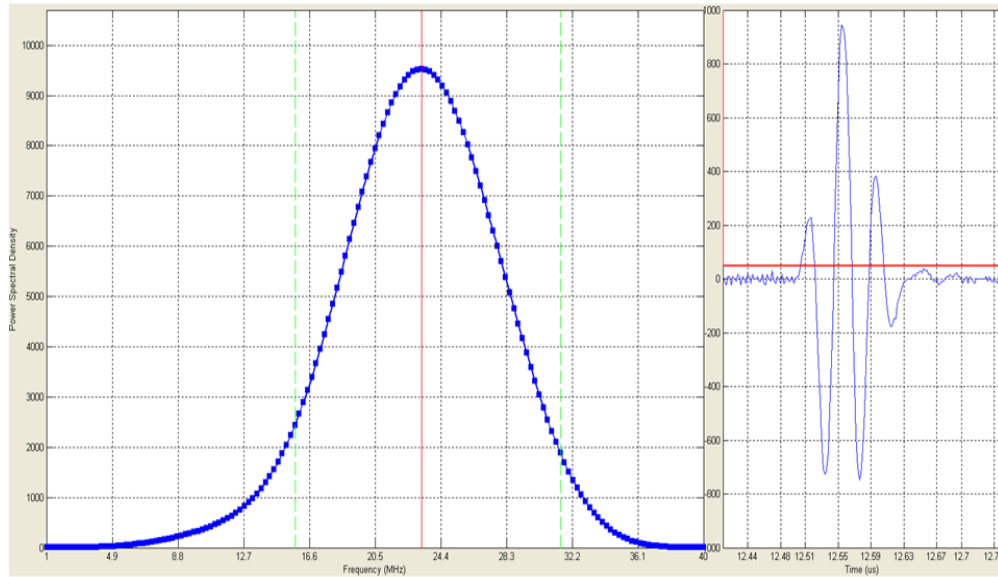


Fig. 10.1 Acoustic spectrum of Olympus ultrasound transducer⁵

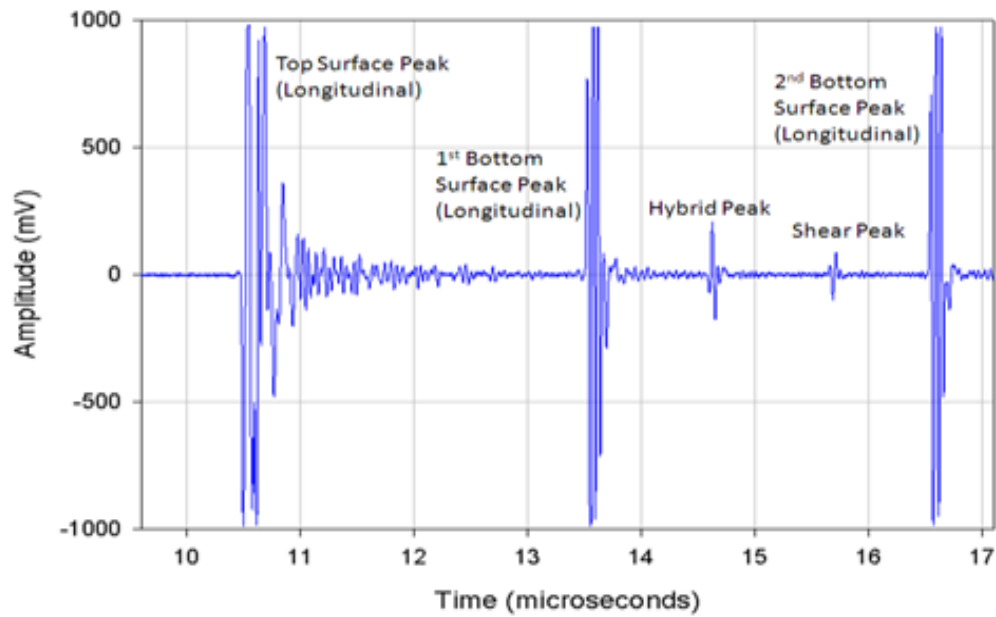


Fig. 10.2 Representative ultrasound trace⁵

Where this work differed from previous NDE studies done at Rutgers was in the use of the acoustic attenuation coefficient (α). In the work of Demirbas and Brennan, areas of the tile were chosen for serial sectioning and microstructural analysis based upon the amplitude of the first bottom surface reflection peak.⁴ In contrast, the acoustic attenuation coefficient is calculated by using a modification of the Beer-Lambert law.⁸ This involves taking a ratio of the amplitude of the first and second bottom surface reflection peaks. It was found that this method was less susceptible to surface finish irregularities than previously employed methods.⁹

Following the scanning process, the data was compiled into ultrasound NDE maps. At the time that this study was taking place, these ultrasound methods represented the state of the art. Based upon these results, 6 group headings were devised with the tiles divided into the 6 groups. Groups 1–4 were compiled based upon the quantitative results of the NDE scans. Groups 5 and 6 were chosen based upon differences seen in the NDE maps. These group headings were the following:

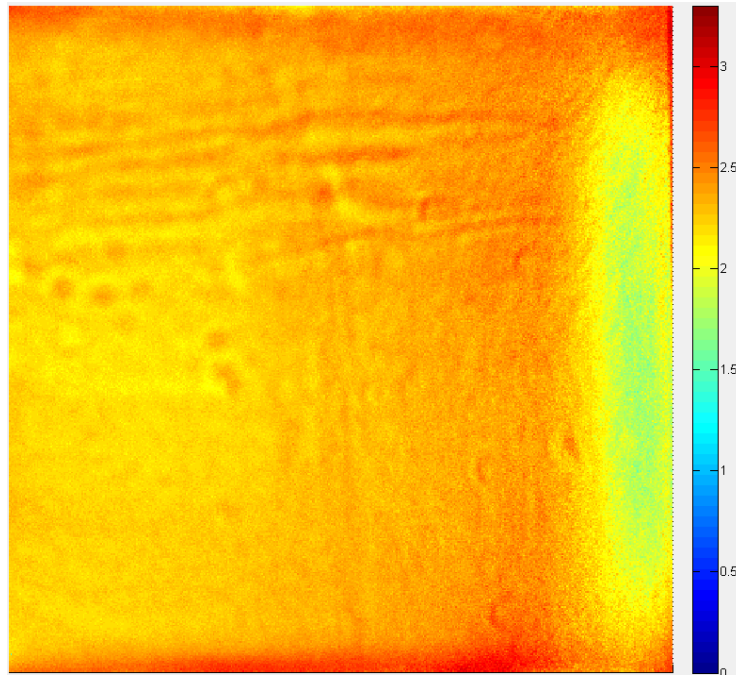
1. High Mean Attenuation Coefficient
2. High Mean Longitudinal Velocity/Young's Modulus
3. High Mean Shear Velocity/Shear Modulus
4. Low Mean Attenuation Coefficient, Low Mean Longitudinal Velocity/Young's Modulus, Low Mean Shear Velocity/Shear Modulus
5. High Zone Variations
6. Low Zone Variations

As the tiles within each group showed differences in acoustic properties, it was hoped that they would show a corresponding difference in mechanical properties.

One tile from each group was designated for machining into ASTM B-type modulus of rupture (MOR) bars.¹⁰ In some instances a tile may have had the highest average value in more than one category. When this occurred, a tile with a slightly lower value was selected for machining. The tile from each group chosen for machining were Group 1, tile 8; Group 2, tile 11; Group 3, tile 4; Group 4, tile 31; Group 5, tile 2; and Group 6, tile 19.

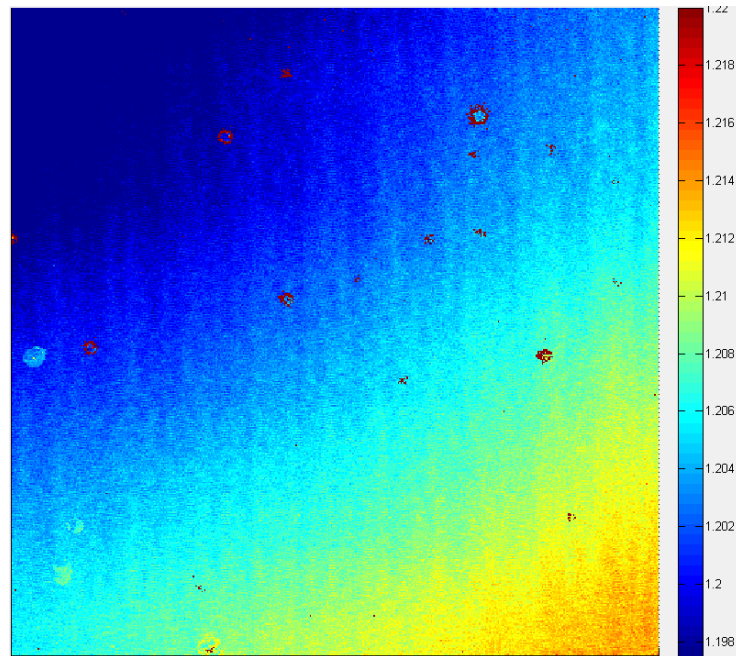
The NDE maps for these 6 tiles can be found in Figs. 10.3–10.8. As detailed in Table 10.1, the NDE maps for Groups 1, 4, 5, and 6 are attenuation coefficient maps while the maps for Groups 2 and 3 are longitudinal velocity and shear modulus maps, respectively. The scale has been tailored for each individual map. This has been done to account for the spread in values in each map along with highlighting

map features such as regions of variation and the presence of any acoustic anomalies. Included in this table is the scale used in each map, the average value, and the standard deviation.



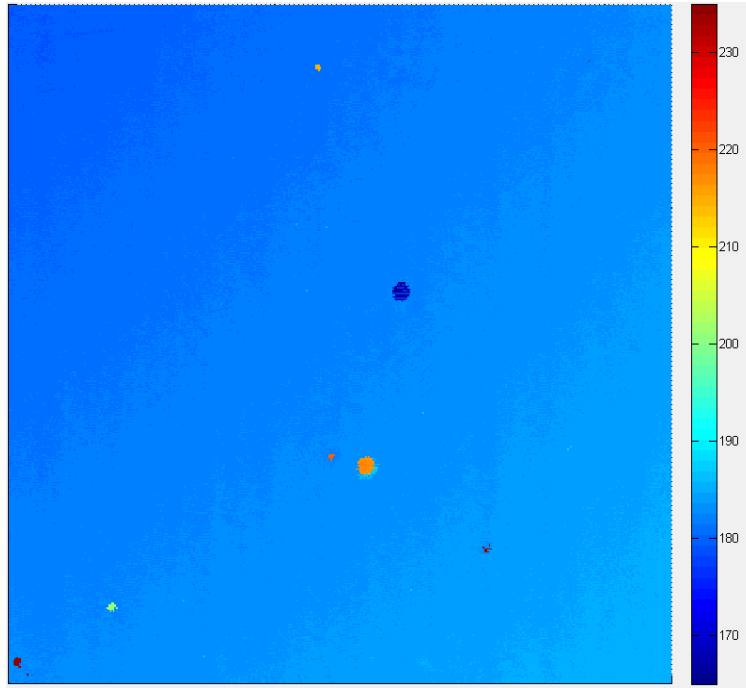
20MHz Attenuation Coefficient NDE Map

Fig. 10.3 Group 1, tile 8; high mean attenuation coefficient



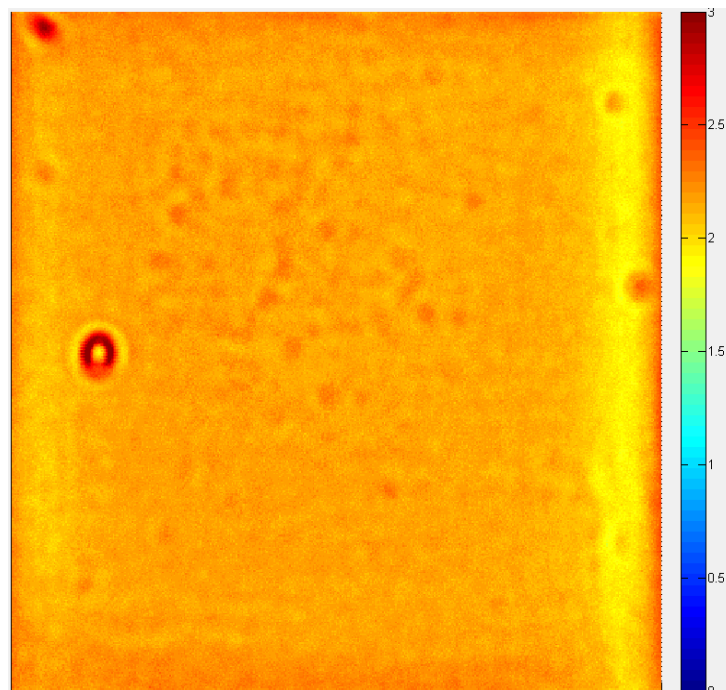
Longitudinal Velocity NDE Map

Fig. 10.4 Group 2, tile 11; high mean longitudinal velocity



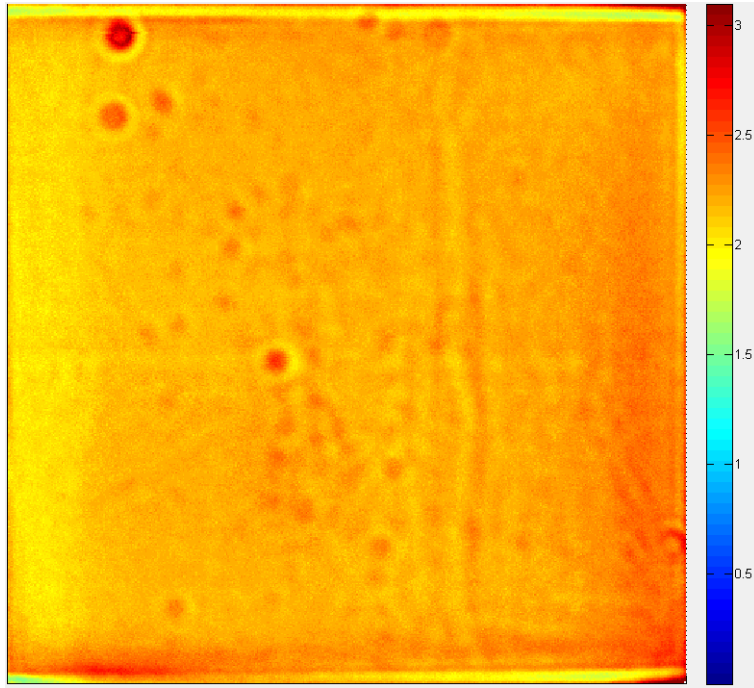
Shear Modulus NDE Map

Fig. 10.5 Group 3, tile 4; high mean shear modulus



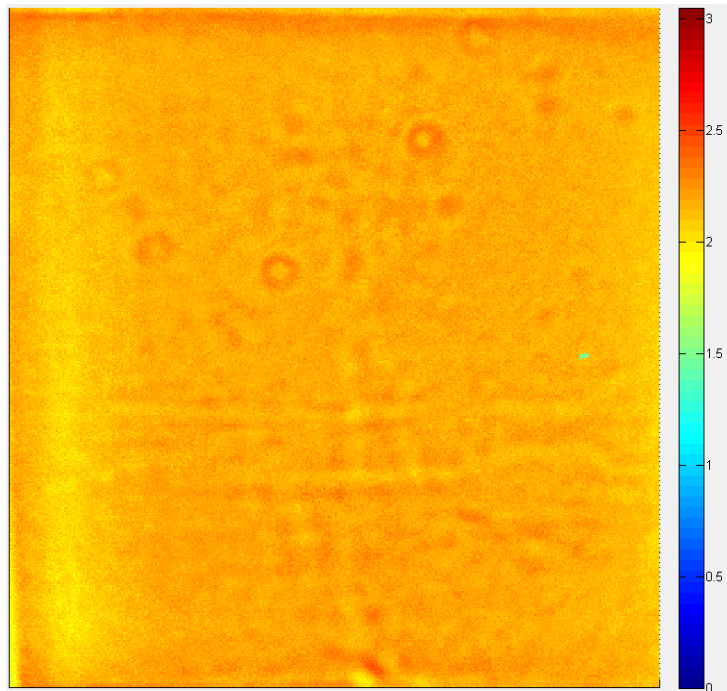
20MHz Attenuation Coefficient NDE Map

Fig. 10.6 Group 4, tile 31; low mean attenuation coefficient



20MHz Attenuation Coefficient NDE Map

Fig. 10.7 Group 5, tile 2; high zone variations



20MHz Attenuation Coefficient NDE Map

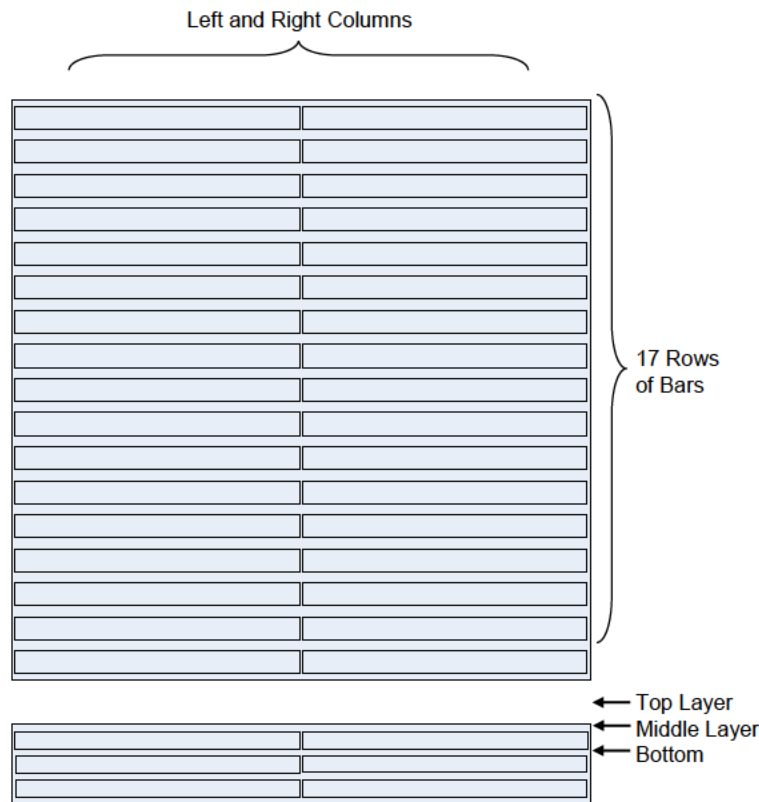
Fig. 10.8 Group 6, tile 19; low zone variations

Table 10.1 Group breakdown/NDE map type and values

Tile No.	Type of Map	Unit	Scale (max)	Scale (min)	Average Value	Std. Dev.
8	Att coeff	dB/cm	3.25	0	2.31	0.09
11	Speed of sound	m/s	12,200	11,975	12,044	113
4	Shear modulus	GPa	235	165	182	3
31	Att coeff	dB/cm	3.00	0	2.15	0.05
2	Att coeff	dB/cm	3.10	0	2.21	0.07
19	Att coeff	dB/cm	3.05	0	2.17	0.05

10.4 Bend Bar Machining

The selected tiles were machined into B-type bend bars ($50 \times 4 \times 3$ mm).¹⁰ As shown in Fig. 10.9, tile 11, the first tile processed, was machined into 102 bend bars. There were 17 rows of bars, a left and a right column, and a top, middle, and bottom layer of bars. The remaining 5 tiles (8, 4, 31, 2, and 19) were machined into 108 bend bars. The machinist was able to reduce the distance between slices, resulting in an extra row of bars. The additional row of bars had the effect of improving the resolution of the modulus of rupture (MOR) analysis and microstructural evaluation. Overall, the machining operation of the 6 tiles resulted in 630 bend bars, as 12 bars were lost to machining difficulties.

**Fig. 10.9 Bend bar machining diagram; tile 11, 17 rows of bars**

One of the key aspects of the machining process was to keep track of the position, identity, and orientation of the bend bars in relation to the original tile to allow for the correlation of the properties of the bend bars to features within the NDE maps.

10.5 MOR/Weibull Analysis

After machining, 4-pt flexure testing was carried out to determine the modulus of rupture of each bar. This testing was done on an Instron 4500/4505 testing system, using a semi-articulating test fixture with a crosshead speed of 0.5 mm/min. A further 6 bars were destroyed without result during flexure testing. The MOR results for the remaining 624 bars can be found in Tables 10.2–10.7, which contain the minimum, maximum, average strength, and standard deviation for each layer of bars from each tile. The ranking of the tiles by average strength, from strongest to weakest, is tile 2, tile 4, tile 19, tile 11, tile 8, and tile 31.

Weibull statistics were used to analyze the MOR results to examine the distribution of strength within each tile and throughout the total data set. Figures 10.10–10.15 contain Weibull diagrams for each group of bend bars. For many of the tiles, it was originally found that a bimodal Weibull distribution better represented the strength data. This was reflective of the high degree of spread within the data, despite the fact that the original 6 tiles were fully dense production tiles of the same material. A significant amount of fractography work went into determining the causes of the bimodal distributions, with both a stereo optical and field emission scanning electron microscopy (FESEM). It was eventually found that errant, deep machining scratches on the tensile and side surfaces of particular bend bars led to the bimodal distributions.

Table 10.2 Tile 8 MOR/Weibull moduli

MOR Summary	Max.	Min.	Avg.	Std. Dev.	M
Top layer	569	357	480	50	11.5
Middle layer	565	255	458	59	8.0
Bottom layer	555	246	466	64	7.6
Entire tile	569	246	468	58	8.7

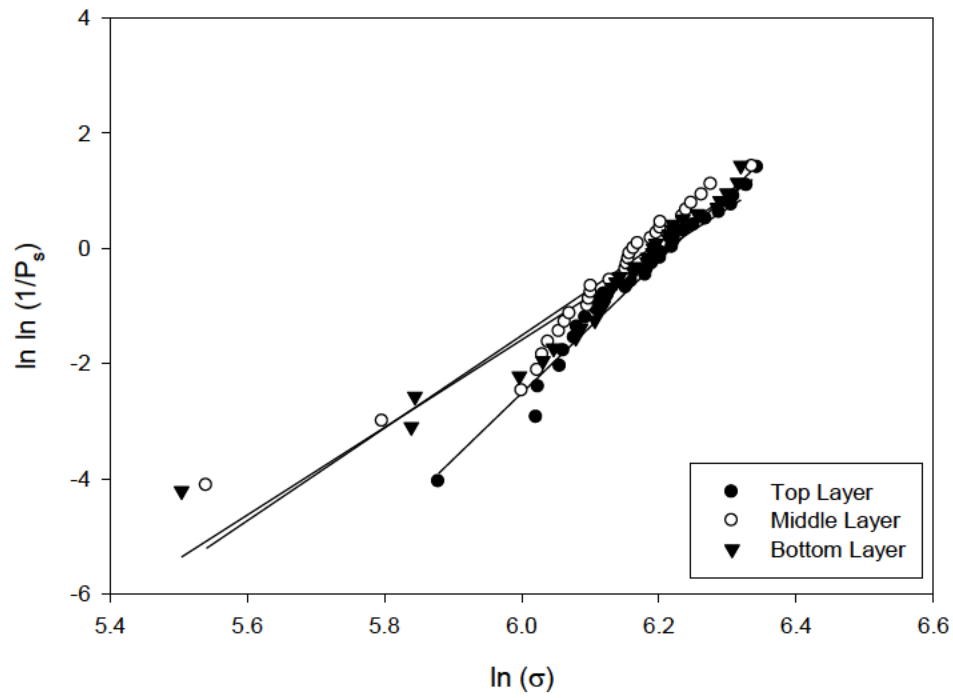


Fig. 10.10 Weibull analysis; Group 1, tile 8

Table 10.3 Tile 11, MOR/Weibull moduli

MOR Summary	Max.	Min.	Avg.	Std. Dev.	M
Top layer	564	275	471	67	7.8
Middle layer	600	246	466	92	5.2
Bottom layer	565	279	475	64	8.2
Entire tile	600	246	470	75	6.9

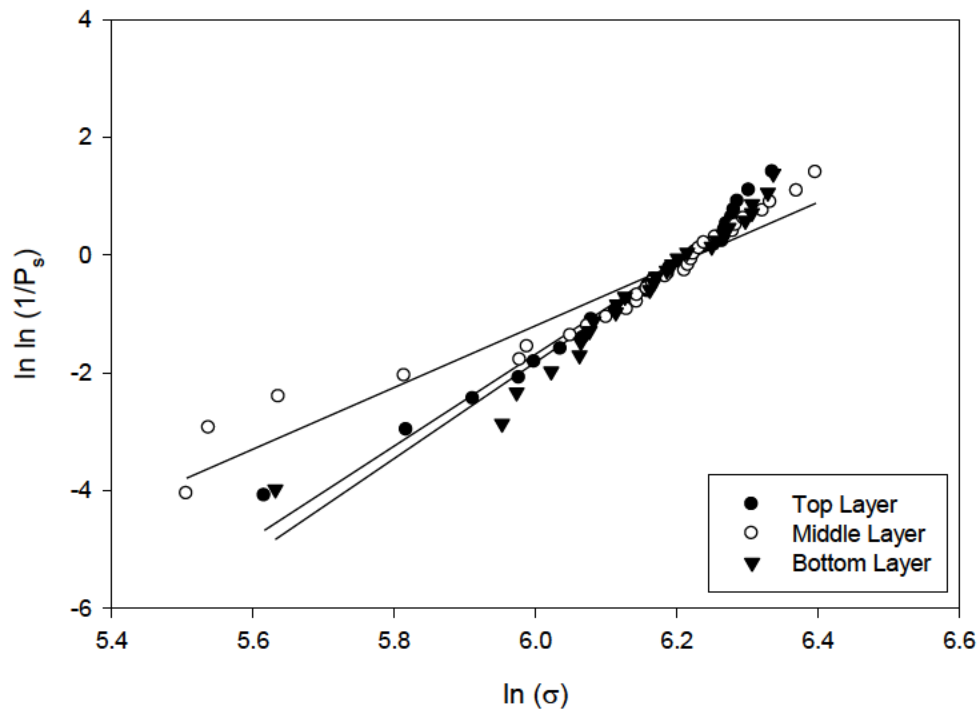


Fig. 10.11 Weibull analysis; Group 2, tile 11

Table 10.4 Tile 4, MOR/Weibull moduli

MOR Summary	Max.	Min.	Avg.	Std. Dev.	M
Top layer	595	287	486	68	7.8
Middle layer	583	351	489	56	10.4
Bottom layer	592	333	484	68	8.2
Entire tile	595	287	488	61	10.3

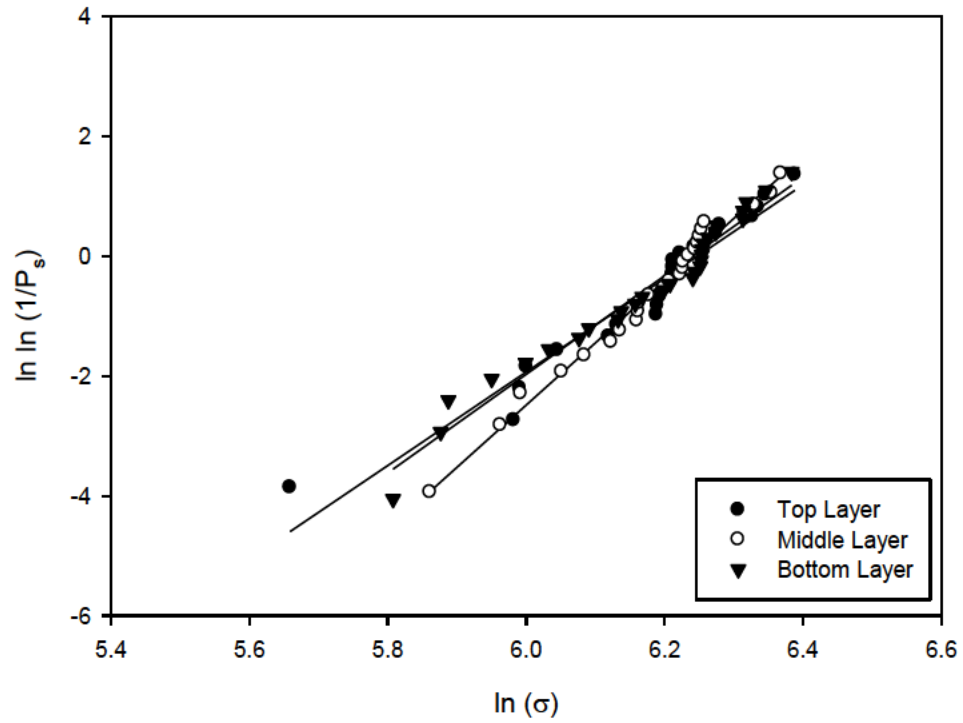


Fig. 10.12 Weibull Analysis; Group 3, tile 4

Table 10.5 Tile 31, MOR/Weibull moduli

MOR Summary	Max.	Min.	Avg.	Std. Dev.	M
Top layer	537	367	452	47	11.5
Middle layer	576	370	454	56	9.7
Bottom layer	522	314	435	60	8.6
Entire tile	576	314	447	55	9.9

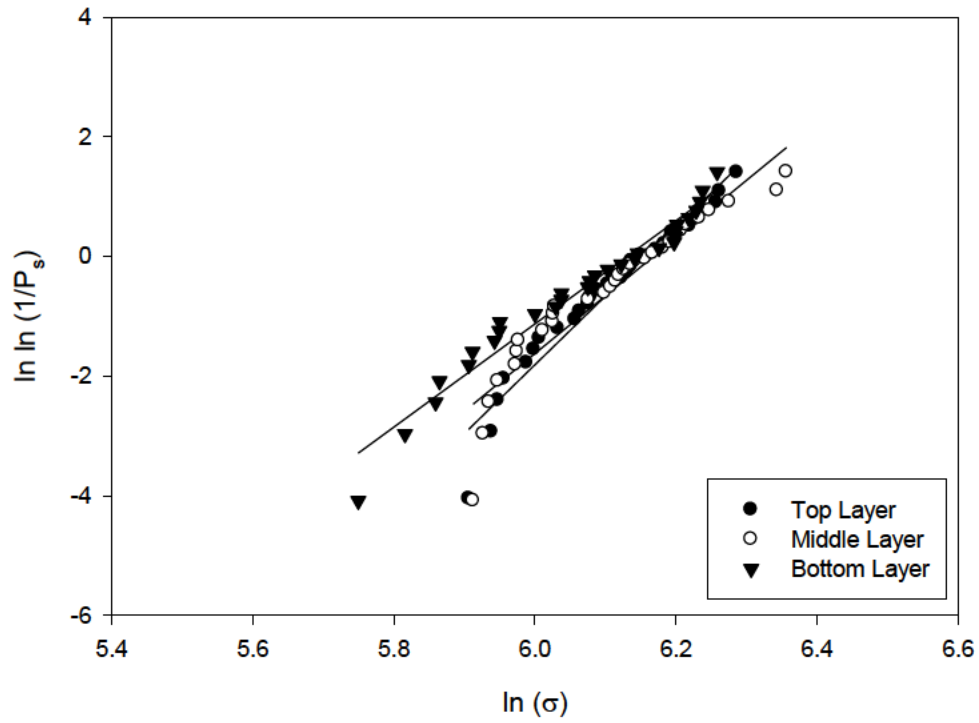


Fig. 10.13 Weibull plot; Group 4, tile 31

Table 10.6 Tile 2, MOR/Weibull moduli

MOR Summary	Max.	Min.	Av.g	Std. Dev.	M
Top layer	561	389	483	49	11.7
Middle layer	561	408	497	33	18.5
Bottom layer	595	431	504	45	13.5
Entire tile	595	389	494	43	14.0

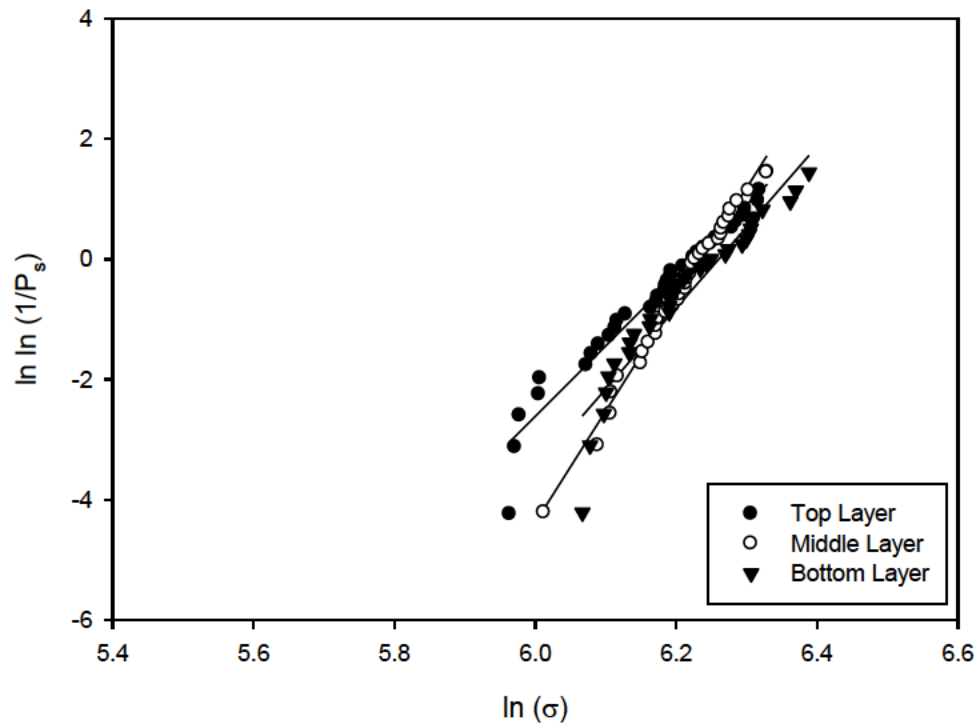


Fig. 10.14 Weibull plot; Group 5, tile 2

Table 10.7 Tile 19, MOR/Weibull moduli

MOR Summary	Max.	Min.	Avg.	Std. Dev.	M
Top layer	581	369	490	56	10.4
Middle layer	555	284	470	55	9.3
Bottom layer	537	325	467	53	10.5
Entire tile	581	284	475	55	10.3

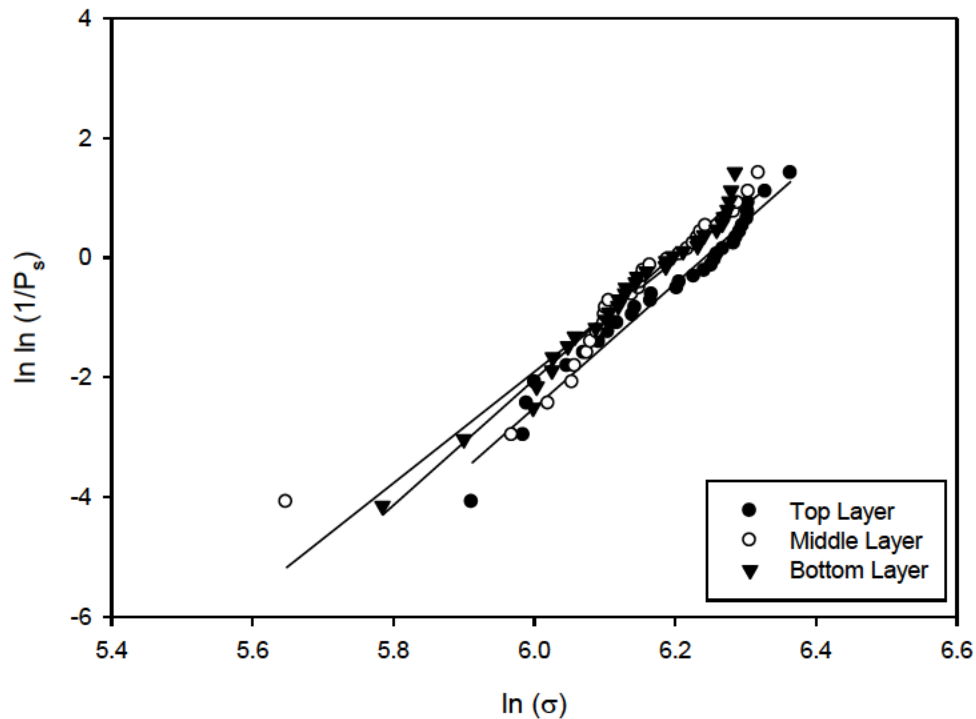
**Fig. 10.15 Weibull plot; Group 6, tile 19**

Figure 10.16, a FESEM image of the tensile surface of a very-low-strength broken bend bar, contains a very evident example of this type of damage. There are a number of scratches that can be seen in the image, 2 of which have been indicated by long black arrows. Although these scratches can be challenging to discern in the FESEM, they become much more evident when viewed with an optical microscope. The scratch believed to have been the initiation point of fracture makes an angle of approximately 75° with the long axis of the bend bar. In the area the crack initiated, it followed the machining scratch for a period of time. This is denoted by the 2 short horizontal arrows in the image. As the applied stress field changed during fracture, the fracture initiating crack changed direction and grew perpendicularly to the long axis of the bend bar.

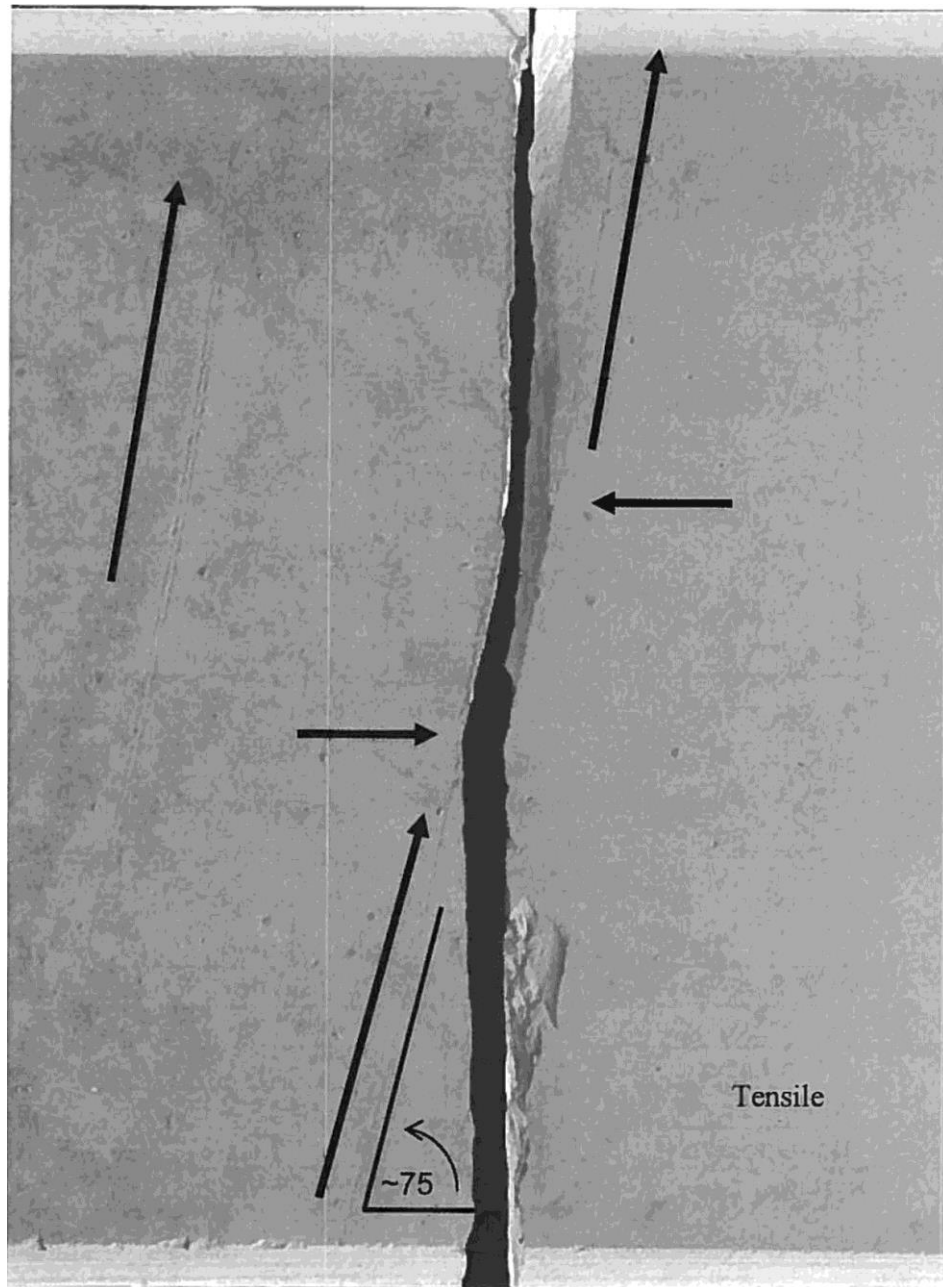


Fig. 10.16 Errant machining scratch; tensile surface of low-strength bend bar (A)

Confirmation that this was the fracture initiation location can be found in Fig. 10.17, which contains a FESEM image of the 2 sides of the primary fracture location for the bend bar discussed in the previous paragraph. A broad fracture plane, shown by the dashed line, can be found on both end faces, which is indicative of low fracture strength.¹¹ As indicated by the arrows, texture on the surface indicates that fracture began at the tensile surface near the center of the bar. This is in agreement with the approximate location determined from the previous image.

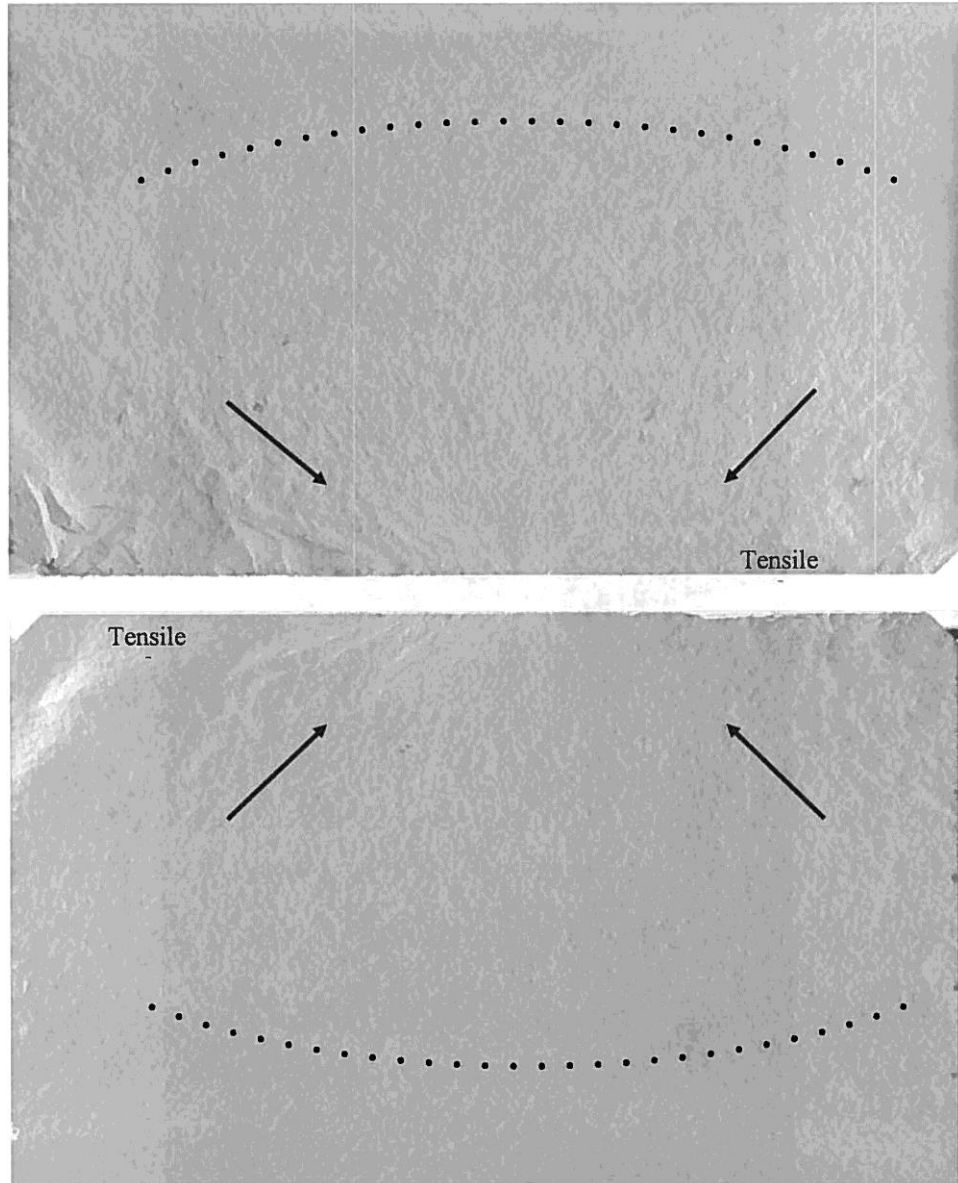


Fig. 10.17 Fracture surface; left and right faces, low-strength bend bar (A)

A second type of errant machining scratch can be found in Fig. 10.18, which is a FESEM image of the side of another low-strength broken bend bar. In this case, the side of the bend bar was scratched at a perpendicular or high angle to the long axis of the bend bar along the whole side of the bar. In this example, 2 evident scratches can be seen. A 30-mm-wide scratch runs down the side of the bend bar. The fracture path follows the scratch for the first 0.5 mm of travel and then branches off. Even if this scratch was not present, there is also a 15-mm-wide scratch that most likely would have caused fracture. This damage had to be induced before the chamfering operation for the scratch to reach the tensile surface.

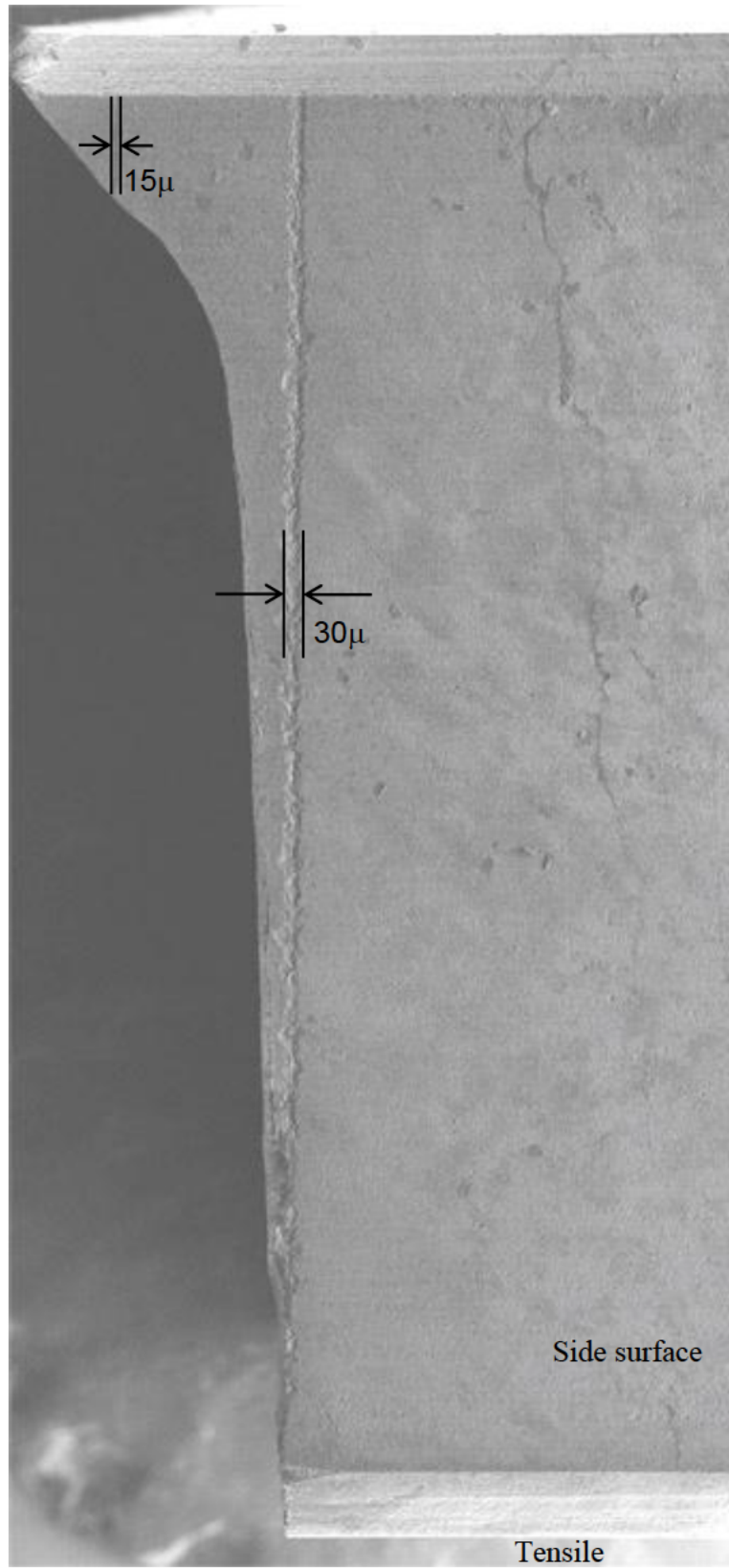


Fig. 10.18 Errant machining scratch; tensile surface of low-strength bend bar (B)

FESEM images of the left and right faces of the fracture surface of this bend bar can be found in Fig. 10.19. When the fracture surfaces for this bar were first examined, the fracture behavior was initially puzzling, as the bars appeared to have fractured from the side. It is now known that this bar did in fact break from the lower corner, as shown in the previous image. As this was a low-strength bar, the fracture surface is characterized by a broad, flat fracture plane, as indicated by the dashed line.

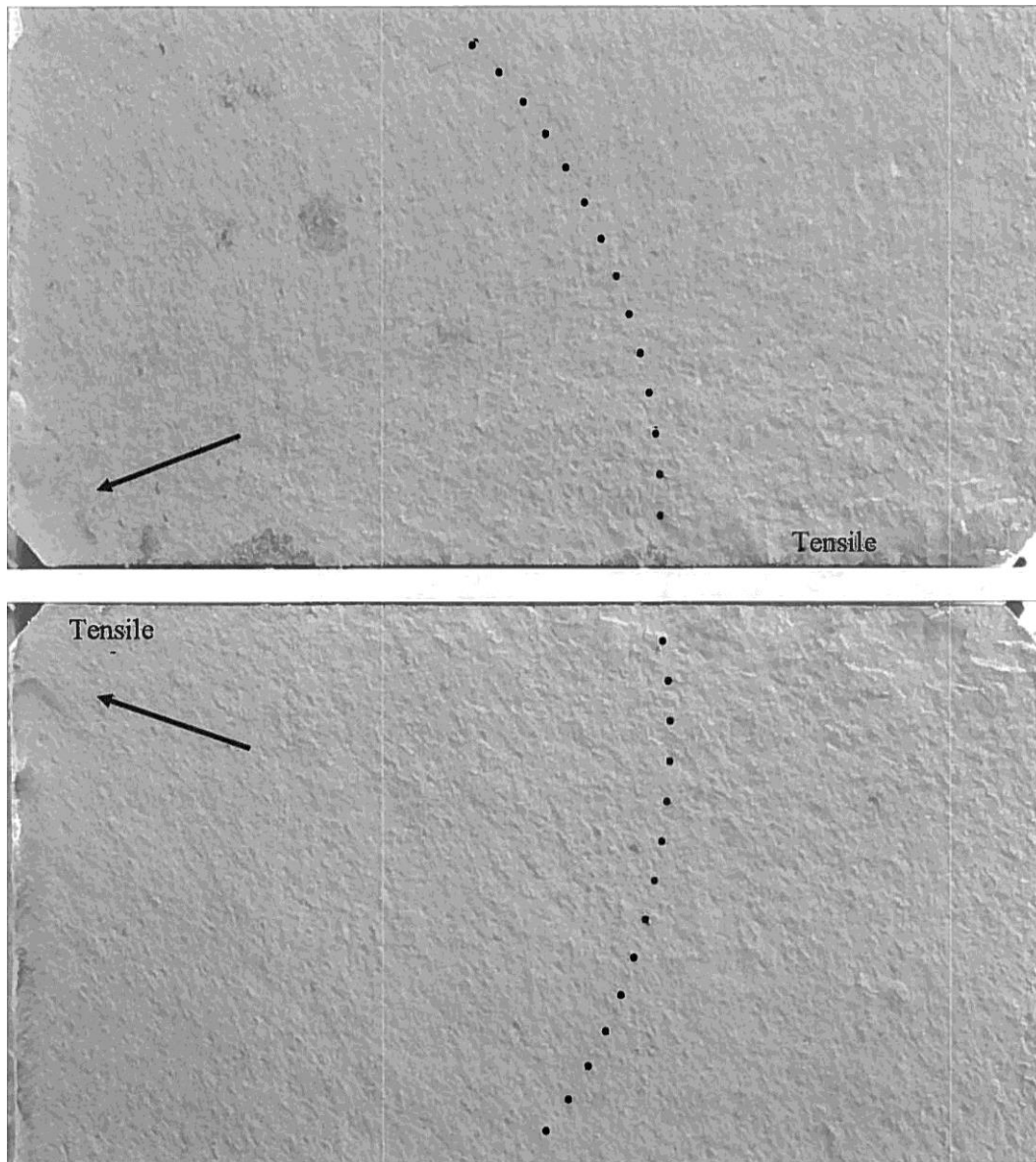


Fig. 10.19 Fracture surface; left and right faces, low-strength bend bar (B)

As expected, this damage had a deleterious effect on the strength values for the different sets of bars, especially considering that the damage occurred on the tensile or lower side surface of the bars. Seventy-seven bars were found to have fractured

from either errant tensile or side surface scratches. Table 10.8 contains a breakdown of each type for the 6 groups of bend bars. For some tile groups, the number was close to 20% of the bars. In addition, 3 bend bars were found to have a “step” machined into the side of the bar, as shown in Fig. 10.20. This resulted in a nonuniform stress distribution through the bar during the test, so these results have also been removed from the bend strength statistics.

Table 10.8 Breakdown of bend bars

Damage Type	Tile 8	Tile 11	Tile 4	Tile 31	Tile 2	Tile 19
Side (no. of bars)	5	9	19	6	1	10
Tensile (no. of bars)	7	3	1	10	4	2

Almost 13% of the bars in the study had one of these types of damage. Removing the MOR values for these values had an effect on the Weibull statistics. The Weibull moduli increased for all tile groups, and any bimodal Weibull distributions were replaced with unimodal distributions. The errant machining scratches documented in this section are considered an anomaly, as they are not representative of machining damage that one would expect to find in a longitudinally ground ASTM bend bar.

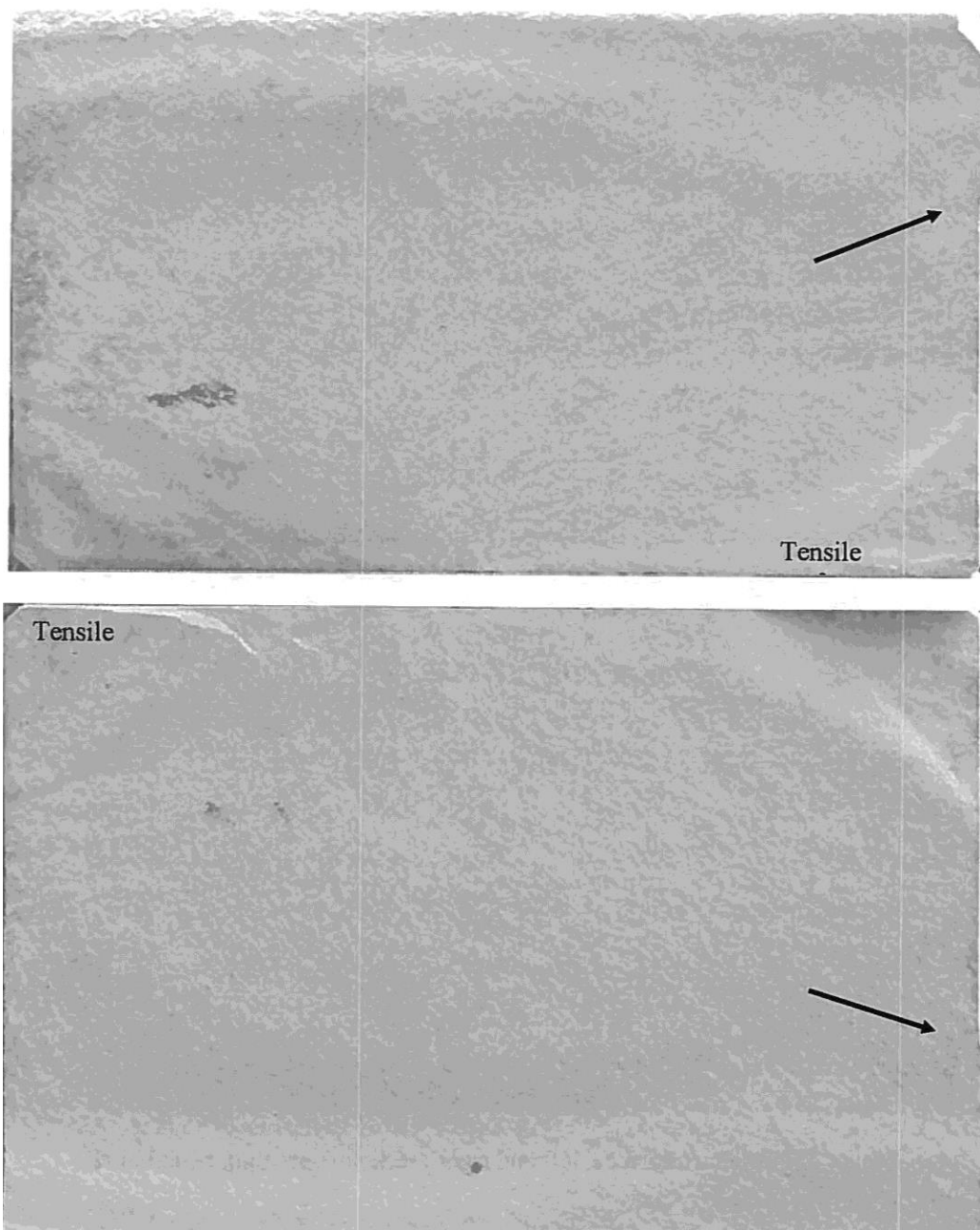


Fig. 10.20 Fracture surface; left and right faces, low-strength bend bar (C)

10.6 Primary Fracture Location/NDE Map Overlay Diagrams

As part of the strength testing analysis, the primary fracture position was determined for each bend bar. This is considered to be the fracture position that contains the fracture initiating feature. In this exercise, each piece of a broken bar must be examined. As a general rule, for a low-strength bar, the primary fracture position is the only fracture position. However, a proportionate amount of energy is built up in a bar as the applied stress increases before fracture. When fracture does occur, the shockwave caused by the sudden release of energy can result in the occurrence of secondary fractures, which may break the bar into many pieces.

If there are multiple fracture locations, it is necessary to determine at which location fracture began. ASTM Standard C1161 contains examples of fracture behaviors in a 4-point bend test that can aid in this determination.¹⁰ Fracture behavior may differ whether it was a high-, medium-, or low-energy fracture. The presence of cantilever curls and the relation between the fracture position and the location of the loading pins can also offer clues when determining the primary fracture position. Fracture may also occur outside of the loading pins. This may be the result of misalignment of the test setup, in which case the MOR value must be removed from the Weibull statistics, or due to the presence of a large flaw located outside of the primary loading zone of the test. When testing a B-type bend bar, this is a volume that is approximately 20.0 mm long, 4.0 mm wide, and 1.5 mm high that experiences the full applied stress just before the initiation of fracture. In the instance where there are multiple fracture locations or fracture occurred outside of the primary loading zone, the fracture surface must be examined by either optical or electron microscopy methods for clarification.

In this analysis, scale diagrams of the bend bar layout were constructed and overlaid on top of the NDE maps for each group to determine if a correlation exists between the presence of an acoustic anomaly in the NDE maps and fracture location. Also included in these diagrams are marks indicating the fracture position for each layer of bars. Positions from the top layer are shown in black, positions from the middle layer are shown in white, and positions from the bottom layer are shown in red. The primary loading zone of the bend test is also indicated in the diagrams by a black rectangle.

The assembled fracture overlay diagrams for the 6 tiles are found in Figs. 10.21–10.26. In these maps, red regions are “high”-value regions, while blue regions are scaled as “low”-value regions. When examining the fracture positions for each of the tiles, there does not appear to be a pattern in the primary fracture locations. In Fig. 10.21, there is a region of reduced attenuation coefficient toward the right side

of the map. This region did not appear to have an effect on fracture location, as it was located outside of the primary loading zone of the flexure test. In Fig. 10.22, the values of longitudinal velocity increase when moving from the upper-left region to the lower-right region of the map. The gradient in the values did not appear to have an influence on fracture position. In Fig. 10.23, it can be seen that although the NDE tests have resulted in a consistent shear modulus map, there appears to be no discernible pattern to the location of fracture. Figures 10.24–10.26 contain fracture location diagrams overlaid on top of attenuation coefficient NDE maps. Again, there does not appear to be a pattern to fracture locations or a correlation between fracture location and NDE map features. Overall, it is challenging to make a definitive statement about the correlation between the position of the primary fracture location and any features found in the NDE maps.

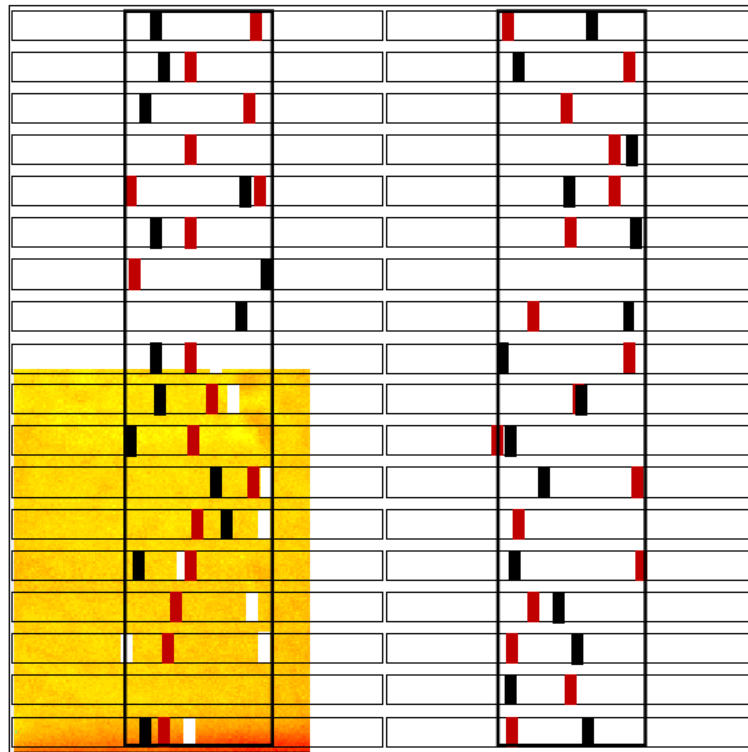


Fig. 10.21 Fracture location overlay, attenuation coefficient; Group 1, all layers

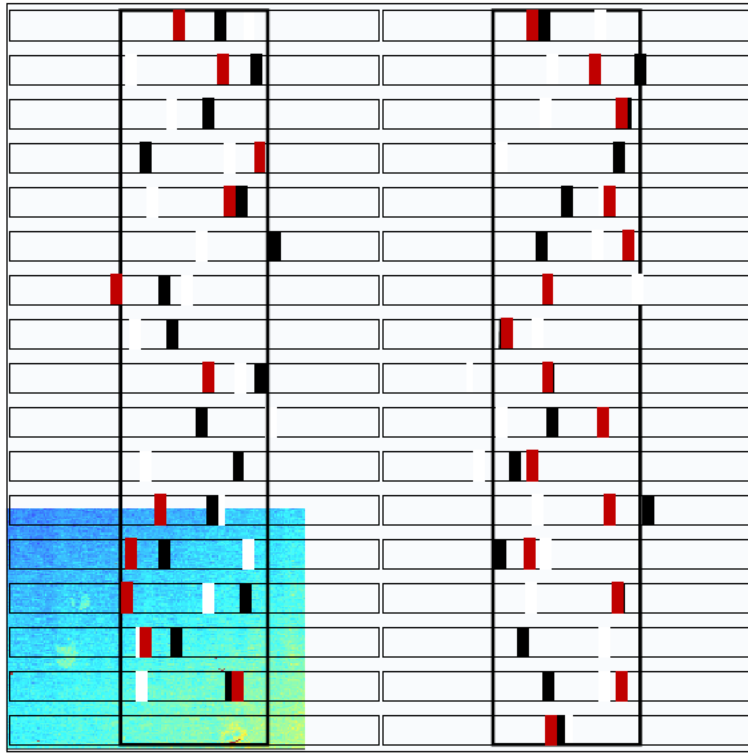


Fig. 10.22 Fracture location overlay, longitudinal velocity; Group 2, all layers

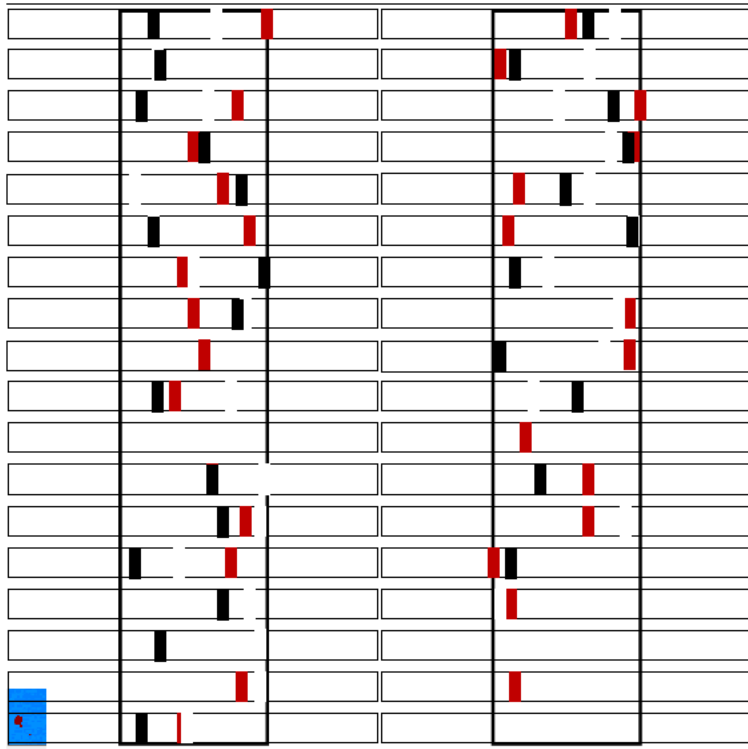


Fig. 10.23 Fracture location overlay, shear modulus; Group 3, all layers

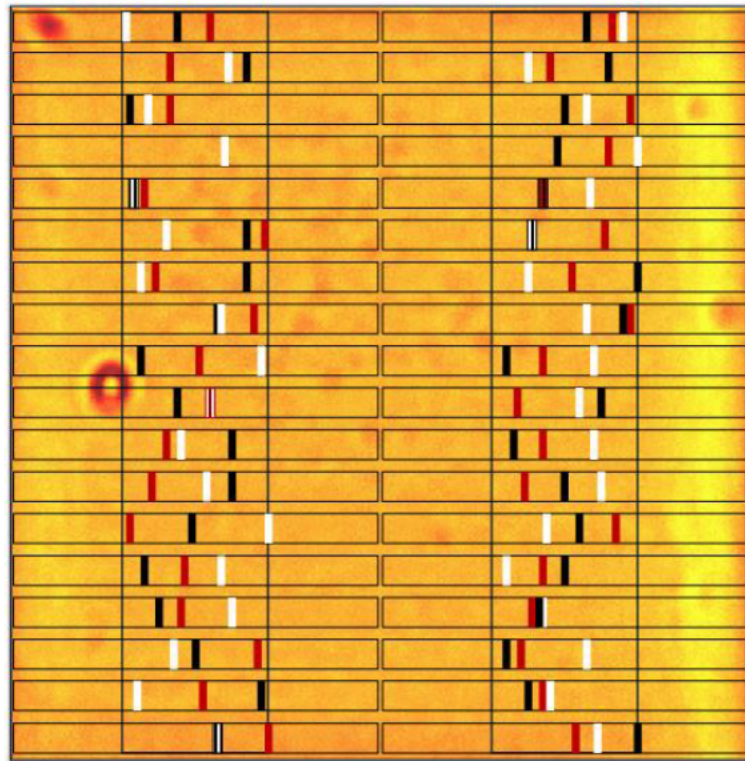


Fig. 10.24 Fracture location overlay, attenuation coefficient; Group 4, all layers

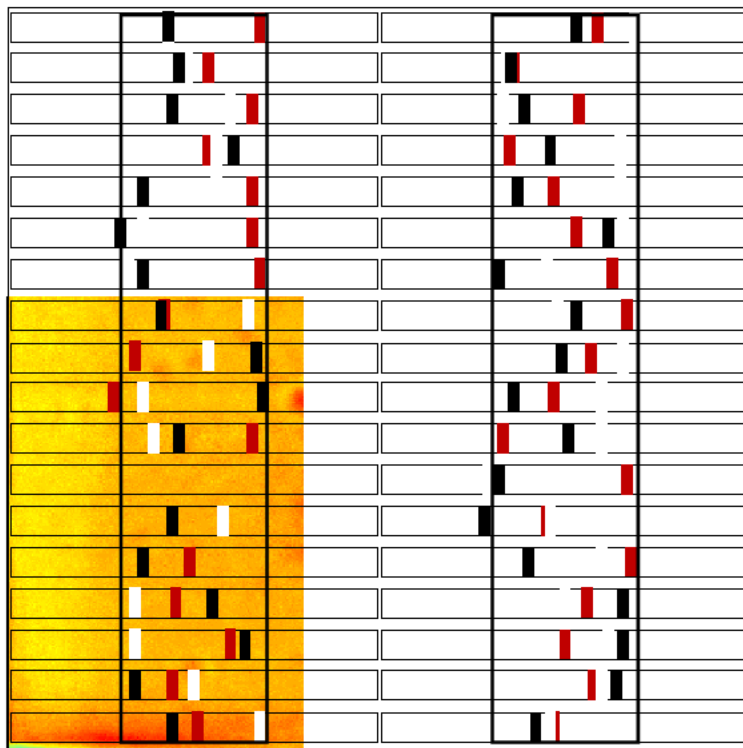


Fig. 10.25 Fracture location overlay, attenuation coefficient; Group 5, all layers

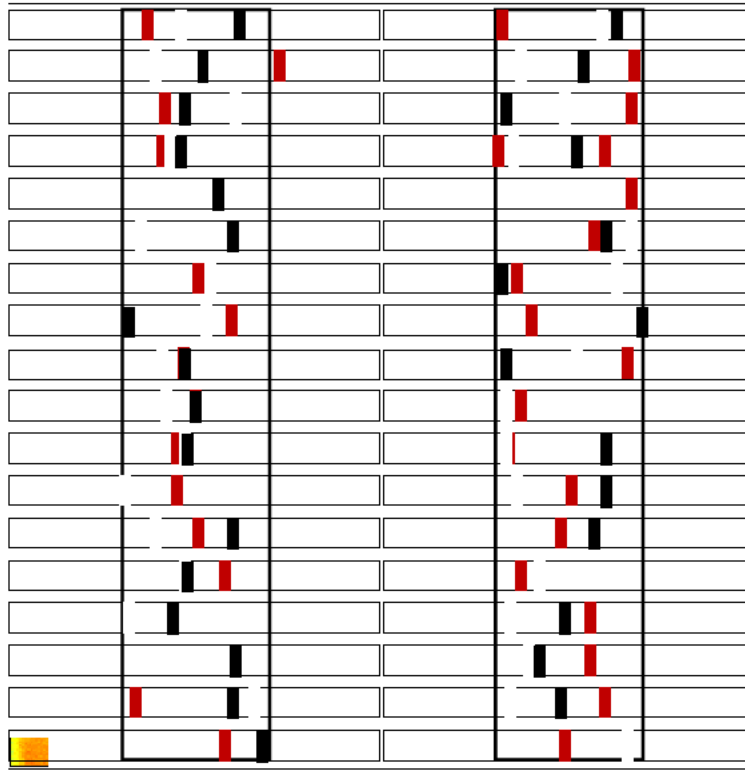


Fig. 10.26 Fracture location overlay, attenuation coefficient; Group 6, all layers

One aspect of this exercise to keep in mind is that while the NDE maps are 2-dimensional, the tiles being examined are 3-dimensional. The value recorded at each scanning point contains the contributions of all Z values associated with that particular set of X,Y coordinates. Also included in the summation are contributions due to surface roughness. This can make it challenging to determine what the origin of an acoustic anomaly may have been. The 4 attenuation coefficient maps each contain acoustic anomalies. These are considered to be ring-shaped regions of increased attenuation coefficient that produce a “halo-like” affect around a center region.

When the original ultrasound work was completed, it was not possible to determine whether an acoustic anomaly was the result of a pit in the surface of the tile or from a feature within the bulk of the tile. A work-around for this has been employed in subsequent ultrasound evaluation testing, where an additional detection gate is defined for the region in the A-scan between the top surface and first bottom surface reflection peaks. If a feature with a high enough acoustic impedance mismatch, such as a large pore, is encountered by the ultrasound beam, it will produce a strong

reflection. By determining the time of flight between the peak and the top or bottom surface reflections, it is possible to determine where in the depth of the sample the feature is located.

10.7 Fractography

Initial fractography work focused on the fracture surfaces of the bend bars, the intent being to locate the fracture-initiating feature. While this was done for many of the bars, work has progressed to also include features of interest on the fracture surfaces and within the microstructure of the material. In the next set of images, a series of low-strength bend bars will be discussed. The bars will be introduced in order of decreasing fracture strength.

Images that include the entire fracture surface of a bend bar are composite images consisting of 9–10 separate SEM micrographs that were recorded at 200× magnification in a raster pattern across the fracture surface. The images were then manually stitched together using image processing software. These composite images have proved to be very useful for analyzing overall fracture behavior by “mapping” the fracture surface for later analysis. Examples of these images can be found in Figs. 10.27–10.29. The tensile surface from the flexure tests has been indicated in the images as a frame of reference.

Tensile Edge

Tensile Edge



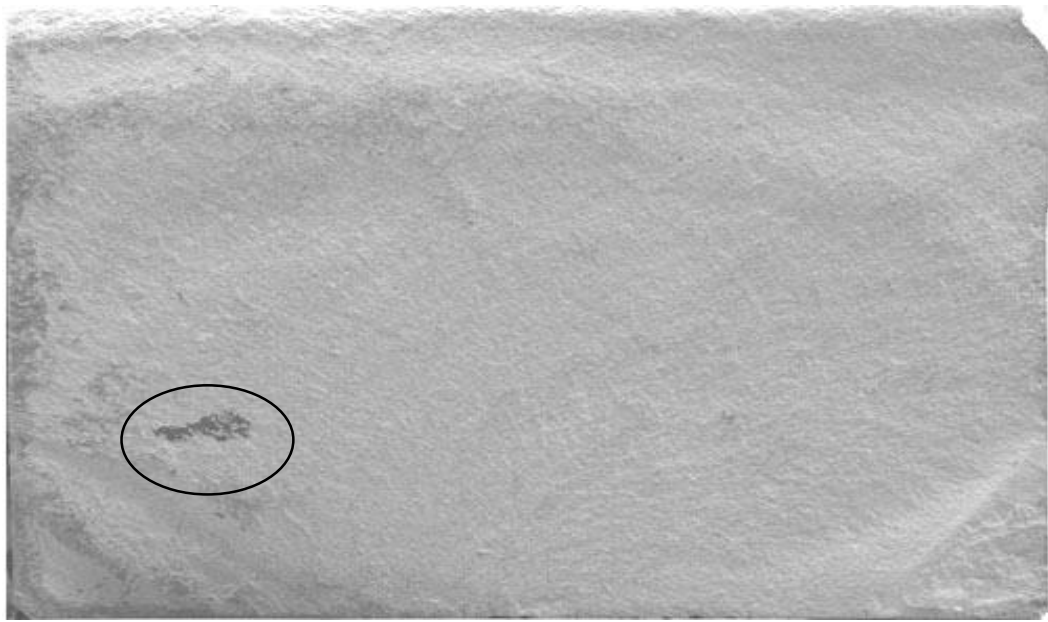
Fig. 10.27 Bar 1, fracture surface end faces, composite (200× magnification)

Tensile Edge

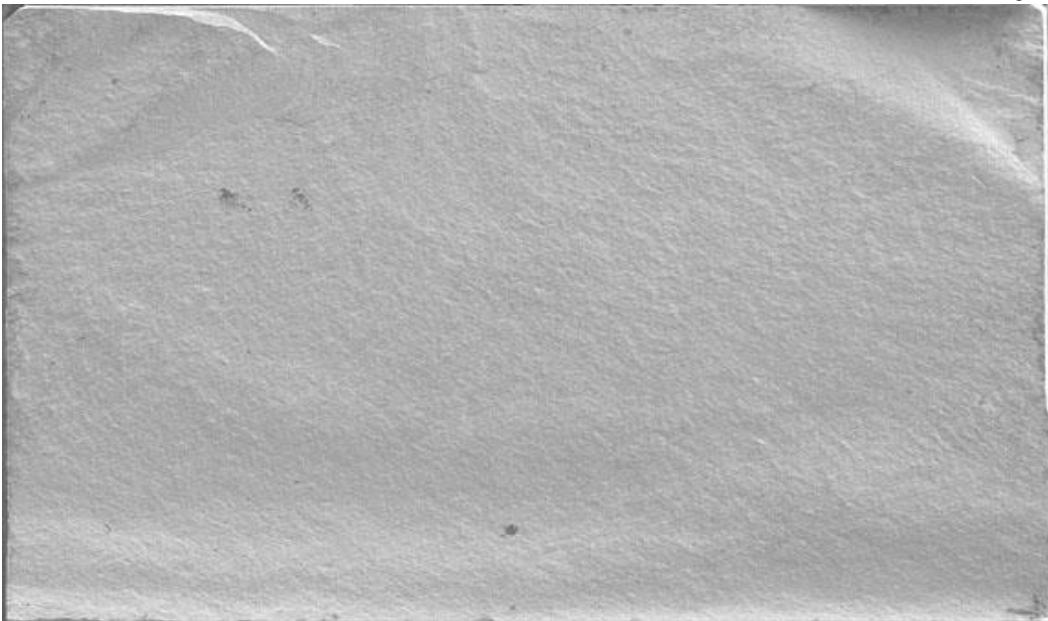
Tensile Edge



Fig. 10.28 Bar 2, fracture surface end faces, composite (200× magnification)



Tensile Edge



Tensile Edge

Fig. 10.29 Bar 3, fracture surface end faces, composite (200× magnification)

Figure 10.28 contains both the left and right end-faces of the primary fracture surface of bar 1, which was originally from the second row of the right hand column in the middle layer of tile 31. This bar broke at a fracture stress of 383 MPa, placing it within the lower 15th percentile of strength values for this particular set of bars. Evidence of the primary fracture path and fracture initiating can be seen on both sides of the primary fracture position. This is not always the case, as secondary

cracking during fracture can obliterate one or both of the sides of the primary fracture surface. It appears that fracture began near the center of the bar, close to the tensile surface.

The primary fracture surface of bar 2 can be seen in Fig. 10.28. Bar 2 broke at an applied stress of 378 MPa and was originally located in the 11th row of the right-hand column in the middle layer. Like bar 1, bar 2 was also originally part of tile 31. In contrast to the previous example, remnants of the fracture path and what is believed to be the fracture initiating feature appear on only one side of the fracture surface. Based on the texture of the fracture surface, it appears that fracture began in the lower-right corner of the cross section of the bar.

Images of the likely fracture-initiating features for these 2 bars can be found in Figs. 10.30 and 10.31. Arrows have been added to the images to indicate the likely path of fracture. In both cases, the fracture path appears to fan out from the feature in a relatively smooth pattern before altering direction as the stress field changed during fracture.



Fig. 10.30 Bar 1, fracture path (200× magnification)

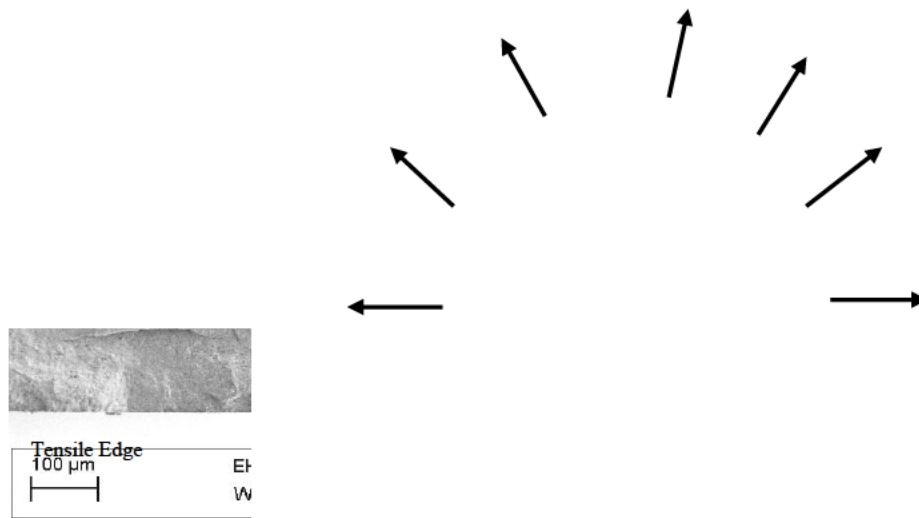
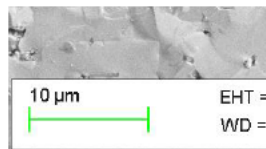
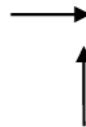
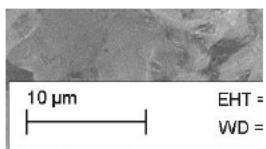
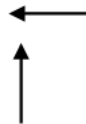


Fig. 10.31 Bar 2, fracture path (200× magnification)

These features of interest can be seen in higher magnification in the next group of figures. Figures 10.32a and 10.32b are images of what is believed to be the fractures-initiating feature of bar 1. Again, the results for this bar were quite interesting as remnants of the likely fracture-initiating feature appeared on both sides of the primary fracture surface. Dimpled and raised areas on a plate-like structure in the feature, as indicated by the arrows in the images, show a “mirror image” of themselves. This seems to indicate that this plate was split during fracture. Energy-dispersive X-ray spectroscopy (EDS) analysis was used to confirm that this feature was a B₄C inclusion. B₄C is added during the mixing process to act as a sintering aid.¹² Adding an excess of these materials or not ensuring proper mixing can result in unreacted material that forms agglomerates in the finished piece. These agglomerates can act as stress-concentrators because of the elastic property mismatch with the SiC matrix.¹³



a)



b)

Fig. 10.32 Bar 1, B₄C inclusion (3,750× magnification)

The major and minor axes of this inclusion were measured at 58.5 and 34.1 μm , respectively, while it was found that the minimum distance to the tensile surface was 235 μm . By taking these factors into account, along with the height of the bend bar, it is possible to estimate the stress applied to the feature in the instant before fracture initiated. This is done by taking a ratio of the stress at the tensile edge of the bar to the stress at the location of the feature. For this sample, this stress was estimated to be 323 MPa.

Figures 10.33 and 10.34 contain higher magnification micrographs of the likely fracture-initiating feature of bar 2. EDS was used to confirm that this feature was also a B_4C inclusion. The major and minor axes of the visible portion of the inclusion were measured at 65.7 and 29.7 μm , respectively. By measuring the nearest distance of the inclusion to the tensile surface of the bend bar at 194 μm , the stress at the feature was calculated to be 329 MPa.

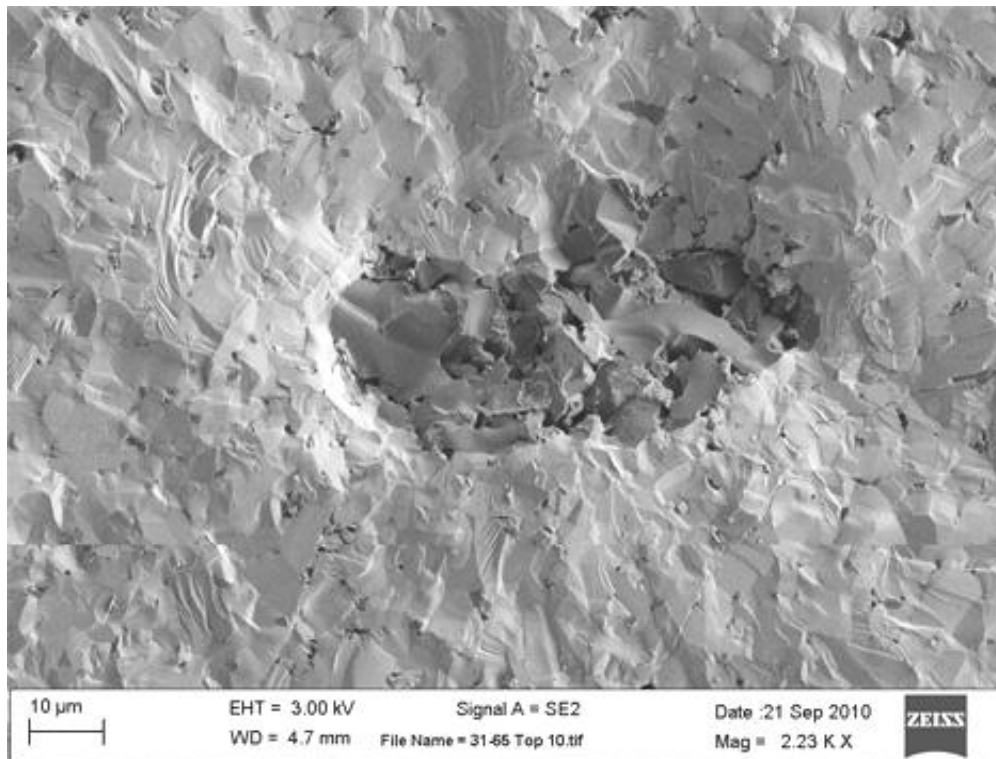


Fig. 10.33 Bar 2, B_4C inclusion (2,230 \times magnification)

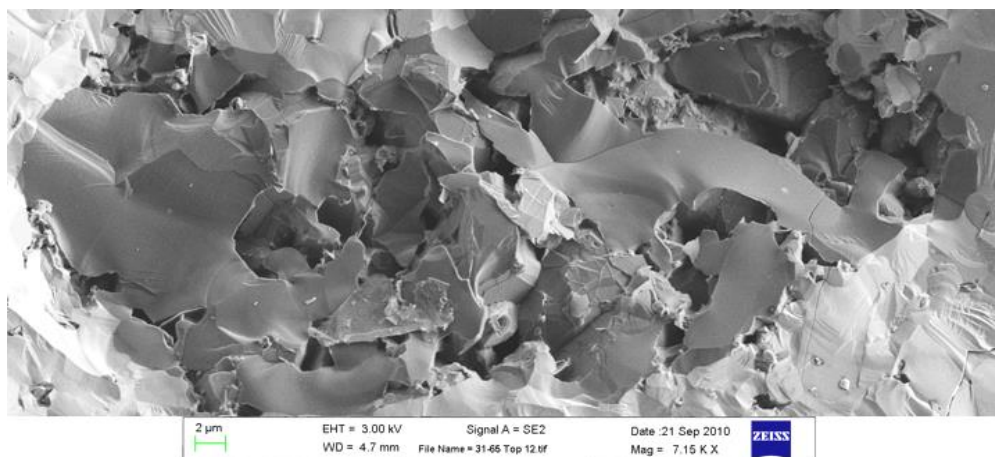


Fig. 10.34 Bar 2, B_4C inclusion (7,150× magnification)

Figure 10.34 is a composite SEM image of this B_4C inclusion recorded at 7,150× magnification. The inclusion appears to be very well integrated within the SiC matrix. The fracture path appears to radiate from the inclusion. It is also interesting that this appears to be a complex, multigrained inclusion.

Beyond determining the fracture-initiating feature, examining these images can give insight into fracture behavior and the presence and effect of microstructural features. Micron-sized C and B_4C inclusions have been observed on many of the fracture surfaces that have been investigated. These inclusions have also been imaged on polished sections of these bend bars. It is important to understand the effect that these features have on the fracture behavior of this material, both in the quasi-static and dynamic strain-rate regions. As part of the future work to be performed, the location and spatial position of these inclusions will be characterized.

After examining these images, it can be concluded that the primary mechanism of crack growth appears to be transgranular fracture. This same behavior was evidenced on all the other fracture surfaces of this material studied. Based on a study of the literature, this behavior likely comes about from a lack of an appreciable grain boundary phase. Materials having a significant grain boundary phase may experience a higher proportion of intergranular fracture as the energy required to fracture the grain boundary is less than that required to fracture a grain. Lack of an appreciable grain boundary phase also makes this material somewhat easier to polish than other types of SiC as the amount of pullout from weakened grain boundaries is reduced.

The final bar that will be discussed appears in Fig. 10.29. Originally located in the left column of the bottom layer of tile 11, this bar fractured at an applied stress of 200 MPa, the second-lowest strength in the entire study. The fracture surface is

characteristic of a low-strength fracture by displaying a very broad, relatively smooth fracture plane. As was the case with the bend bar that appears in Fig. 10.16, this bar broke because of errant machining scratches on the tensile surface of the bar. Even though the MOR value is no longer applicable to this study, there were many interesting features to be found on the fracture surface that warranted further discussion of this sample.

One of the more prominent features on the fracture surface has been indicated by a black ring in Fig. 10.29. Higher magnification views of this feature may be found in Figs. 10.35 and 10.36. What appears to be a dark, glass-like pool was characterized by EDS analysis to be C. This area has a very smooth surface and appears to be well integrated into the matrix of the bar. Surrounding this pool are a great many “glassy”, micron-sized caceous inclusions stretched in a vein from this large feature all the way to the tensile surface of the bar.

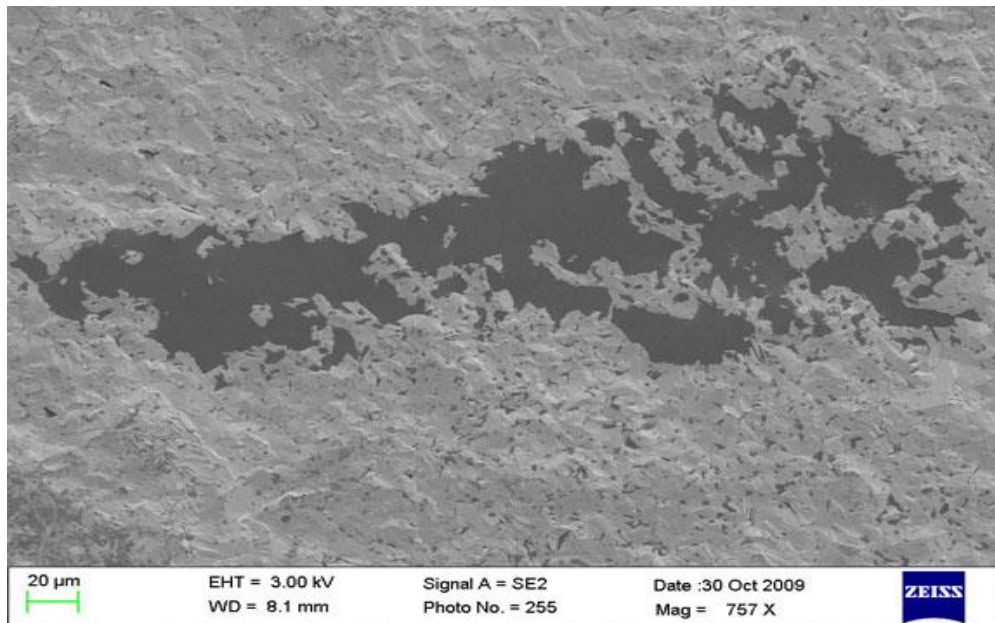


Fig. 10.35 Bar 3, amorphous C region (757× magnification)

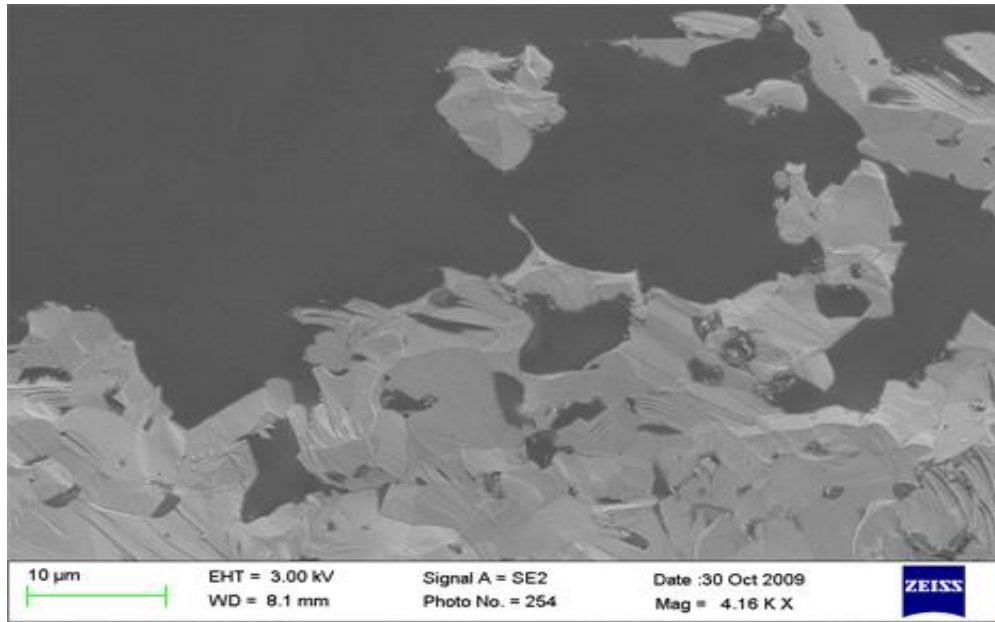


Fig. 10.36 Bar 3, amorphous C region (4,160× magnification)

10.8 NDE Analysis

When the NDE data was examined qualitatively, it was found that it was difficult to determine if a correlation existed between features within the NDE maps and fracture location for the 3 layers of bars from within each tile. In follow-on analyses, a quantitative examination of the ultrasound data was made instead to look at variation within the NDE maps. Table 10.9 contains an expansion of the data found previously in Table 10.1. The percentage of the standard deviation to the average value has been calculated for the NDE measurements for each tile, with values ranging between 0.09% and 3.9%.

Table 10.9 Ultrasound data, standard deviation as a percentage of average value

Tile No.	Type of Map	Unit	Average Value	Std. Dev.	Std. Dev. as a % of Average
8	Att coeff	dB/cm	2.31	0.09	3.9
11	Speed of sound	m/s	12044	113	0.9
4	Shear modulus	Gpa	182	3	1.6
31	Att coeff	dB/cm	2.15	0.05	2.3
2	Att coeff	dB/cm	2.21	0.07	3.2
19	Att coeff	dB/cm	2.17	0.09	2.3

In the time since these measurements were performed, a full characterization of the ultrasound test set has been performed. It was shown that the detectable variation in the attenuation coefficient measurement is 0.05 dB/cm.⁵ This value was exceeded for only 2 of the tiles used in the MOR study.

As a comparison, the strength values from the different layers of each tile were looked at in the same way. These data can be found in Table 10.10. Tile 2 had the least amount of variation while tile 11 had the greatest. The variation in the strength data for all of the tiles was much greater than the measured variation in the ultrasound data. One conclusion that may be drawn from this result is that the microstructural features that cause variations in the MOR values are not the same features that cause variation in attenuation coefficient, speed of sound, or elastic constant measurements, or that they cause a dissimilar degree of variation.

Table 10.10 MOR data, standard deviation as a percentage of average value

Tile Partition	Tile 8 (%)	Tile 11 (%)	Tile 4 (%)	Tile 31 (%)	Tile 2 (%)	Tile 19 (%)
Top layer	10.4	14.2	14.0	10.4	10.1	11.4
Middle layer	12.9	19.7	11.5	12.3	6.6	11.7
Bottom layer	13.7	13.5	14.0	13.8	8.9	11.3
Entire tile	12.4	16.0	12.5	12.3	8.7	11.6

The quantitative NDE data was also examined using different methods. Using a program developed at Rutgers, it is possible to graphically manipulate and interpret the raw data from an ultrasound C-scan. A screenshot of this program, called Hermes, can be seen in Fig. 10.37. Raw data is loaded into the program as a .txt file. As long as the data is present in the file, the user may select from multiple data sets to work with. The input boxes on the left are used to define the X,Y space for analysis as well as to set the scale in the image. By default, the program selects all of the data contained in the file, which for this study is the full X and Y extents of a tile. Statistical information such as maximum and minimum value, range, and the average value and standard deviation is displayed for the selected data.

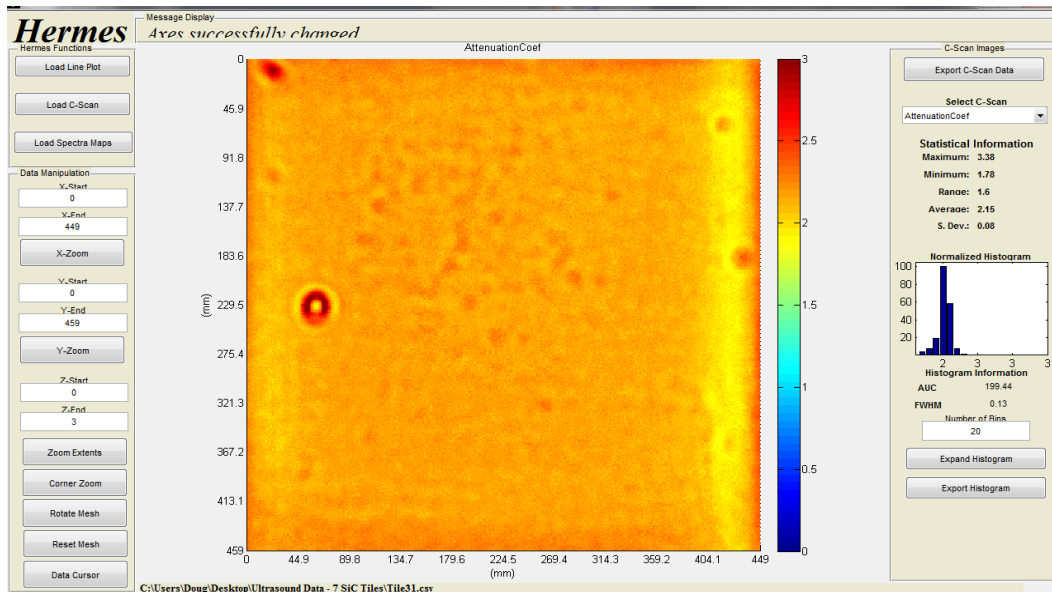


Fig. 10.37 Screenshot, Hermes NDE data analysis program

Using this program, the MOR/ultrasound data correlation was looked at in a different way. Hermes was used to determine the average value of an ultrasound produced measurement within the area of each bend bar position. This was done for all 108 bend bar positions from each tile. These data were compiled along with the MOR data and plotted in Figs. 10.38–10.43.

Although the spread in the data was different for each group of bars, the X and Y axes were kept constant for a comparison to be made between the tiles. Within each tile group, the data has been displayed by layer. All 6 figures contain plots of average attenuation coefficient value versus MOR. Even though group breakdowns were based upon different types of values, it was believed that it was more important to keep the plots consistent for comparison purposes. Linear regression lines have been included for the data from each layer to allow trends in the data to be more pronounced.

What is apparent when examining these figures is that there does not appear to be a pattern to the data. For 5 of the 6 tiles, the range in the Y-axis was less than 0.2 dB/cm. For the sixth tile, tile 8, bands of increased attenuation coefficient were located across the top and bottom of the tile corresponding to the upper-most left and right bend bar positions. If these 6 values are removed from the evaluation, the range in the data for this tile decreases to approximately 0.2 dB/cm. What appears to be clear from these results is that there was not enough measured variation within these tile sets.

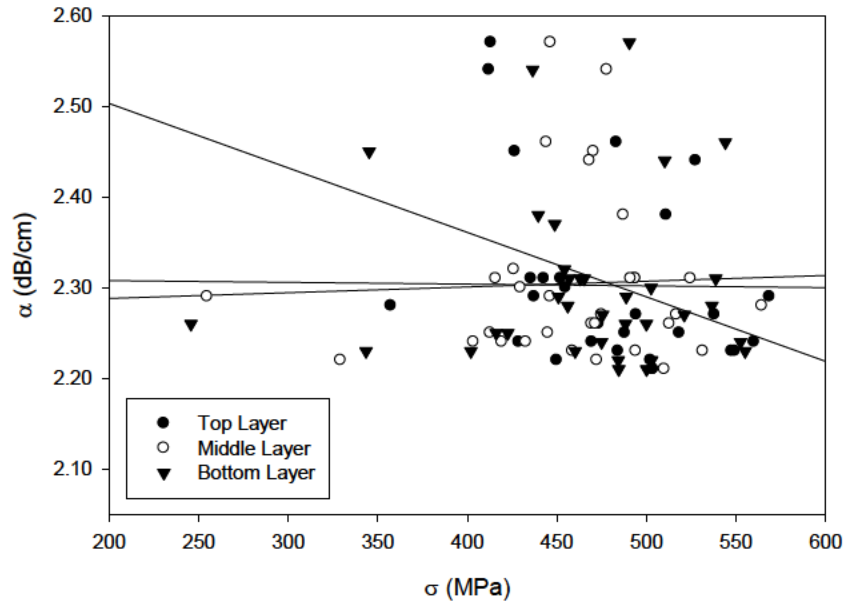


Fig. 10.38 Bend bar MOR vs. attenuation coefficient; Group 1, tile 8

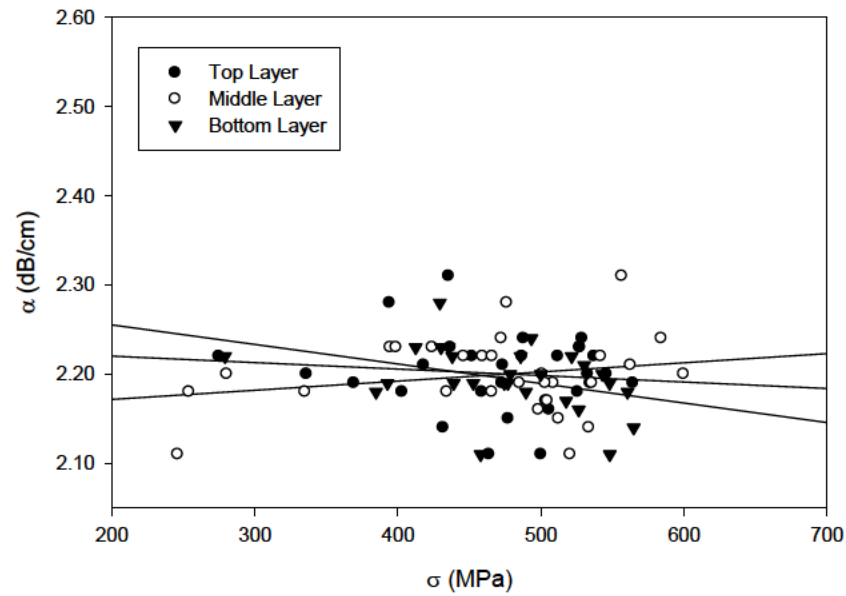


Fig. 10.39 Bend bar MOR vs. attenuation coefficient; Group 2, tile 11

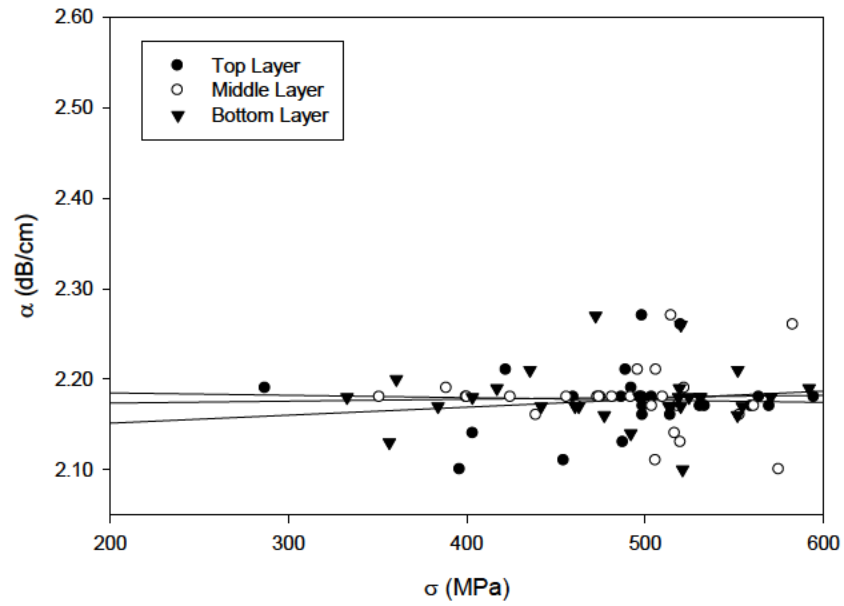


Fig. 10.40 Bend bar MOR vs. attenuation coefficient; Group 3, tile 4

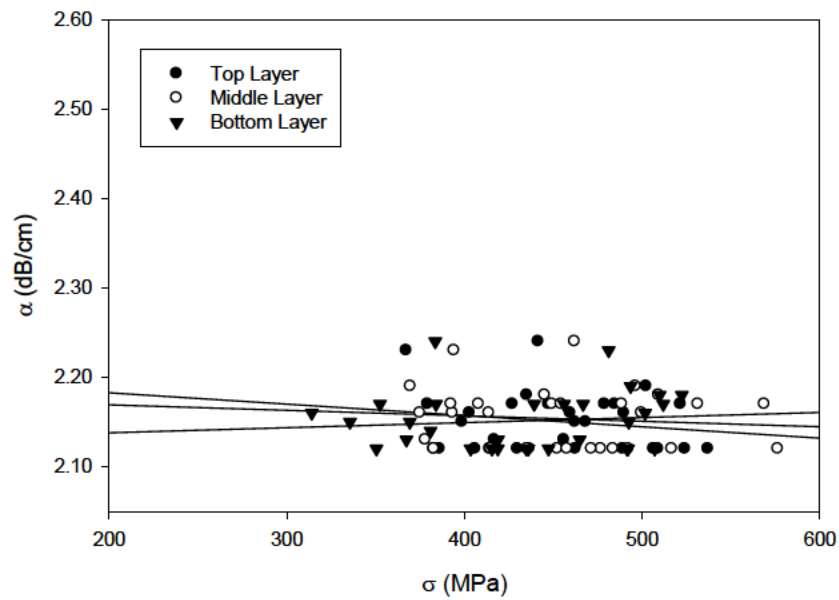


Fig. 10.41 Bend bar MOR vs. attenuation coefficient; Group 4, tile 31

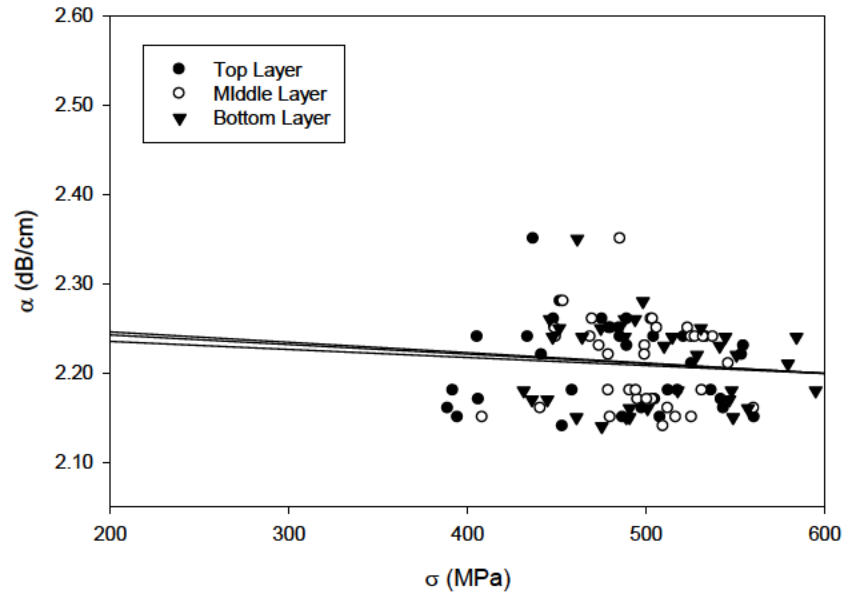


Fig. 10.42 Bend bar MOR vs. attenuation coefficient; Group 5, tile 2

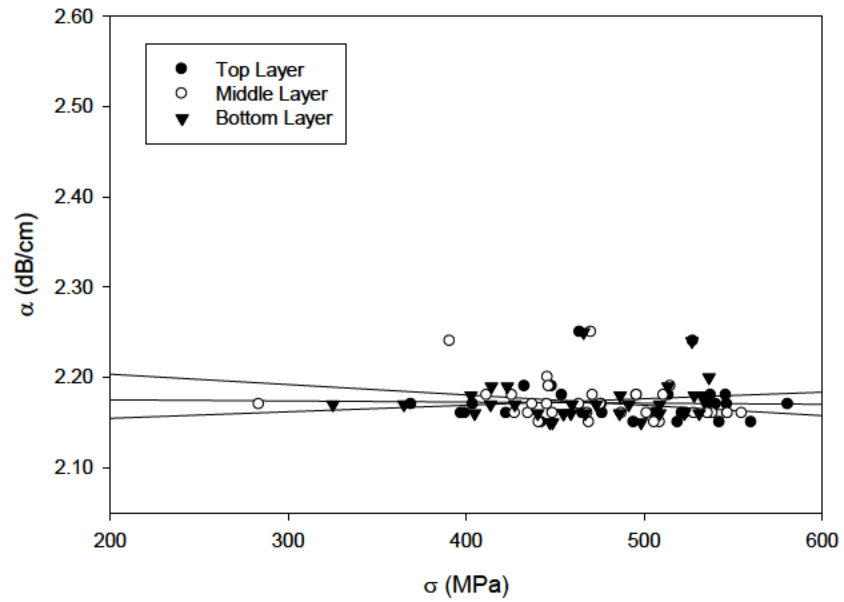


Fig. 10.43 Bend bar MOR vs. attenuation coefficient; Group 6, tile 19

10.9 Future Work

This study was performed on a lot of fully-dense, “good”, commercial off-the-shelf tiles. It was carried out in the hope that there would be a measurable difference between the tile sets based upon the type of ultrasound scans performed. An alternative route would have been to manufacture or produce samples, based upon an understanding of the mechanisms involved in the interaction between the acoustic energy and the material, such that there would be a measurable difference amongst the samples.

Attenuation coefficient measurements are frequency-dependent measurements that are affected by the wavelength range of the ultrasound transducer along with the type and size of the microstructural feature and matrix material present in the sample. These features may include inclusions, pores, and matrix material grains. Speed of sound measurements are most highly affected by the density of the material being scanned.

Work performed at Rutgers by Andrew Portune has furthered the understanding of loss-mechanisms of ultrasound energy in polycrystalline ceramics.⁵ These new insights have provided an avenue for how to direct further experimentation in this area. A number of samples sets are currently being readied to pursue this work.

One approach involves manufacturing SiC tiles that are produced with highly increased levels of porosity and therefore greatly reduced density. Another set of tiles are being produced with an excess of B₄C additives with the intention that these will form many large agglomerates in the final tile.

The second approach involves altering a commercially available tile by heat treatment to promote grain growth. The tile will be divided into quarters, with 3 of the quarters receiving different degrees of heat treatment. One of the quarters will be held back as a control sample. NDE testing by ultrasound C-scan will be performed before and after heat treatment. Microstructural evaluation, strength measurements, and polytype determination by XRD will also be performed on the different SiC sections. The hope with both of these avenues of experimentation is that the changes made to the material will produce a corresponding change in the ultrasound results and mechanical properties.

10.10 References

1. Demirbas MV, Haber RA. Microstructural property relationship in silicon carbide armor ceramic. [thesis]. [New Brunswick (NJ)]: Rutgers University; 2008.
2. Demirbas MV, Haber RA. Defining microstructural tolerance limits of defects for SiC armor. Ceramic Armor and Armor Systems II, Ceramic Transactions. 2005;178:109–122.
3. Demirbas MV, Haber RA. Microstructure-property relationship for armor materials. Presented at the 30th International Conference on Advanced Ceramics and Composites; 2005 Jan 23–28; Cocoa Beach, FL.
4. Demirbas MV, Haber RA, Brennan RE. Spatial distribution of defects in silicon carbide and its correlation with localized property measurements. Advances in Ceramic Armor III: Ceramic and Engineering Science Proceedings. 2008;28(5):143–154.
5. Portune AR. Nondestructive ultrasonic characterization of armor grade silicon carbide. [dissertation]. [New Brunswick (NJ)]: Rutgers University 2010.
6. Brennan R, Haber R, Niesz GS, McCauley J. Elastic property mapping using ultrasonic imaging. Ceramic Engineering and Science Proceedings. 2008;28(5):213–222.
7. Bottiglieri S, Haber RA. Corrective techniques for the ultrasonic nondestructive evaluation of ceramic materials. Advances in Ceramics Armor VI: Ceramic Engineering and Science Proceedings. 2010;31:57–67.
8. Krautkramer J, Krautkramer H. Ultrasonic testing of materials. Berlin: Springer-Verlag; 1990; Fourth revised edition.
9. Portune AR, Bottiglieri S, Niesz D, Haber RA. Non-destructive evaluation of armor grade ceramics. US Army Research Laboratory Annual Program Plan Review. Aberdeen (MD): Army Research Laboratory (US); 2008 Nov.
10. ASTM C1161-13. Standard test method for flexural strength of advanced ceramics at ambient temperature. West Conshohocken (PA): ASTM International; 2001.
11. Quinn GD. Fractography of ceramics and glasses. Washington (DC): Government Printing Office (US); 2006; p. 5–7.

12. Stobierski L, Gubernat A. Sintering of silicon carbide. I. effect of carbon. *Ceramics International*. 2003;29:287–292.
13. Bakas MP. Analysis of inclusion distributions in silicon carbide armor ceramics. [dissertation]. [New Brunswick (NJ)]: Rutgers University; 2006.

Task 11: Nondestructive Characterization of Armor Ceramic

Core Faculty: R Haber

US Army Research Laboratory (ARL) Collaborator: J McCauley

Graduate Student: S Bottiglieri, V DeLucca

11.1 Long-Range Objectives

- Use ultrasonic nondestructive characterization (NDC) in armor ceramic materials to image microstructural variations that impact the material's ballistic performance.
- Establish a method for a quantitative assessment of heterogeneity population within dense armor ceramic materials and large sample areas.
- Investigate the correlation between ultrasound and microstructural variations by characterizing defect engineered samples of armor ceramic materials.
- Determine the causal relationship between acoustic loss mechanisms and the microstructure of dense armor ceramics.

11.2 Objectives for Performance Period

- Transition from nondestructive examination (NDE) to NDC.
- Establish a greater understanding of specific acoustic loss mechanisms in heterogeneous ceramic materials.
- Creation of analytical equation to determine secondary phase grain size distributions in ceramic materials.
- Determination of scattering prefactors for use with general scattering equations.
- Develop the basis for an interpretive algorithm for transforming attenuation coefficient spectra to grain and secondary phase size distribution estimations.

11.3 Accomplishments

- Development of full-wave acoustic signal analysis software (Zeus).
- Upgrade of motion control unit for automated raster C-scans.
- Gain in understanding of scattering attenuation mechanisms.
- Characterization of custom engineered aluminum oxide (Al_2O_3) sample set and determination of thermoelastic energy loss in 2 phase materials.
 - Al_2O_3 + mullite
 - Al_2O_3 + titanium carbide (TiC)
- Determination of spatial and bulk homogeneity of silicon carbide (SiC)–nitrogen (N) samples.
- Ultrasonic NDC for determining grain size estimations in coarse-grained spinel.
- Evaluated densification variation in Al_2O_3 .
- Determined relationship between attenuation coefficient and grain size of commercially available Al_2O_3 .
- Use of derived analytical equation to determine mullite grain size distributions in Al_2O_3 .

11.4 Background

NDE of materials is an improvement over destructive methods, as it leaves the sample unharmed and ready for application. This ensures that virtually every piece can be tested for quality assurance before use. Ultrasound has previously been shown to have the capability to detect anomalous defects in ceramic armor that could lead to reduced strength, toughness, and ultimately to failure. High-frequency (greater than 10 MHz) testing is critical in detecting these flaws, as the shorter acoustic wavelength can resolve smaller features within the material. Such features are believed to degrade the performance capabilities of the material. Both reflected peak amplitude and top-to-bottom surface time-of-flight (TOF) measurements can be used to locate different kinds of anomalies, including density variations, defect inclusions, and secondary phases. Point analysis using contact transducers can also be used to detect changes in elastic properties throughout the material, which could indicate defects which may be too small to be resolved otherwise. Signal processing

allows for measurement of acoustic attenuation as the sound wave propagates through the sample bulk. This enables an indirect characterization of bulk sample microstructure.

By using high-frequency ultrasound NDE, it is possible to resolve anomalous defects within a dense ceramic, image these defects to locate their position, quantitatively define the degree of homogeneity within a sample, and determine fundamental sound velocities within the material that can be used to calculate elastic properties. Ultrasound NDC improves upon NDE by providing insight into bulk elastic and thermal heterogeneity distributions through analysis of frequency-dependent acoustic attenuation. Acoustic spectroscopy can be employed to identify the composition and likely size of anomalous defects within armor ceramics. Additionally, this technique can potentially estimate the volumetric defect density and size distribution, key factors in determining the high strain-rate performance of the material.

11.5 Current Work

11.5.1 Full-Wave Acoustic Signal Analysis Software, by Andrew Portune, Steve Bottiglieri, and Vincent DeLucca

Custom software has been written that facilitates analysis of data acquired with phased-array equipment. While the software detailed in this report is also capable of analyzing full-wave data recorded using single-element transducers, emphasis in this report has been given to its utility in examining phased-array datasets. Current phased-array test setup requires use of TomoView, an Olympus product, for data acquisition and analysis. While TomoView includes advanced functionality for control of the phased-array instrument, it unfortunately does not allow for advanced manipulation of received signals. TomoView can adequately measure the amplitude or TOF of up to 2 peaks of interest, but cannot calculate extrinsic materials properties such as elastic moduli or the acoustic attenuation coefficient. Additionally, TomoView is incapable of performing frequency-dependent measurements, an essential component of ultrasonic microstructural characterization. TomoView was judged to be unqualified for implementation of advanced ultrasound characterization techniques developed at Rutgers.

To solve this problem, custom software was authored using MATLAB. The software package was named the Zeus Full Wave Analyzer and will be referred to as Zeus for the remainder of this report. Zeus does not manipulate the phased-array instrument and has no role in the acquisition of data. Its purpose is to perform analysis on A-scans recorded during phased-array testing. TomoView automatically records complete A-scans at each point measured during C-scan

testing. An example of data recorded by TomoView in analysis of a defect-engineered SiC tile with the TRS 64 element 10-MHz phased-array probe is shown in Fig. 11.1. TomoView is capable of exporting the full wave A-scan data from each point in a .txt file, as shown in Fig. 11.2.

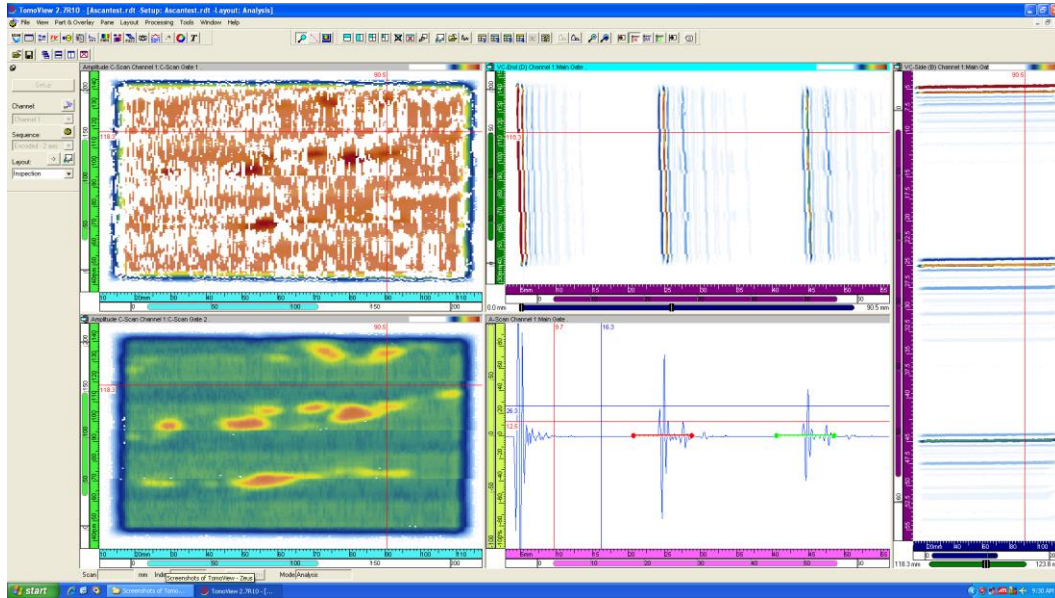


Fig. 11.1 Data recorded by TomoView after a full C-scan. The sample examined was a defect-engineered SiC tile characterized using the TRS 64 element phased-array probe.

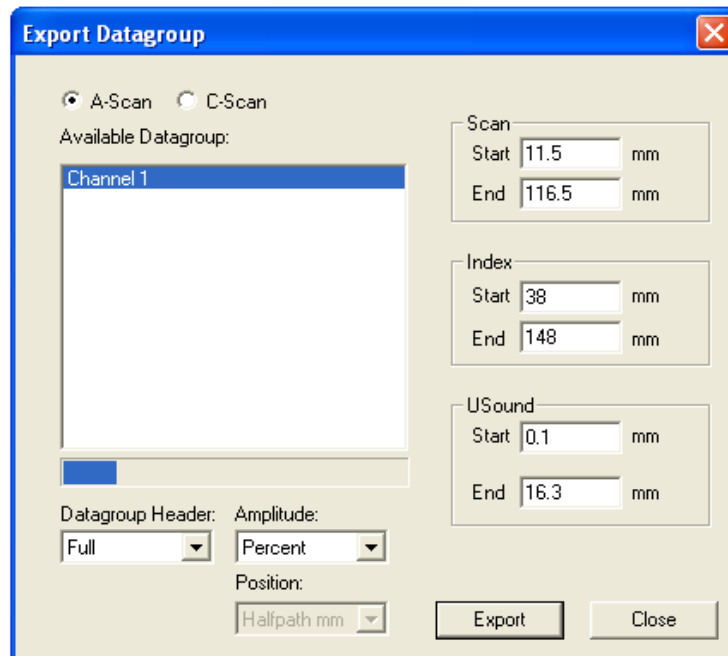


Fig. 11.2 Export data window from TomoView, allowing for control of x and y bounds as well as the time duration of the A-scan signals

Full wave A-scan data exported by TomoView are stored in a .txt file that tends to occupy 50–150 Mb depending on the size of the sample. When this file is loaded into Zeus, the datagroup header is read and interpreted to define the sample's lateral dimensions and the time duration of individual A-scan signals. Once loaded, Zeus displays preliminary information about the sample on a graphic user interface (GUI), as shown in Fig. 11.3. This information includes an A-scan, B-scan, temporary C-scan, and D-scan. The C-scan is temporary, as it has not been requested by the user and is shown simply to convey the area that the sample occupies. This is especially useful for nonrectangular samples. The A-scan shown in the top window corresponds to the point at the crosshairs on the C-scan image. This point can be changed by double-clicking on the C-scan directly. The B-scan corresponds to the series of A-scans along the horizontal line seen on the C-scan, while the D-scan corresponds to the series of A-scans along the vertical line.

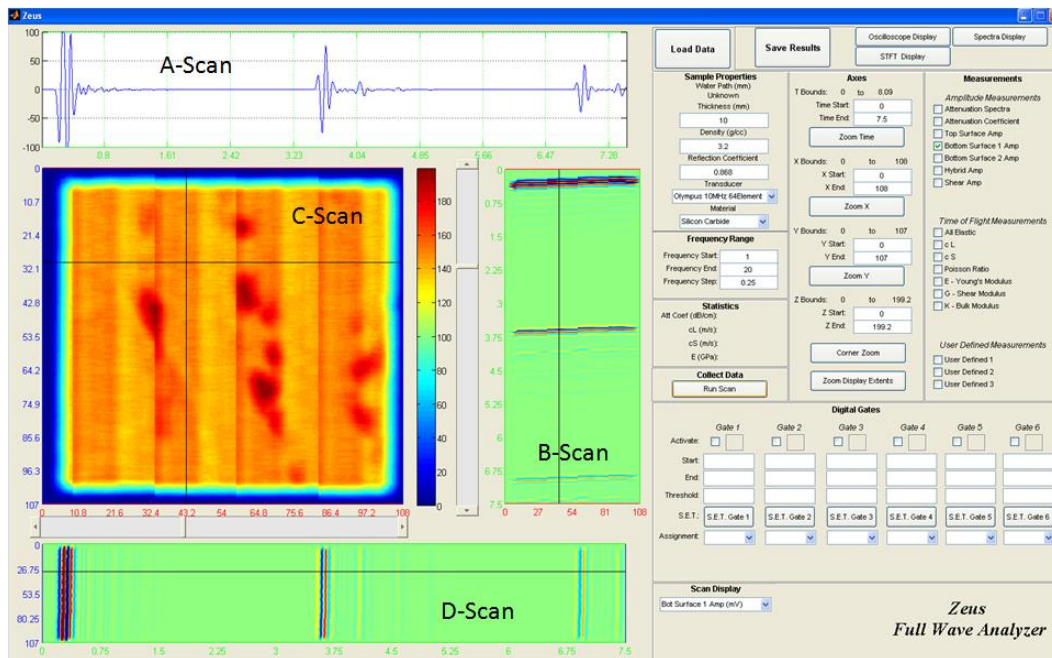


Fig. 11.3 Zeus GUI. Top window shows an A-scan corresponding to the point at the crosshairs in the C-scan. The B-scan corresponds to the horizontal line on the C-scan, while the D-scan corresponds to the vertical line. The panels on the right allow for control of sample properties, designation of measurements, gate assignments, and statistics related to the current point.

Before measurements can be made, digital gate assignments are necessary. Zeus allows for up to 6 separate gates to be concurrently assigned to peaks of interest, tripling the number provided by TomoView. Gates can be assigned either manually, by entering values for a start time, end time, and threshold, or more simply by clicking 3 times on the A-scan directly. Once the gate parameters have been set, the user can define which sample peak the gate corresponds to. Choices include the top surface peak, first bottom surface peak, second bottom surface peak, hybrid peak,

shear peak, and tank reflection peak. Gate assignments to specific peaks facilitate property measurements by informing the software where to look for particular data. Gate assignments are shown in more detail in Fig. 11.4.

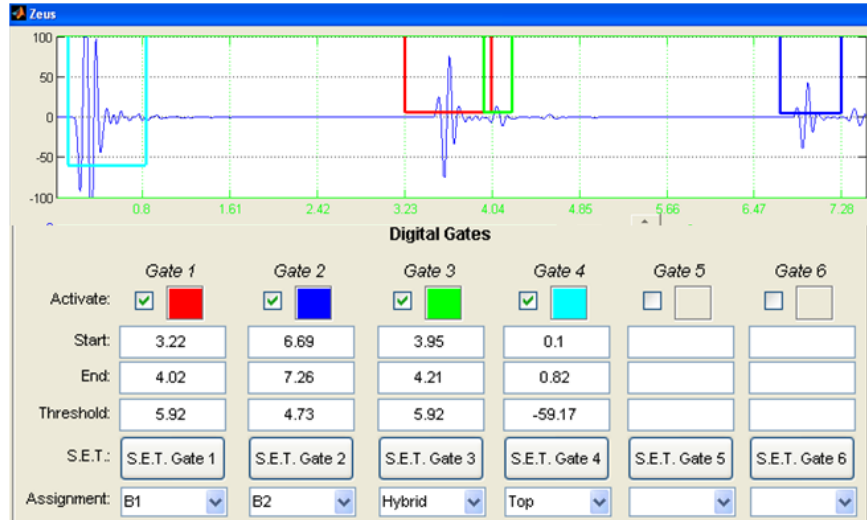


Fig. 11.4 Digital gate assignment options present in the Zeus software

Once gates have been assigned, the user may take advantage of the panels on the right side of the user interface. Sample properties including thickness, top surface interface reflection coefficient, and density must be set to ensure accurate properties measurements. The transducer used in data acquisition is automatically detected by the software and used to set defaults for the measurable frequency range. This range, as well as the interval between frequency measurements, can be altered in the frequency panel. This property is important for short-time Fourier transform (STFT) measurements of a peak's spectral composition, used to determine the frequency dependence at the acoustic attenuation coefficient.

The measurements panel contains a list of 15 different properties that can be determined simultaneously over the sample area. These fall into 3 broad categories: 1) measurements based upon peak amplitudes, 2) measurements based upon peak TOF, and 3) user-defined measurements. Amplitude-dependent measurements include the frequency-dependent attenuation coefficient spectrum, the overall signal attenuation coefficient, and peak amplitudes for top surface, first bottom surface, second bottom surface, hybrid, and shear peaks. TOF-based measurements include the longitudinal speed of sound, shear speed of sound, Poisson's ratio, Young's modulus, shear modulus, and bulk modulus. User-defined measurements allow the user to combine amplitude or TOF information from up to 2 peaks using basic arithmetic operations. For example, the user may want to record the amplitude of the peak contained in gate 5. Or the user may want to measure the amplitude ratio between 2 peaks of interest. Measuring TOF between 2 peaks is also possible.

User-defined measurements enable customization of sample characterization beyond conventional tests. Figure 11.5 shows the GUI after measurement of the first bottom surface peak amplitude.

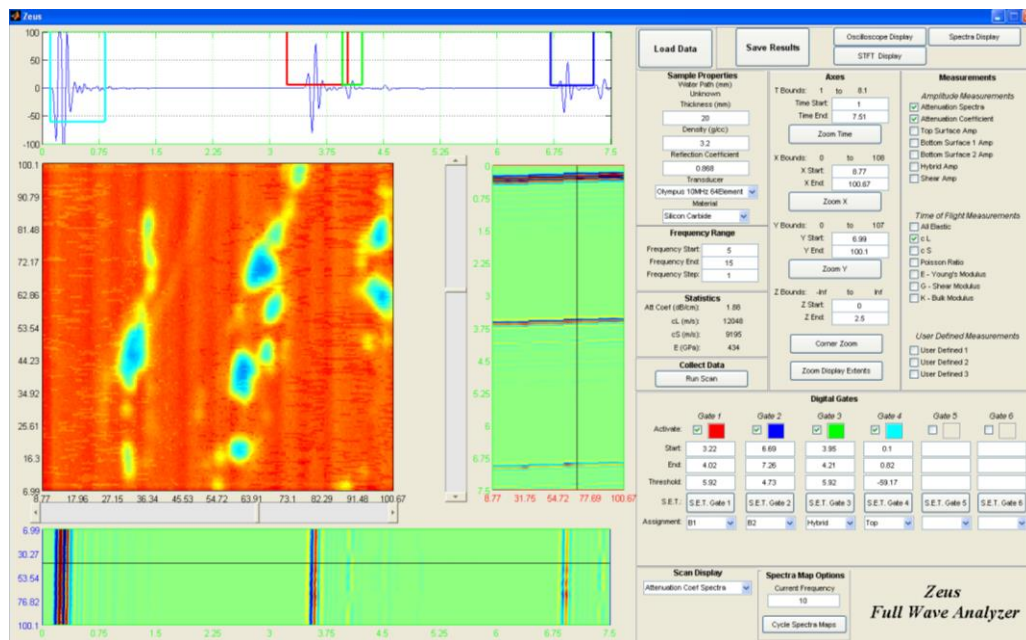


Fig. 11.5 Zeus GUI after measurements have been run

Measuring multiple sample properties simultaneously is common in the characterization of solid materials. Zeus allows the user to check each property map before saving the data, ensuring that measurements were performed adequately and to the user's satisfaction. The C-scan display in the GUI can be switched to show each property map once measurements are complete. The color scale can be zoomed to allow for greater scrutiny of property variances.

Once the user has checked results of property measurements, the collected data can be saved. Zeus contains a great deal of sample information and allows the user to save any or all of it if desired. The user can save the A-scan from the currently selected point, the STFT of a peak of interest, the attenuation coefficient spectrum from the currently selected point, the currently displayed B- or D-scan, and all of the C-scan maps. Additionally, if attenuation coefficient spectra were measured at each point in the sample, spectra maps displaying the attenuation coefficient at individual frequencies can be saved as well. B-, C-, and D-scans are saved in xyz columnar format and can be easily imported into commercial graphing software such as Microsoft Excel or SigmaPlot. An attached side header contains relevant scan data to help identify the sample.

In addition to its primary functionality, Zeus provides 2 optional modes for examining A-scan data at points of interest. The first looks at the STFT of a peak of interest while the second calculates the attenuation coefficient spectrum. The user has the option of switching the B- and D-scan displays from time-dependent to frequency-dependent to visualize variations in these 2 properties over horizontal and vertical sample lines. This is shown in Fig. 11.6 for both optional display modes.

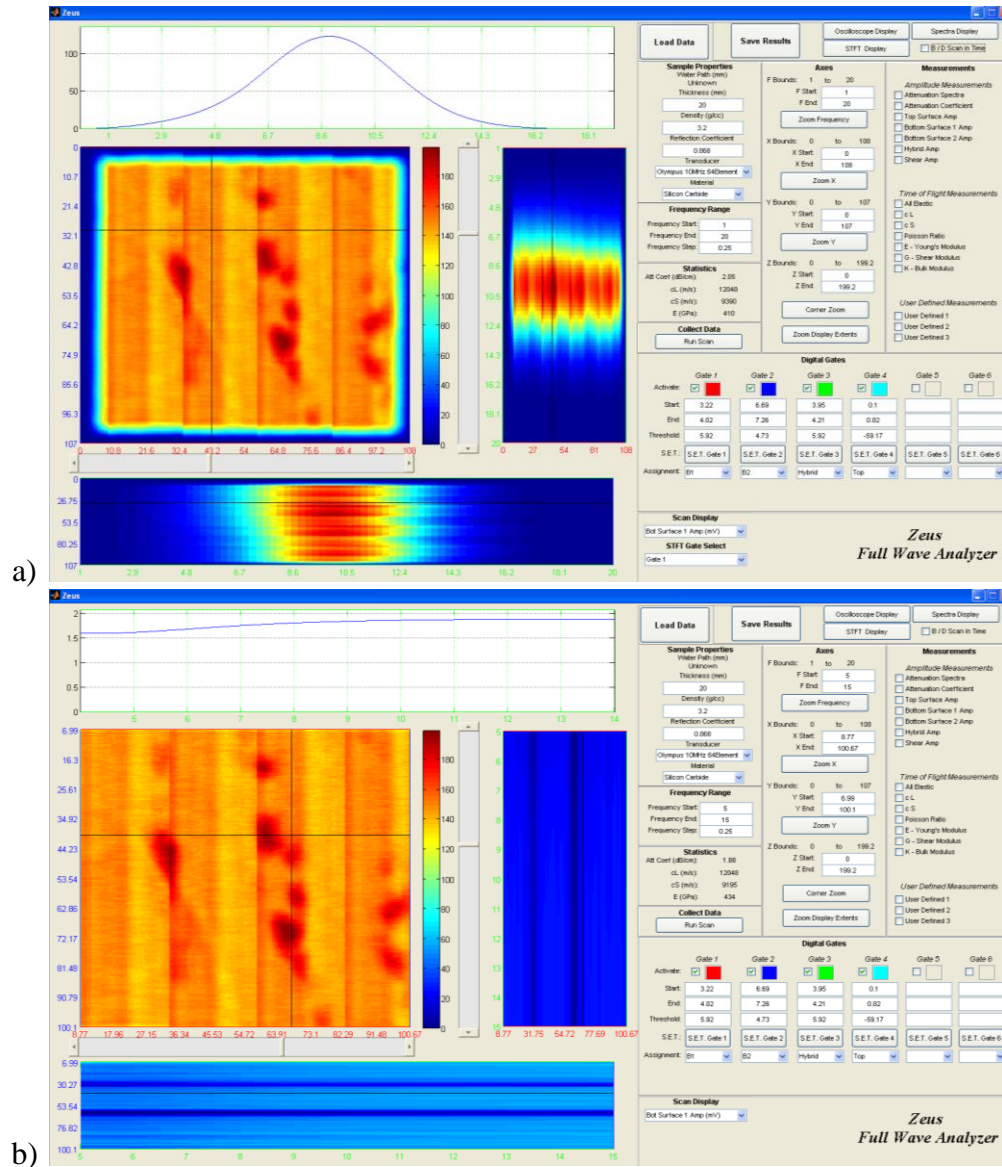


Fig. 11.6 Zeus optional display modes showing a) the power spectral density of a peak of interest as determined by the STFT and b) the frequency-dependent attenuation coefficient spectrum. The B- and D-scan displays have been changed to show these property variations across horizontal and vertical sample lines.

Zeus software has been designed to easily interface with output from TomoView. It is also capable of examining full-wave data from single-element transducer testing. The functionality provided by Zeus allows for advanced ultrasonic characterization of solid materials exceeding that which is possible through use of TomoView alone. Property measurements made by this software for conventionally sized samples typically required 1–5 min. The exception to this is measurement of the attenuation coefficient spectrum at each point, an advanced technique that can require over 1 h. This advanced technique is often not necessary when looking for anomalous defects. Zeus software has demonstrated the ability to rapidly process data acquired in ultrasound phased-array tests.

11.5.2 Technique Optimization: An Understanding of Scattering in Ceramics, by Steve Bottiglieri

Scattering is the redirection of a wave caused by grains, grain boundaries, solid inclusions, and pores. Attenuation, or energy loss, of a transmitted acoustic wave caused by scattering occurs when a portion of the wave never makes it back to the transducer. Scattering attenuation in dense polycrystalline ceramics is typically dominated by grains and grain size. Classically, types of scattering have been defined by a relationship between the wavelength of the interrogating acoustic beam and the size of the scatterer. Three regimes of scattering exist, and their dependencies of attenuation on frequency, wavelength, and scatterer size are shown in Table 11.1.

Table 11.1 Scattering regime, size-to-wavelength relationship, and attenuation coefficient dependence

Scattering Regime	ka Relationship	f Dependence
Rayleigh	$ka \ll 1$	$\alpha = C_R a^3 f^4$
Stochastic	$ka \approx 1$	$\alpha = C_S a f^2$
Diffuse	$ka \gg 1$	$\alpha = C_D a^{-1} f^0$

Where a is the scatterer size, k is wavenumber defined by $k = 2\pi/\lambda$, f is frequency, and the C factors are related to morphology and elastic mismatch and are material-dependent.

For polycrystalline ceramics such as SiC and Al₂O₃, where the grain sizes are on the order of microns or less, scattering does not dominate an attenuation coefficient spectra until approximately 50 MHz and higher. In materials where there is a large spread in grain size distribution, all 3 types of scattering will be operable and convolute with each other, as shown in Figs. 11.7 and 11.8. The degree of

attenuation for each scattering mechanism is ordered as diffuse, stochastic, and Rayleigh, with diffuse scattering lending the most amount of energy loss. Diffuse scattering will theoretically give a horizontal line for an attenuation spectrum, but in actual practice diffuse scattering presents with what are known as Mie resonances. Mie resonance presents as an exponentially decaying sine function where the average attenuation value of these resonances across frequency is independent of frequency. Figure 11.8 explains why a measured attenuation coefficient spectrum that shows strong scattering behavior may have peaks overlapping the general power-law-type curve. It is important to keep this in mind when evaluating an attenuation coefficient spectrum.

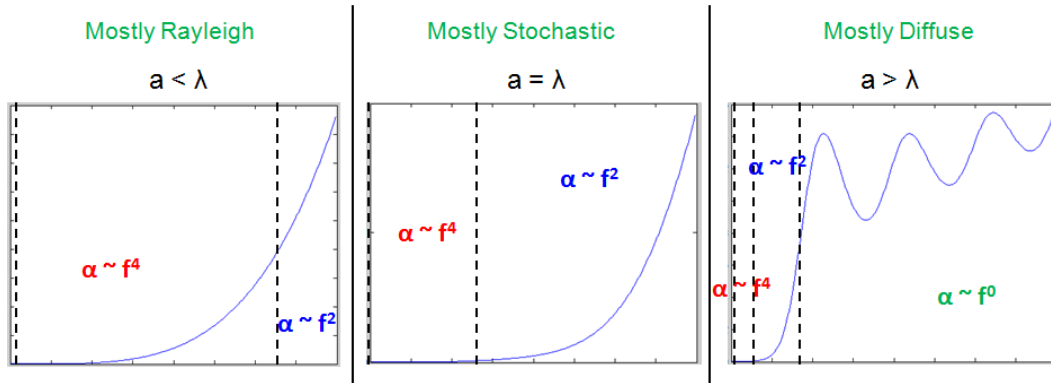


Fig. 11.7 Idealized attenuation coefficient spectra showing dominant scattering regimes. Abscissa is normalized frequency and ordinate is normalized attenuation coefficient. For single particles, the degree of attenuation actually increases from Rayleigh to diffuse scattering.

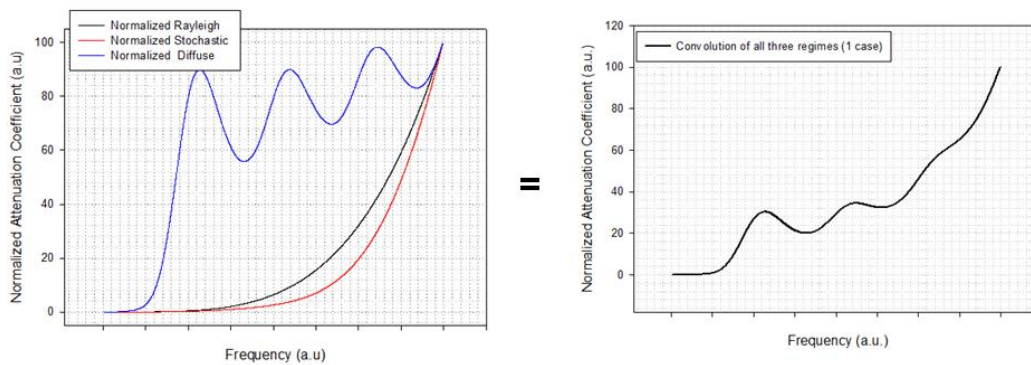


Fig. 11.8 Convolution of 3 scattering types

11.5.3 Ultrasonic NDE for Homogeneity of SiC-N, by Vincent Delucca

Seven SiC-N composite samples were tested using ultrasound NDE methods to determine bulk homogeneity and detect flaws. Each of the SiC-N samples was hexagonal with a side length of approximately 58.7 mm and thickness of approximately 30 mm. Ultrasonic testing was conducted using a 20-MHz central frequency planar transducer in a water-filled immersion tank to generate C-scan maps of the overall attenuation coefficient. Point measurements were also taken over the center of each sample to determine elastic properties. The attenuation coefficient C-scan maps for these samples are shown in Fig. 11.9 and elastic properties are shown in Table 11.2. All attenuation coefficient images are on the same scale, 0–1 dB/cm.

|

Fig. 11.9 Overall attenuation coefficient C-scan maps for SiC-N hexagons

Table 11.2 Measured elastic properties for SiC-N hexagons

Sample	Thickness (mm)	Density (g/cc)	C _L (m/s)	C _S (m/s)	ν	E (GPa)	G (GPa)	K (GPa)
TS20100224-3	30.05	3.21	12166	7725	0.162	445	192	220
TS20100231-1	30.05	3.21	12215	7705	0.170	446	191	225
TS20100234-1	30.05	3.21	12215	7705	0.170	446	191	225
TS20100237-1	30.05	3.21	12191	7715	0.166	446	191	222
TS20100318-3	30.05	3.21	12191	7695	0.169	444	190	224
TS20100320-2	30.05	3.21	12191	7695	0.169	444	190	224
TS20100337-2	30.05	3.21	12191	7695	0.169	444	190	224

As seen in Table 11.2, these samples showed very little variation in their elastic properties, which were taken only as a point measurement over the center of each sample. Full elastic property C-scan maps could not be generated because the thickness of the samples attenuated the shear signal too much to be reliably measured by the automated scanning software.

The bulk of the samples appear to be fairly homogeneous, as seen in Fig. 11.9, although some features are apparent in the attenuation coefficient maps. The features visible on the top-left edges of sample TS20100231-1, the corners of sample TS20100234-1, and the bottom-right edges of sample TS20100237-1 appear to be caused by defects on or slightly below the surface of the samples that are visible as regions of slight discoloration. Each of the samples except for TS20100231-1 show small circular features with low attenuation in the middle of the feature surrounded by a ring of slightly higher attenuation. Examination of A-scans at these points did not show any direct reflections, indicating that they were not caused by any single large inhomogeneity. These features are most likely caused by slightly higher or lower than average concentrations of sintering aids or secondary phases in these regions. Samples TS20100318-3 and TS20100337-2 show slightly higher average attenuation over the entire sample area and the circular features are also more abundant and more pronounced. This may indicate a higher total concentration of sintering additives or perhaps poorer mixing of additives in these 2 samples compared with the others.

From this testing it appears that these samples were fairly homogeneous and free of bulk defects. Some of the samples did appear to have some slight surface flaws or other features in the bulk. Without further analysis of the cause of these features, it cannot be determined whether they are simply cosmetic or if they would impact performance in the final application.

11.5.4 Ultrasonic NDC for Grain Size Determination in Spinel, by Vincent Delucca

Several transparent aluminate spinel samples were received to perform ultrasonic nondestructive characterization to determine mean grain size in the samples. Although the samples were transparent, many small features were visible within the bulk of each sample, indicating the presence of large grains or inclusions. Preliminary testing was conducted using a 20-MHz central frequency planar transducer in a water-filled immersion tank on a sample labeled 24-0275-3. Sample 24-0275-3 was approximately 50×50 mm square with a thickness of approximately 5 mm. Only half of the sample surface had been polished, and the thickness was not consistent over the entire sample area; as a result, full area maps were unable to be obtained. Point measurements were taken over the center of the polished half of the sample to measure frequency-dependent attenuation coefficient.

Figure 11.10 shows A-scan data from sample 24-0275-3 using the 20-MHz transducer. Multiple direct reflections were detected in the bulk of the sample. This implies that there are many features on the size scale of the order of the wavelength of the ultrasound used in this material. The wavelength is determined by the equation $C_L = \lambda f$ where C_L is the speed of sound, λ is the wavelength, and f is the frequency. In spinel, where the speed of sound is approximately 9,750 m/s, this corresponds to features between approximately 300 and 1,000 μm in the measured frequency range. Elastic properties for this sample could not be measured because the direct reflections from these features interfered with measurement of the shear peak time of flight.

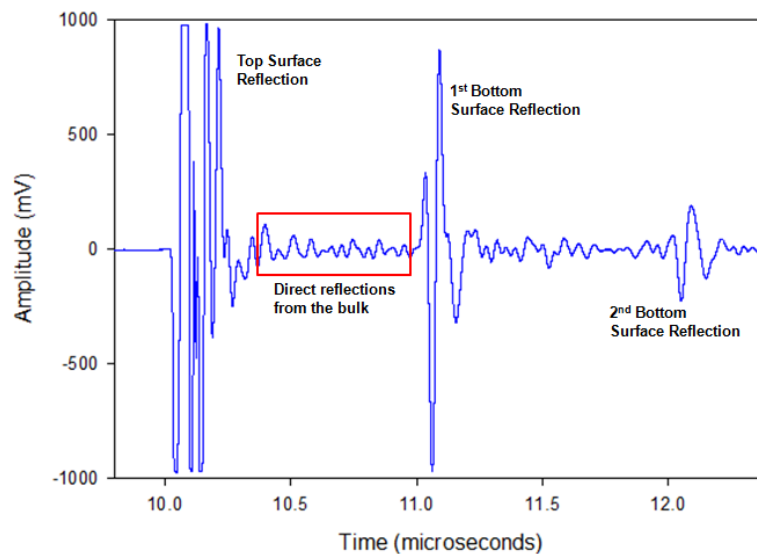


Fig. 11.10 A-scan data from spinel sample 24-0275-3 showing direct reflections in the bulk

Figure 11.11 shows the frequency-dependent attenuation coefficient spectrum taken from sample 24-0275-3. The shape of the measured spectrum indicated strong scattering behavior at all measured frequencies. Between 5 and 18 MHz, the curve appears to follow a power law dependence, which indicates either Rayleigh or stochastic scattering. Rayleigh scattering occurs when the scattering features are much smaller than the wavelength of the ultrasound and exhibits an f^4 dependence. Stochastic scattering occurs when the scattering features are on the order of the wavelength of the ultrasound and exhibits an f^2 dependence. At approximately 19 MHz, the attenuation spectrum curve levels off and appears to become independent of frequency. This is indicative of diffuse scattering, where the size of the scattering features is larger than the wavelength of the ultrasound. Below about 10 MHz, there appears to be some peak-like behavior in the curve superimposed on the power-law behavior. This could be indicative of thermoelastic absorption by features in the microstructure. Attenuation by the scattering mechanism tends to be dominated by grains of the material, while attenuation by thermoelastic absorption tends to be dominated by solid inclusions or secondary phases.

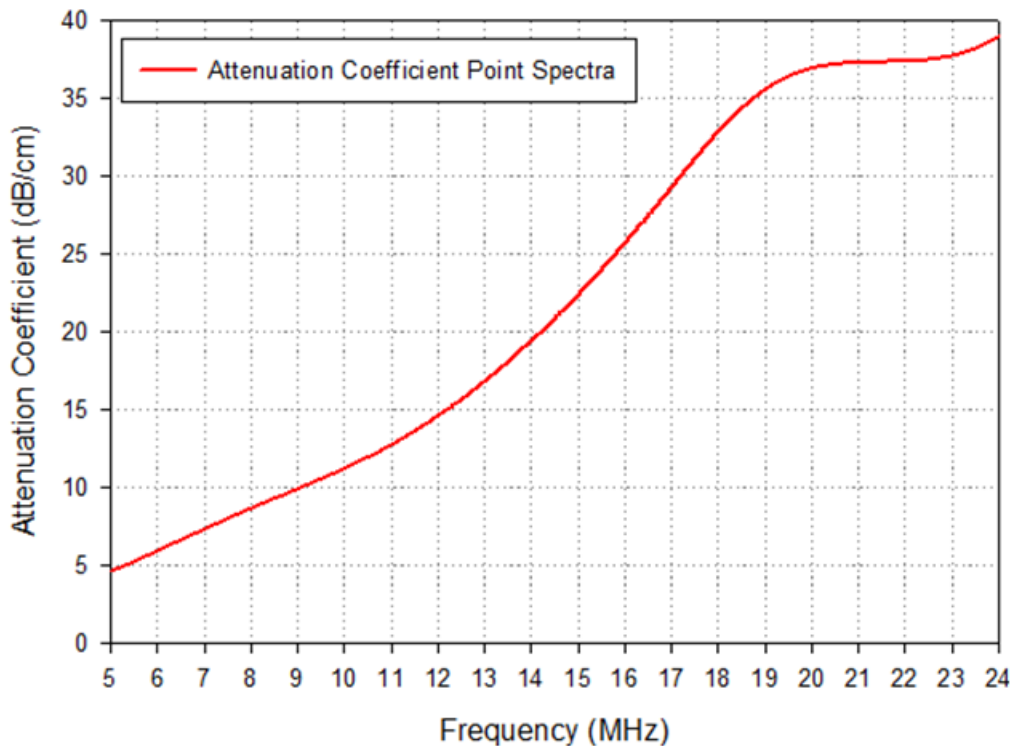


Fig. 11.11 Frequency-dependent attenuation coefficient from spinel sample 24-0275-3

To determine whether Rayleigh or stochastic scattering was dominant in this frequency range, a power-law curve fit was applied to the portion of the attenuation spectrum curve between 10 and 18 MHz. The portions of the curve below 10 MHz and above 18 MHz were excluded from this calculation to avoid the effects of the

thermoelastic absorption and diffuse scattering on the power-law curve fit. The truncated attenuation spectrum was fit to $\alpha = Cf^n$, where α is the attenuation coefficient, C is the power law prefactor, f is the frequency, and n is the power-law exponent. For pure Rayleigh scattering, the power-law exponent would be 4, and for pure stochastic scattering it would be 2. Figure 11.12 shows the curve fit and its associated parameters. The power-law exponent provided by the curve fit is 2.012, indicating primarily stochastic scattering behavior in this sample. In this frequency range, the ultrasound wavelength in the material is between 500 and 1,000 μm , so stochastic scattering would be caused primarily by spinel grains in that size range.

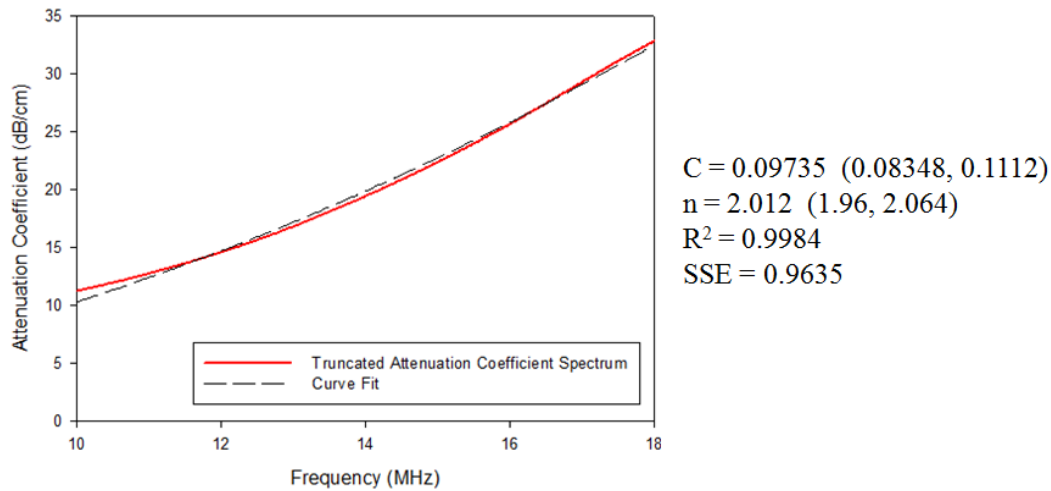


Fig. 11.12 Curve fit for spinel sample 24-0275-3 attenuation spectrum, 10–18 MHz

The attenuation coefficient spectrum shown in Fig. 11.12 shows a slight deviation from pure power-law behavior below 10 MHz. This could possibly be caused by a small peak centered between approximately 7 and 9 MHz convoluted with the dominant power-law behavior. This type of behavior is typically caused by thermoelastic absorption, which is governed by the Zener equation.

$$a = \sqrt{\frac{\pi\chi}{2\rho C_v f}}, \quad (1)$$

where f is the frequency of maximum absorption, a is the diameter, χ is the thermal conductivity, ρ is the density, and C_v is the specific heat of the absorbing particle. Table 11.3 shows these properties for magnesium aluminate (MgAl_2O_4) spinel and lithium fluoride (LiF), a common sintering aid in this system. Using these values in the Zener equation for the frequency range between 7 and 9 MHz, the sizes of the attenuating features would be approximately 1.0–1.143 μm and 0.784–0.889 μm for spinel and LiF , respectively. Because of the strong scattering behavior, it is assumed that the spinel grains would be much larger than required for thermoelastic absorption, so it is more likely that LiF inclusions of this size range would cause

attenuation by thermoelastic absorption in this frequency range. However, LiF was used in this analysis only because it is a common sintering aid in spinel. Full information about what was used to make these samples was not available, so any attenuation not caused by the spinel grains could be caused by some other unknown factor.

Table 11.3 Thermal properties of MgAl_2O_4 spinel and LiF

Material	Density (kg/m^3)	Thermal Conductivity (W/m K)	Specific Heat (J/kg K)
Spinel	3588	17	814
LiF	2635	15	1604

Based on the information gathered by these point measurements, it appears that stochastic scattering is dominating the acoustic attenuation in the measured frequency range. This implies that the spinel grains are large, on the order of 500–1,000 μm . To obtain more accurate grain size information over large sample areas, a standard spinel sample set is required. Having a standard sample set with varying grain sizes would enable determination of the power law prefactor for the spinel system. Grain size measurements in spinel could then be taken quickly over large sample areas.

11.5.5 Ultrasonic NDC for Grain Size Determination in Zirconium Dioxide Absorption, by Steve Bottiglieri

Zirconium dioxide (ZrO_2) is a biocompatible material that is used in dental restoration and replacement joint applications. It is several times stronger than porcelain dental restorative material and mimics natural teeth much better. Zirconia owes its strength and other material properties to its microstructure. For medical applications, the microstructure needs to be controlled and pure. A study using ultrasound to determine grain size variations was performed on a section of ZrO_2 used as a dental restorative material. The section is approximately $10 \times 10 \times 3$ mm and has a density of approximately 5.68 g/cc. Attenuation coefficient point spectra was collected in a frequency range of 12–32 and 40–65 MHz. The gap in frequency is due to different bandwidths of the 2 transducers used. Figure 11.13 shows the collected attenuation coefficient spectrum about a point of the ZrO_2 sample.

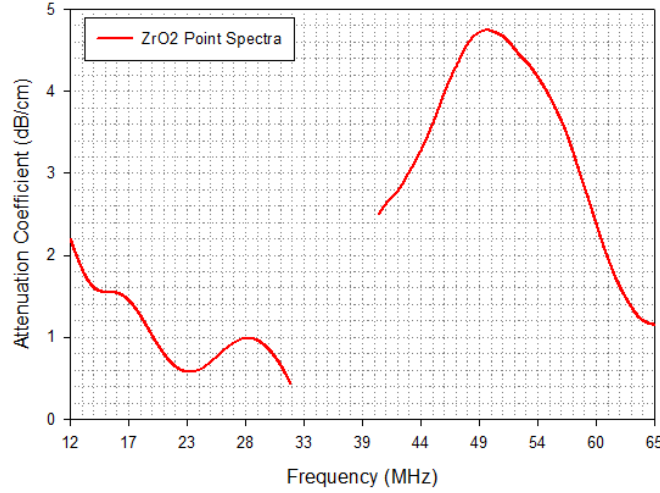


Fig. 11.13 Attenuation coefficient spectrum of ZrO₂ sample

The important features of the spectrum are where the noticeable peaks lie. According to the theory of thermoelastic absorption in polycrystalline materials, these peaks in attenuation coefficient may be caused by an intraparticle or interparticle mechanisms. Intraparticle absorption is the effect of heat flow inside a grain as the acoustic wave causes the grain to compress and rarefact. Interparticle absorption is a similar effect of heat flow but rather between grains. Interparticle absorption occurs due to the slight increase or decrease in grain temperature caused by the passing acoustic wave. Random orientation and anisotropy of thermal expansion coefficient causes localized regions of heating and cooling that lead to thermal flow. In the case of a material without a significant glassy grain boundary phase, interparticle absorption may be prevalent and must be accounted for. Without the low thermal conductivity a glassy boundary provides between grains, thermal flow will be uninhibited between 2 adjacent grains, and energy absorption will increase at specific frequencies.

According to Zener, in his work on the internal friction in solids, the frequency of maximum absorption can be related to the material's thermal properties and grain size for both intraparticle and interparticle absorption, as shown in Eqs. 2 and 3. Eq. 2 is for intraparticle absorption and Eq. 3 for interparticle absorption. Where X is thermal conductivity, ρ is density, C_V is specific heat at constant volume, and d is grain diameter.

$$f_o = \frac{\pi}{2} \frac{X}{d^2 \rho C_V} \cdot \quad (2)$$

$$f_o = \frac{3\pi}{2} \frac{X}{d^2 \rho C_V} \cdot \quad (3)$$

For ZrO_2 (tetragonal), thermal conductivity is $1.66 \text{ W/m}\cdot\text{K}$, density is $5,680 \text{ g/cc}$, and specific heat is $456 \text{ J/kg}\cdot\text{K}$. Table 11.4 shows frequencies of where peaks occur in the measured attenuation coefficient spectrum and the sizes they would relate to according to both intraparticle and interparticle absorption. Frequencies of 9 and 12 MHz are assumed where the left bound may have peaks.

Table 11.4 Frequencies where peaks occur in attenuation and their relation to sizes according to intraparticle and interparticle absorption

Frequency (MHz)	Intra Size (nm)	Inter Size (nm)
9	339	563
12	290	498
16	247	433
28	190	339
50	142	247

This ZrO_2 sample was imaged in the FESEM where several micrographs were collected. A grain size distribution was measured using Lince based off of 4 FESEM images and approximately 300 measured grains. An image of the ZrO_2 microstructure is shown in Fig. 11.14 and a histogram of the size distribution is shown in Fig. 11.15. The histogram shows multimodal behavior of the grain size distribution. Each mode seen in the histogram is labeled at the size it peaked at.

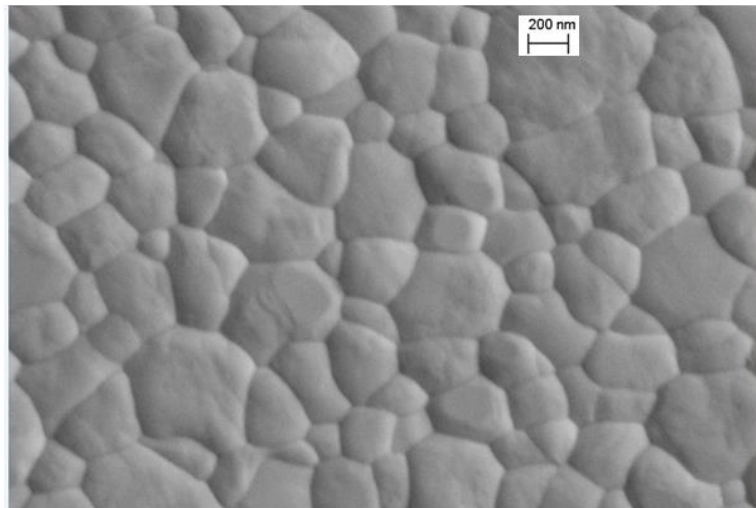


Fig. 11.14 FESEM image of ZrO_2 microstructure

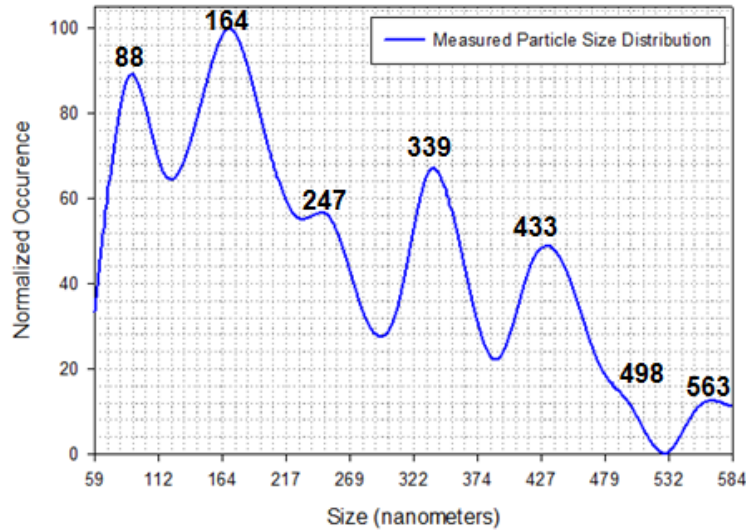


Fig. 11.15 Normalized particle size histogram of ZrO₂ sample

Table 11.5 shows the sizes at where the distribution peaks and calculated intraparticle and interparticle frequencies for such sizes. Highlighted frequencies are those which correspond to the peak frequencies from the attenuation coefficient spectra (Fig. 11.13). While there are frequencies that are currently incapable of being measured at this point, excellent agreement exists with where the attenuation coefficient spectra peaks and what thermoelastic absorption theory predicts for grain size. A method does not currently exist to distinguish between intraparticle and interparticle absorption when viewing an attenuation coefficient spectra. For now, a priori knowledge of the material being examined such as grain boundary phases and additive type and concentration is necessary.

Table 11.5 Measured sizes and their correspondence to calculated intraparticle and interparticle frequencies

Size (nm)	Intraparticle Frequency (MHz)	InterParticle Frequency (MHz)
88	130	390
164	37	112
247	16	49
339	9	26
433	5	16
498	4	12
563	3	10

11.5.6 Ultrasonic NDE Analysis and Microstructural Comparison of Al_2O_3 Densification Variation Samples, by Vincent DeLucca

Several lots of Al_2O_3 samples were acquired and tested using ultrasound NDE methods to generate C-scan maps of overall attenuation coefficient for the manufacturer. Each sample was approximately 50×50 mm square with a thickness of approximately 9 mm. Ultrasonic testing was conducted using a commercially available 20-MHz central frequency planar transducer in a water-filled immersion tank.

After the initial examination, several of the samples showed a peculiar “horseshoe”-shaped pattern of high attenuation in the attenuation coefficient maps. The samples from the lot designated DIP6 showed these patterns most clearly. Another lot, DIP6H, made with the same composition as DIP6, was also tested but did not show the horseshoe pattern. The only reported difference between the 2 lots was that lot DIP6 was fired conventionally (vertically) with the samples standing with the smallest side in contact with the floor of the furnace while lot DIP6H was fired horizontally with the largest side in contact with the furnace bed. The attenuation coefficient C-scan maps for lots DIP6 and DIP6H are shown in Fig. 11.16. All images are on the same scale, 0–3 dB/cm.

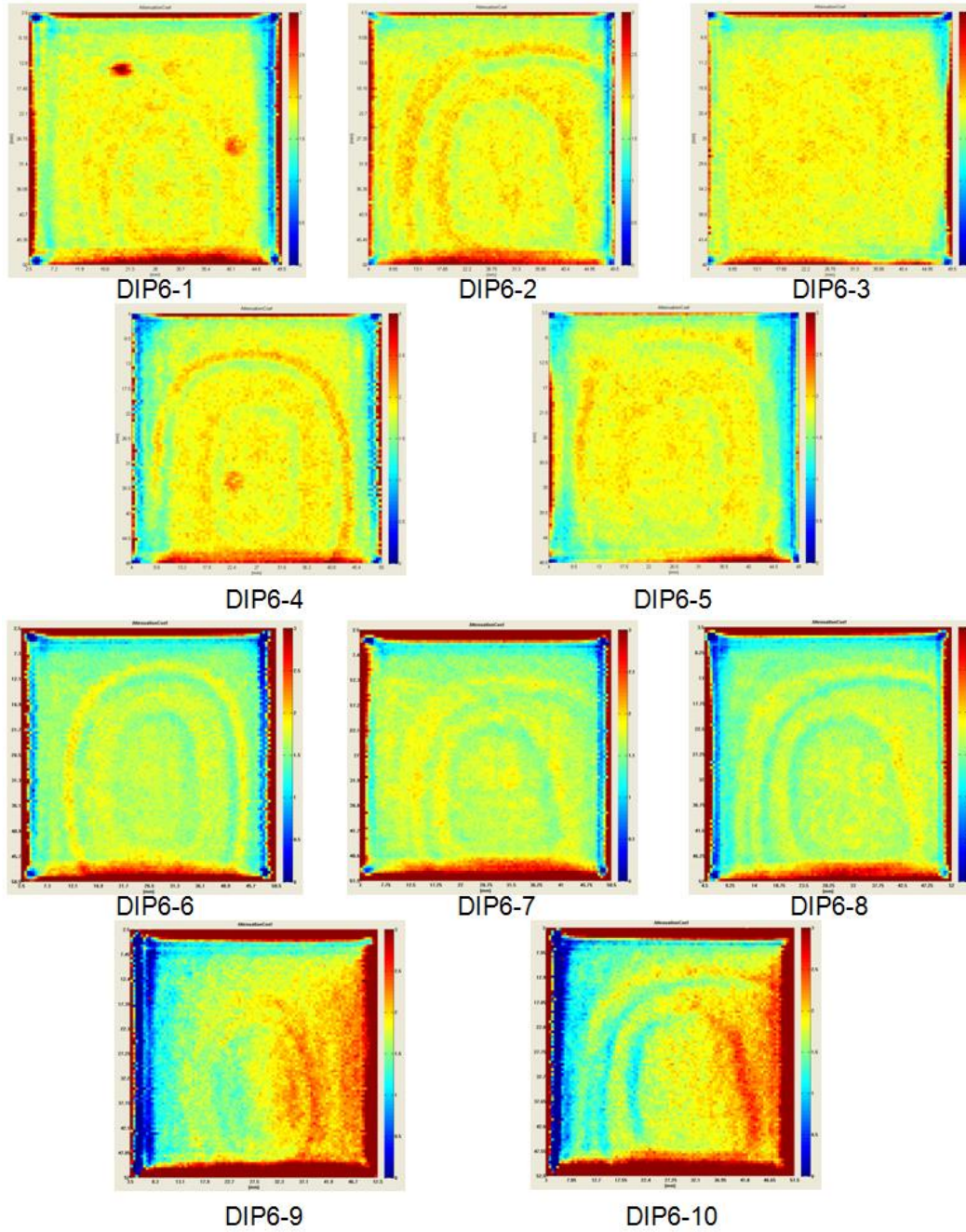


Fig. 11.16 Overall attenuation coefficient C-scan maps for Al_2O_3 lots DIP6 and DIP6H

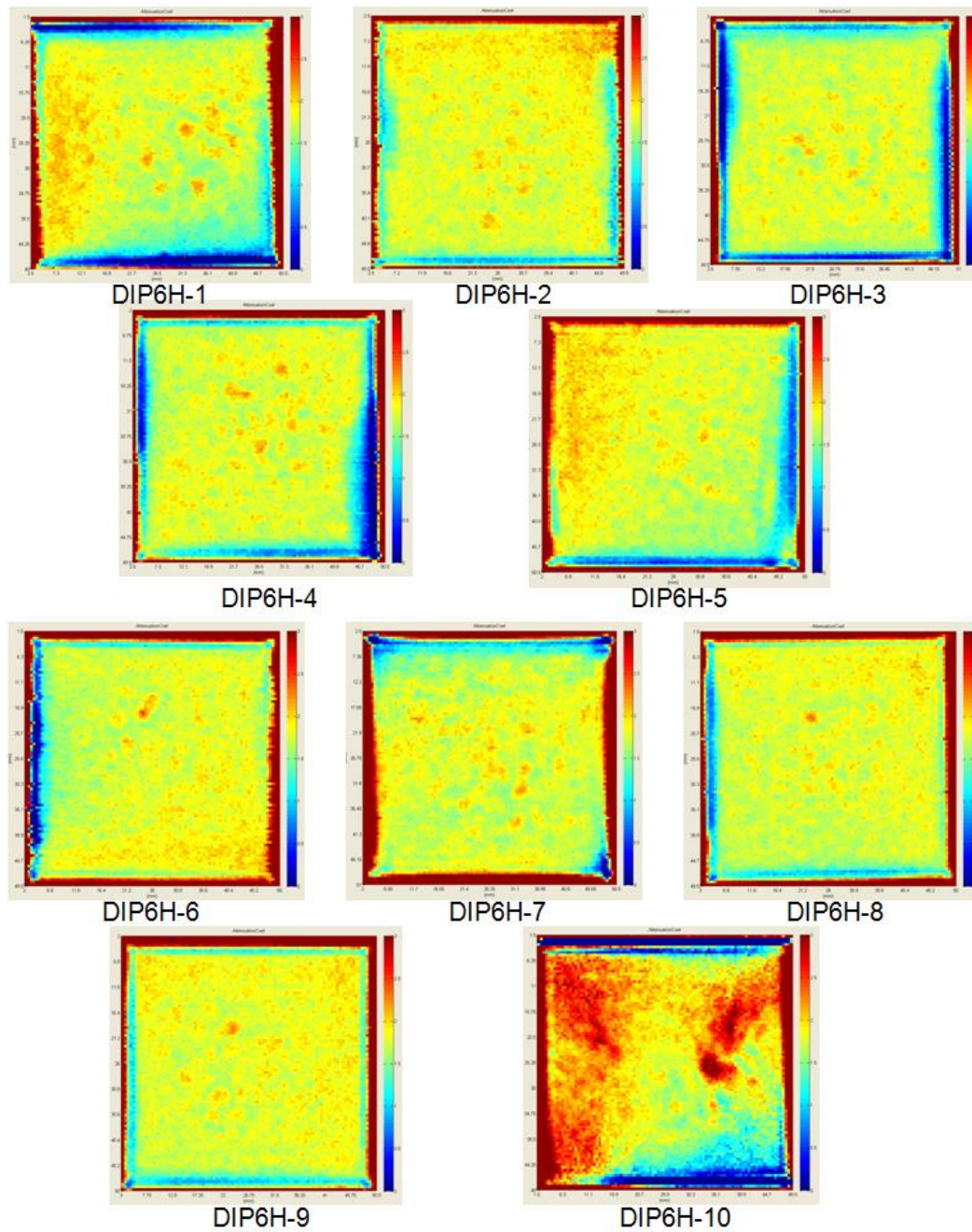


Figure 11.16 Overall attenuation coefficient C-scan maps for Al_2O_3 lots DIP6 and DIP6H (continued)

Each of the vertically fired DIP6 samples, with the exception of DIP6-3, shows a region of higher attenuation coefficient at the bottom of the sample, with rings of relatively high attenuation emanating from it, forming the horseshoe pattern. The DIP6H samples tend to be more uniform, showing no notable patterns in the

attenuation coefficient maps. It is predicted that these patterns are caused by nonuniform densification where the bottom edge of the samples densifies at a different rate than the sides and top due to contact with the floor of the furnace.

Another notable difference between the 2 lots is that the samples from DIP6H all show a number of small “spots” of slightly higher attenuation toward the center of the samples. In lot DIP6, only samples 1 and 4 show such features, and there are only 2 spots in sample 1 and one in sample 4. DIP6H-10 also shows large regions of high attenuation coefficient on the left side and top-right corner of the image in addition to these spots. These coincided with regions of significant surface roughness on the bottom of the sample, likely caused by contact with corundum on the furnace bed. Upon closer inspection, the other samples in lot DIP6H were also found to have some surface roughness but it was not as pronounced as in DIP6H-10. It can also be seen that gradients in attenuation coefficient exist in many of these samples—notably DIP6H-1 and DIP6H-2. Such gradients in properties may be caused by thermal fluctuations in the furnace itself, causing uneven densification in the samples.

To determine the microstructural cause of the features seen in the attenuation coefficient maps, several of the samples were sectioned about the features, polished to a 0.25- μm finish and examined using the FESEM. The images included in this report are from samples DIP6-1 and DIP6-4. Sample DIP6-4 was chosen for FESEM analysis because it most clearly shows all of the notable features of this lot, including the region of high attenuation at the bottom of the sample, the horseshoe pattern, and the spots of high attenuation. The sample was sectioned about these features as indicated in Figs. 11.17 and 11.18.

Figure 11.17 shows micrographs of the section of DIP6-4 taken around the horseshoe pattern. The arrows indicate the direction in which micrographs were taken; the first image was taken toward the top of the sample, with subsequent images taken going toward the bottom of the sample. There does not appear to be any particular feature that immediately stands out in this series of images. The only noticeable feature was that there was more porosity than typically seen in Al_2O_3 made by this manufacturer.

Figure 11.18 shows micrographs of the section of DIP6-4 taken about the red spot near the center of the sample. As with the previous section, there is not any one feature that stands out in the micrographs, and the section is only notable for having more porosity that would normally be expected in Al_2O_3 produced by this manufacturer.

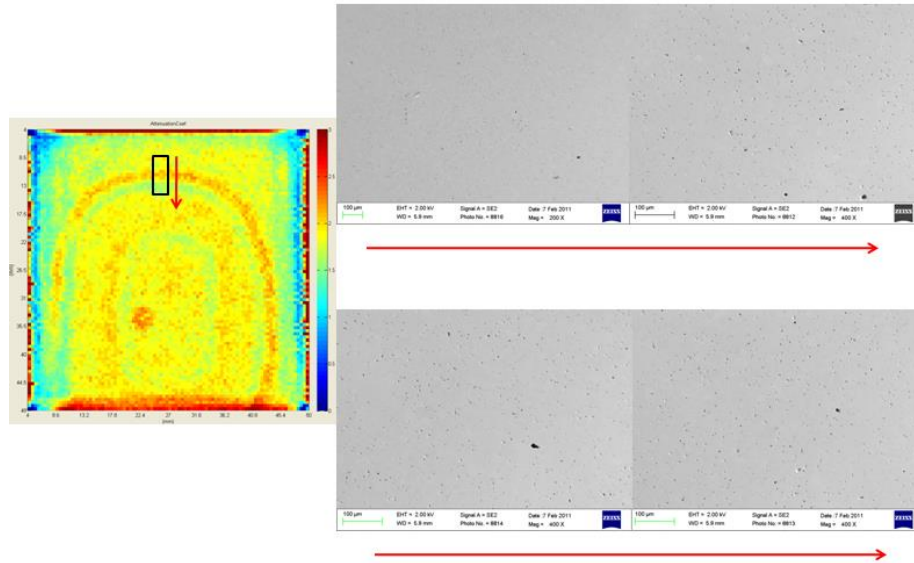


Fig. 11.17 Micrographs of “horseshoe” pattern in sample DIP6-4

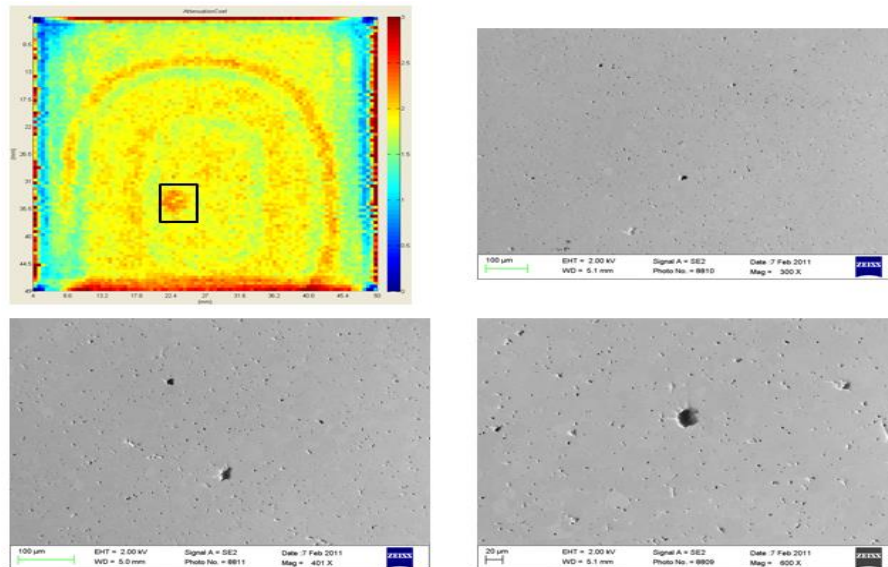


Fig. 11.18 Micrographs of red “spot” in sample DIP6-4

Figure 11.19 shows micrographs of the section of DIP6-4 taken from the region of high attenuation coefficient at the bottom of the sample. Images were taken from both the bottom of the section, where the highest attenuation coefficient values were measured, and from the top of the section, where the measured attenuation was closer to the average value for the rest of the sample. Both regions exhibited a higher degree of porosity than normally found in this manufacturer’s Al_2O_3 , but the image taken from the bottom of the section appears to show more porosity than the image taken from the top of the section. When comparing the top and bottom

sections, all porosity is approximately the same size. The increase in porosity seen in the bottom section is likely due to contact with the bed of the furnace during firing. This would cause the temperature of the sample surface in contact with the furnace floor to be lower than the rest of the sample, leading to incomplete densification.

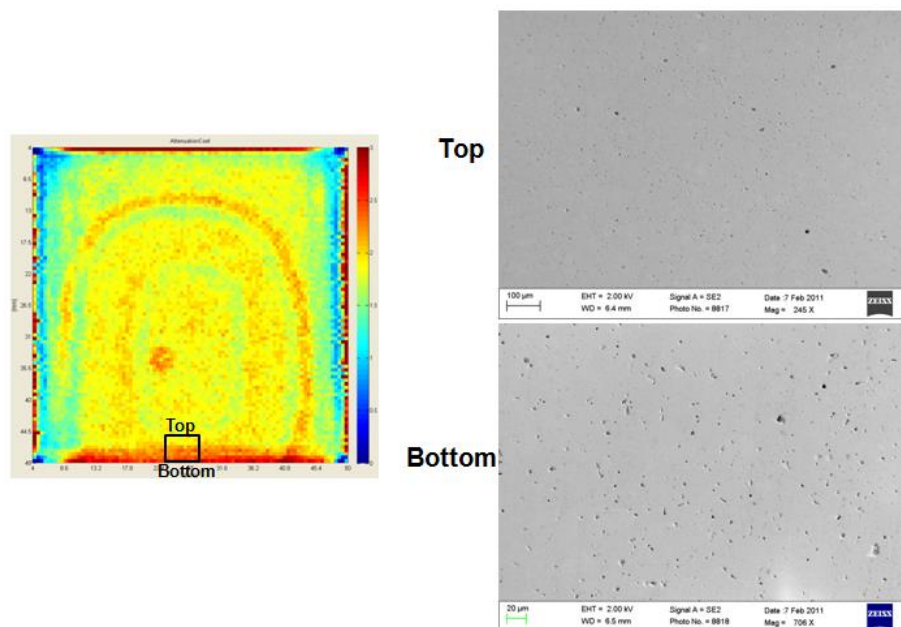


Fig. 11.19 Micrographs of high attenuation region at the bottom of sample DIP6-4

Sample DIP6-1 was chosen for FESEM analysis because it also shows spots of high attenuation. In particular, the feature on the top left of the sample stands out as having much higher attenuation, as indicated by the dark red color, than both the other feature in DIP6-1 and the spot in DIP6-4. Figure 11.20 shows micrographs from a section taken through the dark red feature. This section again shows a high degree of porosity, but the most notable features are large pools of C embedded in the microstructure. The C appears in the micrographs as dark gray areas within the matrix of lighter colored Al_2O_3 . The identity of the C was determined through EDS analysis. As with the other features previously discussed, the porosity in this section likely contributed to the increase in attenuation, but the C had the greatest effect on the attenuation, causing the attenuation in this section to be much higher than in any of the other features seen in these samples. It is believed that the C found in the microstructure is the result of incomplete burnout of an organic binder. Direct comparisons of the microstructures of lots DIP6 and DIP6H cannot be made at this time, as microscopy has not yet been performed on any of the DIP6H samples.

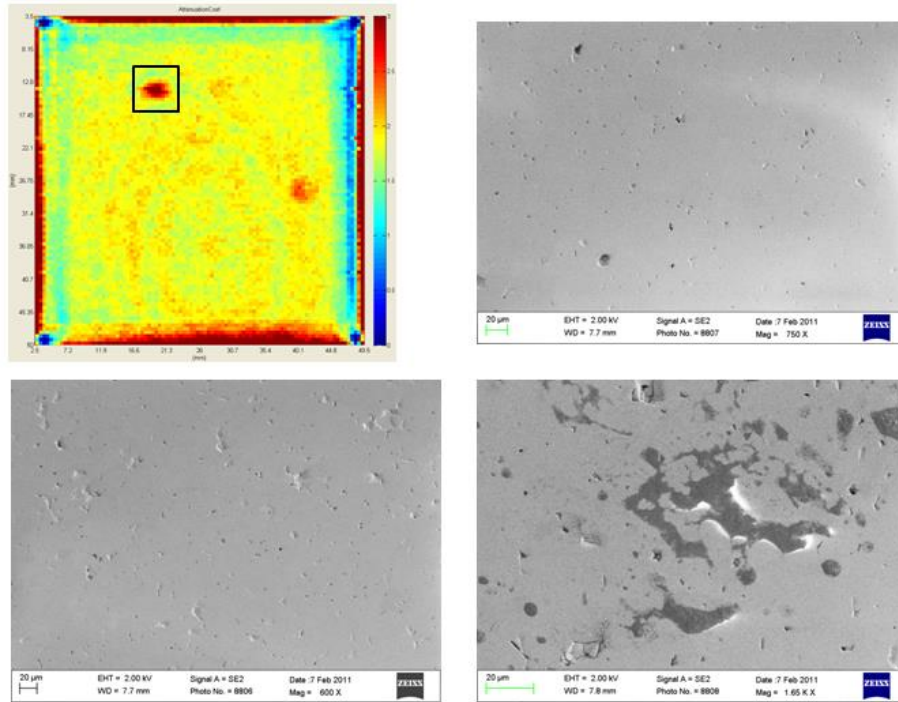


Fig. 11.20 Micrographs of dark red “spot” in sample DIP6-1

11.6 Evaluation of Microstructural Evolution Al_2O_3 Sample Series: Grain Size, Ultrasonic Attenuation Coefficient, and Hardness Relationships, by Steve Bottiglieri

This section reports the results shown for the October 2010 Rutgers Malcolm G McLaren Center for Ceramic Research (Rutgers-CCR) Meeting, and results are a necessary introduction for the continuation of this work shown in the following section.

Nine sample lots of Al_2O_3 containing 8 samples each were created (Industrie Bitossi, Vinci, Italy) to have systematic changes in grain size. This was done by increasing the dwell time and/or the firing temperature of the Al_2O_3 specimens. The formulation and firing cycles of these samples are proprietary to Industrie Bitossi. It is known that each Al_2O_3 tile contains 98% Al_2O_3 and 2% $\text{SiO}_2\text{-MgO-CaO}$. The initial firing temperature and dwell time is denoted as T_0 and D_0 , respectively. Increases in temperature are made in 50 °C increments from T_0 to T_0+100 °C, and increases in dwell time are made as $D_0+5\text{h}$ and $D_0+15\text{h}$. This sample set controls one variable that effects the attenuation of ultrasound: scattering due to grain size. Work has been done by others on the determination of grain size and material properties dictated by grain size in metals; however, at this time it is unsure and unlikely that the relationships determined for metallic systems hold true for heterogeneous ceramic systems.

Initial studies at Rutgers-CCR was performed in verifying that the 9 Al_2O_3 sample lots do indeed change grain, what the average grain size is, hardness, overall homogeneity measured acoustically, and changes in acoustic spectra. Initial results found correlations between changes in grain size and hardness with acoustic attenuation. These results are based on the wave scattering theory of Rayleigh, Mie, Bouda, and others. At the time that this work was performed, the useable acoustic bandwidth was approximately 10–30 and 40–70 MHz. Error in curve fitting results is due to a lack of larger bandwidths. Further studies (to follow) will include extension to higher frequencies (80–110 MHz), larger sampling of FESEM images for measured grain size determination, larger sampling of hardness measurements to decrease variability, and the implementation of acoustic scattering hypotheses created at Rutgers-CCR to draw stronger correlations with measured data.

Lower frequency attenuation coefficient spectra (10–30 MHz) do not show prominent scattering behavior; at these frequencies the spectra between different samples are somewhat indistinguishable. It is not until higher frequencies (40–70 MHz) that there is distinction between dwell time, firing temperature, and acoustic attenuation. Figure 11.21 shows the attenuation spectra of arbitrarily chosen samples from each of the 9 Al_2O_3 samples lots. The spectra shown in Fig. 21 may appear to be convoluted; however, upon graphing the spectra according to either changes in dwell time or firing temperature, one can notice the correlation with attenuation coefficient (shown in Figs. 11.22 and 11.23).

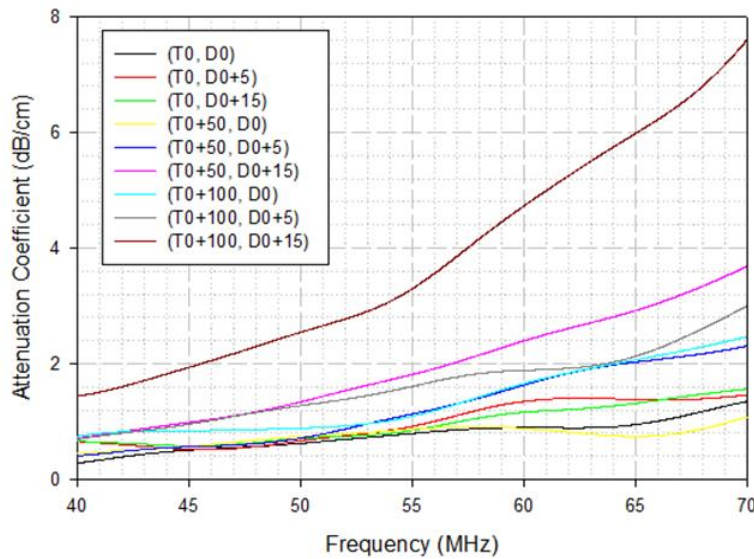


Fig. 11.21 Acoustic attenuation coefficient spectra of 9 arbitrarily chosen Al_2O_3 samples from the Microstructural Evolution Alumina set

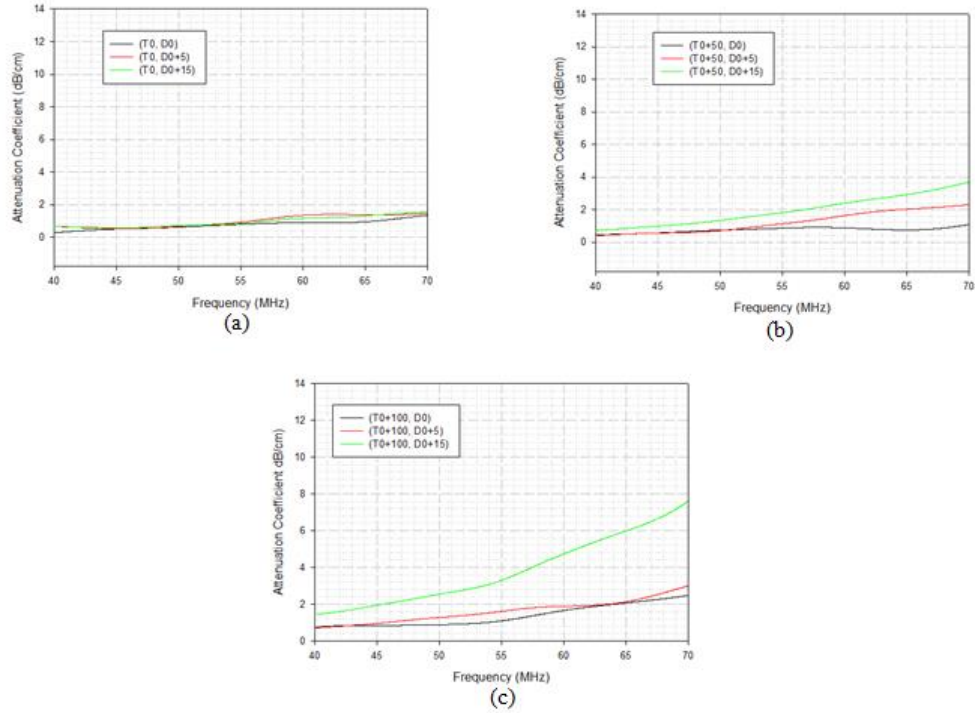


Fig. 11.22 Acoustic attenuation coefficient spectra of samples from the Microstructural Evolution Alumina set: a) T0 held constant, b) T0+50 held constant, and c) T0+100 held constant

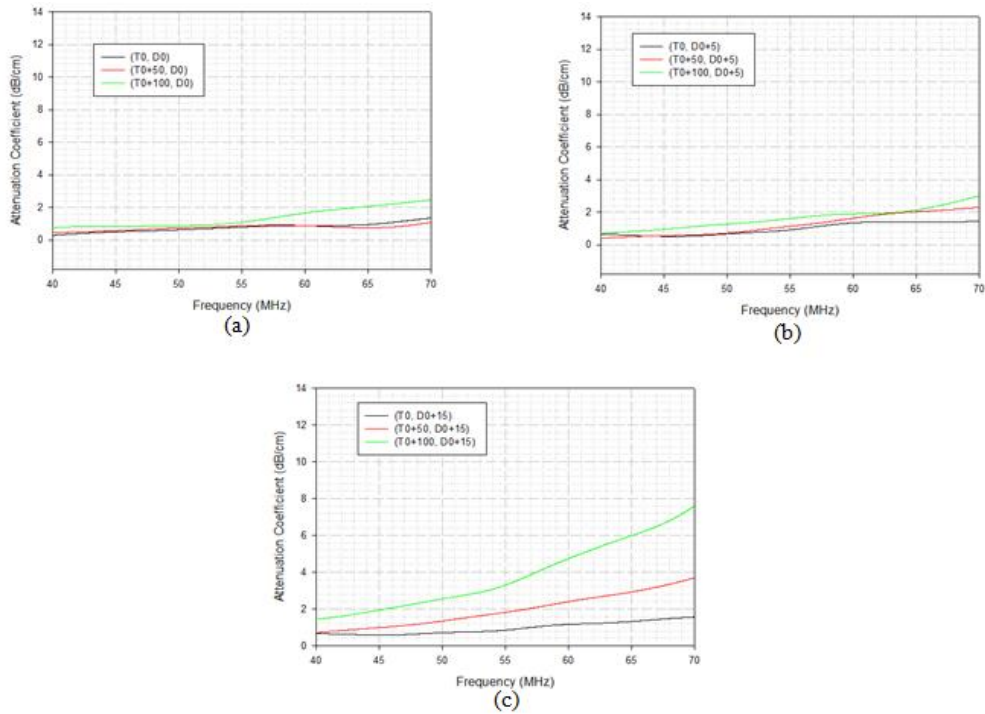


Fig. 11.23 Acoustic attenuation coefficient spectra of samples from the Microstructural Evolution Alumina set: (a) D0 held constant, (b) D0+5 held constant, and (c) D0+15 held constant

According to current acoustic scattering theory, these scattering curves should follow a power law where the exponents are between 2 and 4 (stochastic or Rayleigh scattering). Upon performing a power-law curve fit, it was noticed that the attenuation coefficient scattering curves for this Al_2O_3 (as well as other types of ceramic materials) do not result in having an exponent between 2 and 4. This is believed to be due to the finite bandwidth that is used to measure attenuation coefficient. Extension to higher frequencies has been used for measurement of 9 more Al_2O_3 samples from the same sample set for further study and is shown in Fig. 11.24.

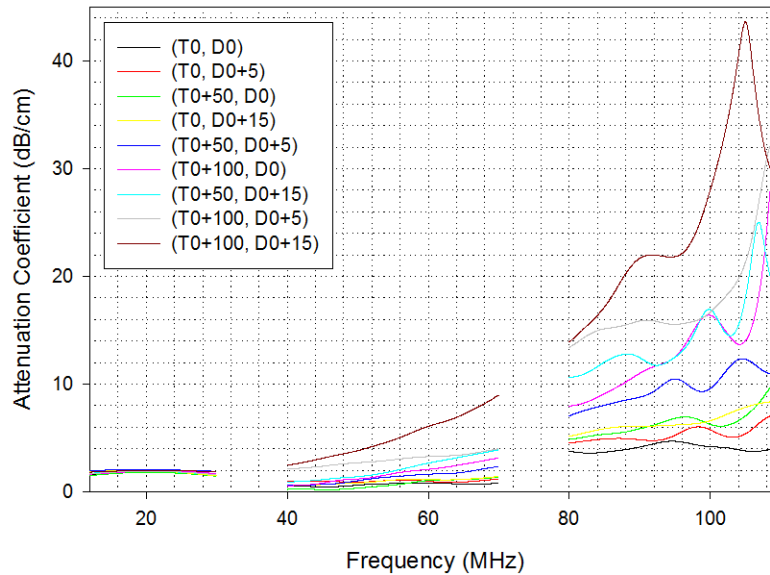


Fig. 11.24 Attenuation coefficient spectrum of second round of arbitrarily selected samples from the Microstructural Evolution Alumina sample series

After obtaining a 150-MHz central frequency transducer, this testing process has begun to be performed again. Nine more samples from each of the Microstructural Evolution Alumina sample set have been arbitrarily chosen for study. The use of the higher frequency transducer will allow for a larger bandwidth of attenuation coefficient data, which will lead to more-accurate curve fitting results. Although the new transducer is nominally 150 MHz, much of the higher frequency sound energy is scattered before it enters the sample. The -6 dB points for the acceptable frequency range in this Al_2O_3 is 80–110 MHz. Figure 11.24 shows the up-to-date attenuation coefficient spectra for 9 arbitrarily chosen Al_2O_3 samples, which vary in grain size.

11.7 Development of a Relationship Between Ultrasonic Attenuation Coefficient and Grain Size Variation in Al_2O_3

Each the 9 Al_2O_3 samples that vary grain size have been sectioned about the point where the attenuation coefficient spectrum was measured. The sections were polished to a mirror finish and etched using boiling phosphoric acid. FESEM micrographs of these etched sections are shown in Fig. 11.25. The arrows indicate the ordering of the samples as according to their increase in grain size. Grain sizing was performed again on each sample to obtain better statistics. Results varied slightly from the last grain size measurements as more data was added. Four micrograph images from each section where approximately 500 grains from each sample were sized and used to create grain size distributions. Statistical data from these distributions was obtained and is shown in Fig. 11.26, which represents what can be perceived as a top-down view of each sample's grain size distribution.

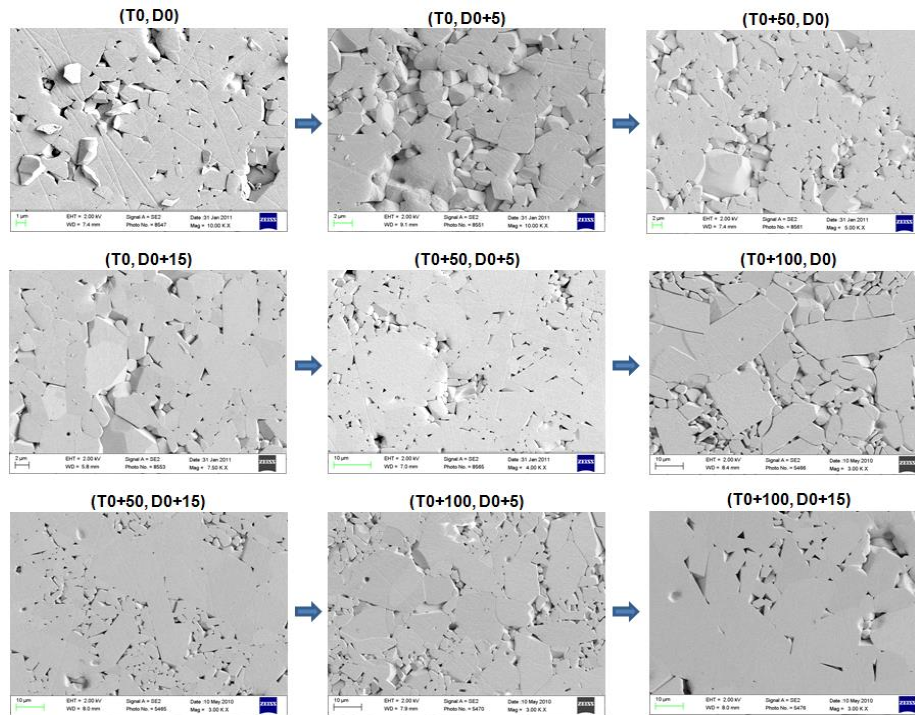


Fig. 11.25 Micrograph images from each Al_2O_3 sample from the grain size variant set. Note the differences in magnification for each image. Arrows indicate order of grain size increase between samples.

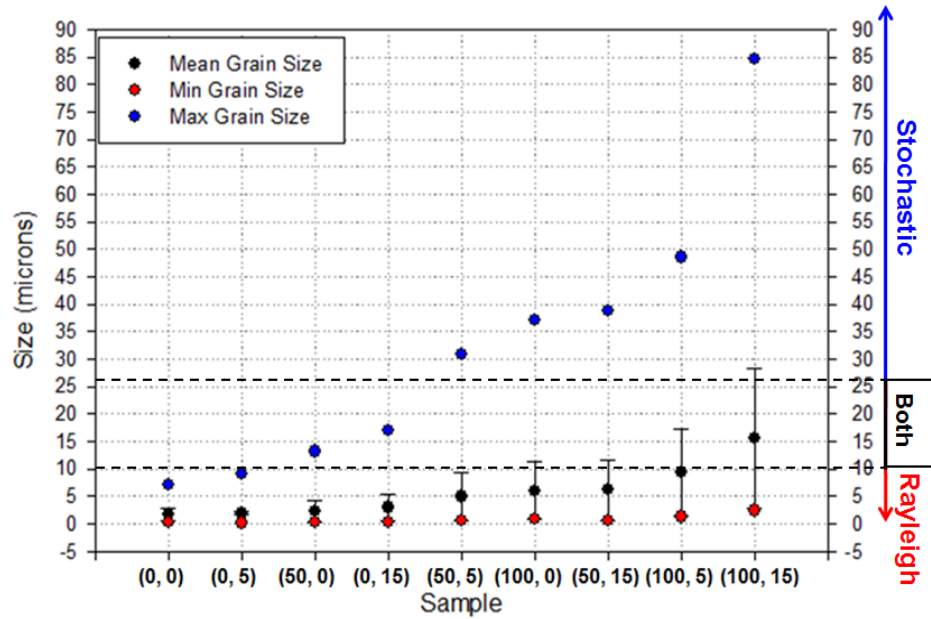


Fig. 11.26 Statistical data from measured grain size distributions; (x,y) represents (+temperature [Celsius] increase from standard, +dwell time (hours) from standard). The 2 operable scattering regimes are shown based on size scale.

The sample name designation for Fig. 11.26 is of the form (x, y) where x represents an increase in firing temperature (in Celsius) and y represents an increase in dwell time (in hours) at the maximum hold temperature. The increase in temperature and dwell time is referenced from the manufacturers proprietary standard firing cycle. Also shown on the right of the graph are regions of where either Rayleigh scattering, stochastic scattering, or both occur according to size. Most samples (the ones with larger grain sizes) all have at least parts of their upper tails of grain size distributions that fall in the stochastic scattering regime. According to the Mie scattering solution, which is valid for any size-to-wavelength ratio, stochastic scattering is approximately 10,000 times stronger than Rayleigh scattering (for single particles of corresponding sizes and frequencies). A question that results from this is, “Do a few large grains outweigh many small grains and cause prominent stochastic scattering”?

The grain size information collected from the FESEM micrographs of each sample was calculated using Heyn’s lineal intercept method. This involves drawing lines across each micrograph image and placing points where the line intersects with a grain. Calibration of pixel length to actual length is performed, and the computer gives measured grain sizes. Stereographic effects must be taken into account. If one assumes the material is made up of spherical grains of different—upon sectioning, polishing, and measuring—grain size, one would find that the measured grain size is an underestimate by 1.5 times. This is because sectioning and polishing is not

likely to reveal the great diameter of each sphere. Therefore, one would never see the true size of the grain in a FESEM micrograph. A visual representation of this is shown in Fig. 11.27.

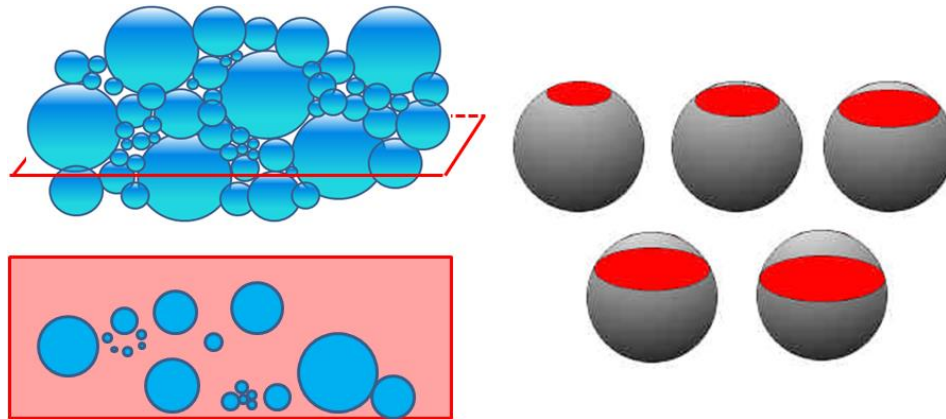


Fig. 11.27 Stereographic effects on FESEM micrograph images

Al_2O_3 grains are hexagonal in nature, so an underestimate of 1.5 times for each measured grain is an upper limit of what the measured deviation from the true grain size would be. Figure 11.28 shows the same statistical data shown in Fig. 11.26 corrected for stereographic effects by using the upper limit of 1.5 times. Results now show that the grain sizes for each sample are in fact a bit larger and would be causing even greater stochastic scattering. The standard baseline sample, (T0, D0), still shows grain sizes that will only cause Rayleigh scattering.

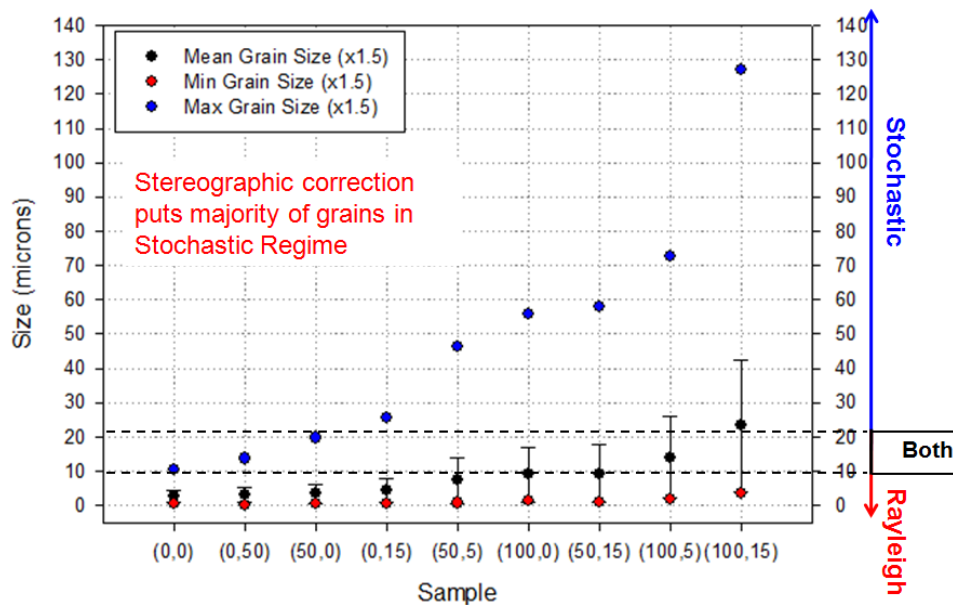


Fig. 11.28 Statistical data from measured grain size distributions. Corrected for stereographic effects: (x,y) represents (+Temperature [Celcius] increase from standard; +Dwell time [hours] from standard). The 2 operable scattering regimes shown are based on size scale.

Curve fitting the measured attenuation coefficient spectra to a general power law (Eq. 4) should give exponents that range from 4 to 2 as grain size increases. The coefficient of a general power law should be linear with average diameter cubed. Each attenuation coefficient spectra was fit to a curve (Eq. 4). The factors A and n were tabulated for each sample and the measured average diameters were used to verify a linear relationship with the A factor. Table 11.6 shows the collected curve fit parameters. Figure 11.29 shows the A parameter of each curve fit as a function of measured average grain diameters. Unfortunately, the expected behavior was not found, due likely to ill-defined information being given to the curve fit algorithm used by MATLAB.

$$\alpha = Af^n. \quad (4)$$

Table 11.6 Curve fit parameters for each sample spectra

Sample	A Parameter	n Parameter
(T0, D0)	1.13E-08	2.28
(T0, D0+5)	5.18E-09	2.52
(T0+50, D0)	3.79E-10	3.14
(T0, D0+15)	2.11E-09	2.76
(T0+50, D0+5)	2.57E-09	2.80
(T0+100, D0)	6.21E-11	3.70
(T0+50, D0+15)	1.15E-09	3.07
(T0+100, D0+5)	1.04E-09	3.14
(T0+100, D0+15)	2.72E-09	3.01

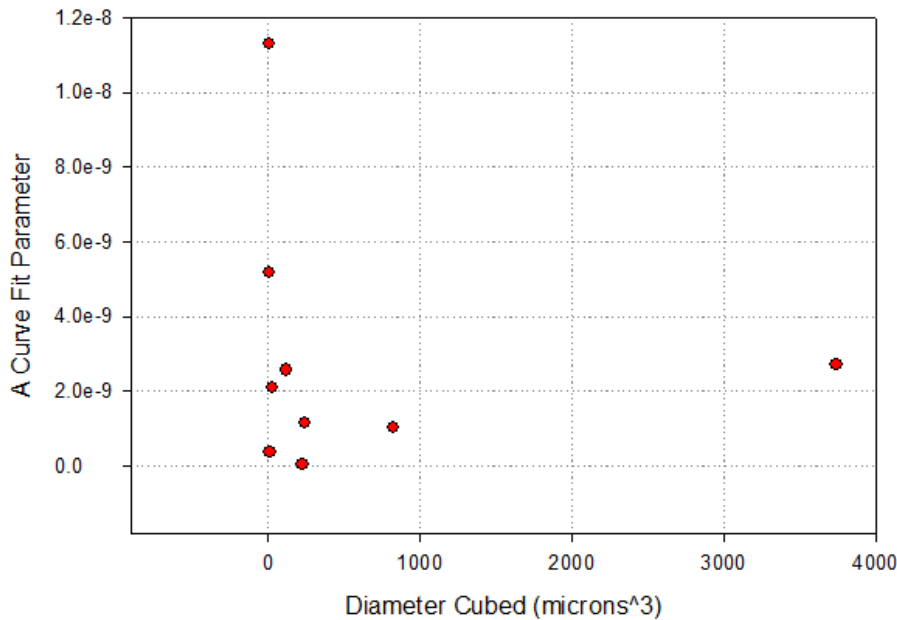


Fig. 11.29 A-curve fit parameter as a function measured average grain diameter cubed for each sample. Graph shows that a linear relationship does not exist.

The next step assumed that each sample follows either Rayleigh or stochastic scattering according to the approximations shown in Table 11.6. For both cases (either f^4 for Rayleigh scattering or f^2 for stochastic scattering), each attenuation coefficient spectra was inverted to solve for the scattering prefactors C_R and C_S at each frequency. The averages of these values for each sample spectra were tabulated and graphed in Figs. 11.30 and 11.31. The measured average grain sizes were used for the diameter terms in each equation. Stereographic correction was not performed for these calculations, as the results will differ by a common, known factor that was corrected for afterward.

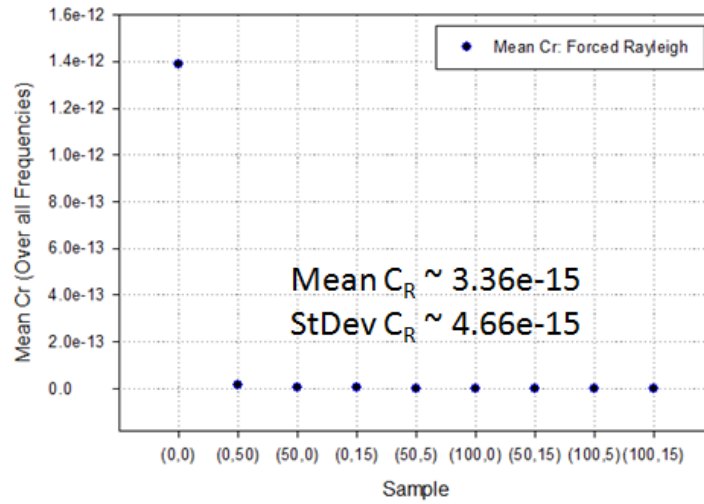


Fig. 11.30 Rayleigh C_R scattering prefactors. Note the large standard deviation.

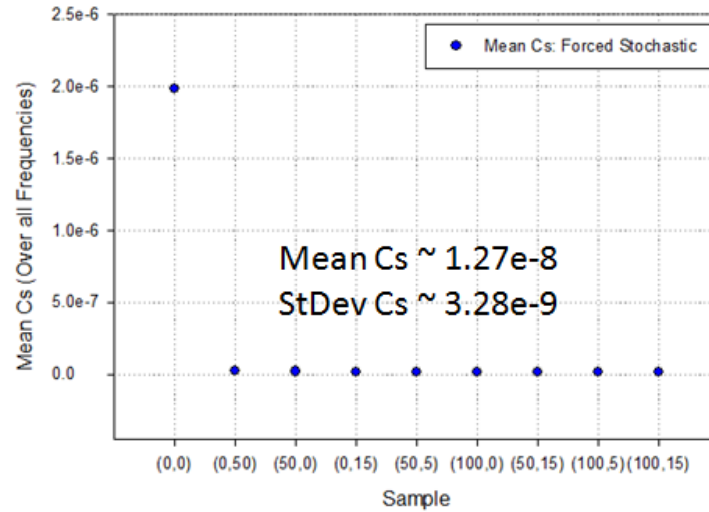


Fig. 11.31 Rayleigh C_S scattering prefactors. Note the smaller standard deviation.

A strong difference between Figs. 11.30 and 11.31 are their differences in standard deviations. Stochastic scattering appears to be a more likely candidate for the dominant scattering mechanism in almost all of these samples. The standard sample (T0, D0) with the smallest grain sizes is the outlier and is showing the disconnect between Rayleigh and stochastic scattering.

After correcting the mean C_R and C_S values for stereological discrepancies, it was decided to use the C_R value calculated from the sample that contained the smallest grain sizes and is showing Rayleigh behavior, (T0, D0), as a standard for the Rayleigh scattering approximation. The sample that contained the largest grain sizes, (T0+100, D0+15), had its calculated stochastic prefactor, C_S , used as a standard as well. The test is to use both prefactors as standard for the rest of the samples and see which one gives a better fit with measured grain size data. The values for C_R and C_S are $4.12\text{e-}13$ and $8.45\text{e-}9$, respectively. Figure 11.32 shows the predicted average grain sizes assuming either Rayleigh or stochastic scattering compared with the stereographic corrected measured mean grain sizes.

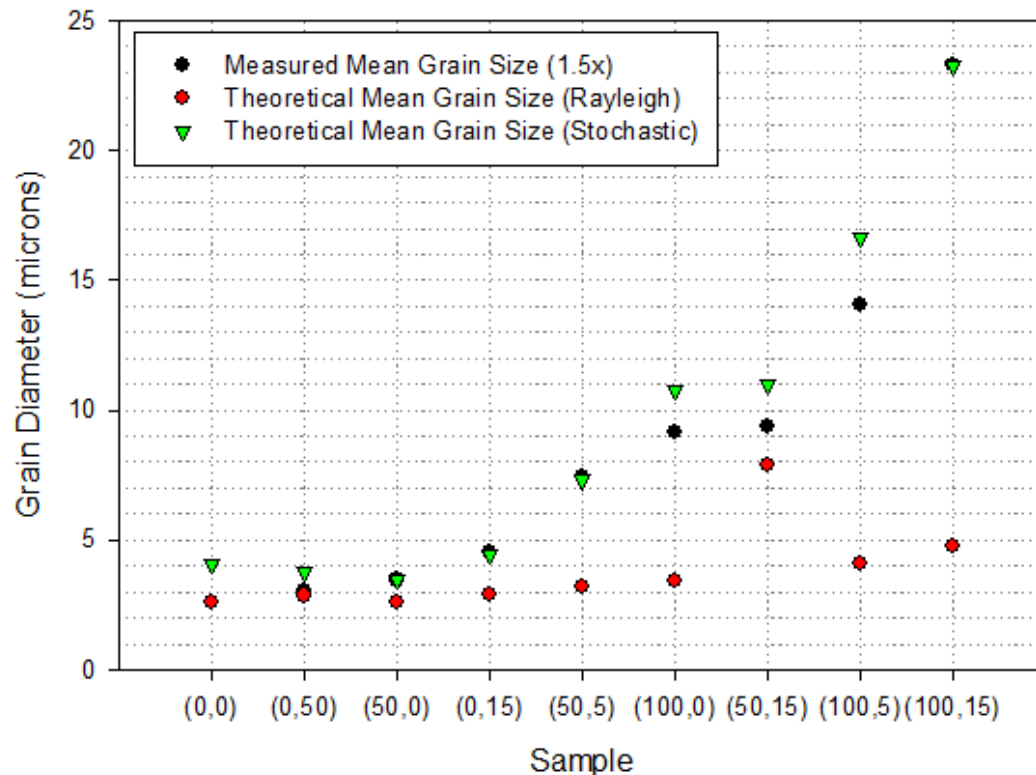


Fig. 11.32 Comparison of measured mean grain size (corrected for stereography) and predicted grain sizes using Rayleigh and stochastic scattering

Figure 11.33 shows comparisons just between measured mean grain size and predicted grain sizes using either Rayleigh or stochastic scattering, respectively. A linear fit between data points with a slope of 1 represents the best fit between measured data and predicted data. Predicted average grain sizes using Rayleigh scattering for these samples show a poor fit with measured average grain sizes with a slope of 0.12, assuming stochastic scattering gives a much better fit with measured data having a slope of 1.01. This complements the concept that a few large grains causing stochastic scattering completely dominates and overwhelms attenuation spectra when compared with many small grains causing Rayleigh scattering.

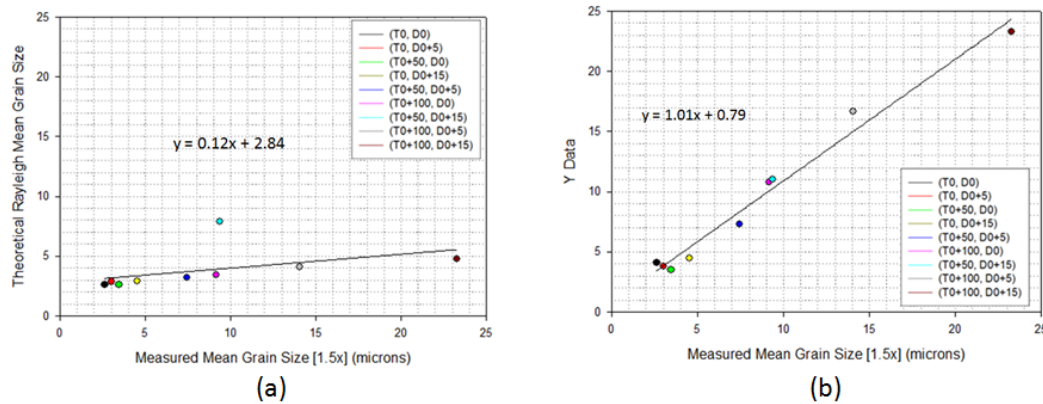


Fig. 11.33 Comparison of measured mean grain size (corrected for stereography) and predicted grain sizes using a) Rayleigh and b) stochastic scattering. Linear fits reveal how well the predicted data matches with measured data.

As a test of this concept, 3 random Al_2O_3 samples (known to have similar additive compositions) were chosen for prediction of mean grain size maps. These samples are labeled as Alumina A, B, and C and their sizes measure 50×50 mm in the lateral dimension and 11, 5, and 6 mm in the axial dimension, respectively. Measurements performed include 20-MHz overall attenuation coefficient C-scan mapping to determine possible large variability or heterogeneity, 75-MHz attenuation coefficient spectra C-scan maps, 75-MHz point attenuation coefficient spectra, and 150-MHz point attenuation coefficient spectra. These data are shown in Figs. 11.34–11.36. The 75-MHz attenuation coefficient spectra C-scan maps were unable to collect full sample information because the samples did not have even enough surfaces (a common problem with scanning samples at higher frequencies). Therefore, portions of each sample were scanned to reduce erroneous data collection. Attenuation coefficient spectra maps were unable to be collected with the 150-MHz transducer.

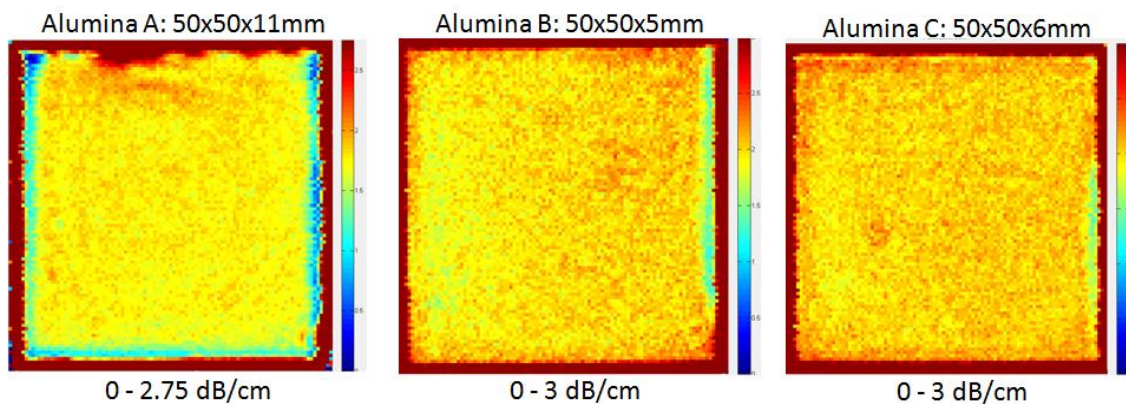


Fig. 11.34 Overall attenuation coefficient C-scan images (20 MHz) of 3 randomly chosen Al_2O_3 samples

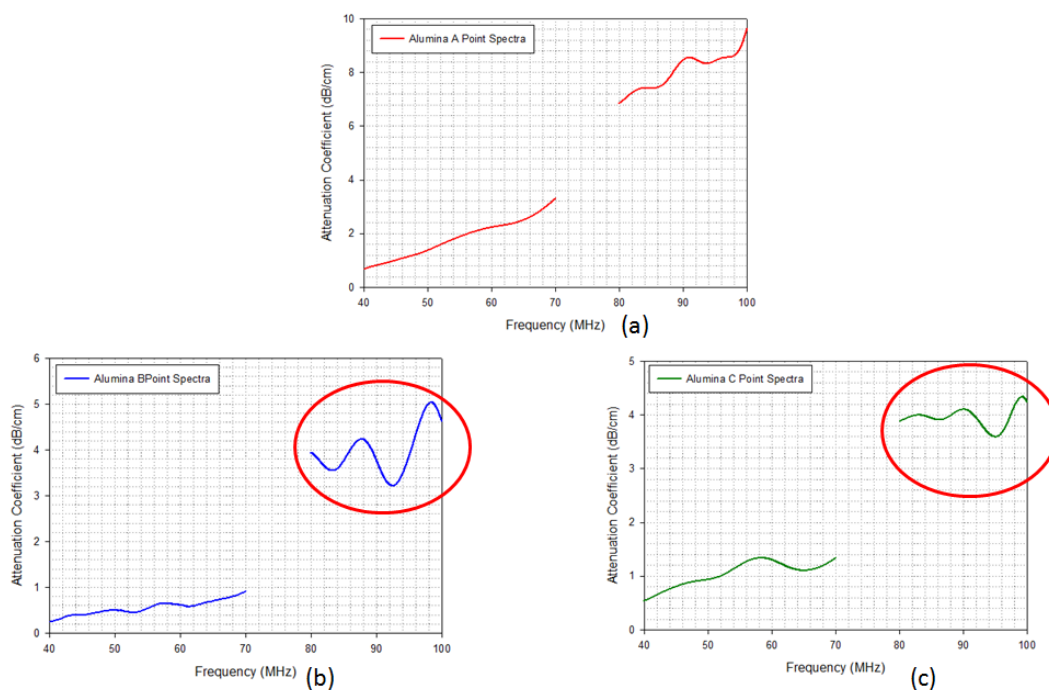


Fig. 11.35 Point attenuation coefficient spectra: a) Alumina A, b) Alumina B, and c) Alumina C

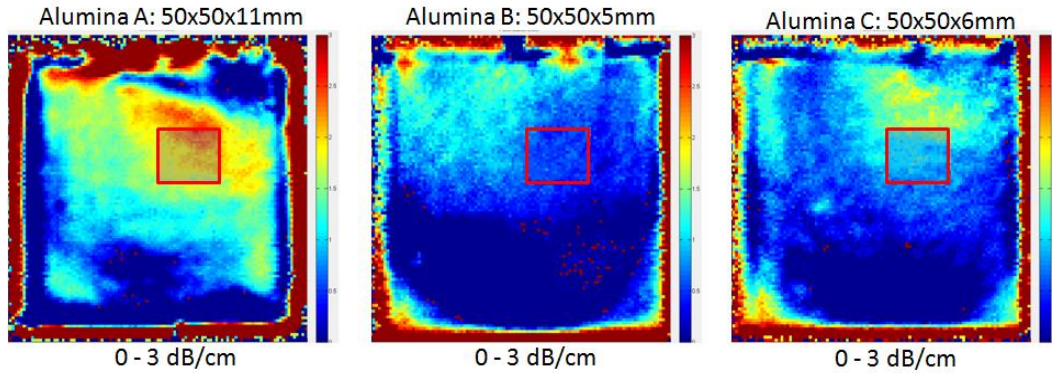


Fig. 11.36 Overall attenuation coefficient C-scan images (75 MHz) of 3 randomly chosen Al_2O_3 samples. Map inconsistency in the maps is due to sample nonuniformity. Red sections indicate where smaller area scans occurred.

Predicted values for grain sizes about single points in these 3 samples were calculated using the attenuation coefficient data collected on frequency ranges of 40–70 and 80–100 MHz, the standard Rayleigh and stochastic scattering prefactors (C_R and C_S) obtained from the previous study, and the scattering approximations given in Table 11.6. Unfortunately, at this time it is unknown whether the samples will have grain sizes that will cause Rayleigh or stochastic scattering; therefore both cases were calculated. The Rayleigh-predicted values for Alumina A–C are 2.23, 1.65, and 1.89 μm , respectively, while stochastic-predicted values for samples A–C are 6.57, 2.41, and 3.22 μm , respectively.

Figures 11.37–11.39 shows mean grain size maps about the points collected from the red sections using only frequencies of 40–70 MHz. Discrepancy between the average of these predicted mean grain size maps and the point measurements is caused by the point measurements having a larger frequency data set than the maps.

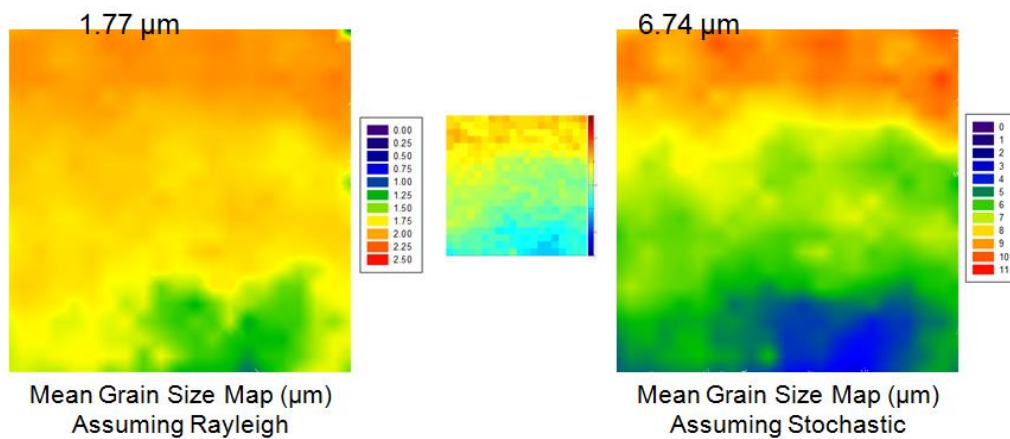


Fig. 11.37 Ultrasound-predicted mean grain size maps of Alumina A. Numbers above maps show average values for entire map. Small map in center is the 75-MHz overall attenuation coefficient C-scan image used to create the grain size maps. Notice the similarity in behavior between C-scan image and predicted mean grain size map.

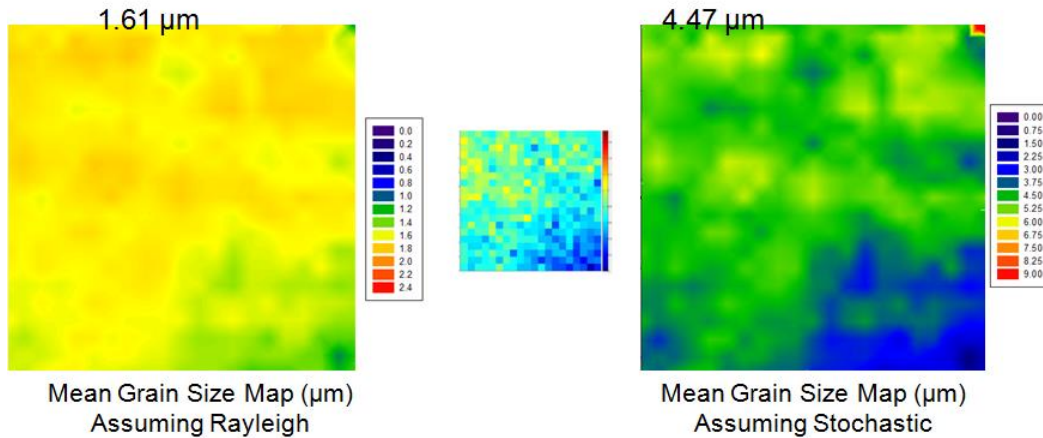


Fig. 11.38 Ultrasound-predicted mean grain size maps of Alumina B. Numbers above maps show average values for entire map. Small map in center is the 75-MHz overall attenuation coefficient C-scan image used to create the grain size maps. Notice the similarity in behavior between C-scan image and predicted mean grain size map.

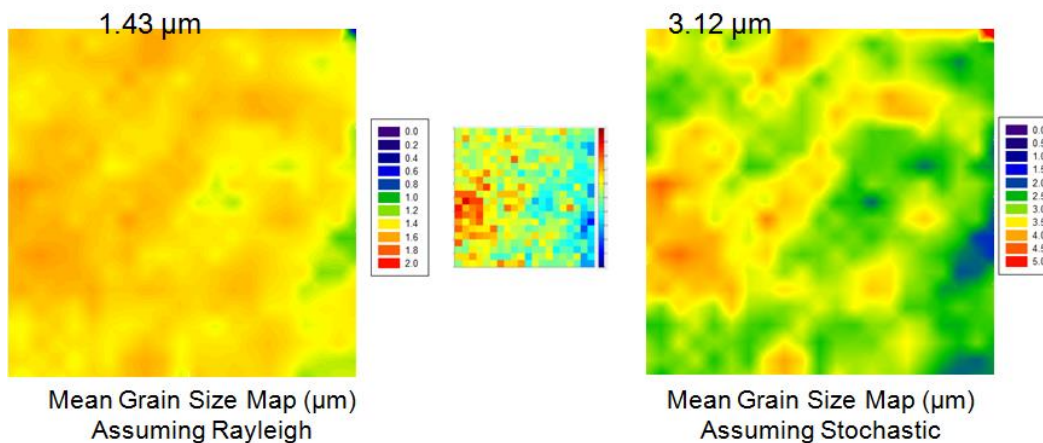


Fig. 11.39 Ultrasound-predicted mean grain size maps of Alumina C. Numbers above maps show average values for entire map. Small map in center is the 75-MHz overall attenuation coefficient C-scan image used to create the grain size maps. Notice the similarity in behavior between C-scan image and predicted mean grain size map.

The mean grain size maps, for both cases of Rayleigh or Stochastic, match with what is seen in the higher frequency (75 MHz) overall signal attenuation coefficient C-scan image. This is in congruence with what was shown in the October 2010 center report with grain size mapping of silicon carbide.

11.8 Investigation of Acoustic Absorption and Secondary Phase Size Distributions in Custom-Engineered Al_2O_3 , by Steve Bottiglieri

Acoustic spectroscopy has been proven as a useful tool for measuring particulate size in dilute suspensions, determining average grain size in metallic systems, and understanding differences in mechanical properties such as hardness in metals. When analyzing an acoustic spectrum, one must consider the frequency bandwidth emitted by the transducer and which attenuation mechanisms are operable in said frequency ranges. Different materials systems, such as particulate suspensions, metals, glasses, and ceramics will cause different types of ultrasonic loss. Scattering and absorption are the 2 general regimes of acoustic loss mechanisms that have been studied. Understanding how scattering and absorption occur in different material systems allows for the calculation of microstructural information by the deconvolution of measured attenuation spectra. Particulate size distributions and average grain sizes in metals may be measured through the use of acoustic spectroscopy and knowledge of how scattering and absorption take place in these specific systems.

The overarching regimes of absorption and scattering are further broken down into specific types of absorption and scattering, for example: thermoelastic, viscoelastic, thermal conduction, hysteresis, phonon-phonon interaction, and Rayleigh, stochastic, and diffuse scattering. Depending on the frequency range and material studied, different absorption and scattering mechanisms will be prevalent. For example, in metallic systems, scattering due to grains dominates losses seen in an attenuation spectrum. Using high-frequency ultrasound (in the megahertz range) to measure attenuation coefficient spectra in polycrystalline ceramic materials, it has been shown that thermoelastic absorption dominates losses seen at approximately 50 MHz and below. At frequencies higher than 50 MHz, scattering begins to overwhelm the attenuation curves and is the prominent loss mechanism. This section focuses on studying the frequency range where thermoelastic absorption is operable (10–30 MHz) for a set of tailored engineered Al_2O_3 samples that have been fabricated to have increasing concentrations of mullite.

Intraparticle thermoelastic absorption is the coupling of the elastic and thermal fields created by the propagating acoustic wave. Local changes in temperature are controlled by the coefficient of thermal expansion and the direction of the acoustic wave. The regions of the material that are in rarefaction will cool slightly, while regions in compression will heat up. Heat flow between the compressed and rarefacted regions occurs to seek equilibrium and maintain field continuity between the elastic and thermal fields. This heat flow is irreversible, which causes a loss in

energy that is in turn measured as acoustic attenuation. In his development on the internal friction in solids, Clarence Zener came up with an expression that relates the frequency of maximum attenuation for a single particle to the size of the particle and its thermal properties (Eq. 5). This relationship is used as the basis in the derivation of how much energy a single particle absorbs.

$$f = \frac{\pi\chi}{2\rho C_v a^2}, \quad (5)$$

where f is frequency, a is particle diameter, χ is thermal conductivity, ρ is density, and C_v is the specific heat at constant volume.

This report makes the assumption that energy loss due to thermal elastic absorption is equal to the number of absorbing particles multiplied by the volume of those particles multiplied by a scaling factor as seen in Eq. 6. The volume of the particle is dictated to be a function of frequency and assumed to be spherical after inverting Eq. 5 to solve for diameter. This volume can be calculated based on the thermal properties of the material of interest and the frequency range used.

$$E_{TE}(f) = S(f) \cdot V_{TE}(f) \cdot N_p(f), \quad (6)$$

where the energy absorbed is in units of joules and volume in meters cubed; S must have units of Pascals as a result. The second assumption of this derivation is that particles of a specific size only absorb at frequencies as dictated by Eq. 5. Another way of stating this assumption is that the thermoelastic absorption occurs on a time scale that can be thought of as instantaneous. A final assumption is that only thermoelastic absorption causes energy loss in the frequency range of interest. This assumption may be remedied if one has considerable scattering losses at these frequencies and can include corrections for such losses.

The energy measured is equal the initial acoustic energy introduced into the specimen by the transducer minus the energy lost due to thermoelastic absorption (Eq. 7).

$$E_m(f) = E_i(f) - E_{TE}(f). \quad (7)$$

The initial energy will depend on the frequency bandwidth of transducer output and can be measured by performing a Fourier transform on a transducer delay line peak measured in an oscilloscope. The result is a power spectral density that has units of W·s, or joules. From the Beer-Lambert law, the following is known:

$$E_m(f) = E_i(f) \cdot e^{-\alpha(f) \cdot x}, \quad (8)$$

where α is the measured attenuation coefficient (corrected for geometric losses) and x is sample thickness. Substitution and rearrangement yields an equation for the S

parameter, which is a function of both the transducer output and the measured sample attenuation (Eq. 9).

$$S(f) = \frac{E_i(f) \cdot (1 - e^{-\alpha(f) \cdot x})}{N_p(f) \cdot V_{TE}(f)}. \quad (9)$$

To determine the S parameter, E_i was measured (Fig. 11.36) and a 100% Al_2O_3 sample was created in a SPS unit to use as a standard for the number of particles. A particle size distribution for the Al_2O_3 sample was measured from FESEM micrographs and then normalized to be equal to what volume is contained in the path of the ultrasound beam, as shown in Fig. 11.40.

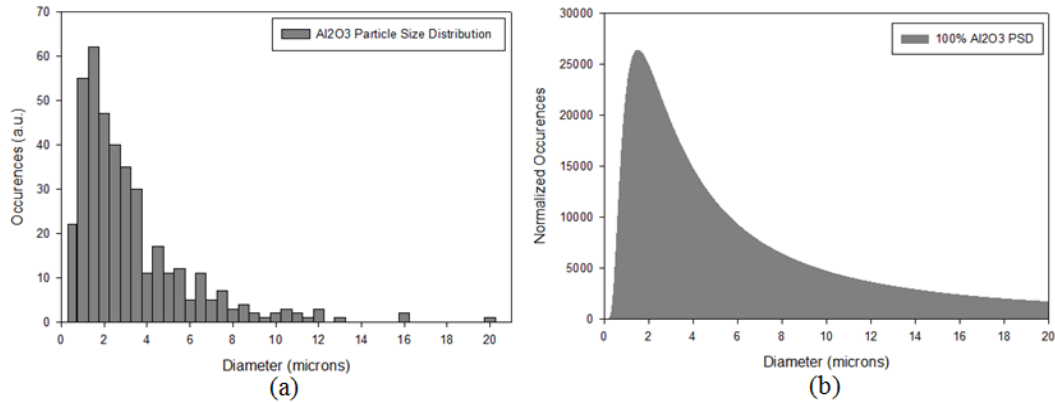


Fig. 11.40 a) Measured particle size distribution of 100% Al_2O_3 sample and b) ultrasound beam volume normalized particle size distribution of 100% Al_2O_3 sample

Taking the power spectral density (PSD) (Fig. 11.41) of the transducer used, the measured attenuation coefficient, and the particle number data from the size range of 0.72–1.25 μm (dictated by Eq. 4) a form for the S parameter is obtained. However, this parameter is in units of pascals and dependent on both the transducer output energy and the volume of the Al_2O_3 grains used as a standard. To obtain a form for the S parameter that is not dependent on the material but rather purely the transducer, we multiply S by the particle surface area at each frequency to obtain the force output of the transducer (Fig. 11.42). After algebraic rearrangement, Eqs. 9 and 10 give the energy loss due to thermoelastic absorption of any number of particles and a form for the number of particles contained in the path of the ultrasound beam, respectively.

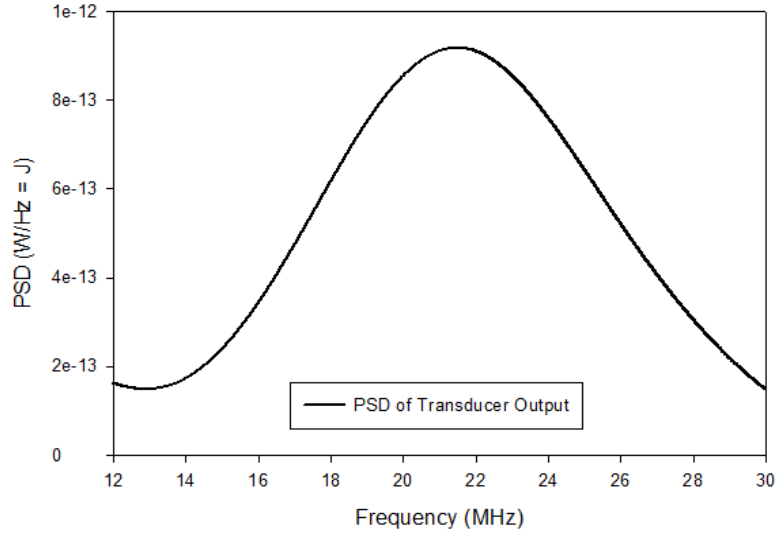


Fig. 11.41 PSD of 20-MHz central frequency transducer (joules)

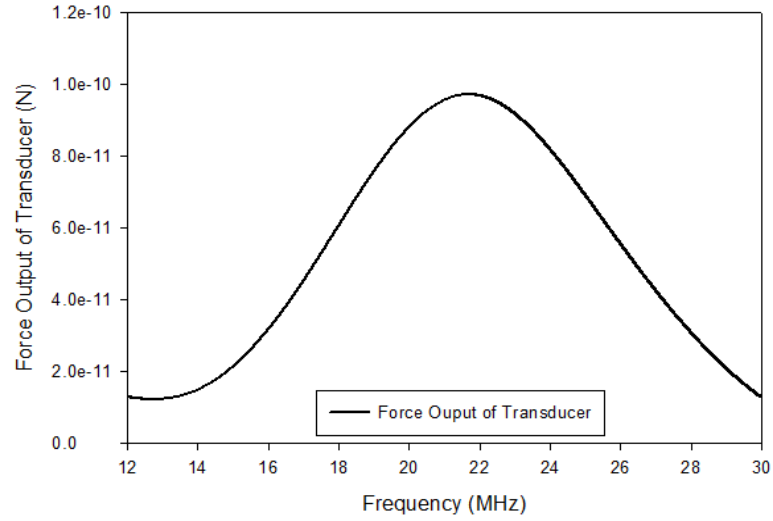


Fig. 11.42 Force output of 20-MHz central frequency transducer (newtons)

$$E_{TE}(f) = \frac{2}{3} F_T(f) \cdot D_{TE}(f) \cdot N_P(f), \quad (9)$$

where F_T is the force output of the transducer and D_{TE} is the diameter of the particles (as given by Eq. 4).

$$N_P(f) = \frac{\pi \cdot E_i(f) \cdot (1 - e^{-\alpha(f) \cdot x})}{4 \cdot F_T(f) \cdot D_{TE}(f)}. \quad (10)$$

Experimental validation of Eq. 10 involves the creation of tailor-made sample sets as described in the following.

Degussa Aerosil silica powder, with an average size of 12 nm, was added to A16 alumina powder, with an average size of approximately 1 μ m, in incremental

amounts between 1 and 5 wt%. These 5 powder mixtures were ball-milled in isopronal for 3 h and allowed to dry to collect the fully mixed products. An SPS unit was used to densify 6 g of each powder mixture. The sintering cycle for each sample used a ramp of 200 °C/min to 1,600 °C and 3.75 MPa/min to 30 MPa and held for 15 min. The sintered products were approximately 20 mm in diameter and 5 mm thick. Each sample had its density measured via the Archimedes method, as shown in Table 11.7. The densities measured were approximately 98% or higher of theoretical based on what was expected to form (from an Al₂O₃-SiO₂ phase diagram—alumina-rich mullite) and a linear rule of mixtures.

Table 11.7 Density and ultrasound measurements of the tailor-engineered alumina sample sets

Sample (% Al ₂ O ₃)	Density (g/cc)	cL (m/s)	cS (m/s)	Poisson ratio	Young's Modulus (Gpa)	Shear Modulus (Gpa)	Bulk Modulus (Gpa)
95	3.76	9908	5945	0.219	324	133	192
96	3.77	10212	6028	0.233	338	137	210
97	3.83	10310	6056	0.237	347	140	220
98	3.84	10414	6040	0.247	349	140	230
99	3.92	10576	6197	0.242	374	151	242
100	3.95	10623	6229	0.234	378	153	237

This study used pulse-echo, immersion-based, automated scanning ultrasound equipment. A 20-MHz central frequency transducer with a bandwidth of 10–30 MHz was used to cover most of the frequency range where thermoelastic absorption occurs. A higher frequency transducer (50-MHz central with a bandwidth of 40–62 MHz) was used to observe scattering behavior. These transducers were acquired commercially from Olympus. The analog to digital converter card (Gage Electronics) has a 3-GHz sampling rate, which allows for the collection of data points every 0.3 ns. The oscilloscope, automated motion, and data acquisition is controlled by a personal computer and software developed at Rutgers-CCR. The motion control unit and scanning frame were acquired through Techno-Isel and the Pulser-Receiver was furnished by JSR Instruments.

Ultrasonic nondestructive characterization makes use of 3 modes of data collection: 1) A-scan, which is a point measurement, 2) B-scan, which is a line measurement, and 3) C-scan, which is a fully mapping of a sample piece. Data is measured by electronically gating specific peaks indicative of sample surface reflections. Time of flight and elastic property measurements are made by recording how long it takes the sound wave to travel through the sample and amplitude and attenuation measurements are collected by measuring the relative change of peak intensity from one bottom surface reflection to another. The ultrasonic data collection mode used for the samples in this study was an A-scan. Speed of sound, elastic properties, and attenuation coefficient spectra were recorded for all samples (Table 11.7).

After ultrasonic testing was performed, the samples were sectioned for ceramographic preparation and XRD analysis. Portions of each sample were set aside for polishing, FESEM imaging, and particle size measurements. This process has yet to be performed and results are not shown in this report. XRD measurements were made on each sample using a Phillips XRD unit. Scans between 10 and 80 two theta with a step size of 0.03° and dwell time of 2 s were taken on each sample. Results show the formation of 2:1 mullite of increasing concentration in the samples containing between 1- and 5-wt% SiO_2 . Comparison between ultrasound results and volume percent of mullite show a one-to-one correlation.

Figure 11.43a shows the measured attenuation coefficient spectra on a range of 10–62 MHz. The disjoint region is due to not having bandwidth overlap between the 2 transducers used. The lower frequency (10–30 MHz) data [Fig. 11.43b] is the frequency range where it is assumed that only thermoelastic absorption is the dominating loss mechanism. The scattering, power-law behavior at higher frequencies is neglected in further analysis. It is assumed that the increase in attenuation from the base 100% Al_2O_3 sample spectra is purely due to thermoelastic absorption. A correlation exists between the amount of the mullite phase present and the increase in attenuation coefficient. The analysis shown in Fig. 11.43 corrects for the increase in attenuation and decrease in alumina as the concentration of the secondary mullite phase increases. This was done by knowing the volume percent of mullite in each sample from XRD measurements.

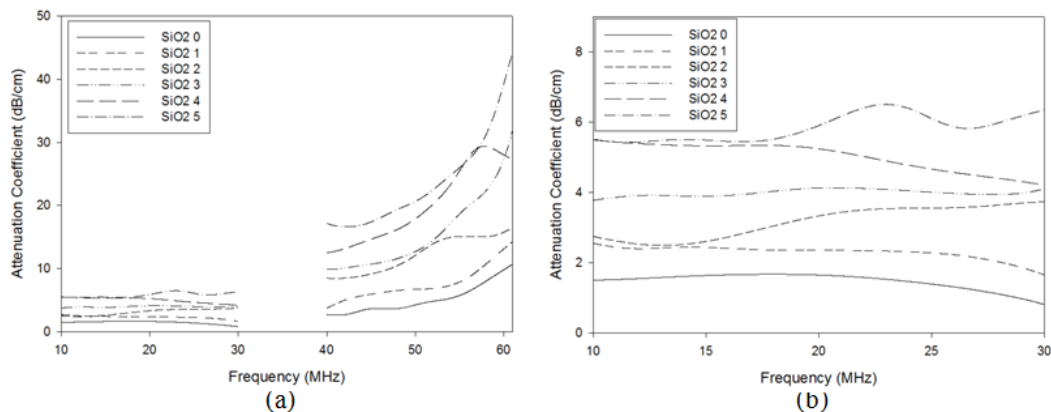


Fig. 11.43 Attenuation coefficient spectra of tailor-made samples: a) 10–62 MHz and b) 10–30 MHz

XRD spectra are shown in Fig. 11.44 (1-wt% SiO_2 ; 5-wt% SiO_2 spectra are from the bottom up). It can be seen (marked by arrows) that these samples have an increase in the amount of the secondary mullite as the SiO_2 concentration increased. This is to be expected and provides a well-defined sample set that correlates to every ultrasound property measured. The volume percents, calculated by XRD

reference intensity ratio method) of 2:1 mullite which formed in samples having between 1- and 5-wt% SiO_2 are 2.1%, 5.6%, 16.3%, 20.6%, and 36.9%, respectively.

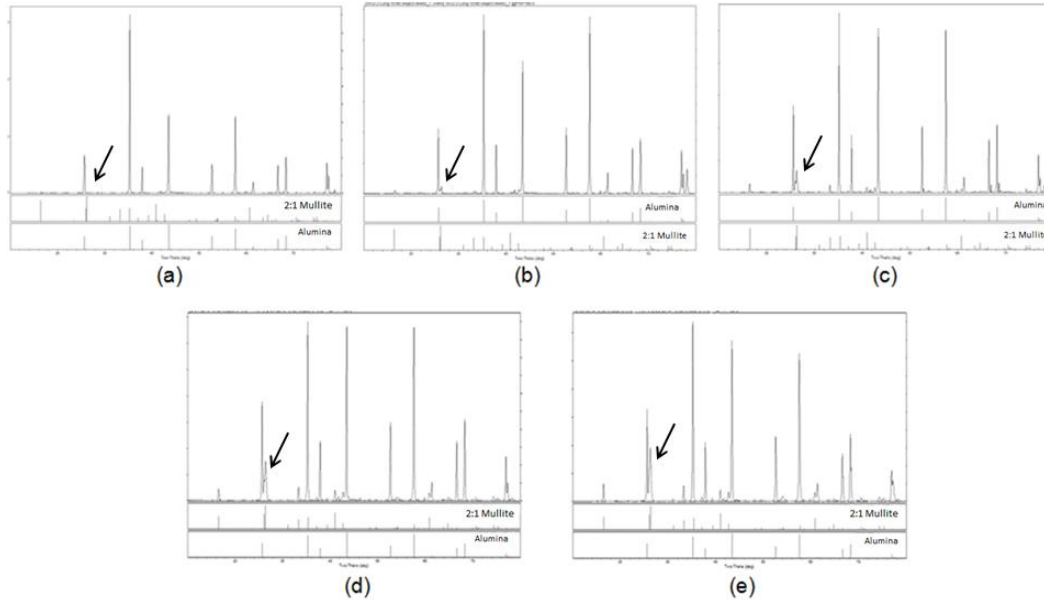


Fig. 11.44 XRD spectra of sample set containing between 1- and 5-wt% SiO_2 . Arrows mark major 2:1 mullite peaks.

Using the derived Eq. 10, the attenuation coefficient spectra from Fig. 11.43b, and accounting for the relative percentages of mullite in each sample obtained from XRD, ultrasonic measurements of particle size distributions were measured on a size scale corresponding to the frequency range as dictated by Eq. 4. The ultrasonic particle size distributions are shown in Fig. 11.45. According to Eq. 4 and using a frequency range of 10–30 MHz, a diameter size range for mullite will be 0.25–0.40 μm . The 5 ultrasound particle size distributions were fit to Gaussian distributions to reconstruct the lower and upper bounds of full-particle-size curves. A lower size limit was set to 0.1 μm and the upper limit was allowed to be as large as necessary. The total volume of the mullite present in the path of the ultrasound beam was calculated from XRD measurements. The reconstructed particle size curves for each sample were extended on the lower and upper bounds from the ultrasound particle size curves such that the total area under the curves was approximately equal to the total volume of the mullite in the volume of the ultrasound beam. The reconstructed curves are shown in Fig. 11.46.

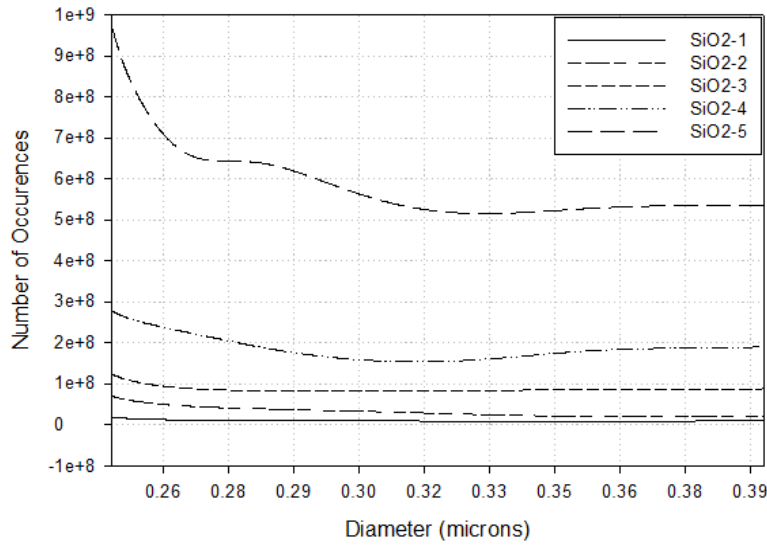


Fig. 11.45 Ultrasonic particle size distribution of SiO₂ sample set

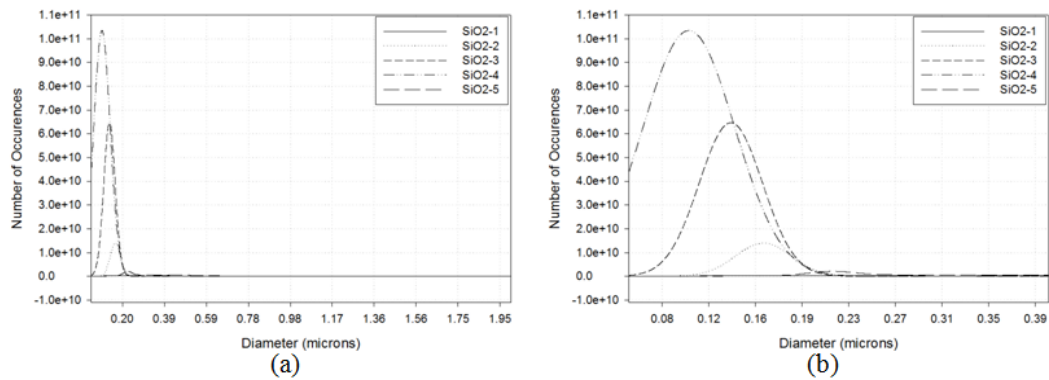


Fig. 11.46 Reconstructed ultrasonic particle size distributions

The reconstructed particle size distributions show an increase in mullite grains, as there is an increase of 1- to 4-wt% SiO₂. The average particle size gets smaller during this increase. For sample SiO₂-5-wt% SiO₂, a different trend is observed: The average particle size increases to approximately 0.21 μm and there are more occurrences of mullite grains up to about 2 μm . This general increase in particle size causes a decrease in the total number of grains at each diameter while maintaining the total volume of mullite in this particular sample. Work is currently being performed to reveal the microstructures of these samples containing varying concentrations of mullite.

11.9 Future Work

11.9.1 Spinel Standard Sample Set for the Determination of Grain Size

Much like how a standard sample that varied grain size for Al_2O_3 was used to determine the Rayleigh and stochastic scattering prefactors C_R and C_S , a standard set of spinel samples is required to predict accurate grain size measurements. This spinel sample set should vary the grain size by a similar method of increasing the firing temperature and the dwell time at the maximum hold temperature. By measuring the average grain size through FESEM imaging, one can obtain the power law prefactors for both Rayleigh and stochastic scattering attenuation. An ideal standard spinel sample set should cover an extremely large range of grain sizes: submicron to hundreds of microns. This will ensure that both Rayleigh and stochastic scattering will be seen across samples.

11.9.2 Custom-Engineered Alumina Sample Set: Varying TiC Concentration

For completeness, another custom-engineered alumina sample set containing incremental amounts of a secondary phase is in the process of being completed. This sample set will include varying concentrations of TiC inclusions, which are to be approximately 0.5–3.0 μm in size, with concentrations ranging from 0 to 35 vol%. This sample set will have similar measurements performed on it to verify what was seen with the SiO_2 custom-engineered alumina sample set. The end result will produce reconstructed-particle-size distributions of the TiC secondary phase. Mechanical sectioning, FESEM imaging, and grain-size distribution analyses will be performed on these samples to corroborate what is predicted through ultrasonic absorption theory.

11.9.3 Custom-Engineered SiC Sample Set: Varying Grain Size and Additive Concentration

Two sets of custom-engineered SiC samples will be produced and examined using ultrasonic NDC techniques. These SiC samples will be made by pressureless sintering with B_4C and C additives. The first set will vary the grain size while keeping additive content constant. The grain sizes in these samples will vary from small 2- to 3- μm grains to large grains of approximately 100 μm in increments of about 10 μm between samples. The second set will vary the additive content while attempting to keep the grain size constant. These samples will ideally contain 0.5, 1, 2, 3, 4, and 5 times the standard production amounts of B_4C additives. Using these sample sets as standards, the constants in the scattering and absorption

equations will be determined for the SiC system. After these constants are determined, it will be possible to nondestructively determine grain sizes and inclusion size distributions in this material.

11.9.4 Ultrasound NDC to Determine Microstructural Homogeneity in SiC Mirrors

SiC mirrors are often used in extreme environments where a conventional mirror material would not survive or perform adequately. Since the process of making and deploying a SiC mirror is expensive and time-consuming, methods for rejecting faulty mirrors prior to deployment must be developed. Additionally, microstructural variations could induce stresses upon thermal cycling that would be deleterious to the lifetime of the mirror in its service environment. In this study, SiC mirrors will be examined using immersion-based ultrasonic NDC techniques. Elastic properties and the overall signal attenuation coefficient will be measured over large sample areas to generate high-resolution C-scan property maps, and acoustic spectroscopy will be performed to measure the frequency dependence of attenuation in the 10- to 80-MHz frequency range. Analysis of elastic property results can identify local variations in density and composition and attenuation coefficient results can be used to estimate relative differences in SiC grain size and secondary phase concentration.

The objective of this study is to determine the feasibility of using ultrasonic NDC techniques to quantify microstructural homogeneity in SiC mirrors, which can be used to determine their suitability for applications in extreme environments. The current sample set for this study includes 2 polished SiC mirrors, including one circular sample and one hexagonal sample, as well as 3 unpolished circular SiC mirror blanks. The samples have varying dimensions and support structures. Previous work had been done on these samples to find large defects and surface aberrations by using conventional NDE techniques like time of flight and amplitude measurements. The new study aims to apply more recently developed NDC techniques to evaluate the microstructural homogeneity of these mirror samples.

11.10 References

1. Uberall H. Dynamics of acoustic resonance scattering from spherical targets: applications to gas bubbles in fluids. *Journal of the Acoustical Society of America*. 1979;66(4):1161–1172.
2. Bouda A. Grain size influence on ultrasonic velocities and attenuation. *NDT & E International*. 2003;36(1):1–5.
3. Schiefer M, Sjöberg L. Physical basis for the resonant acoustic method for flaw detection. [accessed 2015 Jan 26]. <http://www.modalshop.com/techlibrary/Physical%20Basis%20of%20the%20Resonant%20Acoustic%20Method%20for%20Flaw%20Detection%20A6.pdf>.
4. Wolfenden A, Kinra VK. *M³D III: mechanics and mechanisms of material damping*. West Conshohocken (PA): American Society for Testing and Materials; 1997. Special Technical Publication No. 1304.

List of Symbols, Abbreviations, and Acronyms

Al	aluminum
AlN	aluminum nitride
ARL	US Army Research Laboratory
B	boron
B ₄ C	boron carbide
B ₂ O ₃	boron oxide
BZ	Brillouin zone
C	carbon
DFT	density functional theory
DFT-MD	density functional theory-molecular dynamics
DIC	differential interference contract
EDS	energy-dispersive X-ray spectroscopy
FESEM	field emission scanning electron microscope
FFT	fast Fourier transform
GGA	generalized gradient approximation
GUI	graphic user interface
HRTEM	high-resolution TEM
IGF	inter-granular film
LZ	large zone
MCOE	US Army Maneuver Center of Excellence
MD	molecular dynamics (classical)
NDC	nondestructive characterization
NDE	nondestructive evaluation/examination
nm	nanometer
NT	nanotube

PAW	projector augmented-wave
ps	picosecond
SEM	scanning electron microscopy
SiC	silicon carbide
Si ₃ N ₄	silicon nitride
SiO	silicon oxide
SPS	spark plasma sintering
STFT	short-time Fourier transform
TEM	transmission electron microscopy
VASP	Vienna Ab-initio Simulation Package
XRD	X-ray diffraction
Y ₂ O ₃	yttrium oxide

1 (PDF)	DEFENSE TECHNICAL INFORMATION CTR DTIC OCA	T BJERKE D CASEM J CLAYTON (1 HC) D DANDEKAR M GREENFIELD R LEAVY S SEGLETES C WILLIAMS RDRL WMP D R DONEY RDRL WMP E S BARTUS RDRL WMP F N GNIAZDOWSKI RDRL WMS M VANLANDINGHAM
2 (PDF)	DIRECTOR US ARMY RESEARCH LAB RDRL CIO LL IMAL HRA MAIL & RECORDS MGMT	
1 (PDF)	GOVT PRINTG OFC A MALHOTRA	
46 (7 HC, 39 PDF)	DIR USARL RDRL CIH C D GROVE J KNAP RDRL WM P BAKER B FORCH J MCCAULEY (6 HC) P PLOSTINS RDRL WML B I BATYREV B RICE D TAYLOR N WEINGARTEN RDRL WML H B SCHUSTER RDRL WMM J BEATTY R DOWDING J ZABINSKI RDRL WMM B G GAZONAS RDRL WMM E S KILCZEWSKI J LASALVIA P PATEL J SINGH J SWAB RDRL WMP S SCHOENFELD RDRL WMP A S BILYK RDRL WMP B C HOPPEL S SATAPATHY M SCHEIDLER T WEERASOORIYA RDRL WMP C R BECKER	